ABSTRACT

Title of dissertation: ELLIPTIC FLOW AT FORWARD RAPIDITY IN $\sqrt{s_{NN}} = 200$ GeV Au+Au COLLISIONS

Eric Michael Richardson,
Doctor of Philosophy, 2012

Dissertation directed by: Professor Alice C. Mignerey
Department of Chemistry and Biochemistry

Forward rapidity elliptic flow (v_2) of both unidentified charged hadrons and decay muons has been measured from $\sqrt{s_{NN}} = 200$ GeV Au+Au collisions as a function of pseudorapidity (η), transverse momentum, and number of nucleon collision participants. The measurements were performed at Brookhaven National Laboratory's Relativistic Heavy Ion Collider using the PHENIX experiment's Muon Arm spectrometers, located at $1.2 < |\eta| \lesssim 2.4$. To identify hadrons, which consist mostly of pions, kaons, and protons, a longitudinal momentum cut was applied to tracks stopping in the shallow steel layers of the Muon Arms. Those particles traversing completely through the Muon Arms consist of mostly muons from pion and kaon decays. The standard event plane (EP) method was used to measure v_2, whose accuracy was improved ∼20-25% by combining the measured EP angles of several detectors, instead of using the measured EP from a single detector. Additionally, a hit swapping technique was devised to optimize track cuts, estimate background, and apply a background correction. To investigate the ability of the Muon Arms to

accurately measure unidentified hadron v_2, a GEANT simulation was also undertaken.

The forward rapidity v_2 results show good agreement with mid-rapidity measurements for central collisions ($\lesssim$ 20-30% centrality), indicating a longitudinally extended thermalized medium with similar eccentricity, at least out to the Muon Arm η region. Only when compared to very forward BRAHMS measurements ($\eta \approx 3$) is a v_2 suppression seen for central collisions. For increasingly peripheral collisions, a growing suppression in v_2 is observed for the Muon Arm measurements compared to mid-rapidity, indicating increased changes in the medium properties of ever smaller systems. For peripheral collisions of the same/similar centralities, an increased suppression is observed toward forward η.

ELLIPTIC FLOW AT FORWARD RAPIDITY IN $\sqrt{s_{NN}}$ = 200 GeV Au+Au COLLISIONS

by

Eric Michael Richardson

Dissertation submitted to the Faculty of the Graduate School of the
University of Maryland, College Park in partial fulfillment
of the requirements for the degree of
Doctor of Philosophy
2012

Advisory Committee:
Professor Alice C. Mignerey, Chair/Advisor
Professor Thomas D. Cohen
Professor Christopher Jarzynski
Professor Sang Bok Lee
Professor William B. Walters

Acknowledgments

To paraphrase a famous metaphor, the work presented in this dissertation would not have been possible without "standing on the shoulders of giants." However, to mention all the people, living or deceased, who made this analysis possible would require an additional dissertation or two that I will spare both of us from. Instead I will focus on those who most directly aided me in my dissertation research and graduate career while at the University of Maryland and Brookhaven National Laboratory.

I must first thank the best sailor I know, my advisor Alice Mignerey, for navigating me through the treacherous waters of graduate school. Thanks to her guidance and advice I found the lighthouse through the fog. I am also very grateful to ShinIchi Esumi for teaching me the ins-and-outs of azimuthal anisotropy. Taking as much time as he did in answering my many questions was extremely generous and invaluable for my education. I can't stress my appreciation enough.

I also need to thank Chris Pinkenburg and Carla Vale for their computing expertise. Without their help many aspects of this analysis would not have been possible, including producing the background reconstruction data, correcting the SMD channel swap, and performing the PISA simulation. Additionally, both openly welcomed my general computing questions, and Chris specifically welcomed questions about the RXNP online monitoring and my analysis modules when they wouldn't compile. The background reconstruction data would also not have been possible without the guidance of Hugo Pereira Da Costa who helped me modify the Muon

Arm reconstruction code.

My appreciation further extends to several past and present Mignerey group members including Abigail Bickley, who introduced me to PHENIX and its analysis computing framework. While she was at Brookhaven she was a great mentor who set a steller example of how to lead and get things done. And I thank my good friend Richard Bindel for introducing me to C++, ROOT, and heavy-ion collisions. He showed great unselfishness in answering my questions when he could have been working on his own analysis. Our spirited conversations about physics or otherwise were also very enjoyable. I am further grateful to Marguerite Tonjes for not only introducing me to heavy-ion physics, but also providing computing and logistical support to the Mignerey group.

I also thank Robert Pak for his watchful eye on my progress at Brookhaven as well as his guidance and advice. Additionally, I am appreciative of Matt Wysocki for our informative conversations and pointing me to some of his code, which I used as a blueprint for writing some of my own. And I thank John Koster and Seishi Dairaku for their help in correcting the SMD channel swap, and Kohei Shoji for providing me with the physical dimensions of the MuID.

I am further grateful to those members of the RXNP detector group not yet mentioned who helped me along the way, including Wei Xie who was instrumental in all aspects of the RXNP's success, along with Chun Zhang who wrote much of the software. Also critical was Jiangyong Jia who, along with his student Rui Wei, provided me their code for combining event plane angles, which I adapted for this analysis. Thanks also to Yoshimasa Ikeda for his work in constructing, maintaining,

and operating the RXNP. And of course no detector upgrade would be successful without the tireless work of the DAQ team, which was lead by John Haggerty and Martin Purschke.

Of course none of this would be possible without the love and support of my extraordinary family, especially my father and mother, Cody and Margaret Richardson. They provided me with a wonderful childhood along the St. Lawrence River that set the foundation for any past or future success I may achieve. Their enthusiastic interest in all of my endeavors, whether they be sports, hobbies, or academics, has always provided me great comfort. I also want to thank my friends Robert and Kay Smith for their generosity and encouragement in helping me broaden my horizons. I am forever in their debt.

Table of Contents

List of Tables

List of Figures

Glossary of Terms

β	speed parameter
γ	(1) photon, (2) Lorentz factor
$\delta\theta$	opening angle (see Fig. 5.9)
Δz	distance traveled
ϵ_{MB}	min-bias trigger efficiency
ε_{part}	participant eccentricity
ε-F	eccentricity fluctuations
η	(1) pseudorapidity, (2) viscosity (rarely)
θ	polar angle with respect to beam axis
λ_I	hadronic radiation length
μ	muon
π	pion
ρ	nucleon density
σ_{EP}	event plane resolution or event plane correction factor
σ_{NN}	inelastic nucleon-nucleon cross section
σ_x	transverse bunch profile in x direction
σ_{X_n}	distribution widths of the X_n flow vectors
σ_y	transverse bunch profile in y direction
σ_{Y_n}	distribution widths of the Y_n flow vectors
ϕ	azimuthal angle about the beam axis
φ	azimuthal angle with respect the reaction plane
χ^2	variable in a "goodness-of-fit" test quantifying how well an observed distribution fits a hypothesized or theoretical distribution
χ_m	$v_m\sqrt{2N}$
Ψ_{EP}	event plane angle
Ψ_n	n^{th} harmonic event plane angle
Ψ_{RP}	reaction plane angle
$\sqrt{s_{NN}}$	center of mass collision energy per nucleon pair
2D	two-dimensional
a	related to width of nucleus' edge region or "skin depth"
Al	aluminum
ADC	analog to digital converter
AGS	Alternating Gradient Synchrotron
APD	avalanche photodiode
Ar	argon
Au	gold
b	barn
b	impact parameter
BB	Buffer Boxes
BBC	Beam Beam Counter
BES	beam energy scan
BNL	Brookhaven National Laboratory

Glossary of Terms (continued)

c	speed of light
C	carbon
$c\tau$	mean proper lifetime
centrality	% of collisions having more geometric overlap than current collision
CERN	European organization for nuclear physics
CF_4	carbon tetrafluoride
CO_2	carbon dioxide
CPU	central processing unit
Cu	copper
DAQ	data acquisition system
DCM	Data Collection Module
DDG0	opening angle between MuTr track projection to MuID gap 0 and the associated road (see Sec. 5.4.1)
DG0	distance between MuTr track projection at MuID gap 0 and the associated road (see Sec. 5.4.1)
e	electron or positron depending on charge
E	energy
EP	event plane
eV	electron volt
f	beam revolution frequency
f'	bunch crossing frequency
Fe	iron
FEM	Front End Module
FVTX	Forward Silicon Vertex Detector
GF	Gaussian fluctuations
HPSS	High Performance Storage System
i-C_4H_{10}	isobutane
I-Hd	ideal hydrodynamics
IR	interaction region
k	multiplier such that $n = km$
K	kaon
KE_T	transverse kinetic energy
L	(1) integrated depth of absorber material, (2) nuclei's measured length in laboratory's reference frame
L_0	nuclei's length when at rest
$\mathscr{L}$	instantaneous luminosity
$\mathscr{L}_i$	integrated or delivered luminosity
$\mathscr{L}_r$	recorded or collected luminosity
LHC	Large Hadron Collider
m	m^{th} harmonic of azimuthal particle distribution, (2) mass
MC	Monte Carlo simulation
min-bias	minimum bias

Glossary of Terms (continued)

MPC	Muon Piston Calorimeter
MuID	Muon Identifier
MuTr	Muon Tracker
n	(1) n^{th} harmonic of azimuthal particle distribution, (2) number of beam bunches
N	north
N	number of particles
N_2	nitrogen gas
N_{evts}	number of events
N_{MB}	number of min-bias events
N_{part}	number of nucleons interacting in collision
n_q	number of quarks in hadron
ndf	number of degrees of freedom
O	oxygen
p	proton
p	total momentum
P	decay probability
$p\delta\theta$	opening angle between the MuTr station 1 momentum vector and position vector, multiplied by the average of the particles momentum before and after the initial absorber (see Sec. 5.4.1)
p_{st1}	total momentum vector at MuTr station 1
p_T	transverse momentum
p_{tot}	total momentum at MuTr station 1
p_{vtx}	total momentum at the vertex
P_x	floating fit parameter number x
p_z	longitudinal momentum
Pb	lead
$PbWO_4$	lead tungstate
PHENIX	Pioneering High Energy Nuclear Interaction eXperiment
PISA	PHENIX integrated simulation application
PMT	photomultiplier tube
q	quark
$\overline{q}$	antiquark
QA	quality assurance
QCD	Quantum Chromo Dynamics
QED	Quantum Electro Dynamics
QGP	quark gluon plasma
r	distance from center of nucleus
R	nuclear radius
raw_n	n^{th} harmonic raw resolution ($\langle\cos[km(\Psi_m^a - \Psi_m^b)]\rangle$) at 23% centrality
RCF	RHIC Computing Facility

Glossary of Terms (continued)

Reco	reconstructed simulation data
RHIC	Relativistic Heavy Ion Collider
RP	reaction plane
ROOT	object oriented C++ library developed for particle physics analyses
RXNP	Reaction Plane Detector
S	south
SL4	Scientific Linux 4
SL5	Scientific Linux 5
SM	Standard Model
SMD	Shower Maximum Detector
T	Tesla
T_N	particle arrival time at BBC_N
T_S	particle arrival time at BBC_S
v_2	elliptic flow anisotropy parameter (second harmonic)
v_m	m^{th} harmonic anisotropy parameter
v_n	n^{th} harmonic anisotropy parameter
v_{st1}	position vector at MuTr station 1
w	weighting value
W	tungsten
W_n	n^{th} harmonic weighting value when combining the event flow vectors of different detectors
X_n	magnitude of n^{th} harmonic event flow vector in x direction
y	rapidity
y_0	rapidity of nominal vertex
y'	rapidity of traversing particle
Y_n	magnitude of n^{th} harmonic event flow vector in y direction
z	collision position along z-axis, *i.e.* z-vertex
ZDC	Zero Degree Calorimeter
ZDC−SMD	Zero Degree Calorimeter − Shower Maximum Detector

Prologue

Like atomic matter, nuclear matter has different phases that scientists strive to characterize. One of these phases, called the *quark gluon plasma* (QGP), is created in the laboratory using racetrack size particle accelerators that collide heavy-ions at nearly the speed of light. One such collider is Brookhaven National Laboratory's Relativistic Heavy Ion Collider (RHIC), which collides gold (Au) nuclei at a center of mass energy per nucleon pair ($\sqrt{s_{NN}}$) of 200 GeV. Under the extreme temperature conditions provided by RHIC, the Au nuclei's protons and neutrons "melt" into their more fundamental components, quarks and gluons, essentially unshackling them from their nucleon cages. Once liberated, the quarks and gluons are able to move freely throughout the created medium; thus, forming a QGP, if only for a short time.

Scientists search for insights into the properties of the QGP by studying the particles emitted from the collision, in what can be described as the ultimate feat of reverse engineering. Originally, it was thought the QGP would behave much like the weakly interacting plasmas of atomic matter [1]. To their surprise, the QGP exhibited the properties of a strongly interacting liquid undergoing rapid thermalization that could be described well by hydrodynamic models.

One of the key measurements leading to this conclusion was the strong azimuthal anisotropy of emitted particles about the beam axis, referred to as *elliptic flow*. This asymmetric distribution is a consequence of the elliptic shape of the colliding nuclei's overlapping nucleons. If the created medium is strongly interacting,

rapid binary collisions occur between the particles, leading to early thermalization. In turn, this will lead to asymmetric pressure gradients due to the elliptic shape of the medium, with a steeper gradient being in the direction of the shorter axis. This results in more particles moving in the direction of the short axis than the long axis, leading to the measured asymmetry. On the other hand, if the medium was weakly interacting, the pressure gradients wouldn't develop and the medium would expand isotropically.

Elliptic flow, whose strength is quantified by the variable v_2, has been measured by all four RHIC experiments: BRAHMS, PHENIX, PHOBOS, and STAR. Most of these measurements have been done at near perpendicular angles to the beam axis at the collision point, referred to as mid-rapidity. Mid-rapidity is more quantitatively described as $|\eta| \lesssim 1$, where pseudorapidity (η) is a unitless relativistic quantity describing the polar angle of the emitted particle with respect to the beam axis (see Appendix A). v_2 has been less studied at forward η, where additional insights into the created medium await to be discovered.

The analysis performed in this dissertation measured v_2 of unidentified charged particles at forward η using PHENIX's Muon Arm spectrometers, located at $1.2 < |\eta| \lesssim 2.4$. The Muon Arms allow for a unique measurement at RHIC because they are the only detectors capable of measuring a particle's transverse momentum (p_T) throughout the entirety of this region. The STAR experiment has detector coverage within $|\eta| < 1$ and $2.5 < |\eta| < 4.0$, with a gap in-between that is almost completely covered by the Muon Arms. The PHOBOS experiment has detector coverage of $|\eta| < 5$, but only p_T capability within $0 < \eta < 1.5$. The BRAHMS experiment utilizes

a very narrow movable detector, but has not measured flow within the Muon Arm region. These circumstances provide PHENIX the opportunity to perform a unique measurement.

This Muon Arm v_2 measurement can provide additional insights into how the medium's properties evolve toward forward angles. Are there changes to its longitudinal expansion, such as shape or thermalization? Does thermalization breakdown at forward angles or is it similar to mid-rapidity? How much does the system size or energy density play a role? According to PHOBOS and STAR $v_2(\eta)$ measurements, shown in Fig 1, v_2 decreases toward forward η, indicating changes to the medium. However, these measurements do not take into account changes in $\langle p_T \rangle$, which v_2 is heavily dependent on. Therefore, it is not clear whether the change in v_2 is due to a changing medium, a changing $\langle p_T \rangle$, or a combination of the two. With the ability to measure a particle's p_T, the Muon Arms provide the capability to address these and other questions by disentangling the $\langle p_T \rangle$ effects. It will also give theorists complementary constraints to their models from those constraints provided by mid-rapidity, allowing them to develop a more complete 3-dimensional understanding of the created medium.

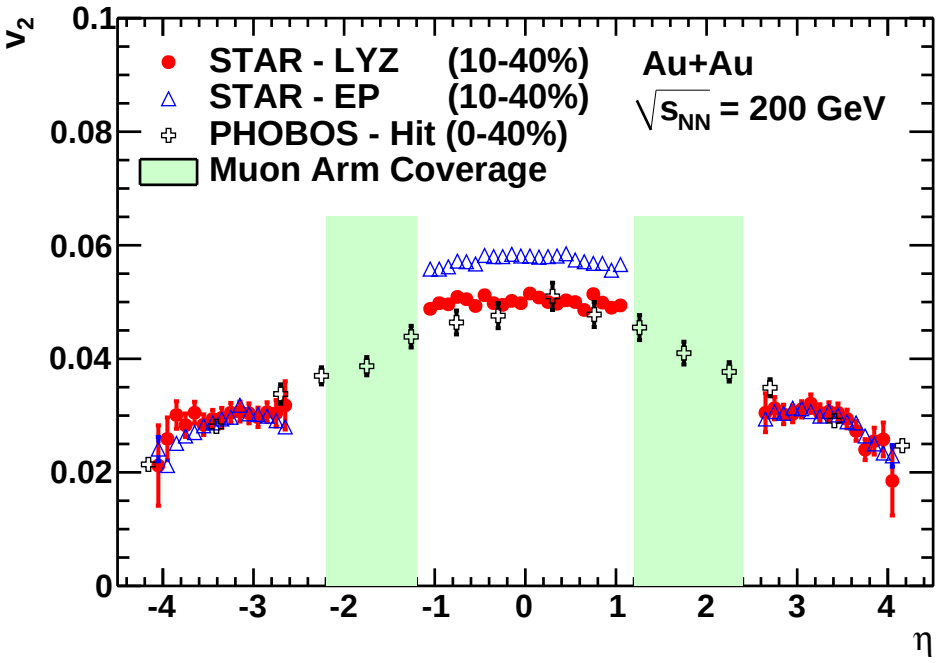

Figure 1: STAR and PHOBOS $v_2(\eta)$ from $\sqrt{s_{NN}} = 200$ GeV Au+Au collisions [2, 3]. Two STAR results from 10-40% centrality collisions and 0.15 GeV/c $< p_T <$ 2.0 GeV/c are shown using independent methods: Lee-Yang Zero (LYZ) method (circles), and Event Plane (EP) method (triangles). PHOBOS results from 0-40% centrality collisions using an Event Plane Hit-based (Hit) method requiring no p_T information are displayed using crosses. Only statistical errors are shown. The coverage of the Muon Arms is indicated by the green bands. For a discussion about collision centralities or the Event Plane Method used in this analysis see Sec. 4.2.2 and 5.1, respectively.

Chapter 1

Introduction

1.1 The Standard Model

As we wake up in the morning we immediately encounter the effects of two of natures fundamental forces, gravity and electromagnetism. Gravity is the force that keeps us grounded to our bedroom floor and electromagnetism is the force that prevents us from falling through it. At the macroscopic level these forces are mediated through smooth and continuous fields known as the gravitational and electromagnetic fields. However, at the quantum scale, forces are mediated by fields of quantized force carriers called *quanta*, where, in the case of the electromagnetic force, the quanta is the photon (γ).

This intuitively bizarre theory is called the *quantum field theory* and it is one of the key elements to what is known as the *Standard Model* (SM). The SM is simply a theory, supported by experimental evidence (see Sec. 1.1.2), that describes how matter interacts at the most fundamental quantum scale. Some of the key aspects of the SM are as follows.

1.1.1 Fundamental Particles

At the heart of the SM are the three types of fundamental particles: *quarks* and *gauge bosons*, collectively referred to as *partons*, and *leptons*. Gauge bosons,

Table 1.1: Gauge Bosons [4, 5]

Gauge Boson	Interaction	Mass (GeV)	Strength	Range	Acts on
gluon	strong	0	1	10^{-15} m	hadrons
γ	electromagnetic	0	10^{-2}	$1/r^2$	electric charges
$W^{\pm}$, Z^0	weak	80.4, 91.2	10^{-5}	10^{-18} m	hadrons/leptons
graviton	gravity	0	10^{-39}	$1/r^2$	masses

previously referred to as quanta, are the force carrying particles that mediate the *strong*, *weak* and *electromagnetic* forces. The gauge bosons for these forces are the *gluon*, $W^{\pm}$ and Z^0, and photon, respectively. Natures fourth known fundamental force, *gravity*, which is not incorporated into the SM, is theorized to be mediated by the *graviton*, but that has not yet been experimentally confirmed. Table 1.1 lists the gauge bosons, including the theorized graviton, along with some of their properties.

The second set of fundamental particles are leptons, listed in Table 1.2 along with their antiparticles. Of the six known leptons, the most well-known is the electron (e), which orbits the nucleus of atoms. The ν_{L} (Lightest), ν_{M} (Middle), ν_{H} (Heaviest), and their antiparticles are categorized as (anti)neutrinos, and can each be *flavored* as an e, μ, or τ (anti)neutrino. For example, an electron flavored neutrino would be ν_{e}. Leptons are divided into three generations, where, for the non-neutrino leptons, the lower the generation number the smaller the mass and the more stable the particle. This is evident by their half-lives. This generation mass trend is generally observed for the neutrinos, but the current uncertainty in their mass determination causes their ranges to overlap. Additionally, all leptons are able to undergo weak interactions, such as in the Feynman Diagram in Fig 1.1(a). However, only those that carry a charge are able to interact through the electromagnetic force

Table 1.2: Leptons [4–6]

Lepton	Antiparticle	Charge	Mass (MeV)	Half-life (s)	Generation
e^-	e^+	± 1	0.511	∞	1
ν_L	$\overline{\nu}_L$	—	$(0 - 0.13) \times 10^{-6}$	∞	1
μ^-	μ^+	± 1	105.7	2.2×10^{-6}	2
ν_M	$\overline{\nu}_M$	—	$(0.009 - 0.13) \times 10^{-6}$	∞	2
τ^-	τ^+	± 1	1777	291×10^{-15}	3
ν_H	$\overline{\nu}_H$	—	$(0.04 - 0.14) \times 10^{-6}$	∞	3

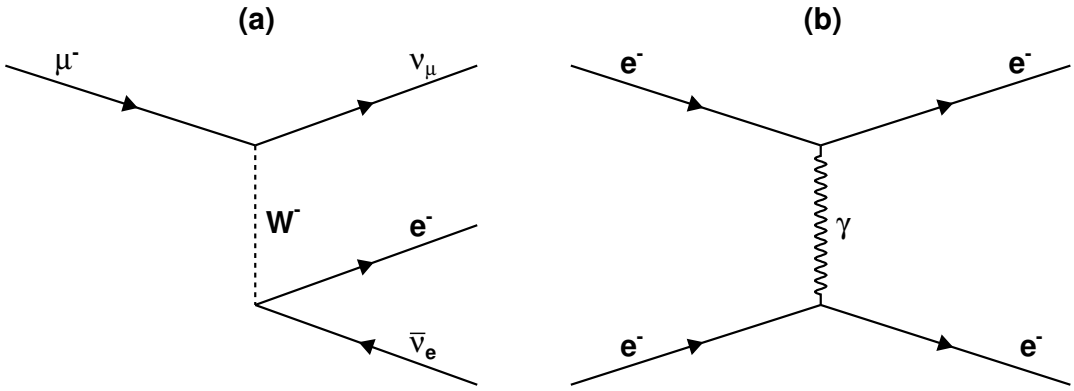

Figure 1.1: Feynman Diagrams of lepton interactions. (a) The weak decay of a μ^- into an e^-, $\overline{\nu}_e$, and ν_μ, with the W^- gauge boson mediating the reaction. (b) An electromagnetic interaction with two electrons exchanging a photon and scattering. Adapted from [5].

via the photon, such as in Fig 1.1(b). Regardless of the mediating force, all reactions involving leptons must conserve charge, lepton generation, and total lepton number, where leptons and their antiparticles have a lepton number of +1 and -1, respectively.

The third and final set of fundamental particles are quarks, listed in Table 1.3. There are six different types or flavors of quarks (q) along with their antiquarks ($\overline{q}$). Like leptons, all quarks[1] can undergo a weak interaction and are divided into three generations with the same trends in mass and stability as the leptons. Additionally, since all quarks carry a charge, they can also all undergo an electromagnetic inter-

[1]Depending on its contextual use, the term "quark" can simultaneously refer to both quarks and antiquarks, such as in this case.

Table 1.3: Quarks [4, 5]

Quark	Symbol	Charge	Antiparticle	Anticharge	Mass (MeV)	Generation
up	u	+2/3	$\overline{\mathrm{u}}$	–2/3	1.7–3.3	1
down	d	–1/3	$\overline{\mathrm{d}}$	+1/3	4.1–5.8	1
strange	s	–1/3	$\overline{\mathrm{s}}$	+1/3	101	2
charm	c	+2/3	$\overline{\mathrm{c}}$	–2/3	1270	2
bottom	b	–1/3	$\overline{\mathrm{b}}$	+1/3	4190	3
top	t	+2/3	$\overline{\mathrm{t}}$	–2/3	172000	3

action with other charged particles, including fellow quarks and charged leptons. However, unlike leptons, quarks carry an additional property called *color*, allowing them to interact via the strong force, but more on that in Sec 1.1.2.

The main difference between a charged particle and its corresponding antiparticle is their opposite charge, with essentially all other properties being identical. This results in a special relationship because, to obey conservation laws such as charge or momentum, a particle cannot be created from the vacuum (empty space) without its antiparticle. Particle-antiparticle pairs can also undergo a unique reaction called an *annihilation*, where the two particles annihilate each other with the release of energy, such as in

$$\mathrm{e}^- + \mathrm{e}^+ \rightarrow 2\gamma. \tag{1.1}$$

This phenomenon is possible due to mass being just another form of energy, as stated in Einstein's famous equation $E = mc^2$, where E represents energy, m mass, and c the speed of light. Neutral particles, like the photon and Z^0, are their own antiparticles and consequently given the name *Majorana* particles. It is not known if neutrinos are Majorana particles, but determining this by searching for the hypothesized neutrinoless double β decay reaction is an active field of study [7].

Table 1.4: Baryons and Mesons [4]

Particle	Quarks	Charge	Spin	Mass (MeV)	Half-life (s)
p	uud	+1	1/2	938	$> 6.6 \times 10^{36}$
n	udd	0	1/2	940	885.7
π^+	$u\bar{d}$	+1	0	140	2.60×10^{-8}
π^-	$\bar{u}d$	–1	0	140	2.60×10^{-8}
K^+	$u\bar{s}$	+1	0	494	1.24×10^{-8}
K^-	$\bar{u}s$	–1	0	494	1.24×10^{-8}

In addition to quarks, leptons, and gauge bosons, particles, including non-fundamental particles, can be classified into other groups as well. For instance, (anti)quarks can coalesce into groups of three (qqq, $\overline{qqq}$) to produce (anti)*baryons* and a quark-antiquark pair ($q\bar{q}$) is called a *meson*. The most familiar baryons are the proton (p), composed of the *uud* quarks, and the neutron (n), composed of the *udd* quarks. The mesons are plentifully produced in particle colliders, but are not stable and quickly decay. Together, baryons and mesons make up what are called *hadrons*, which are simply particles made of quarks that, therefore, interact via the strong interaction. Table 1.4 lists some well-known hadrons. Notice in the table that despite being composed of fractionally charged quarks, all hadrons have an integer charge.

Two other categories of particles called *fermions* and *bosons* distinguish particles based on their integral spin. Fermions have 1/2 integral spin and bosons have integral spin. Since quarks have a spin of 1/2, baryons (qqq, $\overline{qqq}$) are fermions, while mesons ($q\bar{q}$) are bosons. Leptons have $\pm 1/2$ spin and are therefore fermions, while gauge bosons have integral spin and are bosons. Figure 1.2 shows a summary of the particle classification hierarchy.

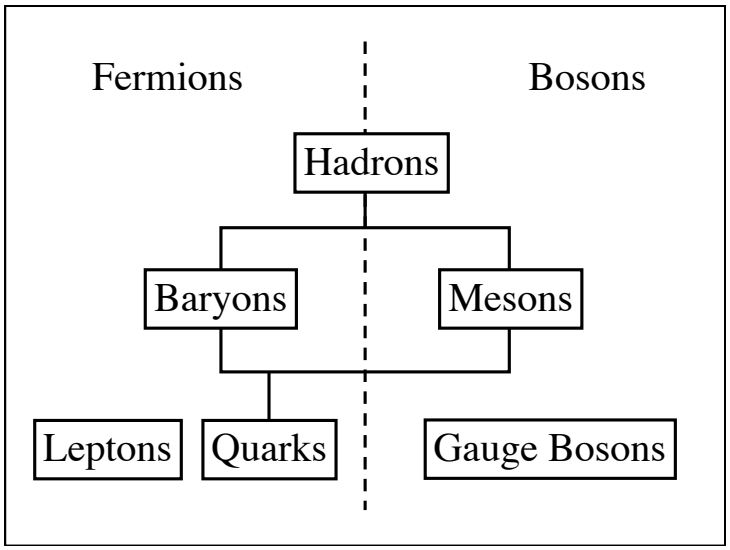

Figure 1.2: Particle classification hierarchy. Adapted from [5].

1.1.2 Quantum Chromodynamics

Incorporated into the SM is the theory of *Quantum Chromodynamics* (QCD), which is the theory of the strong force, or "color force" as it is sometimes referred to, and describes the interactions of quarks and gluons. This theory borrows concepts from a more mature theory, *Quantum Electrodynamics* (QED), which is the theory of the electromagnetic force at the quantum scale and describes how photons interact with charged particles or how charged particles interact with each other by exchanging photons. Chemists are quite familiar with QED through such phenomena as the photoelectric effect, lasers, and spectroscopy, including its plethora of instrumentation.

Similarly to the electric charge in QED, QCD describes the *color charge* inherent in both quarks and gluons, which manifests itself as the strong force. Quarks can have any one of three colors (*red*, *blue*, *green*), while antiquarks can have any one

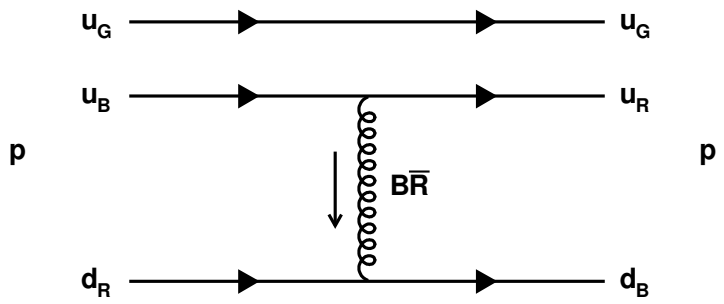

Figure 1.3: Feynman Diagram of a gluon interaction changing the color of two quarks in a proton. Here a blue-antired gluon is transferred from a u_B quark to a d_R quark, effectively swapping their color charge. Adapted from [5].

of three *anti*colors (*anti*red, *anti*blue, *anti*green). However, this property doesn't have actual color, as its used in the vernacular, but is just simply the name given to the property. All hadrons are *colorless* or *color neutral*, meaning that (anti)baryons contain one quark of each (anti)color and mesons contain one quark of color and one antiquark with the corresponding anticolor, for instance red and antired. On the other hand, gluons simultaneously poses color and anticolor and their exchange can change the color of quarks, as shown in Fig. 1.3.

Through exchanging gluons, quarks are held together into hadrons such as the proton and neutron, which are the two *nucleons* that make up the atomic nucleus, with the exception of hydrogen and its proton only nucleus. As is given by its relative strength in Table 1.1, the strong force is significantly stronger than the other fundamental forces. In fact, it is so strong that its residual force is what binds nucleons together in the nucleus. However, its short range, also listed in the table, means that its effects are not felt outside the nucleus.

One of QCD's most peculiar properties is called *asymptotic freedom*. This

strange concept states that the strong force actually decreases in strength the shorter the distance between quarks, and grows in strength the larger the distance. This behavior is converse to gravity and electromagnetism and can therefore be difficult to grasp, but one can think of it as analogous to stretching a rubber-band. This peculiar behavior leads to a phenomena called *confinement*, meaning that quarks are confined to hadrons and cannot freely escape. As illustrated in Fig. 1.4, if energy is added to a $q\overline{q}$ pair, the distance between the quarks will grow and the gluons holding them together will begin to "stretch", increasing the potential energy of the bond. If this process continues, eventually the potential energy between the $q\overline{q}$ pair will grow so great that the gluons will essentially "snap" with the simultaneous creation of a new $q\overline{q}$ pair in-between the original pair. The original quarks then form new quark pairs from the newly produced quarks; thus, relieving the system's stress. Hence, nature has literally deemed the creation of a new $q\overline{q}$ pair more favorable than separating the original $q\overline{q}$ pair any further. This also explains why no individual quark has ever been experimentally observed. This creation of new particles from the vacuum is possible due to Einstein's equation $E = mc^2$ and is the main driver of particle production in particle accelerator collisions. Asymptotic freedom and confinement may seem like fiction, but there is substantial experimental evidence to support the quark and QCD model.

One of the strongest pieces of evidence for quarks comes from deep inelastic scattering experiments [8–10], where inelastic refers to kinetic energy being lost or transferred between the reaction participants. In these experiments a high energy electron with a wavelength much shorter than the radius of a proton is collided with

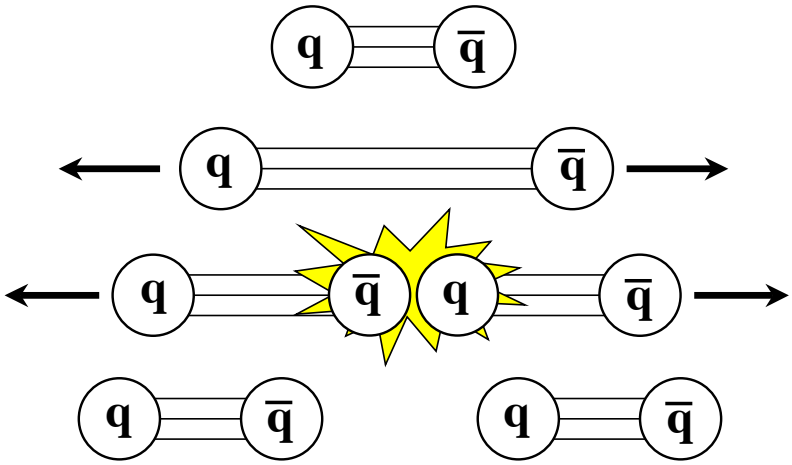

Figure 1.4: Illustration of quark confinement that leads to quarks being confined to hadrons, in this case mesons. See text for details. Adapted from [6].

a proton in order to probe its internal structure. What these scattering experiments have shown is that the proton contains three point like particles, *i.e.* quarks, just as the SM predicted there would be. Other strong evidence arises from the excited states of the proton [11]. Analogous to an atom, which can become excited when an orbital electron absorbs a photon, the proton can also absorb a photon. This leaves the proton in an excited state, indicating that it, like the atom, is not a fundamental particle. Further supporting the quark theory is the discovery of the magnetic moment of the neutron [12, 13], which is hard to explain without the neutron having an internal structure of charged particles.

Along with supporting the quark theory, reactions such as [14]

$$e^- + p \rightarrow e^- + p + \pi^0, \tag{1.2}$$

where a neutral meson is produced while the collision reactants are preserved, also supports the theory of QCD. This is because the reaction is difficult to explain

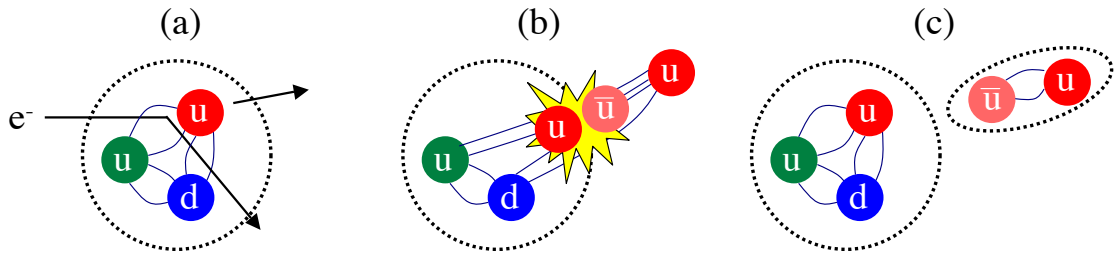

Figure 1.5: Illustration of confinement through the experimentally measured inelastic reaction $e^- + p \rightarrow e^- + p + \pi^0$. See text for a step-by-step explanation. Adapted from [15].

if protons are fundamental particles, but is easily explained using quark and QCD theory, as illustrated in the Fig. 1.5 example. In (a) the incident electron inelastically scatters off one of the proton's u quarks, transferring some of its kinetic energy and "knocking" the u quark out of the proton. In (b), because of quark confinement, the ejected quark cannot freely escape the proton. Instead, the gluons in the proton stretch from the newly added energy until they snap, leading to the production of a $u\overline{u}$ pair from the vacuum. In (c), the newly created $\overline{u}$ forms a π^0 with the ejected u and the newly created u replaces the ejected u in order to reform the proton. This is a simple example of confinement at work.

Another piece of evidence for QCD comes from the fact that quarks are fermions and must therefore obey the Pauli exclusion principle. Thus, multiple quarks cannot occupy the same hadron with the same quantum numbers. However, before the introduction of the concept of color charge, the Δ^{++} baryon with its uuu quark constituents did just that. Introducing the color charge solved this problem by making the quarks distinguishable based on their color charge. For mesons this problem does not arise since they are composed of a quark and antiquark, which are

distinguishable without color charge.

1.2 Heavy Ion Collisions

Analogous to macroscopic atomic matter, nuclear matter can also exist in different phases. For atomic matter, these phases are often represented in a phase diagram with the variables of temperature and pressure. For nuclear matter, the variables are often temperature and baryon density, which is simply the density of baryonic matter, *e.g.* protons and neutrons. Examples of these phase diagrams are shown in Fig. 1.6. In this phase quarks and gluons are confined to hadrons, as illustrated in Fig 1.7(a). The properties of this phase are described well by the liquid drop model and said to be a nuclear liquid phase. With increasing temperature, a phase change occurs to a nuclear gas, which is followed by a transition to a *quark gluon plasma* (QGP) phase that is characterized by the free movement of quarks and gluons beyond hadron boundaries. In this manner, the QGP phase is achieved due to an increase in parton density from particle production (see Sec. 1.2.1). If the density becomes great enough, hadronic boundaries will begin to blur allowing quarks and gluons to overcome hadron confinement. Once *deconfined*, the partons are able to move freely throughout the medium, as shown in Fig. 1.7(b). In this process it is important to point out that although the net baryon density decreases, the overall parton density of the medium increases.

Of particular note in the nuclear phase diagram is the critical point, whose conjectured position is displayed in Fig. 1.6(b). The critical point is the point where

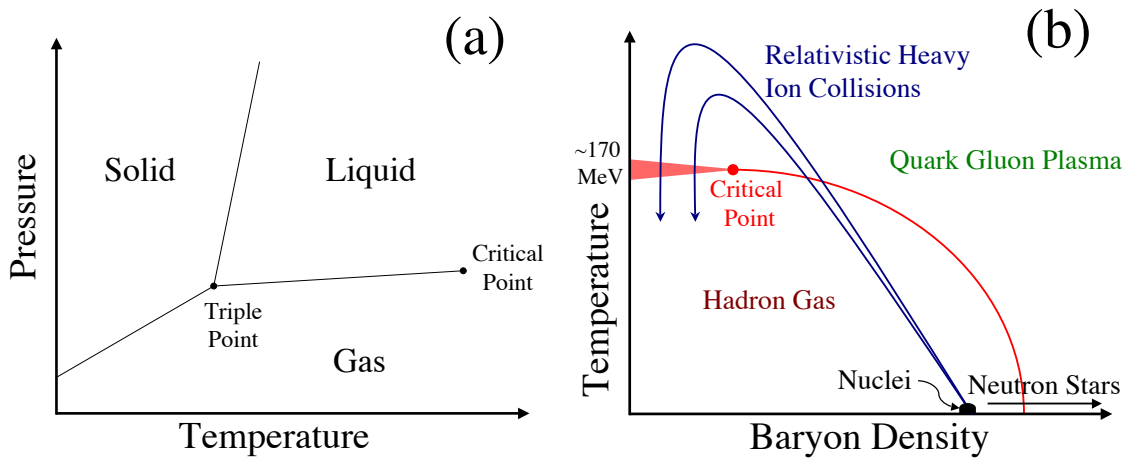

Figure 1.6: A typical phase diagram for (a) macroscopic atomic matter and (b) nuclear matter. Adapted from [16].

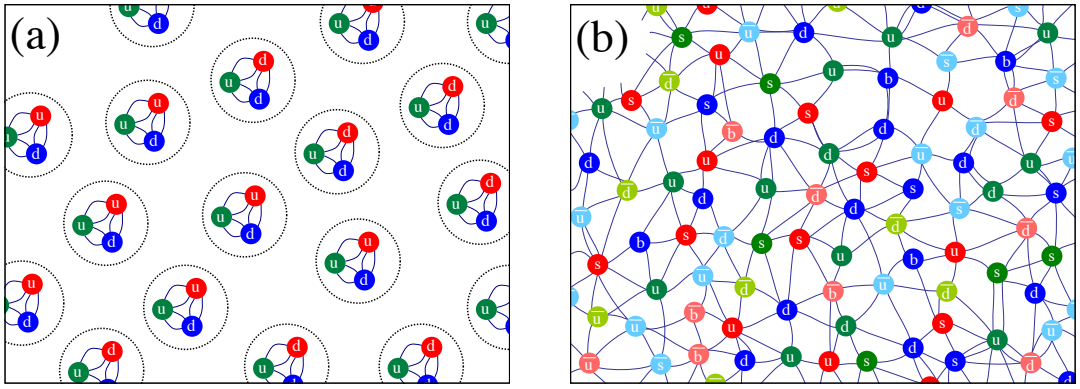

Figure 1.7: (a) The normal hadronic phase of nuclear matter where quarks and gluons are confined to hadrons. (b) Nuclear matter under extreme conditions of temperature, where quarks and gluons undergo a phase transition to a deconfined state of matter called a quark gluon plasma. In this phase quarks and gluons are no longer confined to hadrons, but are able to move freely throughout the medium. Adapted from [15, 17, 18].

the properties of the hadron gas and QGP phases are so alike they are indistinguishable. To its right in the figure there is a sharp phase transition illustrated by the thin red line. To its left there is a smooth crossover between the two phases where both can coexist. This is signified by the broader red band.

Until recently a QGP was not achievable in the laboratory so it was in the realm of the theorists. However, with the commissioning and running of several new particle accelerators [19–22], this new phase of matter can now be researched through the collisions of heavy nuclei. The next section will characterize these heavy-ion collisions and the evolution of the medium they create.

1.2.1 Event Evolution

In principle, two approaches can be taken to access the QGP region of the nuclear phase diagram. The first approach is to increase the baryon density by compressing the nuclear matter. However, these conditions cannot be created in today's laboratories, but can only be done with the large gravitational force of neutron stars. The second approach involves increasing the temperature of the nuclear matter to $\sim$170 MeV[2] $\approx 2 \times 10^{12}$ Kelvin (K) [23], where a phase transition to a QGP is theorized to occur. This is equivalent to an energy density of $\sim$1 GeV/fm^3 or about an order of magnitude higher than cold nuclear matter (0.14 GeV/fm^3 [24]). As indicated in Fig. 1.6(b), this can be achieved in the laboratory with particle accelerators that collide heavy nuclei at nearly the speed of light.

[2]One eV is the amount of kinetic energy gained by an electron after being accelerated through a potential difference of 1 volt.

For instance, the Relativistic Heavy Ion Collider (RHIC) [19, 20] accelerates bare gold (Au) nuclei (79 protons, 118 neutrons, and 0 electrons) to an energy of 100 GeV/nucleon, equivalent to 99.996% the speed of light. At that energy, the ∼14 fm diameter spherical nuclei when at rest would be longitudinally flattened due to *Lorentz Contraction*[3] into an oblate spheroid or thin "disk" having a thickness of 0.13 fm when viewed from the laboratory's frame of reference. Once this energy is achieved, the nuclei are then collided with a beam of oncoming Au nuclei of the same energy, for a total center of mass energy per nucleon pair ($\sqrt{s_{NN}}$) of 200 GeV. From hereafter, any reference to a beam energy will be assumed to be in the context of $\sqrt{s_{NN}}$ unless otherwise indicated. When they collide, the nuclei overlap one another for 0.13 fm/c or $4.38 \times 10^{-25} s$ and have a temporary mean energy density of 2920 GeV/fm^3. Although far above the predicted 1 GeV/fm^3 necessary for creating a QGP, this energy density is fleeting and quickly wanes as the nuclei finish passing through and interacting with one another.

From this interaction, the nuclei become excited and begin to fracture and dissipate, while at the same time radiating particles in their wake. More particles are then created through the particle production mechanism of confinement described in Sec. 1.1.2. If the overlap between the nuclei is large during their crossing, then thousands of particles will be created. These particles generally have a momentum of $\lesssim 3$ GeV/c and are said to come from *soft* physics, while higher momentum particles, called *jets*, come from *hard* physics. Jets result from the elastic or hard scattering of quarks or gluons from the original nuclei and are characterized by a

[3]For a brief discussion of Lorentz Contraction see Appendix B.

large momentum transfer away from the beam direction. To conserve momentum these high momentum particles are often created in pairs called *di-jets* that traverse the newly created medium undergoing gluon radiation, which is similar to the Bremsstrahlung[4] radiation electrons can experience in QED. As the jets exit the medium they fragment due to confinement, producing a cone shaped cluster of particles. Another particle production mechanism is gluon fusion where two gluons can fuse to create heavy particles such as the J/ψ ($c\bar{c}$), but such reactions, along with jets, are rare at RHIC energies. Along with newly produced particles, some of the original particles from the colliding nuclei can become entangled in and interact with the newly created medium as well.

From these and other particle production mechanisms, the particle density of the medium begins to significantly rise, causing the hadronic boundaries of the particles to become blurred and quark confinement to become weakened. If the particle density becomes high enough, deconfinement will occur resulting in a QGP. This phase was illustrated in Fig. 1.7(b), where the quarks and gluons were shown to no longer be bound to hadrons, but able to move freely throughout the system. Deconfinement is possible due to the phenomenon called *Debye screening*, where the color charge of hadronic partners becomes screened from one another due to the close proximity of other quarks, antiquarks, or gluons [25]. This behavior is analogous to the Debye screening of the electric charge in QED and is expected to be easily achieved at RHIC for collisions where the Au nuclei nearly completely overlap. These

[4]Bremsstrahlung radiation is the emission of a photon from a particle, mainly an electron or positron, due to an acceleration that deviates the particle from its straight-line course. The acceleration can be caused by an attraction to a nucleus as the particle traverses a medium or a man-made magnetic field in a particle accelerator.

collisions are estimated to reach an energy density of at least 15 GeV/fm^3 [24], which is significantly higher than the theorized $\sim$1 GeV/fm^3 necessary for onset of a QGP and $\sim$100 times that of cold nuclear matter.

Throughout the process described thus far, the medium is constantly expanding and undergoing binary collisions between the particles. If these particles are strongly interacting then they may result in a quick thermalization of the system before it "evaporates". Using experimental data and hydrodynamic models [26, 27] it is estimated that the system does achieve a rapid thermalization after $\sim$0.15–0.6 fm/c with a temperature of $\sim$300–600 MeV $\approx$ 3.5–7$\times10^{12}$ K[5]. This corresponds to an energy density of $\gtrsim$ 9 GeV/fm^3 [24], well above the estimated QGP phase transition of $\sim$1 GeV/fm^3 and $\sim$170 MeV. As discussed in Sec. 1.3, thermalization can provide a window for important insights and a better understanding of the medium.

As the system continues to evolve it further expands resulting in a more diffuse system with a smaller energy density. Eventually the energy density becomes small enough that there is a phase transition from the QGP to a hadron gas. This process is called *hadronization* and is where confinement reasserts its control over the particles and free (anti)quarks and gluons no longer exist. With continued expansion of the system, inelastic scattering ceases to occur, resulting in a *chemical freeze-out*, where the quark flavors inside the hadrons are frozen and no longer change due to scattering. The last stage of the collision is called *thermal freeze-out* and at this point the hadrons and leptons are so dispersed they no longer interact in any manner, resulting in their properties being fixed unless they undergo a weak decay. From

[5]For comparison, this is $\sim$2.2–4.4$\times10^5$ times hotter than the center of the sun [28].

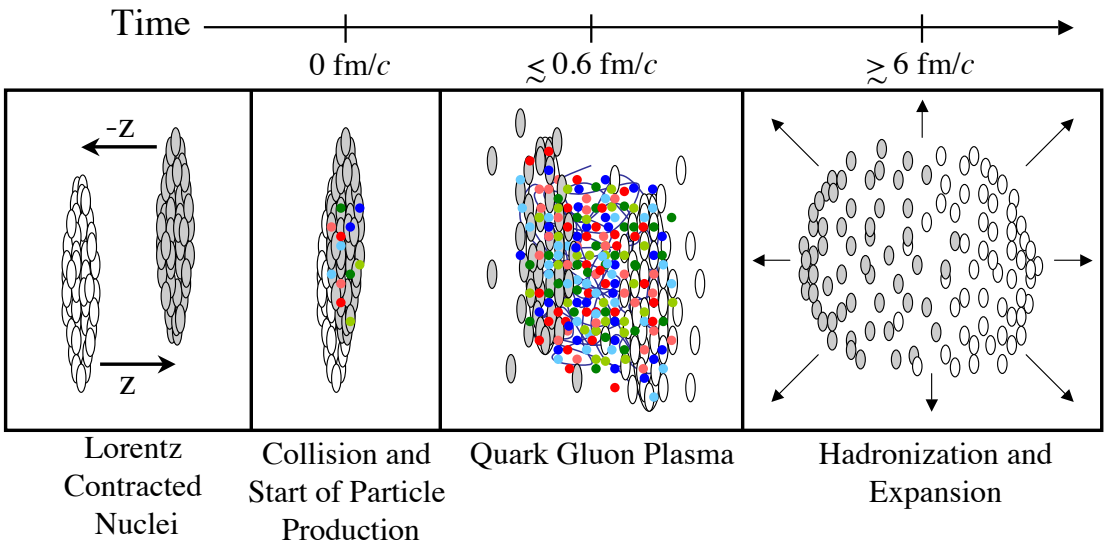

Figure 1.8: Evolution of a heavy-ion collision from *left*→*right*: (1) Lorentz contracted nuclei composed of colorless (white) hadrons move toward one another. For distinction those hadrons moving in the $-z$ direction are tinted gray. (2) Nuclei collide, become excited, and particle production begins. (3) After $\lesssim 0.6$ fm/c the original nuclei are dissociating and a QGP is created from the produced particles. (4) The medium expands, cools, and after $\sim$6 fm/c, hadrons reform, followed by chemical and thermal freeze-out and finally detection. Adapted from [29].

here, the particles propagate to detectors that record their angular and momentum distributions. Fig. 1.8 briefly illustrates and summarizes a few stages of the collision evolution discussed here.

1.2.2 Event Characterization

Because not every collision is the same, several variables are used to categorize them. One of these variables is called the *impact parameter* (b), which is the distance between the centers of the two colliding nuclei. If a collision, or *event* as it is also called, has a large b then the overlap between the colliding nuclei will be small, resulting in the number of interacting nucleons, called *participants*, to be small, while the number of nucleons not interacting, called *spectators*, will be large. Conversely,

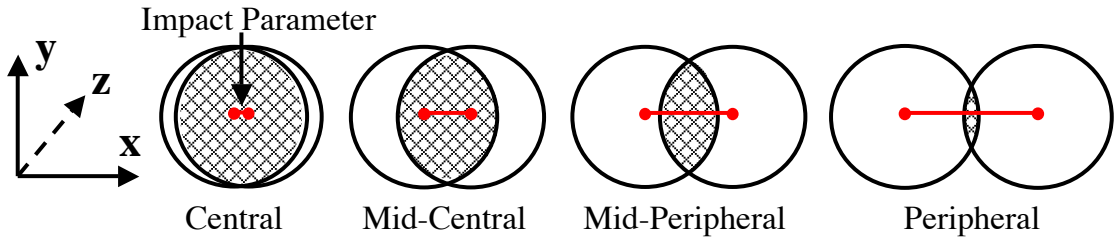

Figure 1.9: Types of collision centralities as viewed from the beam perspective. Notice the changing size of the impact parameter shown in red. The location of nucleon participants is indicated by the hashed region.

if b is small then there will be a large number of participants and a small number of spectators.

Unfortunately, b cannot be measured directly. Therefore, the experimentally determined variable used to describe the nuclear overlap of an event is called *centrality*, with events generally described as one of four centrality types: central, mid-central, mid-peripheral, and peripheral, as shown in Fig. 1.9. Centrality is measured from the number of produced particles in the event, where it is assumed the larger the number of produced particles, the more collision participants and therefore the smaller the b. Centrality is simply the percent of collisions having a larger particle multiplicity than the current collision. For example, if an event had a centrality of 10%, then 10% of events would have a larger multiplicity than the current event However, because nuclei are not rigid systems with nucleons frozen in exactly the same place for every nuclei, but rather dynamic bodies constantly undergoing change based on quantum laws and probabilities, there are fluctuations in the number of produced particles for events having the same b. This results in an uncertainty for an event's overlap determination.

Additionally, it is important to stress that an event with a centrality of 50%

does not by definition have a b that is twice the size of an event with a centrality of 25%. This is due to the geometric probability of the collision overlap. Events with a large b (peripheral) are far more likely to occur than those with a small b (central). To reiterate, centrality is just the percent of events having a larger particle multiplicity than the current event, and is not a direct measure of the size of b. Centrality is further discussed in Sec. 4.2.2.

Besides their overlap, other event properties, such as the angle and momentum of the produced particles, are essential to understanding the created medium. A first step in this process is to set up a static Cartesian coordinate system (x,y,z) in the laboratory frame around the nominal collision point (0,0,0), with one colliding ion beam arbitrarily designated as moving in the z direction and the opposing beam moving in the $-z$ direction. This coordinate system is used for describing such things as the position of detectors and the collision vertex. Polar coordinates are also used, such as θ, which describes the angle of the emitted particle with respect to the beam axis, and ϕ, which is the particle's angle in the (x,y) plane.

Emitted particles can also be described by their *rapidity* (y), which is a dimensionless quantity describing the velocity of a particle in the direction of the z-axis with respect to the nominal collision point. Rapidity is mathematically described as

$$\mathrm{y} = \frac{1}{2}\ln\frac{1+\beta\cos\theta}{1-\beta\cos\theta} = \frac{1}{2}\ln\frac{1+\beta_z}{1-\beta_z}, \tag{1.3}$$

where $\beta = v/c$, with v being the velocity of the particle and c the speed of light.

However, to calculate the rapidity of a particle one needs to know its velocity

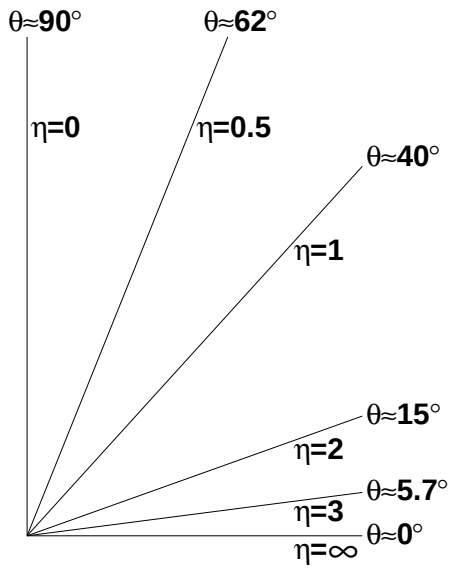

Figure 1.10: Diagram relating η to θ. Adapted from [15].

in order to calculate β. This requires particle identification, which is often not possible. Therefore, the pseudorapidity (η) of the particle is used instead, which only requires knowing the θ angle of the particle. Pseudorapidity is mathematically described as

$$\eta = \frac{1}{2} \ln \frac{1 + \cos\theta}{1 - \cos\theta}, \tag{1.4}$$

and if the emitted particle is traveling at nearly the speed of light, which is assumed for all particles examined in this analysis, then η becomes a nearly indistinguishable estimate for rapidity, except at θ angles near 0° and 180°. Additionally, both rapidity and η can have negative values depending on the z direction of the particle. Figure 1.10 illustrates how the η of a particle relates to its θ angle. For an expanded discussion of rapidity and η see Appendix A.

Another important collision parameter is called the *reaction plane* (RP), which is a plane defined by b and the beam axis, and whose angle (Ψ_{RP}) is determined with

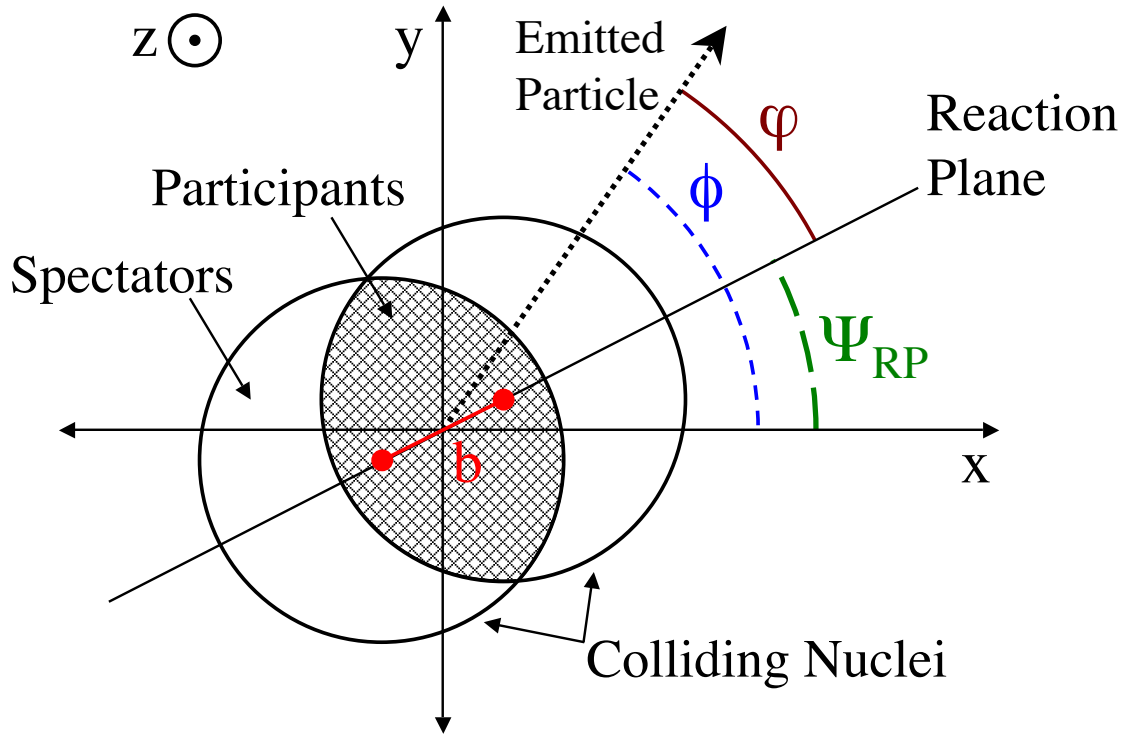

Figure 1.11: Diagram showing from the beam's point of view several variables used to characterize events. See text for a description of the variables. Adapted from [30].

respect to the x-axis. The RP is illustrated in Fig. 1.11 along with a new variable φ, which is simply the angular difference between ϕ and Ψ_{RP}, *i.e.*, $\varphi = \phi - \Psi_{RP}$.

The RP is measured from the azimuthal asymmetry of the produced particle distribution. However, due mainly to finite particle statistics and detector granularity, it is impossible to know Ψ_{RP} with absolute certainty, thus its experimental measurement is referred to as the *event plane* (EP) angle (Ψ_{EP}). The particle anisotropy can be described by the Fourier expansion [31]

$$\frac{d(wN)}{d(\phi - \Psi_{RP})} = \frac{\langle wN \rangle}{2\pi} \left(1 + \sum_n 2v_n \cos[km(\phi - \Psi_{RP})] \right), \tag{1.5}$$

where n represents the n^{th} harmonic of the particle distribution, m is the m^{th} har-

monic of the RP angle, k is a multiplier such that $n = km$, N is the number of particles measured, w are weights, and v_n is the *anisotropy parameter* representing the magnitude of the particle asymmetry with respect to Ψ_{RP}, referred to as the *azimuthal anisotropy* or *flow* for short. Note that any v_n can be measured using any m such that $n \geq m$ and n is a multiple of m. This means, in principle, the 1$^{\text{st}}$ harmonic EP can be used to measure any v_n, while the 2$^{\text{nd}}$ harmonic EP can be used to measure any even numbered n such as v_2, v_4, etc. Figure 1.12 illustrates the 2$^{\text{nd}}$ and 4$^{\text{th}}$ harmonic particle distributions and their corresponding v_n flow signals, whose origins will be discussed in Sec. 1.3. From this same anisotropy the EP angle is measured using

$$\Psi_n = \frac{1}{n}\tan^{-1}\left(\frac{Y_n = \sum_i w_i \sin(n\phi_i)}{X_n = \sum_i w_i \cos(n\phi_i)}\right), \tag{1.6}$$

where Ψ_n is the EP angle from the n^{th} harmonic particle distribution, i is the i^{th} particle, and X_n and Y_n are the event flow vectors.

Measuring Ψ_{EP} is important in heavy-ion collisions because it facilitates the study of how the collective geometry of the participating nucleons affects the anisotropic flow of the system. Such studies provide a wealth of information about the properties of the created matter, as will be discussed in Sec. 1.3, and is the topic of this dissertation.

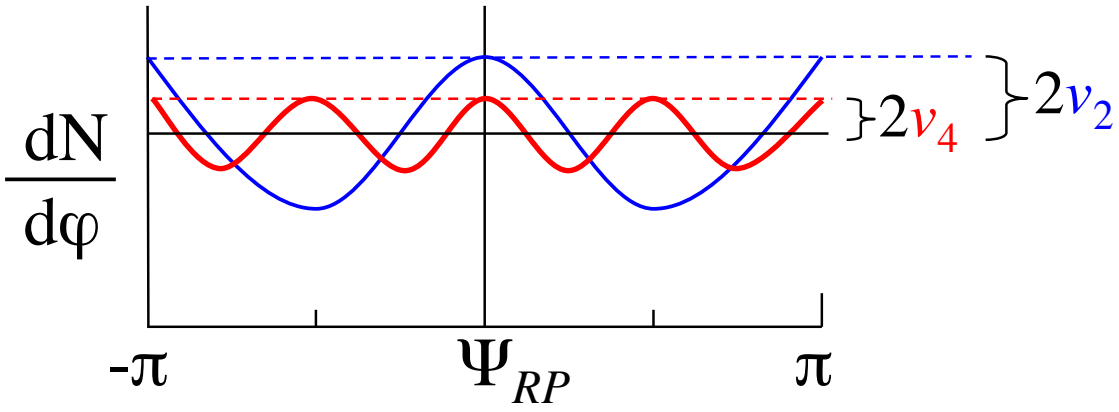

Figure 1.12: Diagram showing the shape of the 2nd (blue) and 4th (red) harmonic azimuthal particle distributions with respect to Ψ_{RP}. The magnitude of the asymmetry is indicated by the v_2 and v_4 parameters, respectively.

1.3 Azimuthal Anisotropy

Studies of azimuthal anisotropy, or flow, have resulted in many key insights into the properties of the QGP. The 2nd harmonic flow signal, v_2, often called *elliptic flow*, has been by far the most studied and revealing flow signal to date and is the topic of this dissertation. The origin of this signal comes from the elliptic shape of the participating nucleons, as shown in gray in Fig. 1.13(a). If the medium is strongly interacting and thermalizes quickly then a pressure gradient will form, as indicated by the concentric ellipses. This gradient will be steeper in the direction of the RP (short axis and indicated by the red arrows), than orthogonal to it (long axis). This asymmetry results in a momentum anisotropy causing the medium to expand non-uniformly, as indicated by the size of the arrows, with a greater number of particles moving in the direction of the RP, thereby causing the particle asymmetry. In brief, the participant asymmetry or *participant eccentricity*[6] (ε_{part}), which is greatly

[6]For more information on eccentricity see Sec. 3.7 of [15]

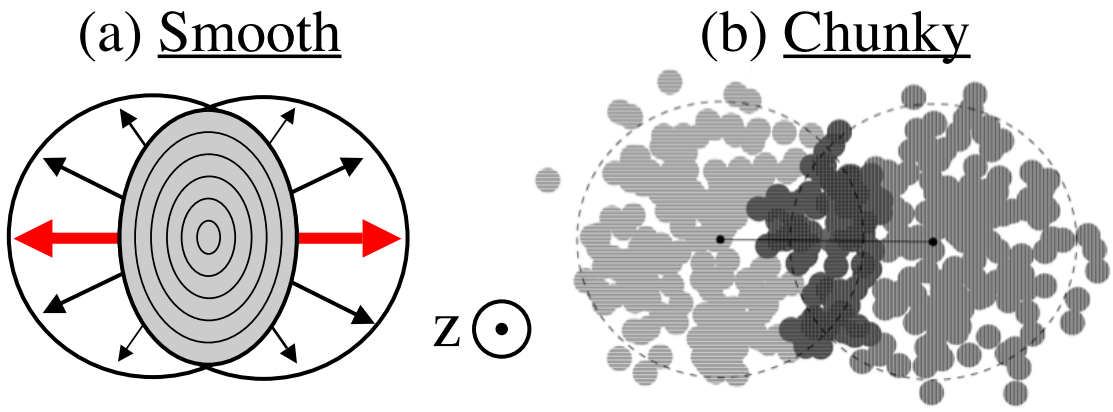

Figure 1.13: (*a*) An illustration of the traditional view of the colliding medium's initial geometry, where it has a smooth textured elliptic shape shown in gray. See text for more details. (*b*) An emerging view of the initial geometry being a "lumpy" or "chunky" ellipsoid due to the randomness of the participants spacial position. Participant and spectator nucleons are represented by the dark and light gray circles, respectively. The impact parameter is shown by the straight horizontal line connecting the centers of the two colliding nuclei [15].

affected by the collision's centrality (see Fig. 1.9), results in a momentum anisotropy that is detectable through the emitted particle asymmetric distribution, assuming the onset of thermal equilibrium. Thus, the larger the ε_{part}, the larger the pressure gradient asymmetry, and the larger the particle distribution asymmetry. However, if the medium is a weakly interacting plasma, as was expected before RHIC startup, then the flow signal would be near zero, with little particle asymmetry.

What emerged from RHIC, to the surprise of many in the heavy-ion community, was in fact a strong v_2 with a maximum asymmetry of $\sim$15% when plotted as a function of transverse momentum (p_T), as shown in Fig. 1.14. This indicated that the medium was not weakly, but rather strongly interacting with rapid thermalization. Additionally, the v_2 of low p_T particles, which make up the vast majority of the emitted particles, was consistent with low viscosity hydrodynamic models. This was the basis for the declaration that RHIC had created the "perfect liquid" [32].

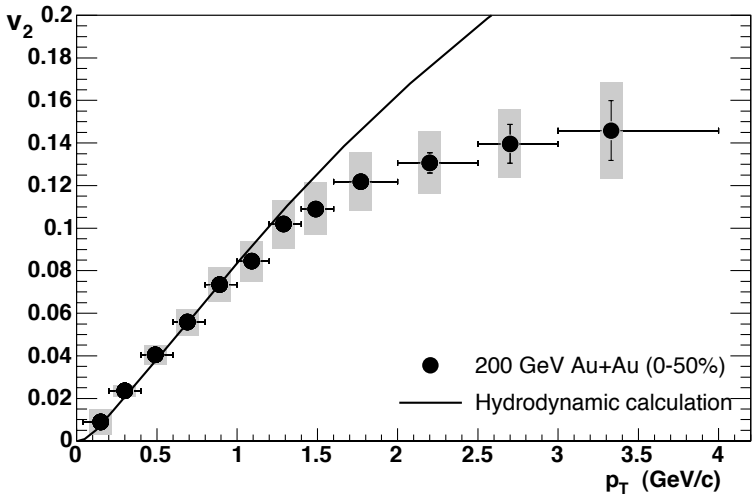

Figure 1.14: The $v_2(p_T)$ of unidentified charged hadrons from the PHOBOS experiment at RHIC. The measurement uses 0-50% centrality events from 200 GeV Au+Au collisions measured between $0 < \eta < 1.5$. The data is compared to a hydrodynamic model (solid line), which matches the data well at low p_T [33].

These discoveries were the first, but certainly not the last, major insights v_2 has provided on the properties of the medium.

For instance, the observation that identified particle v_2 scales with regard to the number of constituent quarks in the particles (n_q), shown in Fig. 1.15, has provided some of the strongest evidence to date that the created medium interacts at the partonic level and is in fact a QGP. Insight into how strongly the medium interacts has been gained by studying the v_2 of high p_T π^0's. This is shown in Fig. 1.16. When $p_T \gtrsim 6$ GeV/c the π^0's come almost exclusively from jets and should therefore be emitted isotropically with a v_2 consistent with zero. However, the figure shows that jets do not emerge from the medium isotropically ($v_2 \neq 0$), but rather depend on the path length they travel through the medium, whether it be the short axis in the direction of the RP or the long axis orthogonal to it. Here jets which travel perpendicular to the RP lose significantly more energy before exiting

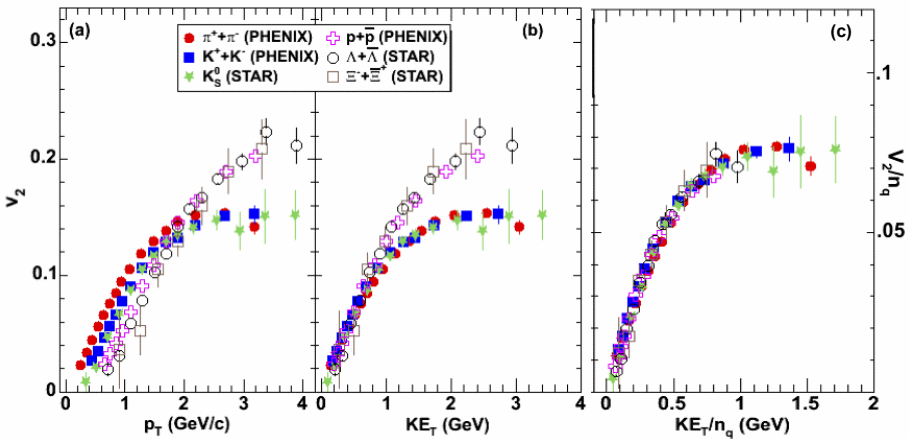

Figure 1.15: Identified particle v_2 is shown in (a) and (b) as a function of p_T and KE_T, respectively. (c) The particle v_2 divided by its n_q plotted as a function of KE_T/n_q. All data are from 200 GeV Au+Au collisions and collected by the PHENIX and STAR experiments at RHIC [34].

the medium or become completely absorbed. This effect is called *jet quenching* and results in the positive v_2. When compared to theoretical models, this measurement can provide a better understanding of energy loss and how strongly the medium interacts.

More recently, higher order harmonic measurements, such as v_3 and v_4, have started revealing insights about the medium's initial geometry. Traditionally, the medium has been thought of as having a smooth texture, as shown in Fig. 1.13(a), in which case the odd harmonics (v_1, v_3, v_5...) would cancel out at mid-rapidity ($\eta \approx 0$) due to symmetry and be consistent with zero. However, recent studies [36] have shown that this may not be the case and the medium may in fact be "chunky", as shown in Fig. 1.13(b), causing fluctuations in the flow signal and resulting in the odd harmonics persisting. Figure 1.17 shows that indeed the v_3 signal is significantly positive at mid-rapidity with a weak centrality dependence, which are both consistent with a chunky initial geometry leading to fluctuations.

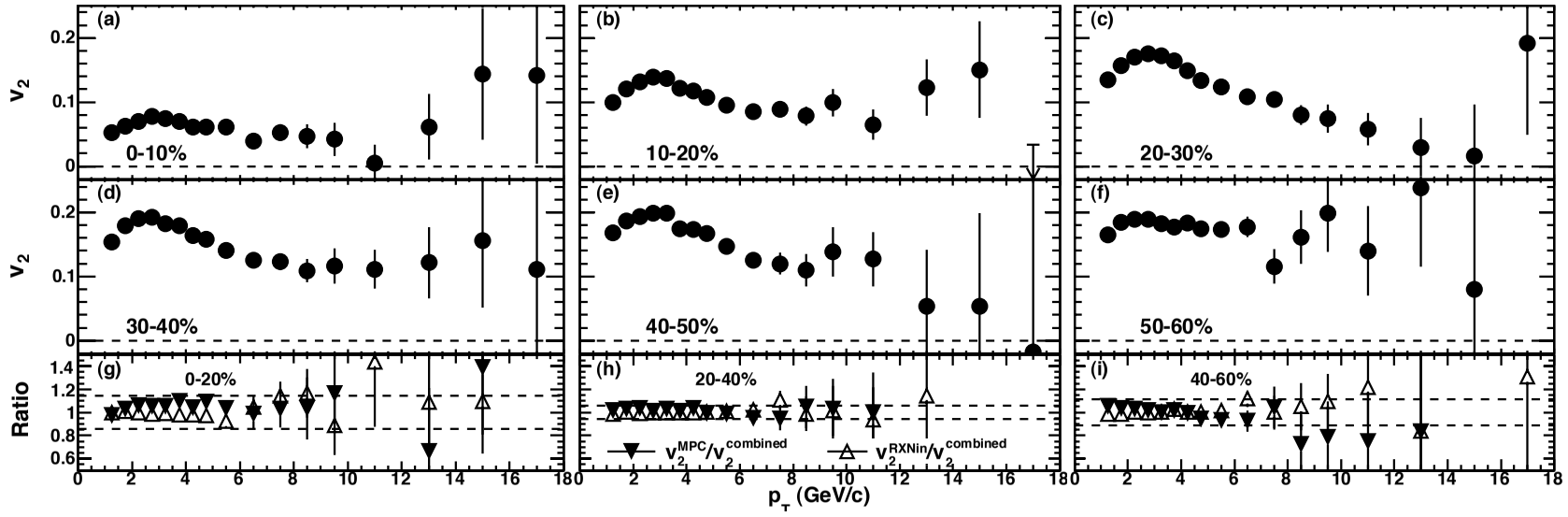

Figure 1.16: High p_T π^0 $v_2(p_T)$ is shown in panels $(a-f)$, while panels $(g-i)$ show the ratio of the measured signal when using different detectors to measure Ψ_{EP}. These EP detectors will be discussed in Sec. 2.2 and Chapter 3. A specific centrality range is shown in each panel in order to fix the participant geometry and allow for path length comparisons. All data is from 200 GeV Au+Au collisions and measured using the PHENIX detector [35].

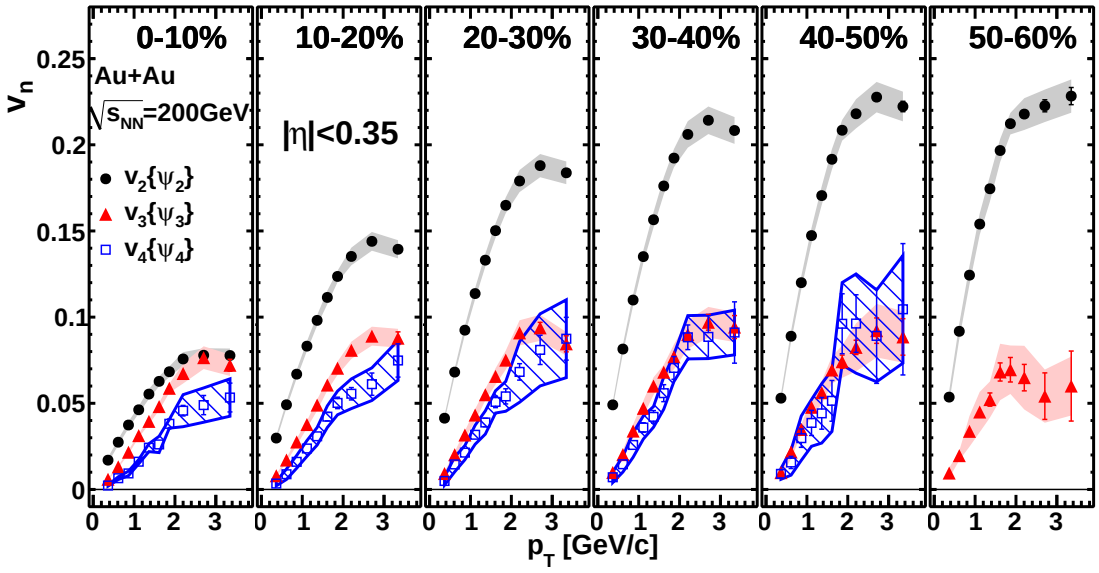

Figure 1.17: PHENIX $v_n(p_T)$ within $|\eta| < 0.35$ of 200 GeV Au+Au collisions for different centrality ranges. Here $n = m$. Statistical and systematic errors are shown by the bars and bands, respectively [37, 38].

Further insights from higher order harmonics have been extracted from $v_4/(v_2)^2$ measurements, where both v_n measurements use Ψ_2. Figure 1.18 (a) and (b) show the v_2 and v_4, respectively, as a function of N_{part}, which is the number of participating nucleons in the collision, while their $v_4/(v_2)^2$ ratio is shown in (c). The N_{part} values were extracted using a Glauber model calculation, which will be discussed in Sec. 4.2.2. Comparing the ratio in (c) to a purely hydrodynamic model (dotted line) shows a poor agreement, but by adding fluctuations and viscosity to the model (dash-dot or solid line) a better agreement is achieved.

Additionally, Fig. 1.19 shows that v_4 measured using Ψ_4 is ∼2x larger than when using Ψ_2 due to Ψ_4 originating not only from the same eccentricity and pressure gradients that drive Ψ_2, but also the same fluctuations as v_4. This results in a stronger correlation and larger signal. These fluctuations are thought to originate

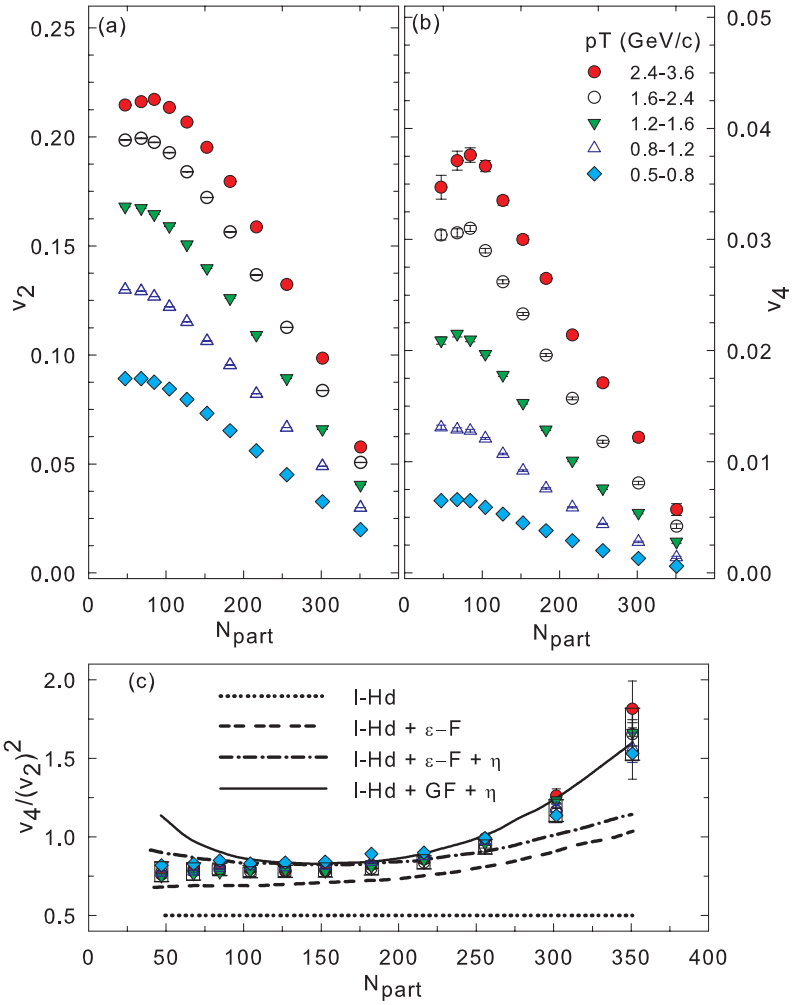

Figure 1.18: (*a*) v_2 and (*b*) v_4 as a function of N_{part} for different p_T ranges, with both measurements using Ψ_2. Notice the difference in the magnitude of the y-axis. (*c*) The $v_4/(v_2)^2$ ratio of this data compared to an ideal hydrodynamic model (I-Hd). The best agreement is seen when eccentricity fluctuations (ε-F) or Gaussian fluctuations (GF) and viscosity (η) are included. The data are from 200 GeV Au+Au collisions using the PHENIX detector [39].

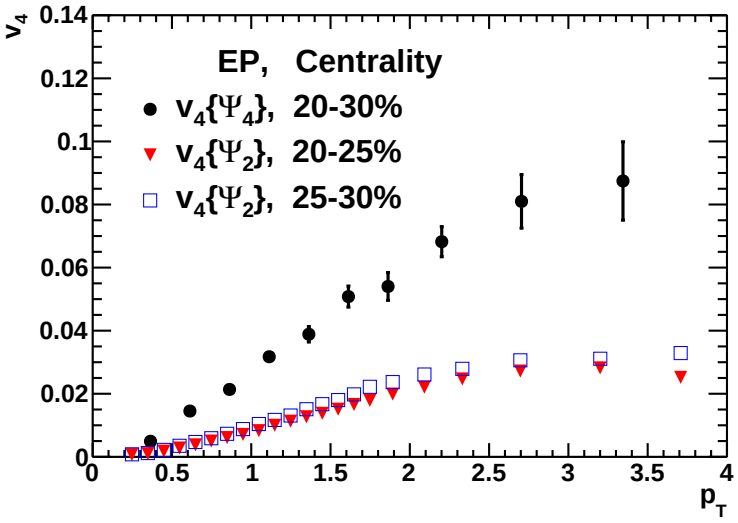

Figure 1.19: Comparison of similar centrality $v_4(p_T)$ measurements using different harmonic EPs. The EP and centrality combinations shown are: Ψ_4 and 20-30% (circles), Ψ_2 and 20-25% (triangles), and Ψ_2 and 25-30% (squares). For clarity only statistical errors are shown. All data is from 200 GeV Au+Au collisions using the PHENIX detector [38, 39].

from the same type of initial geometry or eccentricity fluctuations that drive v_3. Figure 1.19 emphasizes that eccentricity fluctuations are an important component in v_4 and need to be taken into account. To summarize, these higher order harmonic flow measurements provide additional insights into the medium and can be specifically applied to constrain initial geometric fluctuations.

In addition to ongoing top energy collisions, RHIC is also undertaking a staged multi-year beam energy scan (BES), meaning colliding Au nuclei at energies less than its top energy of 200 GeV. The BES is valuable for many reasons, including studying how initial geometry effects change with beam energy, and probing the nuclear phase diagram in an attempt to find the critical point (see Fig. 1.6). For these and other important energy scan measurements, flow is an ideal tool for investigation.

For instance, one might expect that approaching the critical point would result in the medium behaving differently than when in a QGP phase, such as a change in flow signal. Furthermore, the medium would stop interacting at the partonic level, as demonstrated in Fig. 1.15 for 200 GeV data, where the identified particle v_2 scaled with respect to n_q. Figure 1.20 compares RHIC's top energy 200 GeV data to lower beam energies of 62.4 and 39 GeV for flow harmonics with $n = 2$, 3, 4. Despite a factor as large as $\sim$5 difference in beam energy, the flow signals are consistent within errors, meaning that within this energy range the hydrodynamic properties of the medium, as well as initial geometry effects, are similar. Further evidence of similar behavior is seen in Fig. 1.21, where identified particle v_2 is shown for 39 GeV data. In (a), the same mass scaling below $p_T \approx 1.5$ GeV/c and the same baryon/meson splitting above $p_T \approx 1.5$ GeV/c is seen as at 200 GeV (see Fig 1.15), along with the same n_q scaling behavior in (b), indicating partonic level interactions. However, there is a small scaling discrepancy at $KE_T/n_q \approx 0.4$ GeV that is not fully understood.

Conversely, if the v_2 of 7 GeV data is compared to 200 GeV data a significant difference is seen, indicating a change in the medium's properties. This is shown in Fig. 1.22(a). Displayed another way, Fig. 1.22(b) shows $v_2(\sqrt{s_{NN}})$ at $p_T = 0.7$ and 1.7 GeV/c, where the signal flattens between 39 and 200 GeV, but starts decreasing somewhere below 39 GeV. Does this indicate the medium is changing from partonic to hadronic interactions? Can this help reveal the critical point? Investigations are continuing in this transition region which will help in answering these questions, including the collection of new data at 19.6 and 27 GeV during the 2011 RHIC data

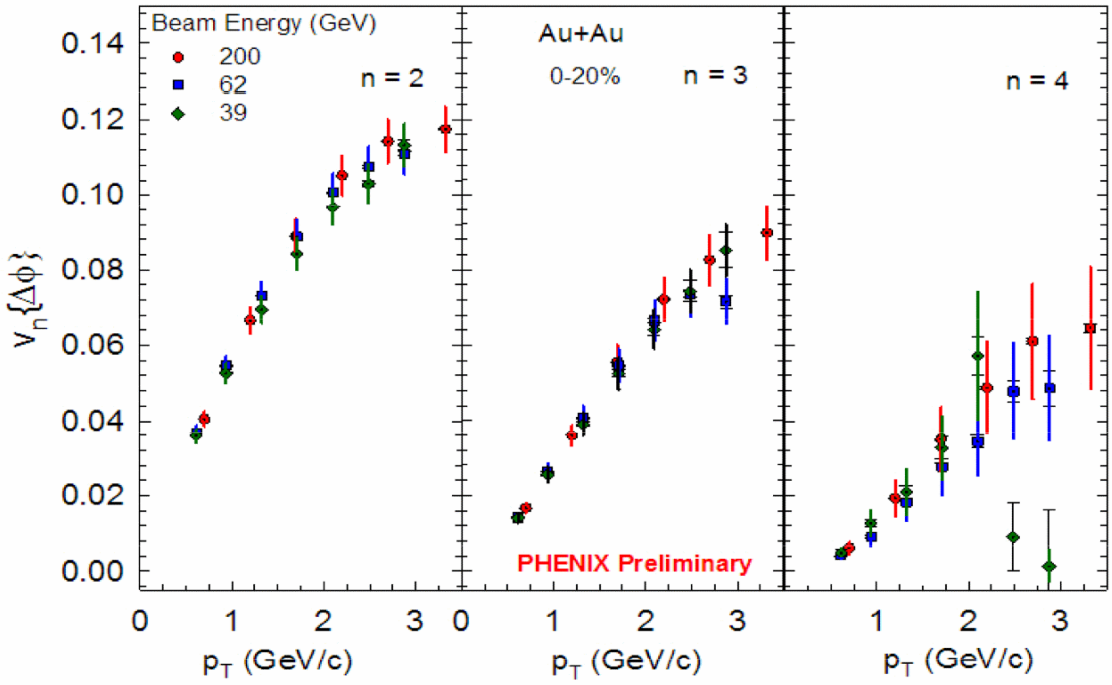

Figure 1.20: PHENIX preliminary $v_n(p_T)$ for 200, 62.4 and 39 GeV beam energies using a centrality range of 0-20%. Despite the significant differences in beam energies the flow signals are consistent within the different harmonics, indicating similar hydrodynamic properties and initial geometry effects. The measurement was done using a two particle correlation method between central and forward rapidities [40].

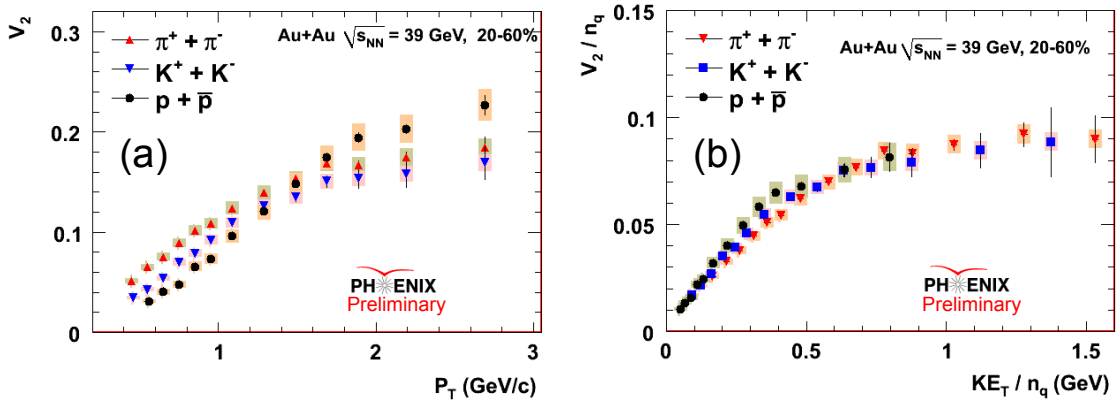

Figure 1.21: (*a*) PHENIX preliminary $\pi^{\pm}$, $K^{\pm}$ and (anti)proton $v_2(p_T)$ for 20-60% centrality Au+Au collisions at 39 GeV; (*b*) $v_2/n_q(KE_T/n_q)$ for the same identified particles. Except for a small deviation for (anti)protons at $KE_T/n_q \approx 0.4$ GeV, both (*a*) and (*b*) demonstrate similar behavior as 200 GeV collisions (see Fig. 1.15) indicating similar medium properties at the two energies [40].

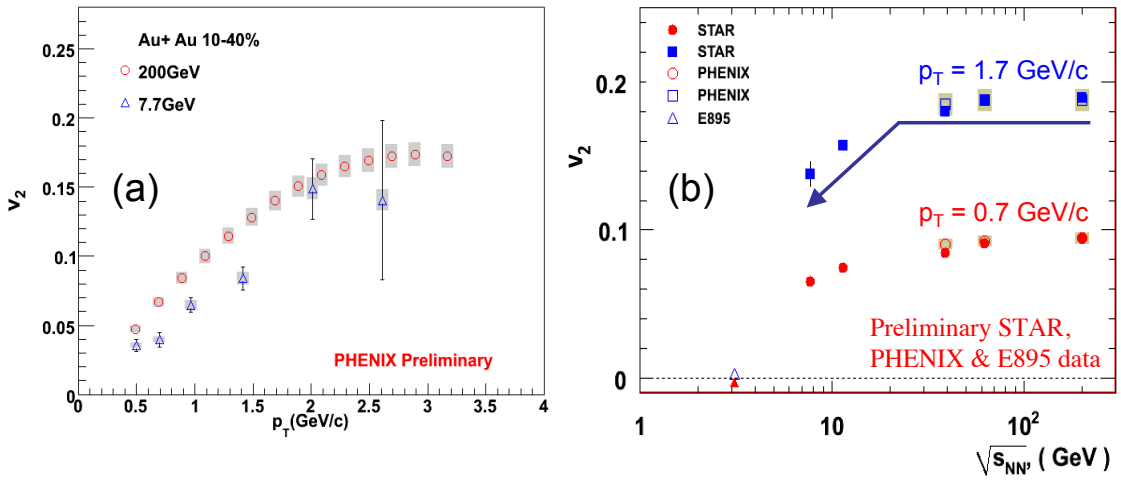

Figure 1.22: (*a*) PHENIX preliminary data for $v_2(p_T)$ at 7 and 200 GeV. The difference in v_2 indicates a change in the medium's properties. (*b*) $v_2(\sqrt{s_{NN}})$ at specific p_T values for various beam energies from PHENIX, STAR, and E895. Here a flattening of the signal is seen above 39 GeV, indicating similar medium properties, while a decrease in signal begins in a transition region somewhere below this energy, indicating a change in the medium's properties [40, 41].

taking period.

As demonstrated here, flow is a powerful tool that has been used to reveal many interesting properties of the QGP created in relativistic heavy-ion collisions. This dissertation builds upon these and other previous discoveries by measuring flow in the sparsely studied pseudorapidity region between $1.2 < |\eta| < 2.4$. From this it is hoped that a fuller picture of the created medium's bulk properties can be obtained.

Chapter 2

Experimental Overview

2.1 Relativistic Heavy Ion Collider

The Relativistic Heavy Ion Collider (RHIC) [19], shown in Fig. 2.1, is a particle accelerator and storage ring located at Brookhaven National Laboratory on Long Island, New York. One of its main purposes is to facilitate the investigation of the phase transition, formation, and properties of the QGP through the collision of heavy-ions at relativistic speeds. As discussed in Sec. 1.2.1, the 200-GeV Au+Au collisions at RHIC are expected to produce sufficiently high temperatures to produce a QGP.

RHIC is made of two 3.8 km circumference concentric rings composed of 1740 helium cooled (< 4.6 K) superconducting magnets. Figure 2.2 is a photograph of the rings in the tunnel. When filled, the rings hold counter-circulating beams of ions that can be brought into collision at 6 locations called *interaction regions* (IR). From its commissioning in 1999 through 2005, the larger PHENIX and STAR and smaller PHOBOS and BRAHMS experiments [43–46] were each located at one of these collision points. However, in 2005 PHOBOS concluded its data collection followed by BRAHMS in 2006, leaving PHENIX and STAR as the remaning detectors in operation today. The analysis performed in this dissertation used the PHENIX detector, which will be discussed in Sec. 2.2.

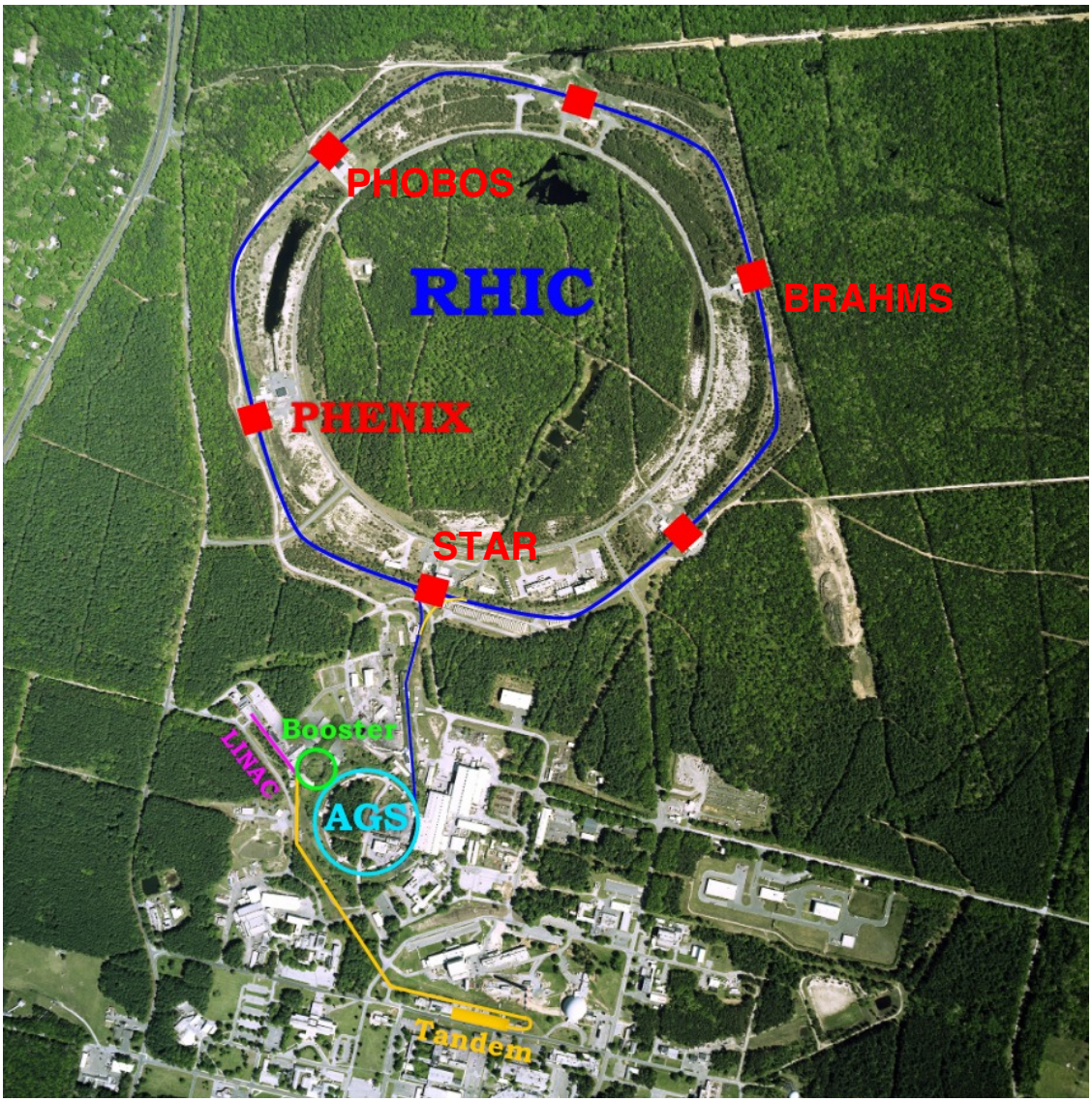

Figure 2.1: A satellite photograph of RHIC, located at Brookhaven National Laboratory on Long Island, New York. Also shown are RHIC's supporting accelerators used to inject lower energy ions into RHIC. PHENIX, the detector used in this analysis, is located at the "8 o'clock" position of the RHIC ring. The location of the STAR, PHOBOS, and BRAHMS experiments are also labeled [42].

Figure 2.2: Photograph inside the RHIC tunnel showing the two concentric rings of beam tubes [47].

RHIC is a flexible machine that can collide species ranging from p $\rightarrow$ Au and even up to uranium with the recently completed EBIS upgrade [48]. Heavy-ions such as Au can be accelerated up to 100 GeV/u in each ring and as low as 3.85 GeV/u [41], as was demonstrated in the 2010 RHIC running period, which is referred to as *Run*-10[1]. Protons, on the other hand, have a smaller mass/charge ratio and can be accelerated up to 250 GeV/u, as was done in Run-9 and 11. RHIC can even collide asymmetric species such as d+Au, which was accomplished in Runs-3 and 8 to investigate cold nuclear matter effects. Collisions of Cu+Au are planned for the current Run-12, but have not yet been done.

A chain of smaller accelerators, shown in Fig. 2.1, is used to "feed" the ions into RHIC, where they are then accelerated (or decelerated in some circumstances) to the desired collision energy. For Au this process starts by using a pulsed sputter ion

[1] A "Run" such as Run-7 should not be confused with nominal one hour data collection "runs". For instance, one Run is composed of many runs. This is further discussed in Sec. 4.1.

source to generate negative ions in a Tandem Van de Graaff, where they are passed through a stripping foil to achieve a +12 charge and accelerated to 1 MeV/u. Upon exiting the Tandem, further electron stripping is performed, along with a charge selection through bending magnets, yielding a +32 charge state in the Au ions. These ions are then sent to the Booster Synchrotron and accelerated to 95 MeV/u before exiting and being further stripped of electrons to reach a +77 charge state. From there the ions enter the Alternating Gradient Synchrotron (AGS) in 24-ion bunches. They are then debunched and rebunched into 4 bunches before being accelerated to 10.8 GeV/u. The bunches then exit the AGS one at a time, where their Au ions are stripped of their 2 remaining electrons, yielding a final charge state of +79. Finally, the bunches are transfered to their respective *buckets* in RHIC. This process is repeated until the desired or maximum number of bunches (120) is achieved in each ring. However, at least several buckets are kept empty of ions to allow for background studies and a clean beam dump. In total, it takes $\lesssim$ 1 min to fill each ring and $\sim$2 min to accelerate the Au ions to 100 GeV/u using radio frequency cavities. After the top energy is achieved the bunches are shortened to $\sim$1 m in length and the two beams synchronized so their respective bunches pass through the interaction region at the same time, before finally being steered into collisions.

As time passes during a *store*[2], the *luminosity*[3] of the beams decrease due

[2]A store is when beams are circulating in the storage rings. It starts when the beams are injected and ends when they are lost or dumped.

[3]Luminosity is a parameter used to characterize the effectiveness of colliding beams. It is essentially defined as the ratio of the bunch crossing frequency to the colliding bunch's transverse cross section, assuming equivalent transverse profiles and complete overlap. The bunch's particle population is also taken into account. For a brief overview of luminosity see Appendix C.

mainly to intrabeam scattering from inelastic Coulomb interactions, which causes emittance blow up along with enlargement of the bunch length beyond the bucket. Also contributing to the loss in luminosity are such processes as beam-gas collisions due to an imperfect vacuum, and beam scrapping. Further contributing factors are electromagnetic interactions from, for instance, bunch crossings, resulting in scattering or electron capture due to electron-positron pair production. This process would change the charge on the Au ion resulting in its loss. For these and other reasons, a store is kept $\sim$4$-$5 hours before being dumped and a new store injected. For further details about RHIC see [19, 20, 49].

2.2 PHENIX Detector

The Pioneering High Energy Nuclear Interaction eXperiment (PHENIX) [46] is a multipurpose particle detector capable of measuring a variety of physics processes, but specializes in measuring rare processes, such as J/ψ, heavy flavor, or high p_T particles. This is done mainly through photons or leptons, but also through hadrons. During Run-7, when the data for this analysis was collected, the PHENIX experiment had approximately 500 scientists, engineers, and students participating from 64 institutions in 14 countries. The detector, shown in its Run-7 configuration in Fig. 2.3, stands $\sim$3 stories tall and is composed of many sub-detectors or *subsystems*, which are a part of either the Central Arms, Muon Arms, or global detectors.

The Central Arms [51–53] are shown in Fig 2.4. They are composed of an

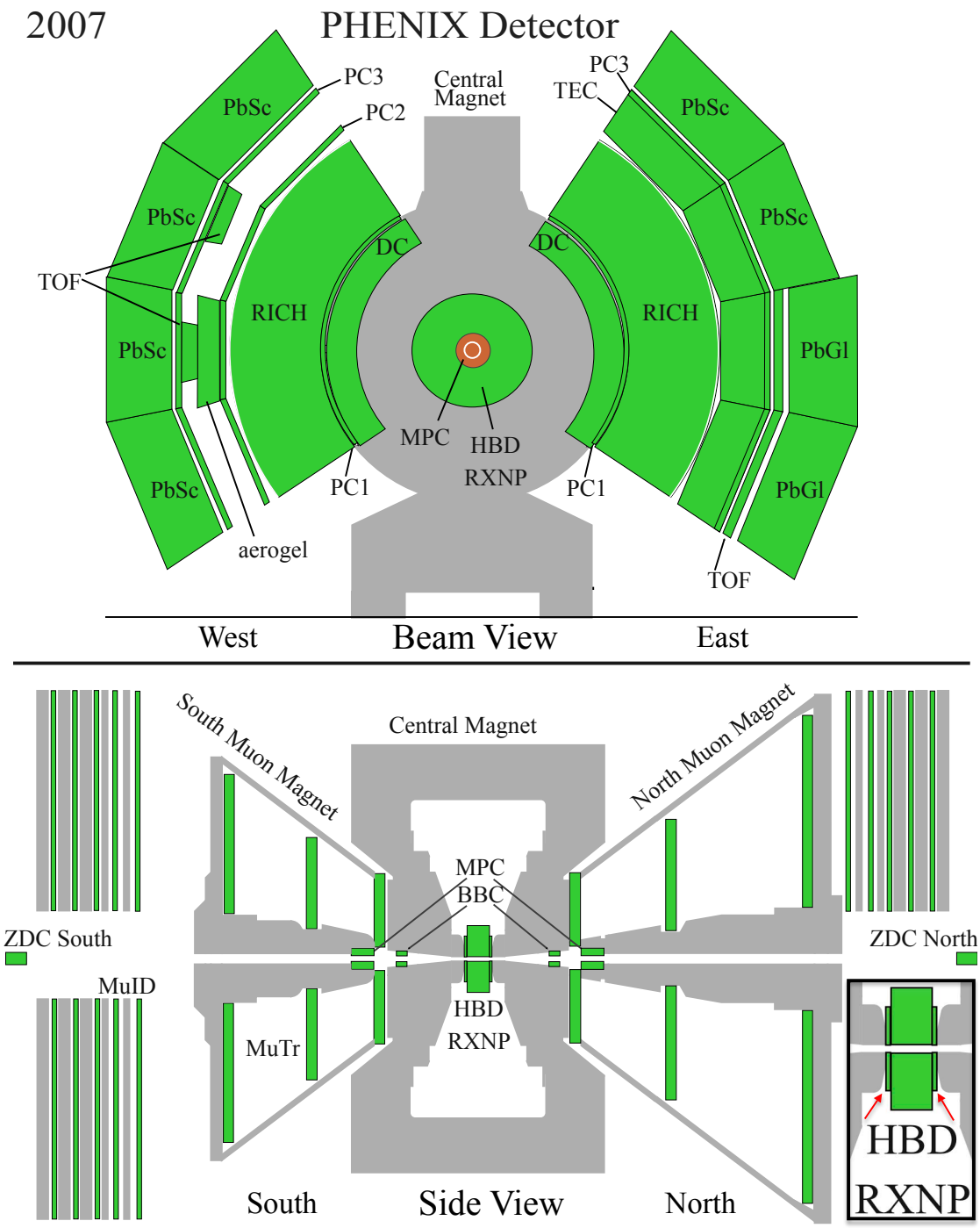

Figure 2.3: An illustration of PHENIX's Run-7 detector configuration [50]. The top illustration gives the Beam View of the Central Arms, while the bottom gives the Side View of the Muon Arms. Active detectors are shown in green, with steel and magnets shown in gray. Notice in the bottom right of the Side View an insert of the innermost central region, where the Reaction Plane Detector (RXNP) (indicated by the red arrows) is sandwiched between the Hadron Blind Detector (HBD) and the central magnet nosecone. The RXNP was integral in the success of this analysis and will be further discussed in Chapter 3.

East and West spectrometer, each situated perpendicular to the beam pipe at the nominal collision point ($x = 0$, $y = 0$, $z = 0$) covering an opposite 90° in ϕ and occupying $|\eta| < 0.35$. The Central Arms integrate a plethora of subsystems including a Drift Chamber, Pad Chamber, Electromagnetic Calorimeter, and Time of Flight detector, among others. A Central Magnet [54] with a maximum magnetic field strength of ∼1 Tesla (T) is situated between the Central Arms, as shown in the Beam View of Fig. 2.3, and is used to bend the trajectory of the charged particles as they pass through the Central Arms in order to determine their momentum. The Central Magnets are run in either the "++" or reversed "+-" field configurations. The former provides the better momentum resolution, while the latter provides an approximate zero field integral within 50 cm of the beam pipe, as is shown in Fig. 2.5. In Run-7 the "+-" field was used.

The Muon Arms [55] consist of South and North spectrometers located in the $-z$ and $+z$ directions from the nominal collision point, respectively. The South Arm covers $-2.2 < \eta < -1.2$, while the North Arm covers $1.2 < \eta < 2.4$, with both arms having 2π coverage in ϕ. Each arm is composed of a Muon Tracker that sits inside the Muon Magnet [54] and is used for particle tracking and momentum determination. Located behind the Muon Tracker is the Muon Identifier used for particle identification.

The global detectors are positioned at various locations in PHENIX and serve a variety of purposes including acting as event triggers and determining the event's centrality and EP angle. For this analysis the global detectors and Muon Arms were used, described in more detail in Sec. 2.2.1 and 2.2.2, respectively.

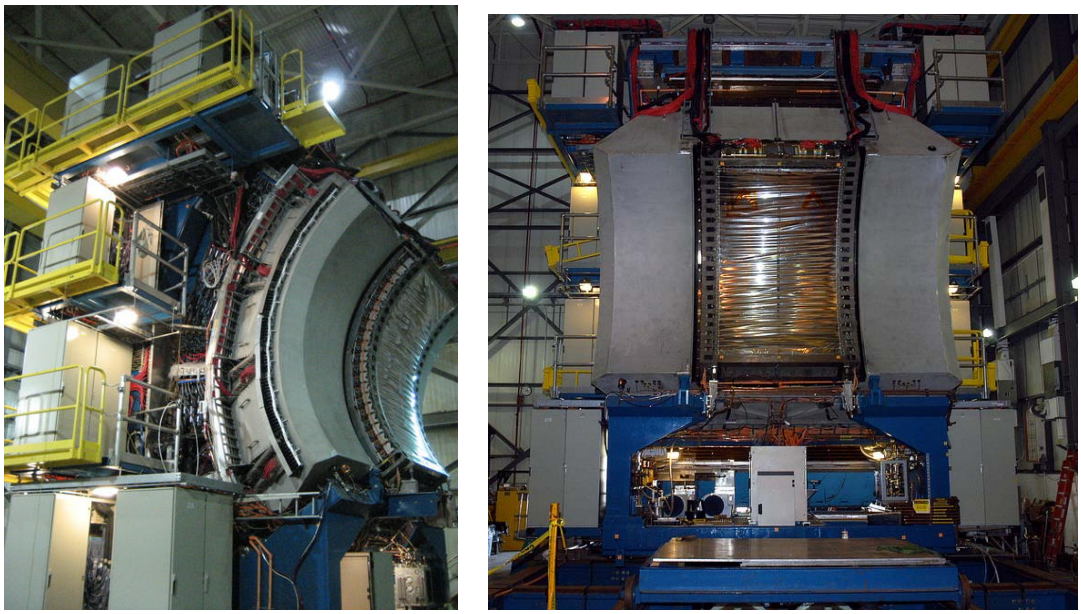

(a) (b)

Figure 2.4: (*a*) A side view and (*b*) a front view of the East Central Arm. The Drift Chamber is seen at the face of the arm, while the other subsystems are generally blocked by shielding and support structures. For a size reference notice the different levels of scaffolding.

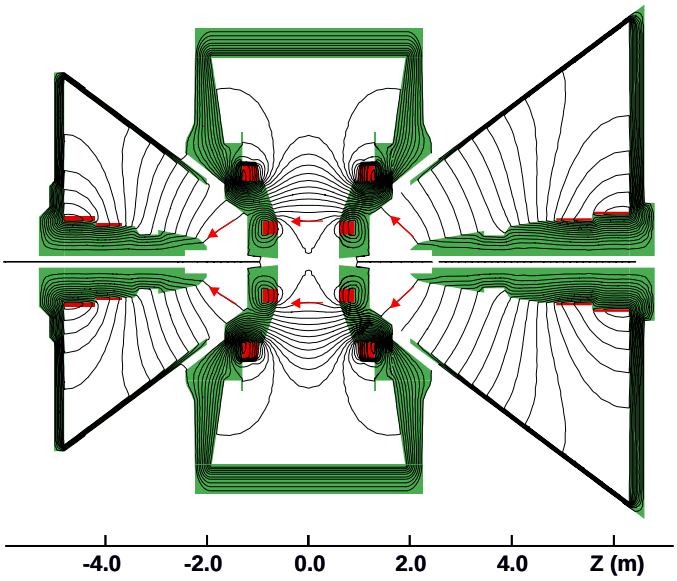

Figure 2.5: The PHENIX magnet system and field lines for the "+-" mode, which was used in Run-7. In this mode there is an approximate zero field integral within 50 cm of the beam pipe [50].

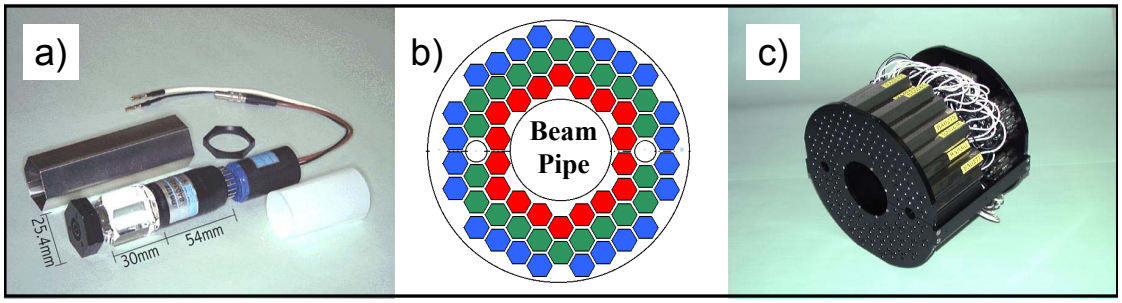

Figure 2.6: (*a*) The components of each BBC element including the quartz Cherenkov radiator and PMT. (*b*) Illustration of the position of each element once assembled. (*c*) A fully assembled arm [56].

2.2.1 Global Detectors

2.2.1.1 Beam Beam Counter

The Beam Beam Counter (BBC) is a multipurpose detector used to determine the event start time, vertex, centrality, and is also one of several detectors capable of measuring Ψ_{EP}. The BBC is composed of two mirror image arrays, a South and a North Arm, that surround the beam pipe 144 cm on opposite sides of the nominal collision point just behind the Central Magnet, covering $3.0 < |\eta| < 3.9$ and 2π in ϕ. Each BBC arm is made of 64 elements each composed of a 3-cm length quartz Cherenkov radiator connected to a 1-in diameter Hamamatsu R6178 mesh dynode photomultiplier tube (PMT), as shown in Fig. 2.6. The outer and inner diameters of the BBC are 30 cm and 10 cm, respectively, allowing for a 1 cm clearance of the beam pipe.

With a timing resolution of 52$\pm$4 ps, the BBC is used to mark the event start

time for the entire PHENIX detector by averaging the emitted particles arrival time at each BBC arm. The timing difference between each arm is used to determine the collision's *z-vertex* or simply *vertex* or z by

$$z = \frac{T_S - T_N}{2} \times c, \tag{2.1}$$

where $T_{S,N}$ are the particle's arrival times for each arm and c is the speed of light. In 200-GeV Au+Au collisions the BBC vertex resolution is 0.5 cm and the (x,y) collision position is always assumed to be (0,0). Determining the z-vertex aids in particle track reconstruction and in eliminating events that occurred outside the PHENIX acceptance of -30 cm $< z <$ 30 cm.

The BBC is also used as a Level-1 minimum-bias (min-bias) trigger detector, which initiates the recording of an event. Here, min-bias refers to applying the minimum number of requirements to an event before acceptance. For Run-7 the min-bias requirements were $>$ 1 BBC element firing in each arm, the vertex being within -30 cm $< z <$ 30 cm, the event start time being within the narrow time window of a bunch crossing, and an offline hit requirement in the North and South Arms of the ZDC$-$SMD detector (see Sec. 2.2.1.2). Additionally, the BBC was used to determine the event centrality by summing the charge collection of each BBC element; it is assumed the larger the charge collection the more central the event. This will be further discussed in Sec. 4.2.2. Moreover, the BBC can measure Ψ_{EP} using Eq. 1.6, where ϕ_i is the ϕ angle of an element and w_i its collected charge. For further BBC details see [57, 58].

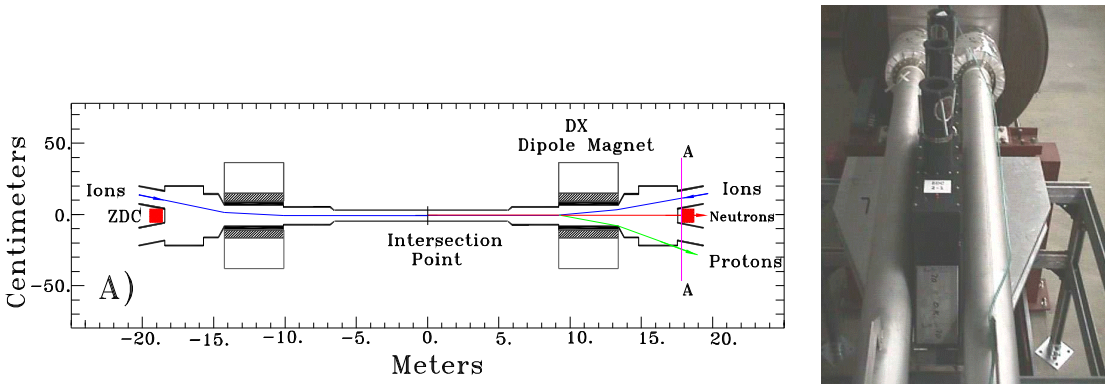

(a) (b)

Figure 2.7: (*a*) The ZDC location behind the DX magnets in the IR. Notice that charged particles such as protons are swept away from the ZDC and out of beam circulation, while the neutrons hit the ZDC. (*b*) Picture of a ZDC arm in-between the beam pipes. The gray box between the beam pipes contains the calorimeter material and the black box on top protects the Cherenkov fibers, which run to the PMTs placed on top [59, 60].

2.2.1.2 Zero Degree Calorimeter−Shower Maximum Detector

The Zero Degree Calorimeter (ZDC) is a hadronic calorimeter common to all RHIC experiments. It is designed to provide event characterization by measuring the energy and arrival time of the spectator neutrons from RHIC's heavy-ion collisions. The ZDC consists of a South and North Arm, each positioned ∼18 m from the nominal vertex behind the DX magnets and between the counter-circulating beam pipes, as shown in Fig. 2.7. The DX magnets are used to not only steer the beams into collision, but also "sweep" away the collision's remnant charged particle fragments, such as protons and deuterons. However, neutrons being of neutral charge, escape this sweep and continue their trajectory to the ZDC.

The ZDC is composed of 3 block modules (one behind the other) of 27 alternating layers of 5-mm Cherenkov fiber for light collection and 5-mm Tungsten (W)

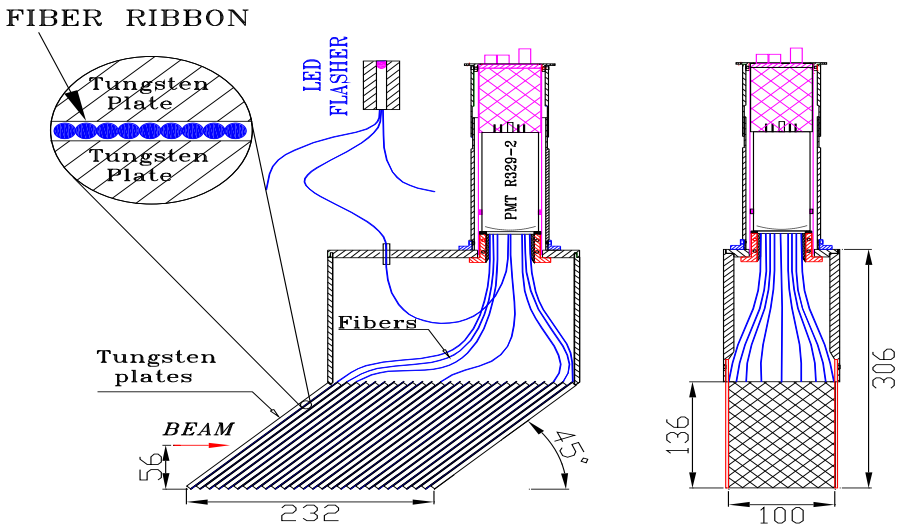

Figure 2.8: Diagram of the internal components of a ZDC block module as described in the text [59].

alloy plates for stochastic showering. These components are illustrated in Fig. 2.8. Together the 3 block modules yield 5.1 hadronic interaction lengths (λ_I) worth of material (see Sec. 2.2.2.3 for a definition and discussion of λ_I). In each module the fibers are bundled together and read out using a Hamamatsu R329-2 PMT. The ZDC is also angled 45° with respect to the beam axis in order to maximize light collection by coinciding with the fibers Cherenkov angle. The ZDC's height is 13.6 cm, but constrained by the surrounding beam pipes to a 10 cm width, giving it a pseudorapidity coverage of $|\eta| > 6.5$. In previous Runs the ZDC was used along with the BBC for centrality determination and min-bias triggering. However, in Run-7 the ZDC was only used for the offline filtering of min-bias events. For more information on the ZDC see [59].

A limitation of the ZDC is that it has no transverse segmentation to determine particle position. To remedy this shortcoming a Shower Maximum Detector (SMD)

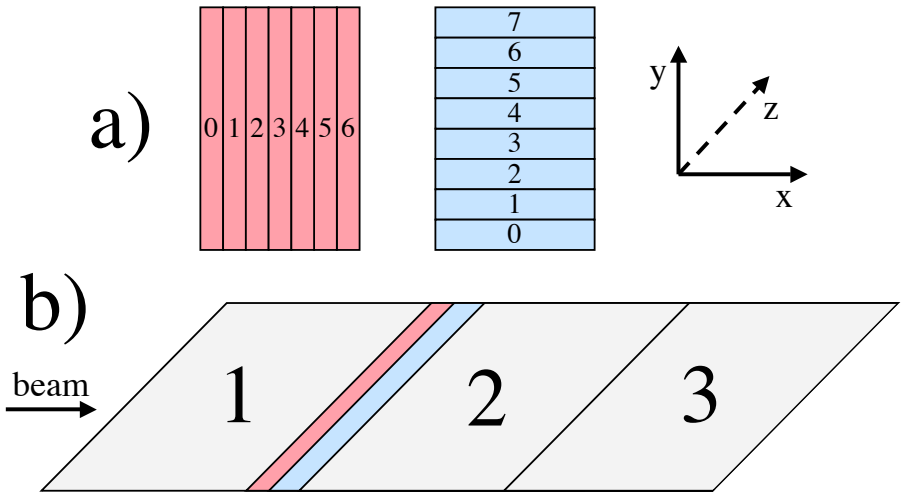

Figure 2.9: (a) Beam view of the vertical (red) and horizontal (blue) SMD slats. (b) A side view of their position in-between the gray ZDC block modules 1 and 2.

was also installed. The SMD is a scintillator slat hodoscope between the 1st and 2nd ZDC modules, as diagramed in Fig. 2.9, which approximately corresponds to the maximum hadronic shower depth of the ZDC. The SMD has seven 1.5-cm width vertical and eight 2.0-cm width horizontal slats that are read out by a multichannel PMT. This provides an active area of 10.5-cm width x 11.3-cm height, with respect to the beam.

With transverse segmentation, the SMD is able to measure Ψ_{EP} using Eq. 1.6 in a similar, but slightly different manner than the BBC. For the SMD, ϕ_i is the distance from the nominal (x,y) beam position to the slat center and w_i its collected charge. However, only the vertical (horizontal) slats are used to determine the X_n (Y_n) flow vector.

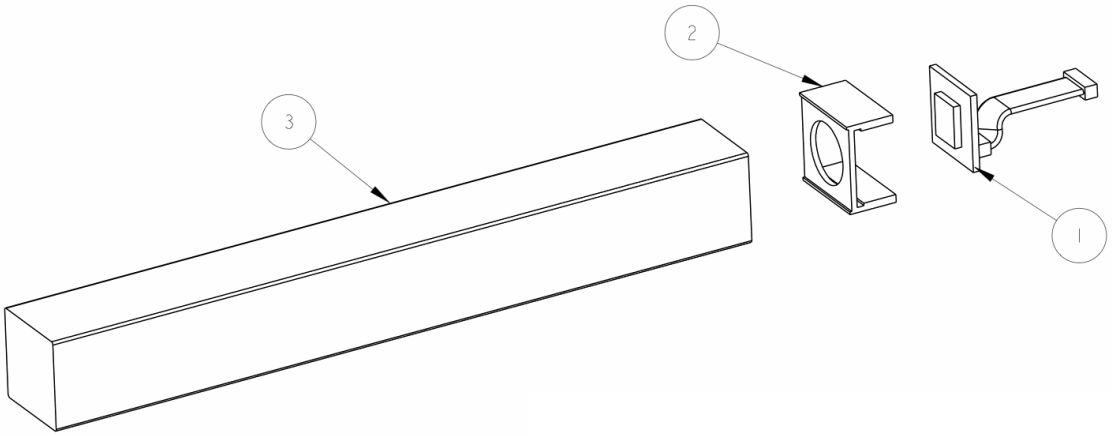

(a) Drawing of a MPC tower: (1) is the APD and preamplifier, (2) the APD holder, and (3) the scintillating crystal.

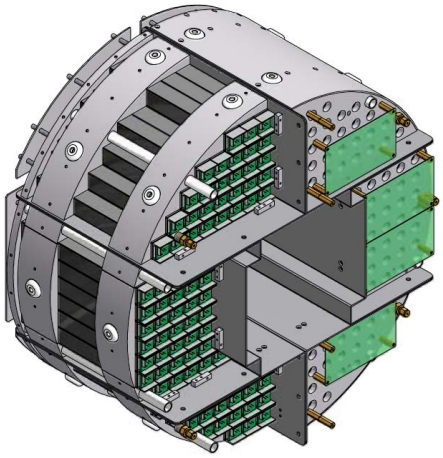

(b) Illustration of the assembled MPC South Arm.

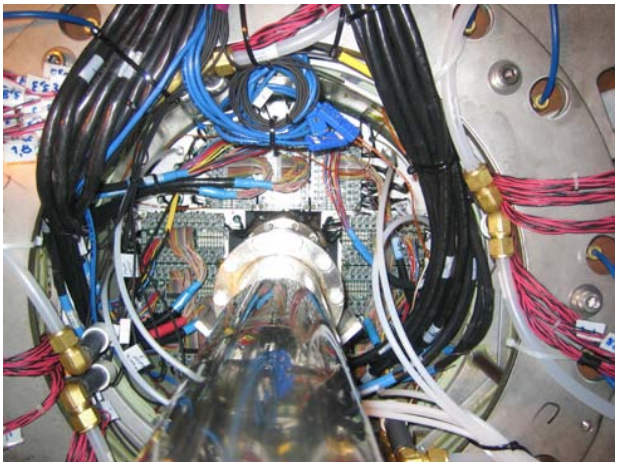

(c) Photograph of the MPC North Arm after installation in the North Muon Arm piston.

Figure 2.10: MPC detector [61].

2.2.1.3 Muon Piston Calorimeter

The Muon Piston Calorimeter (MPC) is an electromagnetic calorimeter whose main purpose is to measure photons from π^0 decays at forward angles. However, this detector can also be commandeered to measure Ψ_{EP}, as is the case in this analysis.

The MPC is composed of a South and a North Arm, which are each positioned in the muon piston holes closely behind the BBC (see Fig. 2.3). Each arm is located 200 cm from the nominal vertex, and like the BBC, covers 2π in ϕ. However, unlike

the BBC, the MPC arms are not symmetric due to differences in the beam pipe width each arm must clear. Therefore, both MPC arms have an outer diameter of ∼45 cm, with an inner diameter of ∼16.51 cm and ∼11.73 cm for the South and North Arms, respectively, corresponding to a pseudorapidity range of $-3.7 < \eta_S < -3.1$ and $3.1 < \eta_N < 3.9$.

The individual cells that make up the MPC are called towers, whose main components are a 2.2-cm x 2.2-cm width x 18-cm length lead tungstate ($PbWO_4$) scintillating crystal, which has a *radiation length* of 0.89 cm, *i.e.*, the thickness of material required to reduce the energy of an electron by a factor of e, mainly from Bremsstrahlung radiation. The crystals are connected to and read out by a Hamamatsu S8664-55 avalanche photodiode (APD), which is a semiconductor device used to measure the energy deposited in the crystal. There are 188 and 228 towers in the South and North Arms, respectively. See Fig.2.10 for a visual reference of the MPC and its components. To measure Ψ_{EP}, the MPC uses Eq. 1.6 in a similar manner as the BBC, where ϕ_i is the ϕ angle of the tower and w_i the measured energy deposited. For more MPC details see [61].

2.2.2 Muon Arm Detectors

As their name suggests, the Muon Arms are designed to measure muons (μ) by placing thick steel plates throughout the spectrometer arms to absorb hadrons, while muons, due to their greater penetrating power, more readily pass through

the steel layers leading to their detection. However, the absorbing material does not stop all the hadrons, and in fact, from the billions of collisions that PHENIX records, many millions of hadrons do make it through the steel layers, providing sufficient statistics to measure hadron v_2. The Muon Tracker and Muon Identifier detectors that make up the Muon Arms, will now be discussed, with much of the details taken from [55].

2.2.2.1 Muon Tracker

The Muon Tracker (MuTr), shown in Fig. 2.11, is composed of independent South and North Arm spectrometers, each having three stations of 100 μm resolution multiplane drift chambers designed to track particles and determine their momentum. Each arm sits inside a Muon Magnet that provides a roughly radial magnetic field (see Fig. 2.5) that bends the moving particles in a spiral shape. Also, notice in Fig. 2.3 that the two MuTr arms are not symmetric due to the need of moving the smaller South Arm during maintenance periods. This results in the South and North Arms covering $-2.2 < \eta < -1.2$ and $1.2 < \eta < 2.4$, respectively, while both cover 2π in ϕ.

Each MuTr station is made of layers called gaps, with each gap having two outer cathode planes of 5-mm wide strips on either side of an inner plane of anode wires. The anode wires run roughly azimuthally around the beam pipe, while one layer of cathode strips runs perpendicular to the anode wires (roughly radial to the beam pipe) with the other slightly offset ($\leq 11.25°$) in "stereo". As illustrated in

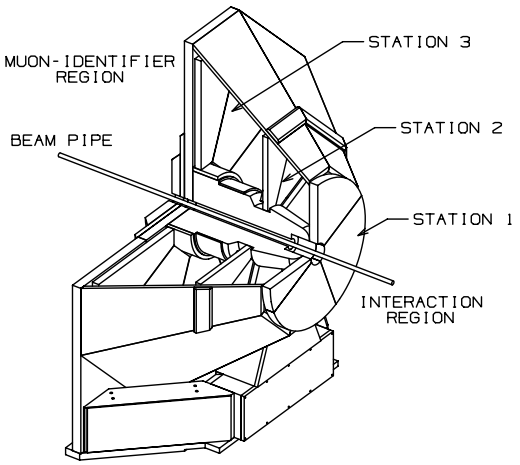

(a)

(b)

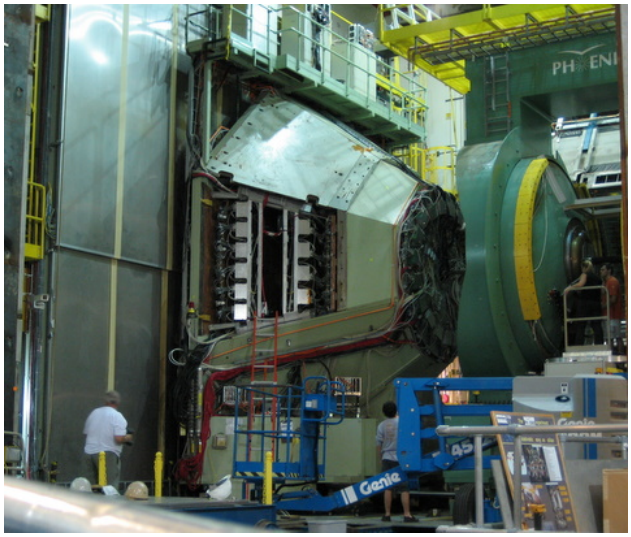

(c)

Figure 2.11: (*a*) A cutout sketch of the South MuTr showing the 3 stations inside the Muon Magnet. (*b*) A picture of the station 1 quadrants during assembly [55]. (*c*) The South MuTr in the IR during maintenance. For size comparison notice the people in the picture.

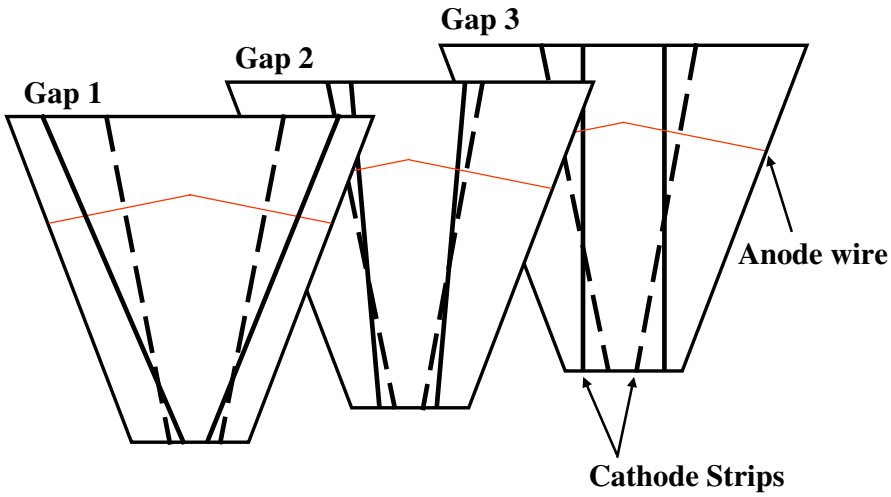

Figure 2.12: Example of the different orientations the cathode strips can have in the MuTr gaps. The strips perpendicular to the anode wire are represented by the dashed lines, while those in stereo are represented by the solid lines. In each gap the anode plane is in-between the two cathode planes [62].

Fig. 2.12, the cathode's exact orientation varies from gap to gap to take advantage of the spiraling particles. There are three gaps in stations 1 and 2 and two in station 3. Only the "hits" from the gap's cathode layers are read out, resulting in a maximum of 16 track hits, as diagramed in Fig. 2.13.

Stations 2 and 3 were constructed in octant pieces, while station 1, due to its smaller size, was constructed in quadrants, each containing two octants. A picture of station 1 is shown in Fig. 2.11(b). At all stations each octant is further divided into half octants by a 3.175-mm gap at its center ϕ angle. The gas mixture that runs through each gap is 50% argon (Ar) + 30% carbon dioxide (CO_2) + 20% carbon tetrafluoride (CF_4). The inner to outer radius of station 1 is 1.25 m, while station 3 extends out to ~2.4 m. The distance from the nominal vertex to the South (North) 1, 2 and 3 stations are 180 cm (180 cm), 300 cm (347 cm) and 460 cm (613 cm),

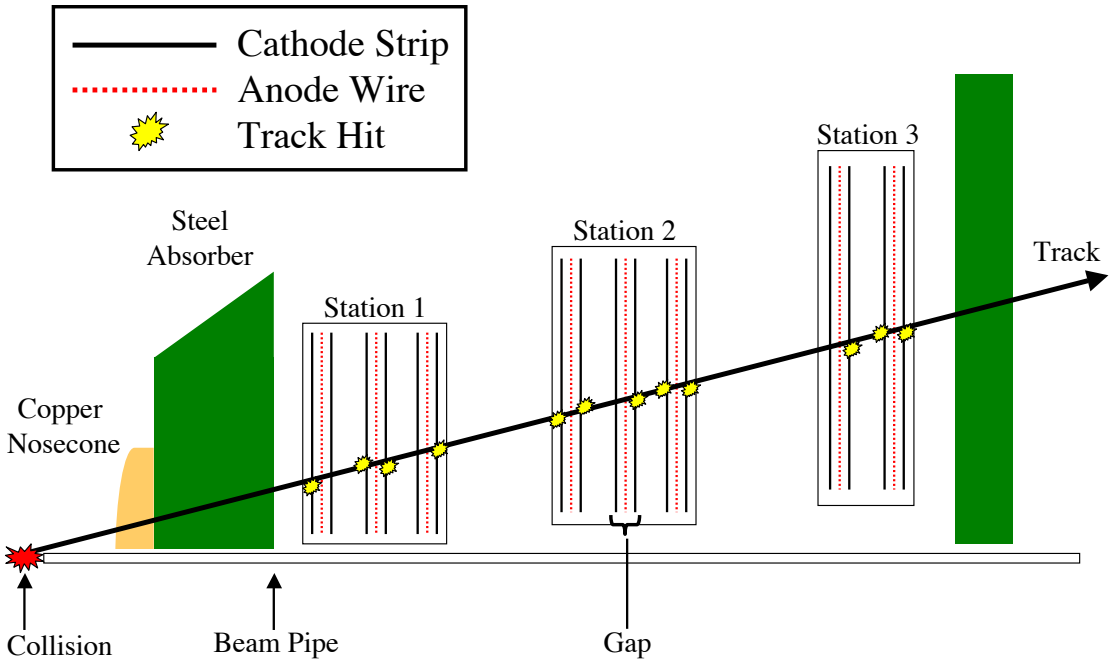

Figure 2.13: Schematic diagram of a track passing through the MuTr and recording 12 of a possible 16 hits in the cathode strip planes.

respectively.

2.2.2.2 Muon Identifier

The Muon Identifier (MuID) is displayed in Fig. 2.14. It is composed of two identical South and North Arms located downstream from the MuTr, covering the same η. The MuID consists of alternating layers of low-carbon steel and low resolution tracking tubes, whose purpose is to identify muon candidates while filtering out hadrons. The details of this process are discussed in Sec. 2.2.2.3. About 40 cm from the nominal collision point the absorber material begins with a 20-cm copper (Cu) nosecone attached to the pole tips of the Central Magnet, which itself is a 60-cm steel absorber. Continuing away from the nominal vertex and past the MuTr is a 20-cm (30-cm) steel backplate at the back of the South (North) Muon Magnet,

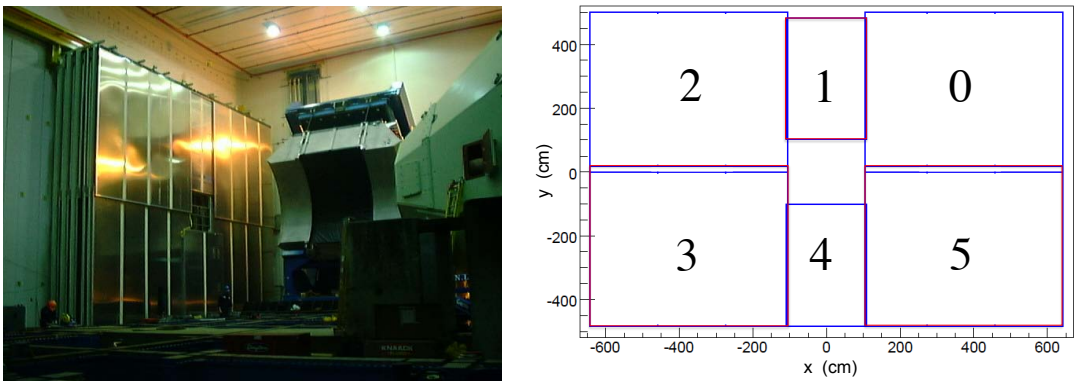

(a) (b)

Figure 2.14: In (a) the MuID South Arm can be seen on the left, the West Central Arm in the middle, and the North Muon Magnet on the right [55]. (b) The MuID six panel layout common to all gaps. Counting from $0 \rightarrow 5$, the even panels are shown in blue and odd panels in red. Notice the spacial overlap in the panels to eliminate dead regions [63].

followed by the 4 steel absorbing layers of the MuID: 10 cm, 10 cm, 20 cm, and 20 cm, respectively. In total a particle must pass through 20 cm of Cu and 140-150 cm of steel to reach the last active layer of the MuID.

The tracking material in the MuID Arms is Iarocci tubes [64], seen in Fig. 2.15, which are 9 mm x 9 mm width drift tubes or cells. Each cell contains a 100-μm Au coated Cu-beryllium anode wire at its center that is supported by a plastic spacer every 50 cm. The walls of the cell are covered by a graphite coated plastic cathode. Eight cells are ganged together forming a tube 8.4 cm wide, which is paired with another tube staggered by half a cell in order to cover each others dead regions. Together they form a "two-pack" and have their signals OR'ed.

The two-packs are contained in aluminum (Al) casings called MuID panels, with each containing a set of vertical and horizontal two-packs running their entire height and width, respectively. This essentially yields 8.4-cm^2 pads that provide

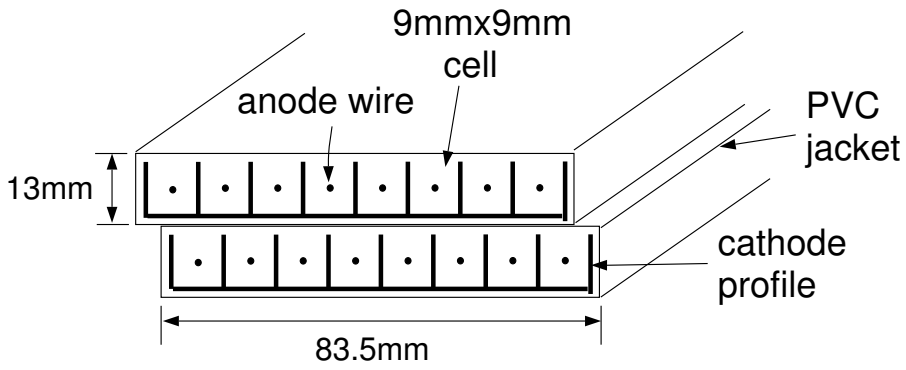

Figure 2.15: Schematic diagram of a MuID two-pack made of two staggered sets of eight Iarocci tubes [65].

enough granularity to match the MuID "roads" with the MuTr tracks. In each gap between the steel absorbers, numbered $0 \rightarrow 4$, there are four large and two small panels numbered $0 \rightarrow 5$, as illustrated in Fig. 2.14(b). In the large panels there are 118 520-cm length horizontal tubes (59 two-packs) and 128 501-cm length vertical tubes (64 two-packs). In the small panels there are 90 250-cm length horizontal tubes (45 two-packs) and 52 382-cm length vertical tubes (26 two-packs). To eliminate dead space, panels overlap at their edges, leaving panels 0, 2, and 4 ten cm closer to the nominal vertex than panels 1, 3, and 5. In total, the panels contain 1268 tubes per gap, 6340 per arm and cover a 13.7-m width and 10.7-m height. The gas running through the tubes is CO_2 with up to 25% isobutane (i-C_4H_{10}), while the Al panels use nitrogen gas (N_2) to keep the tubes clean and dry.

2.2.2.3 Muon Arm Absorber

The purpose of the Muon Arms is of course to measure muons and in particular dimuons from J/ψ ($c\bar{c} \rightarrow \mu^+\mu^-$). However, in heavy-ion collisions muons are significantly outnumbered by the more abundant hadrons and in particular pi-

ons, which constitute ∼80% of the emitted particles [66]. The remaining ∼20% is mostly kaons and (anti)protons, with prompt[4] muons and other rare particles a still smaller percentage. In order to increase the percentage of muons in a measured sample, thereby decreasing the background from the more abundant hadrons, low-carbon steel absorber plates are placed throughout the Muon Arms, as described in Sec. 2.2.2.2. These plates absorb hadrons, while muons, having a much greater penetrating power, pass through the steel to the last layer of the MuID and beyond.

This does not mean muons do not interact with the steel. In fact, in the range of $0.1 \lesssim \beta\gamma \lesssim 1000$, which is applicable to RHIC, a particle's mean rate of energy loss[5] through an intermediate Z material (such as iron (Fe) or Cu) is described to within a few % accuracy by the Bethe-Bloch formula [4]

$$-\left\langle \frac{dE}{dx} \right\rangle = Kz^2 \frac{Z}{A}\frac{1}{\beta^2}\left[\frac{1}{2}\ln\frac{2m_e c^2\beta^2\gamma^2 T_{max}}{I^2} - \beta^2 - \frac{\delta(\beta\gamma)}{2}\right], \tag{2.2}$$

where

$$T_{max} = \frac{2m_e c^2\beta^2\gamma^2}{1 + 2\gamma m_e/M + (m_e/M)^2}, \tag{2.3}$$

and

$$\delta(\beta\gamma) = 2(\ln 10)X + C + a(X_1 - X)^k. \tag{2.4}$$

See Table 2.1 for a description of the symbols. In this Bethe-Bloch region, the energy loss is largely through inelastic scattering with atomic electrons, termed *ionization*. Figure 2.16(a) shows the mean energy loss rate as a function of particle momentum

[4] A prompt particle is one that originates from the collision vertex.
[5] A particle's mean rate of energy loss through a material is known as its *stopping power*.

for muons, pions, and protons in Fe and other materials. Notice in the figure muons and pions have a similar energy loss rate, which is fortunate for this analysis since pions are the most abundantly produced hadrons in heavy-ion collisions and the Muon Arm track reconstruction software uses the muon's energy loss rate to calculate each particle's total energy loss through the initial absorber. This is done to determine a particle's original momentum at the vertex. Figure. 2.16(b) shows the average muon energy loss as a function of muon energy in Fe and other materials. In Fe, ionization is shown to dominate energy loss up to ∼200 GeV, where radiation processes then begin to dominate. These radiation processes include e^+e^- pair production, Bremsstrahlung radiation, and photonuclear interactions, *i.e.*, lepton-nuclear inelastic scattering. However, for this analysis the momentum (p) range of interest is generally 2 GeV/c $\lesssim p <$ 20 GeV/c, allowing radiation loss to be largely ignored.

Examining Fig. 2.16 reveals that the energy loss rate for pions and muons within 2 GeV/c $\lesssim p <$ 20 GeV/c only varies by ∼20%. For instance, in Fig. 2.16(a) a rapid increase in mean energy loss rate is seen for muons and pions below $p \approx$ 0.1 GeV/c. Similarly in Fig. 2.16(b) a rapid increase in average energy loss is seen for muons having an energy $\gtrsim$ 200 GeV. The momentum range of this analysis lies in-between these two extremes in a relatively consistent energy loss region. This stability helps to minimize errors in momentum reconstruction by avoiding situations where a small inaccuracy in the momentum determination from the MuTr would result in a large change in the energy loss rate through the initial absorber.

If enough ionization energy loss is experienced while traversing the Muon Arm

Table 2.1: Bethe-Bloch Formula Symbol Definitions [4, 67]

Symbol	Definition	Value or Units
E	incident particle energy	MeV
N_A	Avogadro's number	6.022×10^{23} mol^{-1}
r_e	electron radius	2.818 fm
m_e	electron mass	0.511 MeV
c	speed of light	2.998×10^8 m/s
K	$4\pi N_A r_e^2 m_e c^2$	0.3071 MeV g^{-1} cm^2
z	incident particle charge	± 1
Z	absorber atomic number	26 (Fe)
A	absorber atomic mass	55.85 g/mol (Fe)
β	incident particle velocity divided by c	unitless
γ	Lorentz factor $(1/\sqrt{1-\beta^2})$	unitless
I	absorber mean excitation energy	286 eV (Fe)
M	incident particle mass	MeV/c^2
X	dependent upon incident particle	$\log(\beta\gamma)$
C	physical property of absorber	-4.2911 (Fe)
X_1	empirical fit to data	3.1531 (Fe)
a	empirical fit to data	0.1468 (Fe)
k	empirical fit to data	2.9632 (Fe)
T_{max}	maximum energy transfer in a single collision	see Eq. 2.3
$\delta(\beta\gamma)$	density effect correction	see Eq. 2.4

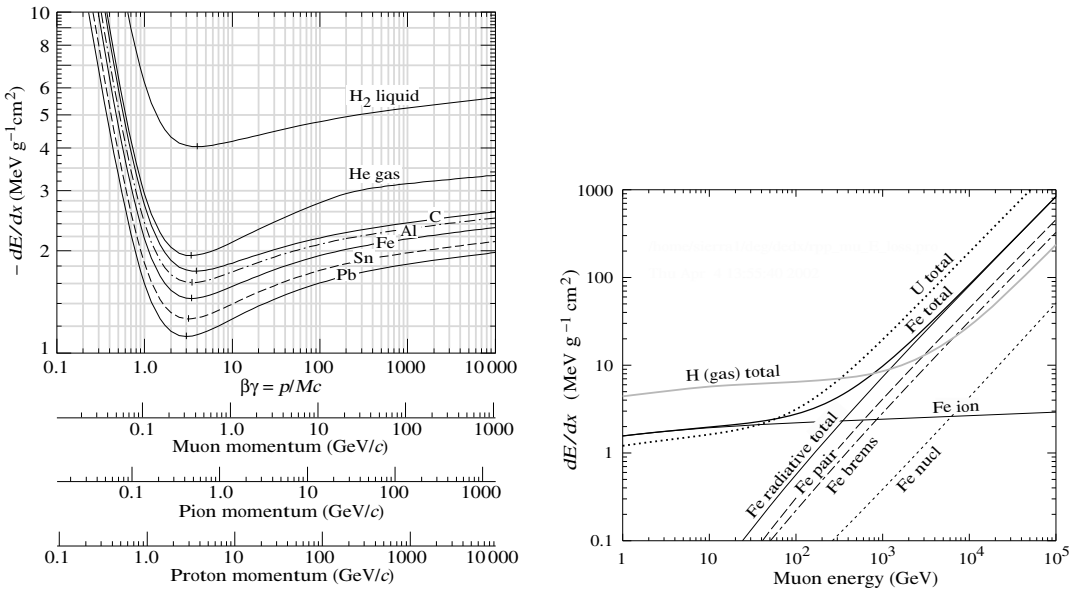

(a) (b)

Figure 2.16: (*a*) The mean energy loss rate in Fe and other materials from ionization as a function of particle momentum for muons, pions, and protons. (*b*) The average muon energy loss in Fe and other materials as a function of muon energy. For Fe the individual contributions to the total energy loss from the different processes are shown, these processes being ionization and the radiation processes of pair production, Bremsstrahlung radiation, and photonuclear interactions [4].

steel layers, both hadrons and muons can "range out" and become absorbed. However, they can, on average, penetrate to the last MuID gap if they have sufficient initial energy, as according to Eq. 2.2. Although this energy loss description works well for muons, it does not describe the whole picture for hadrons. That is because, unlike muons, hadrons can interact via the strong nuclear force and undergo *strong interactions*.

Unlike ionization, where a particle experiences a small energy loss for each of its many interactions, a hadron undergoing a strong interaction can experience a large energy loss from a single interaction, causing a "showering" of lower energy secondary particles, which can be readily absorbed. This susceptibility to large energy loss reveals the significant penetrating power advantage of muons over hadrons, since muons cannot undergo a strong interaction. Therefore, the many layers of steel absorber in the Muon Arms are there to induce hadrons into a strong interaction so they can be absorbed.

A measure of the distance a hadron can travel through a given material before a strong interaction occurs is called the *hadronic interaction length* (λ_I). The probability of a strong interaction occurring is well described by $1-e^{-L/\lambda_I}$, where L is the integrated depth of absorber material. The λ_I varies with hadron type, hadron momentum, and absorber material, but can roughly be described as 16.77 cm for steel and 15.32 cm for Cu [4]. Thus the South (North) Muon Arm and its 140 (150) cm of steel and 20 (20) cm of Cu has $L/\lambda_I \approx 9.65$ (10.25), as displayed in Fig. 2.17. This results in a non-interaction probability of $e^{-9.65}$ ($e^{-10.25}$) $\approx 6.42\times10^{-5}$ (3.54×10^{-5}). This demonstrates the high probability of a hadron interacting with the absorber in

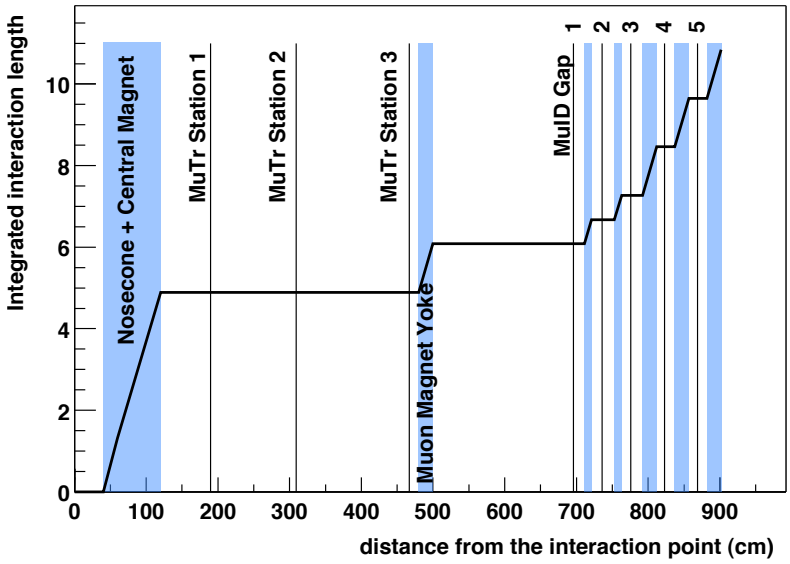

Figure 2.17: Integrated hadronic interaction length of the South Muon Arm. The thickness of the Cu and steel absorbers are represented by the blue bands [62].

the Muon Arms.

However, the probability of an interaction is not the same as the probability of complete absorption. In some of the strong interaction particle showers a secondary particle can emerge that carries much of the momentum of the original hadron. These secondary "knock-on" particles can continue penetrating through the Muon Arms with no way of distinguishing them from the original hadron. This results in the possibility that the hits from the primary and knock-on particles will be reconstructed as one primary particle or, if the showering occurs in the initial absorber, the hits from just the secondary will be reconstructed as the primary. This mechanism results in a lower hadron rejection factor than the simple exponential model suggests. As will be discussed in Sec. 5.4, variable cuts are applied to the reconstructed tracks to reduce the number of knock-on particles in this analysis.

Chapter 3

Reaction Plane Detector Upgrade.

The author of this dissertation significantly participated in the assembly, installation, commissioning, operation, and maintenance of the Reaction Plane Detector (RXNP) that was installed in the PHENIX experiment prior to Run-7. Reviewed here is the RXNP's final detector geometry, and the simulations and experimental tests done to optimize its design and material compositions. Also covered is the RXNP's online performance during Run-7 when Au nuclei were collided at 200 GeV. Finally, a discussion of the detector's calibrations and performance is included. Most of the information reported here is taken from [68], whose lead author is also the author of this dissertation.

3.1 Overview

The RXNP is a scintillator paddle detector embedded with optical fiber light guides connected to PMTs, with the design purpose of accurately measuring Ψ_{RP} in heavy-ion collisions. To increase the accuracy of this measurement a 2-cm lead (Pb) converter is located directly in front of the scintillators with respect to the nominal collision region, thereby allowing neutral particles to contribute to the signal through conversion electrons. The converter also increases the overall particle flux through the scintillators, thus acting as a signal amplifier by increasing energy deposition.

However, as mentioned in Sec. 1.2.2, due mainly to finite particle statistics and detector granularity, it is impossible to know Ψ_{RP} with absolute certainty, thus its experimental measurement is Ψ_{EP}. Therefore, the measured v_n using Ψ_{EP} is smaller than if measured using the unmeasurable Ψ_{RP}, as is demonstrated in Fig 3.1. In the figure, Ψ_{RP} for several fictional events is compared to the red colored $m = 2$ particle distribution that passes through an imagined detector used to measure Ψ_{EP}. The left and right horizontal arrows for each event indicate the angular difference between Ψ_{RP} and where Ψ_{EP} is measured by the detector. When summed over many events, this angular difference causes a flattening in the asymmetry of the measured particle distribution in the separate η region where another detector is used to measure φ, resulting in a loss in anisotropy and a reduced v_n or v_{2k} in this instance, where k is a multiplier such that $n = km$ (see Eq. 1.5 for a review of k). Consequently, a dispersion correction must be applied to the flow measurement, called the *EP correction factor* (σ_{EP}) or colloquially the *EP resolution*, principally defined as

$$\sigma_{EP} = \langle \cos[km(\Psi_m - \Psi_{RP})] \rangle, \tag{3.1}$$

which is used to correct a measured v_n by

$$v_n^{corr} = \frac{v_n^{meas}}{\sigma_{EP}}. \tag{3.2}$$

This correction always results in $v_n^{corr} > v_n^{meas}$ since σ_{EP} is always < 1. Greater detail of the EP resolution calculation will be discussed in Sec. 3.6.

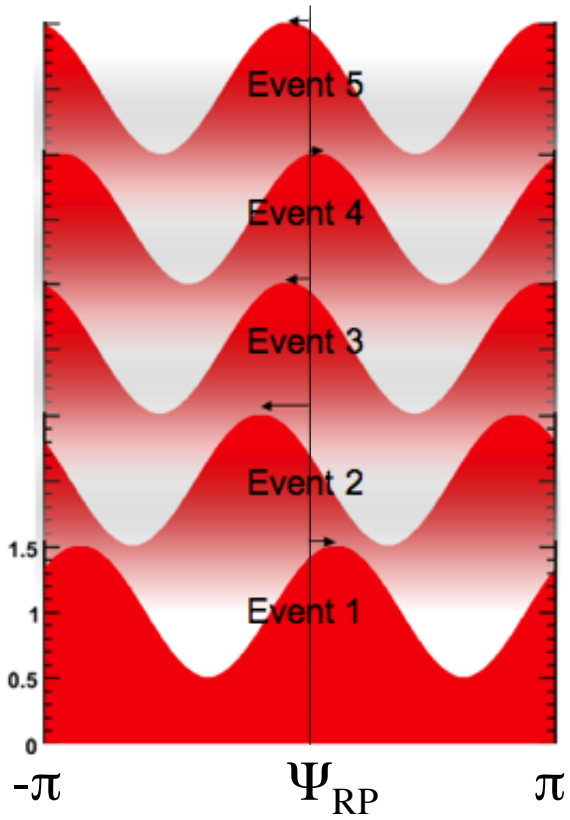

Figure 3.1: Illustration demonstrating particle dispersion with respect to Ψ_{RP} in heavy-ion collisions [69]. See text for an explanation.

Before the installation of the RXNP, PHENIX measured Ψ_n using its BBC detectors [57, 58], which had a 2nd harmonic EP resolution for mid-central 200 GeV Au+Au collisions of $\sim$0.4, where 1.0 would denote a perfect resolution. This resolution proved sufficient for studying abundant low p_T particles, but was insufficient for making new discoveries with photons and rarer probes, such as J/ψ and high p_T particles. A better EP resolution was required to increase the physics capabilities of these data sets. The RXNP was designed and built to fulfill this need.

3.2 Design and Geometry

The RXNP is composed of two sets of 24 scintillators, a North (N) and a South (S), located $\pm$39 cm from the nominal vertex position with the South Arm being located in the negative direction. The scintillators are arranged perpendicular to and surround a 10-cm diameter beam pipe in 2 concentric rings (inner, outer), with each ring having 2π coverage and 12 equally sized segments in ϕ. All scintillators are trapezoidal in shape, 2-cm thick, made of EJ-200 material from Eljent Technology (equivalent to BC408), and individually wrapped with an inner layer of aluminized mylar sheeting for light reflection and an outer layer of black plastic for light tightness. A schematic diagram showing the arrangement of the scintillators and their sizes is shown in Fig. 3.2. The edges of the inner ring are positioned at radial distances of 5 and 18 cm from the ion beam covering $1.5 < |\eta| < 2.8$. Uninterrupted coverage continues outward with the outer ring to 33 cm or $|\eta| = 1.0$. The length of the inner and outer edges of the inner scintillators are 2 and 9 cm, respectively.

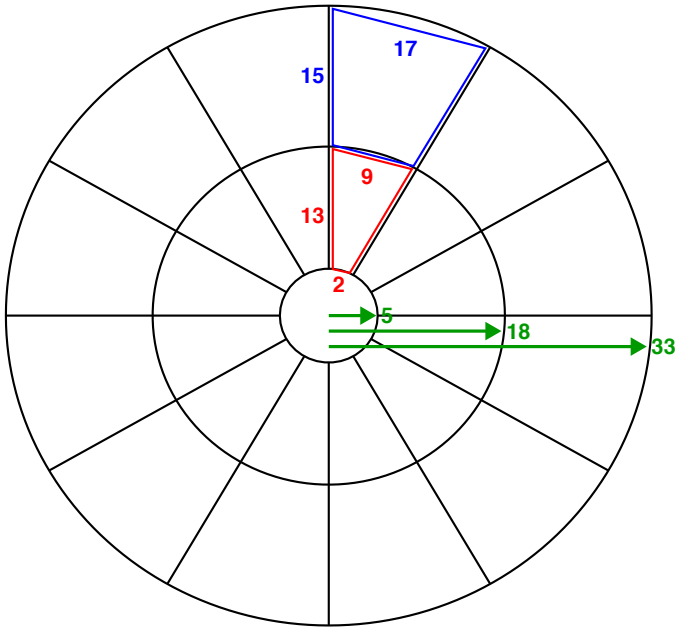

Figure 3.2: Schematic diagram illustrating the arrangement of the inner (red) and outer (blue) scintillator rings. The distance from the nominal beam position to the scintillator edge is shown by the green arrows. All lengths are given in cm's.

The length of the outer edge of the outer scintillators is 17 cm.

Each 24 scintillator set is housed in 4 identical Al structures each consisting of a tray covering 90° in ϕ and a support arm extending radially ∼80 cm. As shown in Fig. 3.3(a), each tray contains three compartments for an inner and outer scintillator with each scintillator having wavelength shifting fiber light guides embedded into its surface every 0.5 cm and running its entire length. To allow the inner scintillator's fibers to run radially out the back of the tray in tandem with the outer scintillator's fibers, an offset between the two is created by placing a 2-mm plastic spacer underneath the inner scintillator, as diagramed in Fig. 3.3(b). On top of the scintillators sits another 2-mm spacer for protection, followed by a 2-cm thick converter composed of 98% Pb doped with 2% antimony to increase hardness.

As the fibers exit each scintillator they are individually sheathed in black

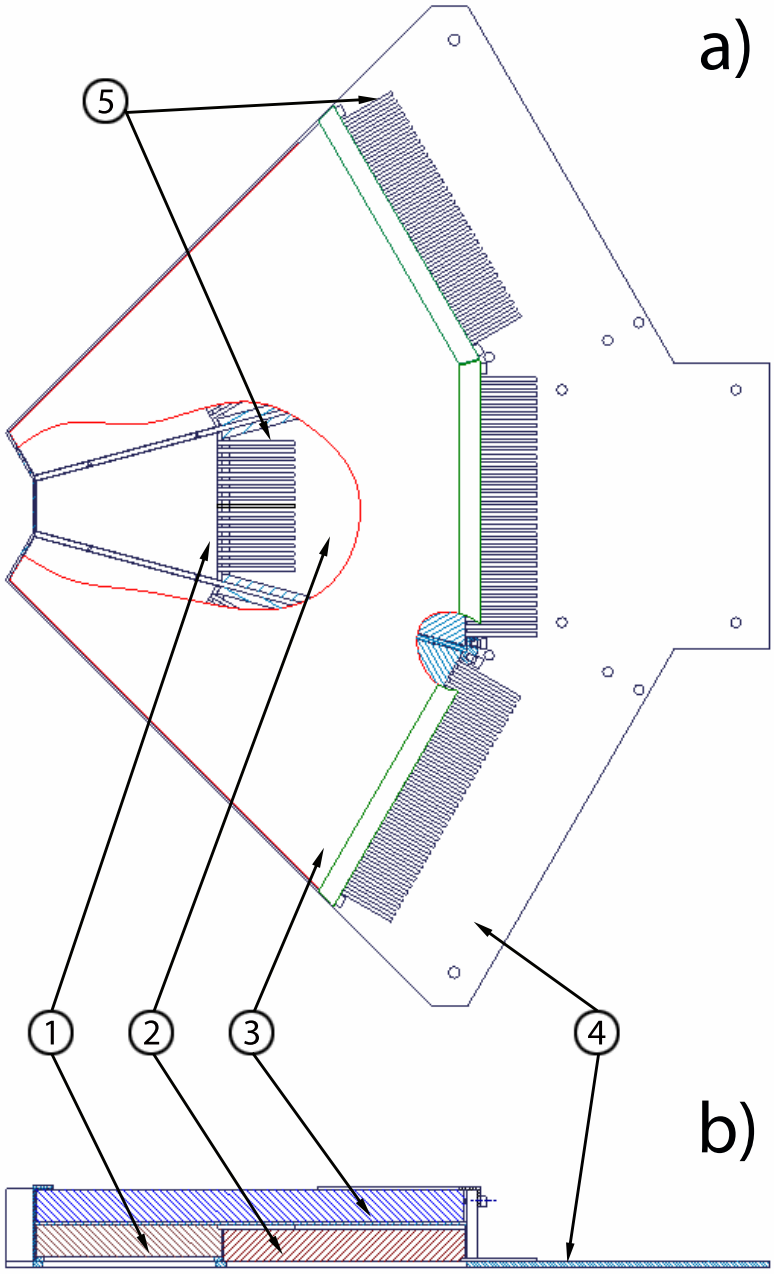

Figure 3.3: (*a*) A top view of an assembled tray with a cutout of the Pb converter (3) showing the inner (1) and outer (2) scintillators underneath in their compartments with their optical fibers (5) emerging to their rear. (4) identifies the Al tray. (*b*) A side view of an assembled tray with the Pb converter above the scintillators. Notice the plastic spacer directly underneath the inner scintillator, offsetting it from the outer scintillator, allowing its fiber light guides to exit the tray.

plastic tubing for light tightness, bundled together inside flexible plastic tubing for stability, and protected by an Al cover. They then run the length of the support arm fastened by plastic ties and protected by two more Al covers. At the end of the arm each scintilltor's fibers are unsheathed from their individual tubing, yet still encased in the larger flexible tubing, bundled together into a plastic end cap and attached to a "cookie" covering the face of a PMT. Here the cookie guides the light from the fibers into the PMT using a 45° reflective surface to bend the light a total of 90°. Along with black tape, a custom built Delrin cap is used to fasten the cookie onto the PMT and make the connection light tight. Each PMT is then fastened to the end of the arm and positioned parallel to the beam pipe, giving each quadrant a length of ∼124 cm.

Hamamatsu R5543 3-inch fine mesh PMTs are used to measure the signal. Although not the same type of PMT used in the original magnetic field tests discussed in Sec. 3.3, these PMTs are also designed to operate in a high magnetic field with similar behavior expected. Moreover, these PMTs did undergo their own magnetic field testing as mentioned in Sec. 3.4. Once assembled each quadrant was fastened to the Central Magnet's nosecone, giving the tray portion of the assembly a total thickness of ∼5 cm. A photograph of the RXNP's North Arm after installation is shown in Fig. 3.4.

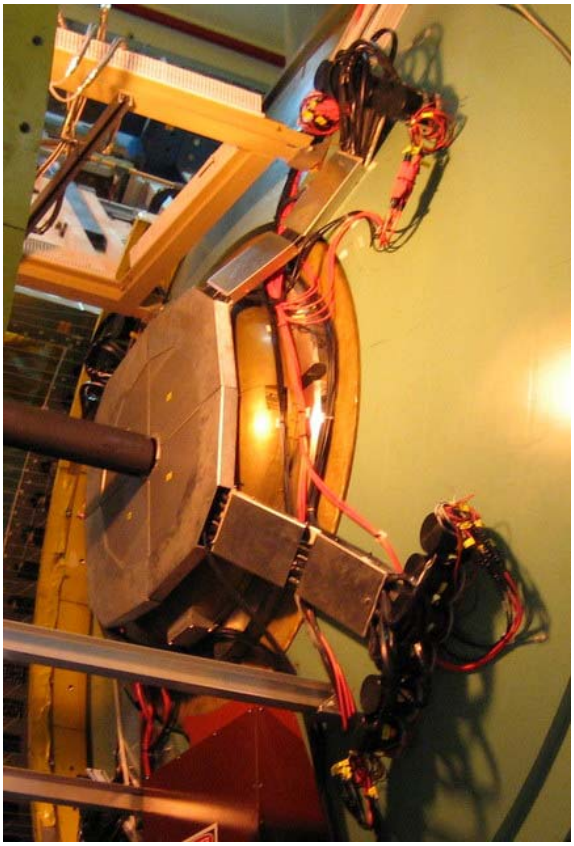

Figure 3.4: Photograph of the RXNP's North Arm installed on the Central Magnet's copper nosecone prior to the installation of the HBD.

3.3 Simulations and Testing

The RXNP was designed to optimize the resolution of the 2nd harmonic EP measurement, while not interfering with the location and particle acceptance of existing PHENIX subsystems. One contributing factor that strongly influences the EP resolution is the particle multiplicity that is incident on the detector, where a large multiplicity is desirable. This can be maximized by designing the RXNP to include a large η coverage, while placing it close to the nominal vertex position. Within the PHENIX experiment, shown in Fig. 2.3, this region is largely occupied by existing subsystems, magnets and support structures. After considering the space available for a new detector, it was decided that the RXNP would be composed of two mirror image halves of radiating paddles located approximately $\pm$40 cm from the nominal vertex position and attached to the face of the Central Magnet's copper nosecones.

This location provided several design challenges including: (1) there being only 7 cm of available space between each nosecone and the soon to be installed Hadron Blind Detector (HBD) [70], and (2) the detector had to be able to operate effectively in the high magnetic field environment of PHENIX's central region, where the field strength can be as high as $\sim$1 T. In order to satisfy these requirements and answer many outstanding design questions, including material composition, converter effectiveness, and signal readout, extensive studies were performed.

Some of these issues were addressed in GEANT3 [71] based simulations using realistic 200 GeV Au+Au collision v_2 and multiplicity distributions in η, p_T, and ϕ.

The RXNP was modeled as two scintillating disks surrounding the beam pipe and evenly divided into 8 segments in ϕ, while located at either ± 34 or ± 39 cm from the nominal vertex. The η coverage for these simulations varied, but was always between $0.8 < |\eta| < 2.8$. Placed immediately in front of the scintillators was a similarly shaped metal converter whose purpose was to increase the EP resolution through conversion electrons.

The effectiveness of the converter in accomplishing this is seen in Fig. 3.5, which shows 2^{nd} harmonic EP resolution vs. centrality. Here an average of 16% increase in the resolution is seen when all the charged particles of a collision are used to measure the EP, compared to using only primary charged particles. A major reason for this improvement is displayed in Fig. 3.6, where the primary, secondary and background particle distributions are shown with respect to Ψ_{RP}. With no converter (a) a strong flow signal from primary particles is seen, but this is diluted by the secondary particles showing a nearly flat distribution. However, if a 0.5-cm brass converter is added, as in (b), the secondary particles not only increase in number due to the production of conversion electrons, as demonstrated by a similar simulation in Table 3.1, but they also carry a strong flow signal themselves that originates from the distribution of the parent particles, thereby reinforcing the flow signal from the primary particles. The addition of a converter was also shown to reduce the low energy background.

Increasing converter thickness was also shown to increase the 2^{nd} harmonic EP resolution, as presented in Table 3.2, while increasing scintillator thickness was shown to give a better correlation between the number of particle hits and energy

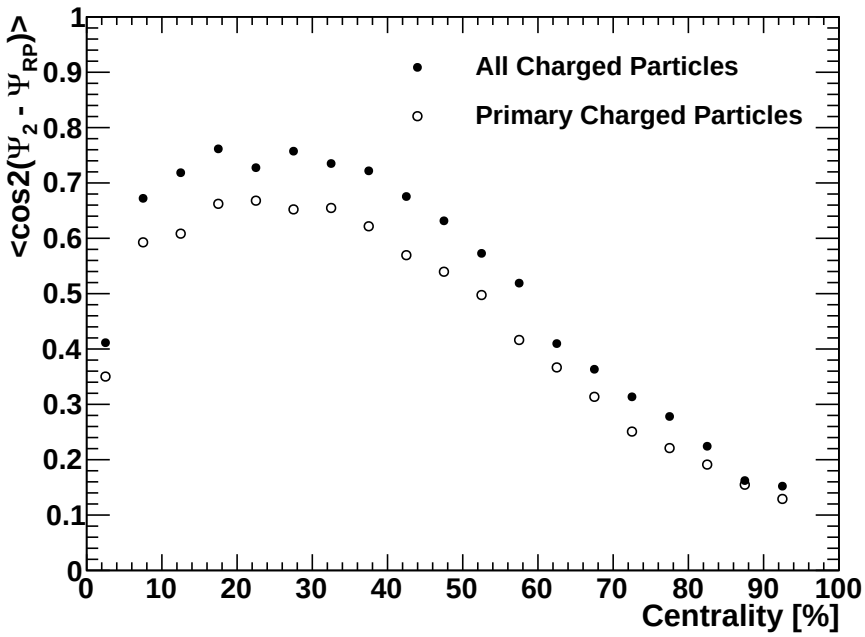

Figure 3.5: RXNP 2nd harmonic EP resolution (Eq. 3.1) vs. centrality using a GEANT3 based simulation. Open circles pertain to only primary charged particle hits and closed circles are for all charged particle hits. Here the effectiveness of the converter is demonstrated by the secondary charged particles increasing the detector's resolution compared to using only primary charged particles. Also notice the resolution varies as a function of centrality, where it is at a maximum between 20-30%. This is caused by a combination of changing event multiplicity and v_2 signal.

Table 3.1: Charged Particles Per RXNP Segment Using Different Thickness Brass Converters

Converter Thickness	Primary	Secondary	Total
No Converter	151	78	229
1.5 cm	132	340	472
4 cm	103	723	826

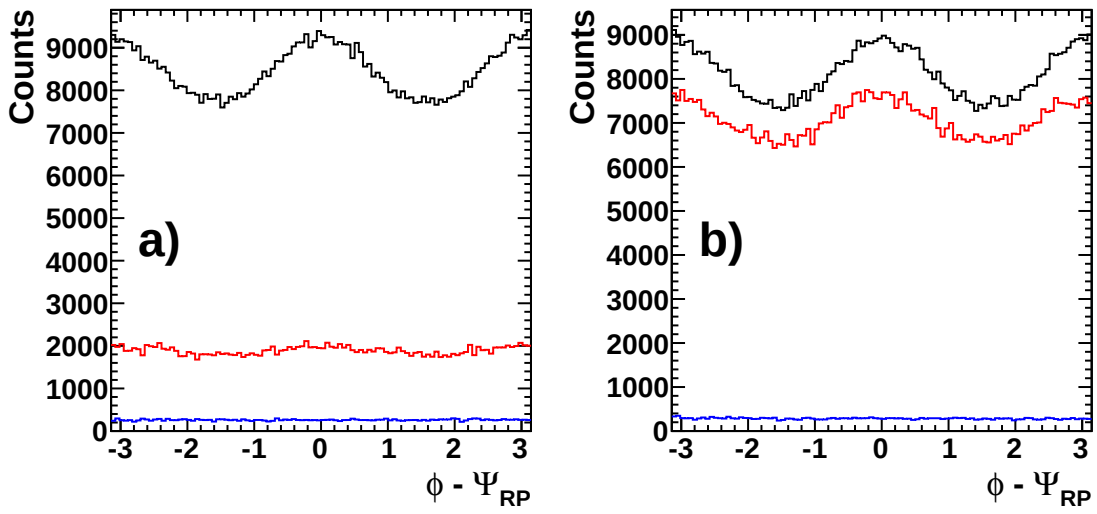

Figure 3.6: Particle distribution with respect to Ψ_{RP} for primary (top, black), secondary (middle, red) and background (bottom, blue) particles without (a) and with (b) a converter. Without the converter the secondary particles have a nearly flat distribution, but with a 0.5 cm brass converter the secondary particles exhibit a strong flow signal (strong anisotropy), thereby reinforcing the flow signal from the primary particles.

deposition, as depicted in Fig. 3.7. To optimize the converter and scintillator thickness within the constraints of the limited space available between the nosecone and HBD, it was decided to restrict the thickness of the converter and scintillator to 2 cm each. Therefore, 2-cm thick brass, Pb, and W converters were simulated with a 2-cm thick scintillator to compare energy deposition. The results are shown in Fig. 3.8. Using the same thickness scintillator and converters, the 2$^{\text{nd}}$ harmonic EP resolution for mid-central collisions was also simulated and found to be 0.70, 0.74 and 0.76 for brass, Pb, and W, respectively. For both energy deposition and EP resolution, W performed best, but only marginally so compared to Pb, which is significantly less expensive. Therefore, Pb was chosen as the converter material.

The optimum radiator ϕ segmentation for the 2$^{\text{nd}}$ harmonic EP resolution was also studied. Figure 3.9 shows that the resolution improves only marginally above 8

Table 3.2: RXNP 2nd Harmonic EP Resolution for Mid-central Events Using Different Thickness Converters and a 2-cm Thick Scintillator

Converter Thickness (cm)	0.0	1.0	2.0	4.0	8.0
Brass	0.53	0.65	0.71	0.76	0.80
Pb	0.53	0.73	0.75	0.75	0.68

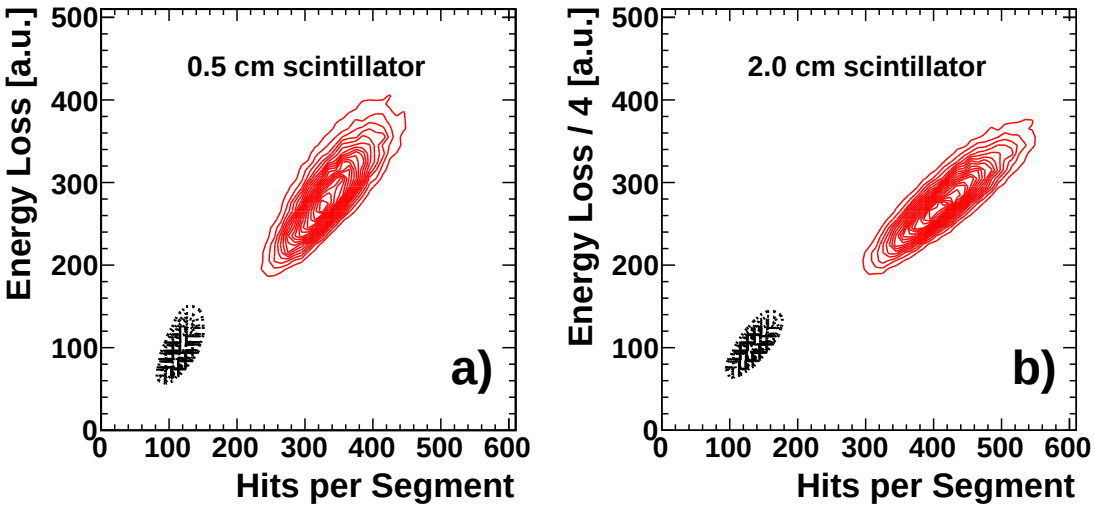

Figure 3.7: Number of particle hits per scintillator segment vs. energy loss. The scintillator thickness is 0.5 cm and 2.0 cm for (a) and (b), respectively. The dotted contour lines (black) use no converter, while the solid lines (red) use a 2.0-cm brass converter. Notice the energy loss in (b) is divided by 4. Both with and without the converter, the correlation is better with the thicker scintillator.

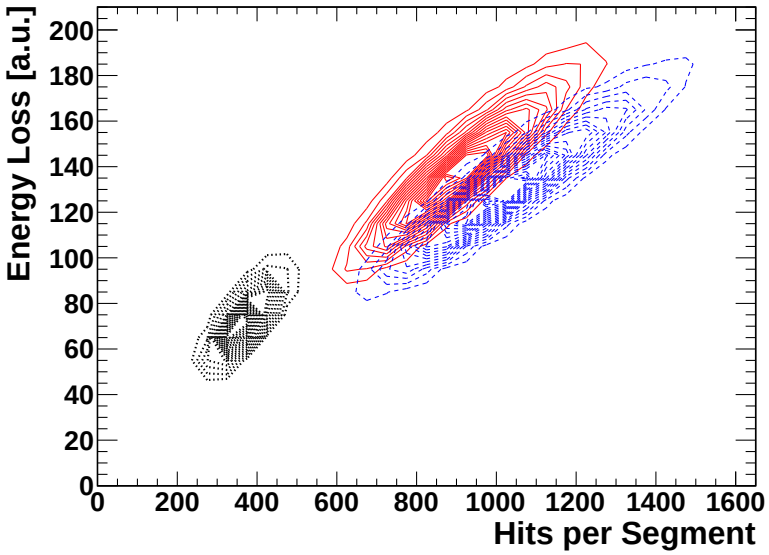

Figure 3.8: Particle hits per scintillator segment vs. energy loss using 2.0-cm brass (dotted, black), Pb (solid, red), and W (dashed, blue) converters. Tungsten provides the best hit to energy loss correlation, but only marginally so over Pb, which is significantly less expensive. In all cases a 2-cm scintillator was used.

segments; however, to protect against failing segments it was decided to partition the detector into 12 paddles in ϕ. The RXNP was further divided into two radial sections covering $1.0 < |\eta| < 1.5$ (outer ring) and $1.5 < |\eta| < 2.8$ (inner ring) as a result of a series of simulations incorporating the PHENIX Central Arm spectrometers ($|\eta| < 0.35$) that showed a centrality and η dependent fake v_2 signal from jets when using the EP of the RXNP. These studies showed an increasing non-flow bias the closer in proximity the RXNP's η coverage is to the Central Arms and the more peripheral the event, as demonstrated in Fig. 3.10. This bias can result from back-to-back di-jet correlations, as well as correlated particle production from the near-side jet cone, which can have a size of 0.7 units in η. Therefore, to minimize the impact of this bias on a wide range of physics analyses, the RXNP was divided into two η sections resulting in the inner ring section experiencing only a minimal bias effect.

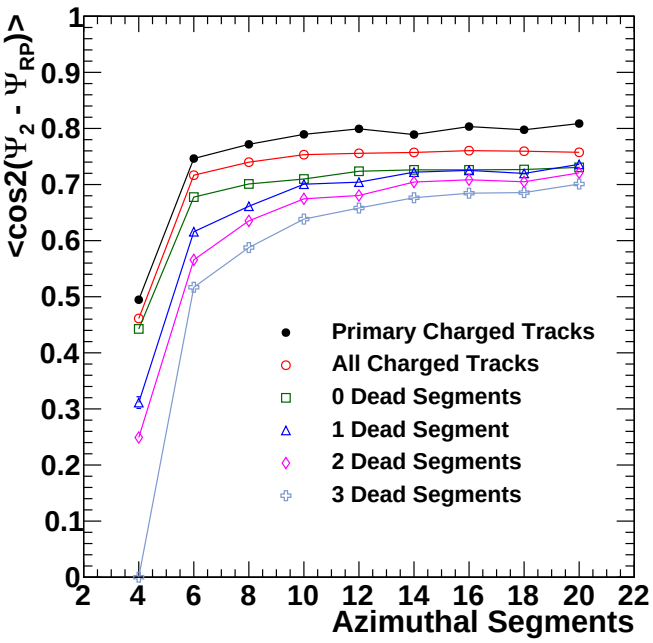

Figure 3.9: Dependence of the 2nd harmonic EP resolution of mid-central collisions on the azimuthal segmentation of the RXNP's scintillators. The closed circles use only the number of primary charged particles in each segment as the weight, with each particle having a weight of 1. The resolution for the open circles is similarly calculated, but uses all charged particles (primary, secondary and background). The square, triangle, diamond, and cross data points all calculate the resolution using the energy deposition into the scintillators from charged particles as the weighting factor, while at the same time having 0, 1, 2 or 3 dead scintillator segments, respectively. In all cases a 2-cm scintillator and 2-cm brass converter were used.

This added flexibility was proven effective in [35], where only the inner ring was used in measuring the v_2 of high p_T π^0's, and in [39], which used both η sections in examining the η dependence of non-flow effects, such as jets or fluctuations in participant geometry.

Avalanche photodiodes (APDs) and PMTs were considered for signal readout. APDs have several advantages over PMTs, including being unaffected by magnetic fields, significantly cheaper, and allowing for a simpler design by jettisoning the need for light guides. However, after performing calculations and bench tests, it was confirmed that the signal to noise ratio from APDs was insufficient for this

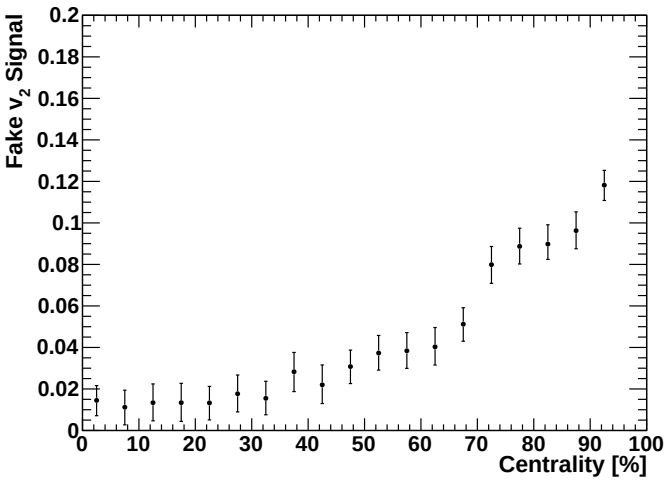

Figure 3.10: Fake v_2 signal from jets with respect to centrality in the PHENIX Central Arm spectrometers ($|\eta| < 0.35$) when using the EP calculated from the full RXNP and requiring each event's leading hadron to have a $p_T > 6$ GeV/c. 1 σ statistical error bars are shown.

application; therefore, it was decided to pursue a PMT design.

To confirm that PMTs could function well in PHENIX's strong magnetic field and to investigate an optimal radial position and angular orientation with respect to the field lines, a series of magnetic field tests were performed. One of these tests involved constructing and positioning a test stand in PHENIX's central region that simultaneously held two sets of four PMTs, separated by 120°, at radial positions where their gains were predetermined to be best: 80, 90, 110, and 130 cm. Hamamatsu R5924 fine mesh PMTs were used, which are specifically designed to operate in a high magnetic field environment. Using an LED pulser, each tube's gain was recorded at zero and full field for PHENIX's "++" and "+−" field configurations. In addition, because the region in which the RXNP was to be installed is near the magnetic field return, the field lines exhibit non-uniform behavior that is not well-known. Moreover, with PMT performance in a magnetic field known to be sensitive

Table 3.3: Fraction of PMT Gain Observed at Full Field Compared to Zero Field

Distance (cm)	"++" 30°	"+−" 30°	"++" Parallel	"+−" Parallel
80	0.61	0.00	0.76	0.56
90	0.39	0.33	0.78	0.23
110	0.50	0.32	0.96	0.54
130	0.44	0.35	0.85	0.66

to the alignment of the tube with respect to the field lines, two configurations were tested for each field setting: PMTs aligned parallel and at 30° to the beam pipe. The results of this test are given in Table 3.3, where the numbers are averaged from the two PMTs located at each distance. Based largely on these results and the fact that the magnetic field would be in the "+−" configuration for Run-7, it was decided the PMTs would be placed parallel to the beam pipe at a radial distance of 130 cm. Here, they would experience a magnetic field strength of ∼0.66 T (∼0.61 T) for the "+−" ("++") field configurations.

With much of the design solidified, the remaining element to be determined was the radiator and light guide configuration. This was resolved through beam tests performed at KEK-PS in Japan using a momentum selected charged particle beam. The purpose of these tests were to examine different radiator (scintillator vs. Cherenkov) and light guide (solid vs. embedded fiber) combinations. These tests showed that, although the solid light guide resulted in more light collection, it also had a signal size that was dependent on the incident particle's position in the radiator, as seen before in [72], which would likely worsen the EP resolution. This effect was significantly less pronounced using the embedded fibers, which when combined with their reasonable light collection and flexibility in positioning and

grouping PMTs, led to their selection. The Cherenkov radiator was eliminated because it yielded too small a signal when used with embedded fibers, while the scintillator signal was reasonable. Thus scintillator radiators with embedded fiber light guides were chosen for the RXNP.

3.4 Online Performance

Prior to final assembly and installation, each PMT was tested for noise, signal linearity, and signal strength in and outside a magnetic field. After installation one PMT in the South Arm became disabled prior to the start of Run-7, decreasing the detector acceptance to ∼98% of design, which remained throughout the Run. Figure 3.11 shows a typical ADC spectrum from a RXNP PMT during Run-7 min-bias data taking. At the high end of the distribution several hundred charged particles, including conversion electrons, are measured in the scintillator segment. The dynamic range of the ADC is 12 bits or 4096 quantized units, of which ∼2000 are typically used.

The gain of the tubes was monitored throughout Run-7 and was found to decrease over time with no pattern seen regarding scintillator location. Figure 3.12 shows the relative gains of six representative PMTs starting at the beginning of Run-7 and continuing until its end. During Run-8 and 9 similar voltages were used while colliding species of p+p and d+Au at the same energy, along with p+p at 500 GeV. The p+p data showed no signal degradation, while for d+Au some degradation was observed in both RXNP arms, although not as severe as with Au+Au. For Run-10,

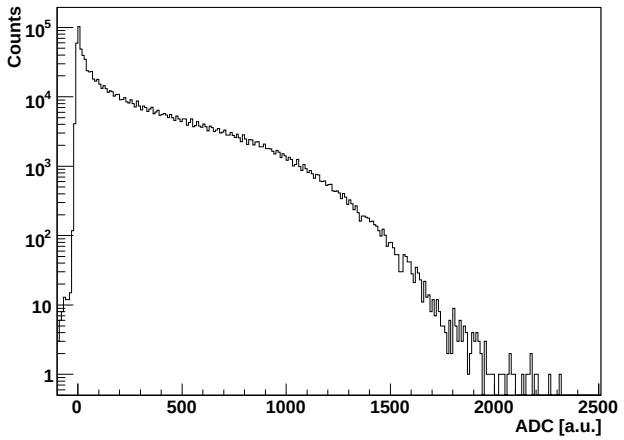

Figure 3.11: Typical raw ADC spectrum of a RXNP PMT during Run-7 min-bias data taking. The distribution results from frequent peripheral (low multiplicity) and rare central (high multiplicity) interactions, which are proportional to the geometrical cross-section.

where Au+Au was again collided at 200 GeV, the RXNP high voltage was increased to counter the loss in gain observed in Run-7. Again the signal decreased over the course of the Run, although not quite as severely as in Run-7. The cause of the gain loss remains unexplained, but appears related to the use of heavy-ions at higher energies, since no degradation was seen during the Run-10 lower energy ($\leq$ 62.4 GeV) Au+Au running period.

The observed signal degradation has a negligible effect on the RXNP's 2^{nd} harmonic EP resolution, except in the most peripheral events where the change is less than 5%. The effect of the removal of the west half of the HBD $\sim 1/3^{\text{rd}}$ through the Run was also examined and found to be negligible for central events, but does increase the resolution of peripheral events by up to 10%.

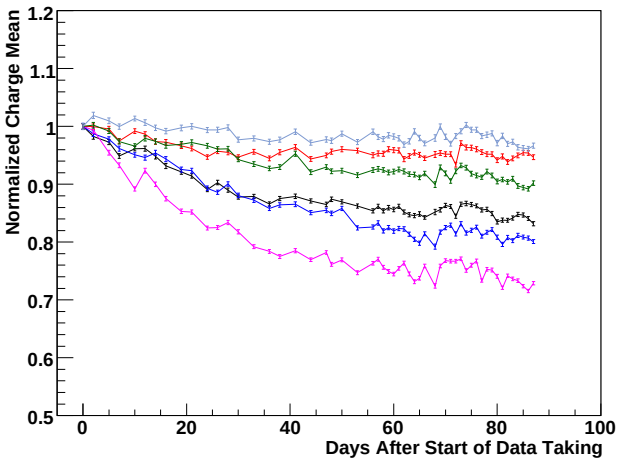

Figure 3.12: Normalized mean gain values of 6 representative PMTs taken periodically during Run-7. Each PMT is normalized to its own charge mean at the start of data taking. 1 σ statistical error bars are also shown.

3.5 Calibrations

Equation 1.6 is used to measure Ψ_{EP} from the RXNP in a manner similar to the other EP detectors, where ϕ_i is the ϕ angle at the center of each scintillator and w_i the charge collected by that scintillator's PMT. After pedestal subtraction, three calibrations are performed on a run by run basis to flatten the Ψ_{EP} distribution, which, by definition, should be flat since the RP from the two colliding nuclei has an equal probability of occurring at any angle. However, due to effects such as the broken PMT, unequal PMT gains, and beam offset, the EP angular distribution from the raw data is not flat. To correct this, each PMT's gain is first calibrated to have the same mean ADC value. The second step recenters the X_n and Y_n event flow vector distributions to zero along with adjusting their width to unity by [31]

$$X_n^{corr} = \frac{X_n - \langle X_n \rangle}{\sigma_{X_n}}, \qquad Y_n^{corr} = \frac{Y_n - \langle Y_n \rangle}{\sigma_{Y_n}}, \tag{3.3}$$

where X_n^{corr} and Y_n^{corr} are the corrected flow vectors for reinsertion into Eq. 1.6, and σ_{X_n} and σ_{Y_n} are the uncorrected distribution widths, *i.e.* standard deviations.

The third step fits a Fourier expansion to the modified distribution and performs an event-by-event shifting of the angles using [73]

$$\Psi_n^{corr} = \Psi_n + \frac{1}{n}\sum_i \frac{2}{i}\left[-\langle \sin(in\Psi_n)\rangle \cos(in\Psi_n) + \langle \cos(in\Psi_n)\rangle \sin(in\Psi_n)\right], \quad (3.4)$$

where Ψ_n^{corr} is the corrected and final EP angle. The result from each of these steps for the 2$^{\text{nd}}$ harmonic EP is shown in Fig. 3.13. Notice the final distribution has six remaining "spikes". These spikes result from the flattening of the distribution to the 5$^{\text{th}}$ harmonic in the final calibration step, along with the combination of finite detector granularity and low multiplicity peripheral events. For these events it is possible for only one paddle to be hit causing its angular center to be assigned as that event's EP angle. This causes an overrepresentation of that angle in the EP distribution that is not eliminated by the calibrations. However, these spikes do disappear for event centralities $< 70\%$. Calibration steps 2 and 3 were also applied to the other EP detectors: BBC, SMD, and MPC. For step 1, the BBC and SMD applied their own PMT gain correction technique, while the MPC did not apply a gain calibration during Run-7.

3.6 Event Plane Resolution

The RXNP measures the EP angle from nine different detector segment combinations: N+S, N+S inner ring, N+S outer ring, N (S), N (S) inner ring, and N

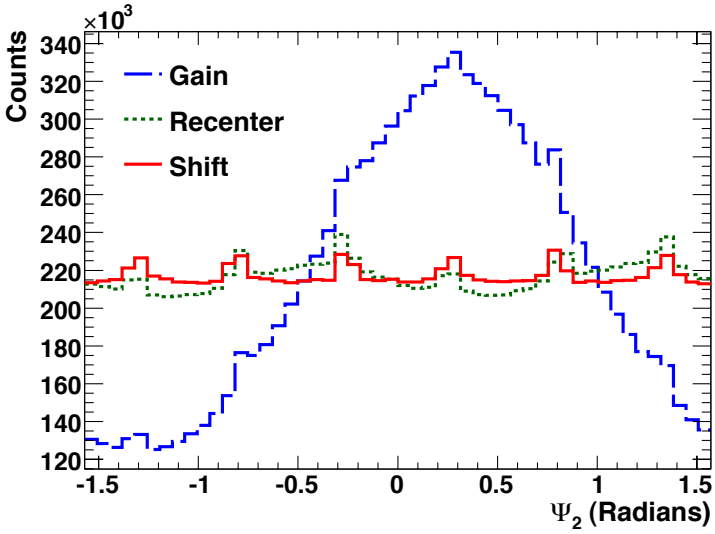

Figure 3.13: RXNP 2nd harmonic EP distribution of min-bias events from a typical run after each calibration step. The dashed line (blue) is after the gain correction, dotted line (green) is after recentering, and the solid line (red) is after angular shifting. Notice the y-axis does not start at zero.

(S) outer ring. Two methods can be used to determine the EP resolution of the different detector segments, which are explained in detail in [31], but will be briefly outlined here. Essentially these methods work by comparing the Ψ_{EP} measured from different detectors, or *subevents*, located at different η. The first method uses the EP angle determined from two equal multiplicity subevents, (a) and (b). For example, (a) = RXNP_S and (b) = RXNP_N. The resolution of each subevent is

$$\langle \cos[km(\Psi_m^a - \Psi_{RP})] \rangle = \sqrt{\langle \cos[km(\Psi_m^a - \Psi_m^b)] \rangle}. \tag{3.5}$$

Recall from Eq. 1.5 that m denotes the harmonic of the measured EP and k is a multiplier such that $n = km$. The resolution of the combined subevents $(a+b)$,

RXNP_NS in this case, is determined using

$$\langle \cos[km(\Psi_m^{(a+b)} - \Psi_{RP})]\rangle = \frac{\sqrt{\pi}}{2\sqrt{2}}\chi_m \exp(-\chi_m^2/4) \times [I_{(k-1)/2}(\chi_m^2/4) + I_{(k+1)/2}(\chi_m^2/4)], \tag{3.6}$$

where $\chi_m = v_m\sqrt{2N}$ with v_m being the measured flow signal for harmonic m, and $I_{(k-1)}$ and $I_{(k+1)}$ are modified Bessel functions. This method is called the *2-subevent method*.

For this analysis, the 2$^{\text{nd}}$ harmonic EP resolution calculated using the 2-subevent method was not solved for exactly, but rather estimated through an iterative process. First the resolution of a single subevent, such as (a) = RXNP_S, was solved for exactly using Eq. 3.5 with (b) = RXNP_N. Then the χ_m value pertaining to this resolution was estimated using Eq. 3.6, by first guessing what χ_m could be for this resolution and then applying increasingly finer iterative corrections to the guess until the approximation was essentially indistinguishable from the real value. This χ_m was then multiplied by $\sqrt{2}$ to get the value for the combined subevents $(a+b)$, RXNP_NS in this example, which was then inserted into Eq. 3.6 and the resolution solved for.

The second method, called the *3-subevent method*, uses three subevents and the multiplicity of each is <u>not</u> required to be equal to the others, such as (a) = RXNP_S, (b) = RXNP_Nin, and (c) = BBC_NS. The resolution for this method is calculated by

$$\langle \cos[km(\Psi_m^a - \Psi_{RP})]\rangle = \sqrt{\frac{\langle \cos[km(\Psi_m^a - \Psi_m^b)]\rangle \, \langle \cos[km(\Psi_m^a - \Psi_m^c)]\rangle}{\langle \cos[km(\Psi_m^b - \Psi_m^c)]\rangle}}. \tag{3.7}$$

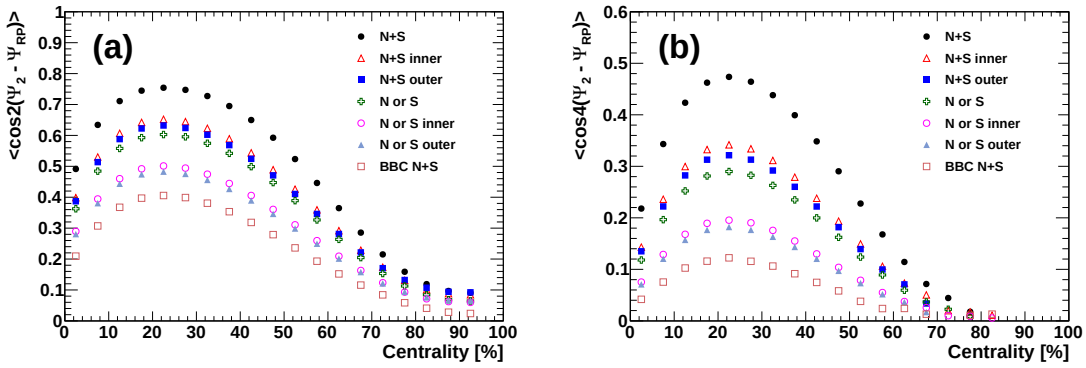

Figure 3.14: The EP resolution for different RXNP detector segments using min-bias events for (a) the 2$^{\text{nd}}$ harmonic and (b) the 4$^{\text{th}}$ harmonic. For reference, the corresponding BBC resolution is also shown. Notice (a) and (b) have different size y-axes.

Using the 2-subevent method with $m = 2$, the 2$^{\text{nd}}$ and 4$^{\text{th}}$ harmonic min-bias EP resolutions for the different segments of the RXNP are shown vs. centrality in Fig. 3.14. There is a factor of ∼2 increase in the 2$^{\text{nd}}$ harmonic EP resolution when using the full RXNP detector compared to the BBC, which is what was expected from simulations (see Fig. 3.14). This factor is even greater (∼4x) when using the 4$^{\text{th}}$ harmonic plane. The 1$^{\text{st}}$ harmonic resolution was also examined, but showed inconsistencies, making it unreliable. These inconsistencies included significantly overestimating the EP resolution for central events when using the first method. When using the second method the resolution varied significantly depending upon which of PHENIX's other sub-systems were used in measuring the Ψ_1^b and Ψ_1^c angles. Also, when Ψ_1^b and Ψ_1^c are from each RXNP arm, the resulting resolution of the third detector's EP angle (Ψ_1^a) was significantly underestimated. Possible causes of this behavior include momentum conservation between the two RXNP arms and the small 1$^{\text{st}}$ harmonic anisotropic flow signal within the RXNP's η coverage (see [74]).

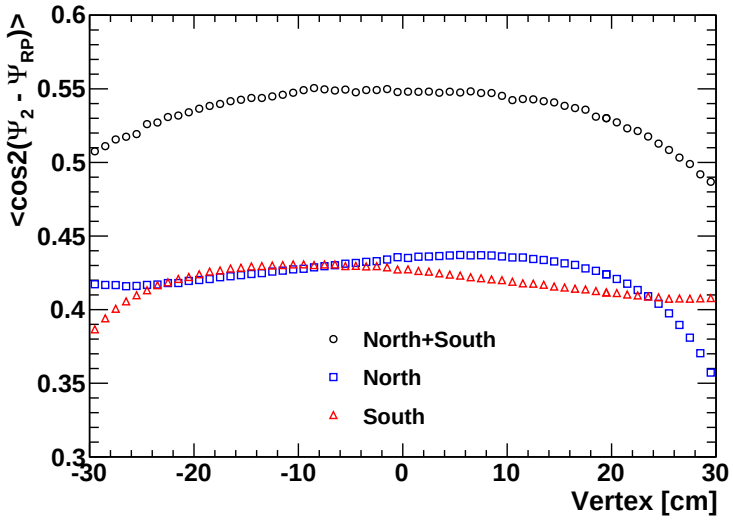

Figure 3.15: RXNP 2nd harmonic EP resolution vs. vertex for the South Arm (red triangles), North Arm (blue squares) and combined arms (black circles) for min-bias events within the PHENIX vertex acceptance of ±30 cm. The resolution is calculated using the 3-subevent method (Eq. 3.7), where Ψ_2^b and Ψ_2^c are from the BBC North and BBC South when calculating the combined resolution and RXNP opposite arm and BBC_NS when calculating the individual arm resolutions. In all cases $m = 2$.

Using the 3-subevent method, where again $m = 2$, the RXNP's 2nd harmonic EP resolution is shown vs. vertex in Fig. 3.15. This figure shows that each detector's resolution varies by $< 4\%$ within ±20 cm of the nominal vertex; however, at the edge of PHENIX's vertex acceptance of ±30 cm the resolution varies by up to 10% for the South Arm, 18% for the North and 11% when combined. The effect doubles for the 4th harmonic. For each arm the maximum resolution is achieved at ∼7 cm closer to the arm than the nominal vertex or ∼32 cm from each arm.

The decrease in resolution away from this position is the result of a complex interplay between a number of factors related to a changing η with changing vertex. The slow rise in resolution as the vertex approaches a detector arm can largely be explained by the η dependence of v_2 as measured by PHOBOS in Fig. 3.16.

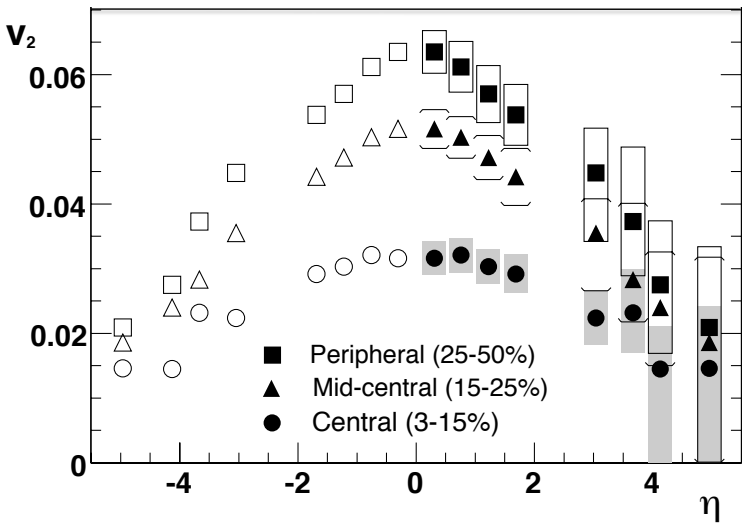

Figure 3.16: The $v_2(\eta)$ of unidentified charged particles from the PHOBOS detector. Shown are centralities of 3-15% (circles), 15-25% (triangles), and 25-50% (squares). The $\eta > 0$ data points are reflected across $\eta = 0$. Corresponding statistical and systematic errors are shown [33].

The v_2, or 2$^{\text{nd}}$ harmonic azimuthal particle asymmetry used here to measure the EP, increases as η approaches 0, resulting in a more accurate EP measurement the closer the event vertex is to an arm of the RXNP. However, this effect is eventually offset due to the decreasing size of the detector acceptance (smaller η coverage) leading to a smaller multiplicity of particles used in the EP determination, resulting in a less accurate EP and lower resolution.

The change in the observed multiplicity in the RXNP with respect to event vertex is roughly proportional to the change in energy deposition, shown in Fig. 3.17. However, it is important to note the closer the event vertex is to an arm, the longer the average path length the particles have passing through the scintillators, which results in more energy being deposited on a per particle basis. This effect acts counter to the loss in energy deposition due to the lower detector multiplicity,

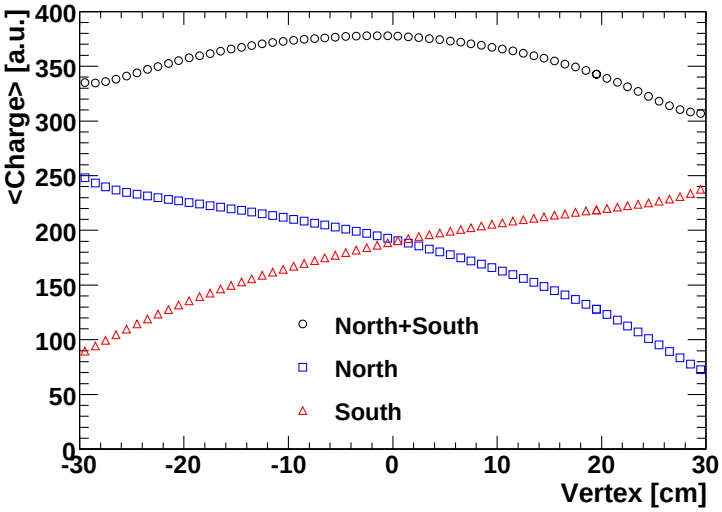

Figure 3.17: Mean charge deposited into the RXNP South Arm (red triangles), North Arm (blue squares) and combined arms (black circles) as a function of collision vertex position for min-bias events. In the case of the individual arms, the charge deposited increases as the event vertex occurs further away.

making the energy deposition only a guide to how the particle multiplicity changes with event vertex.

3.7 Summary

The PHENIX Collaboration successfully designed, installed, and commissioned the RXNP before Run-7 to more accurately measure the Ψ_{RP} of colliding Au nuclei. The RXNP performed as expected from simulations by increasing PHENIX's 2^{nd} harmonic EP resolution a factor of $\sim$2 from the previously used BBC detector. This higher resolution detector expands PHENIX's capabilities and allows for analysis of ever rarer particles and more accurate measurements, which has already been demonstrated in several recent articles [35, 38, 39, 75–79] and will be shown in Chapter 5 to play an intricate role in this analysis. Additional RXNP details can

be found in the RXNP Letter of Intent [80].

Chapter 4

Data Acquisition and Offline Computing

4.1 Data Acquisition

The PHENIX data acquisition system (DAQ) [81] is a complex "orchestra" of hardware and software that enables PHENIX to record data from the thousands of collisions that RHIC provides every second. The DAQ is tethered to the PHENIX detector through each subsystem's Front End Module (FEM) that collects, digitizes, and temporarily stores the data. The temporary storing provides time for a trigger decision on if the data should be recorded or discarded. Several triggers can be used at once including the min-bias trigger, which was used for this analysis and whose primary requirement is > 1 hits in each BBC arm. The timing of the trigger is controlled by the RHIC clock, which alerts PHENIX to when a bunch crossing occurs. This information allows PHENIX to pinpoint small windows of time for data collection, greatly reducing background and increasing efficiency. These bunch crossings occur every 106 ns, with most resulting in no collisions; nonetheless, their high frequency did result in a maximum collision rate of $\sim$5 kHz in Run-7.

Once a trigger accepts the event, the data is sent by fiber optic cable from the FEMs located in the interaction region (IR), to the Data Collection Modules (DCM) located in a nearby electronics room. Each detector has its own DCM which performs error checking, zero suppression (removal of data that recorded no hits),

and data formatting. From here the data from each subsystem is transfered to the Event Builder where it is assembled into a combined event. After assembly, the data is transfered to the Buffer Box (BB) hard drives for temporary storage and analyzed immediately for quality assurance. Periodically the BBs become full and old data must be removed for the collection of new data. When this happens, the oldest data on the BBs is transfered to the RHIC Computing Facility's (RCF) [82, 83] High Performance Storage System (HPSS), where the data is put on tape for long term storage. Overall the PHENIX DAQ is capable of writing data at ∼700 MB/s, which translates into an event rate of ∼5 kHz for 200 GeV Au+Au collisions, matching the maximum collision rate in Run-7, when ∼650 Terabytes of data were recorded.

Depending on funding, the typical RHIC running period is between the months of November and June. While running, the detector must be monitored 24 hours a day 7 days a week by a 5 person shift crew consisting of a Shift Leader to lead the shift crew and monitor the overall situation, a DAQ Operator to operate the DAQ, a Data Monitor to monitor the data in real time to ensure its quality, a Shift Assistant 1 to operate each subsystem's high voltage, and a Shift Assistant 2 to monitor the gas running through those subsystems that use it. The shift crew is located in an adjacent building to the IR where they are tasked with collecting as much high quality data as possible, while ensuring the safety of the detector and anyone who goes into the IR to perform maintenance. They must resolve technical problems as they arise with the DAQ, data monitoring, high voltage, etc., and remedy any alarms that sound, such as a smoke, temperature, or water flow. If they are not able to solve these problems alone then they alert subsystem experts who can. However,

under nominal running conditions the shift crew will collect data in one hour blocks referred to as a *run*, but these blocks are often shorter due to technical issues arising from the DAQ, a PHENIX subsystem, a RHIC fault, or coming upon the end of a store. These individual data collection "runs" should not be confused with a "Run" such as Run-7.

4.2 Offline Computing

4.2.1 Overview

During a Run, preparations begin for reconstructing the raw data hits into useful variables such as p_T, η, ϕ, etc. This starts with running calibration software over the raw data while it is still on the BBs, and storing the results in a database for later use during data reconstruction. After the Run, preparations continue, including fine tuning software, performing additional calibrations, and running small test productions. Once completed, the full production commences, which can take several days to several months to complete, depending on the size of the data set. The production is run using the PHENIX computer farm at RCF [82, 83], which housed ∼500 CPU cores during the Run-7 production and took several months to complete. When finished the Run-7 raw data was condensed into ∼30 Terabytes of reconstructed data and saved to disk.

To allow the end user to run over the data for analysis, PHENIX uses an internally conceived and constructed software framework called Fun4All that utilizes ROOT [84], an object oriented C++ library developed at CERN [85] for the analysis

of particle physics data. This framework provides for a relatively simple coding experience with the end user registering their analysis module with Fun4All, where it is then "feed" events one at at time from the requested data. To access an event's data, the analysis module, in typical C++ fashion, must initialize objects and use its methods to retrieve the variables.

To start this process, several interactive machines are available at RCF that a user can log in to develop and test code before submitting jobs to the PHENIX computer farm. The data that is output from these jobs can be stored on the disk space allotted to each user. For developing code or general analysis tasks, each user is granted a small amount of disk space that is backed up daily. A larger amount of space that is not backed up is also allotted, which is typically used to store a subset of the reconstructed events and variables specific to the user's analysis. This allows the user to more quickly analyze the data they are interested in rather than running over the entire data set. For more details on PHENIX's offline computing see [86].

4.2.2 Centrality Determination

Knowing the initial geometry of an event can play in important role in revealing information the emitted particles carry with them about the collision medium. Unfortunately, parameters such as impact parameter (b), number of nucleon participants (N_{part}), and participant eccentricity (ε_{part}), are unmeasurable quantities. Instead, they are interpreted indirectly through the event's particle multiplicity, where it is assumed the larger the multiplicity the smaller the b, the larger the N_{part}, and

the smaller the ε_{part}, although this isn't always the case as will be demonstrated shortly. The quantity that is measured from the multiplicity is called *centrality*, which is the percent of collisions having a larger multiplicity than the current collision. Therefore, centrality is measured as a "%". For instance, an event having a centrality of 10% would mean that 10% of min-bias events have a higher multiplicity than the current event. By definition, this results in a flat centrality distribution.

Defining centrality in this manner alleviates the potential problem of starting the centrality "count" with peripheral collisions. This is because not all peripheral events activate the min-bias trigger due to their low multiplicity, resulting in not all of them being recorded. Because of this, simulations are employed to determine the *min-bias trigger efficiency* (ϵ_{MB}), which is always less than 100%. After determining a ϵ_{MB} value (discussed shortly), all recorded events are naively assumed to have a centrality value less than the ϵ_{MB} value, leading to the presumption that no events were recorded beyond a certain periphery. This leaves the most peripheral centrality bins empty, while the most central bins will always contain events.

PHENIX measured centrality in Run-7 using the charge distribution collected with the BBC_NS, which was plotted on a run-by-run basis to avoid any gain changes over time. Here, a linear relationship was assumed between charge collection and particle multiplicity. Correction factors were then applied so that each run had the same mean charge. This was followed by summing the charge distributions for all the events from all the runs into 12 distinct 5-cm vertex histograms between -30 cm $< z <$ 30 cm. The distribution in each histogram was then segmented into 1% centrality ranges so the integral of each segment was approximately equal to the

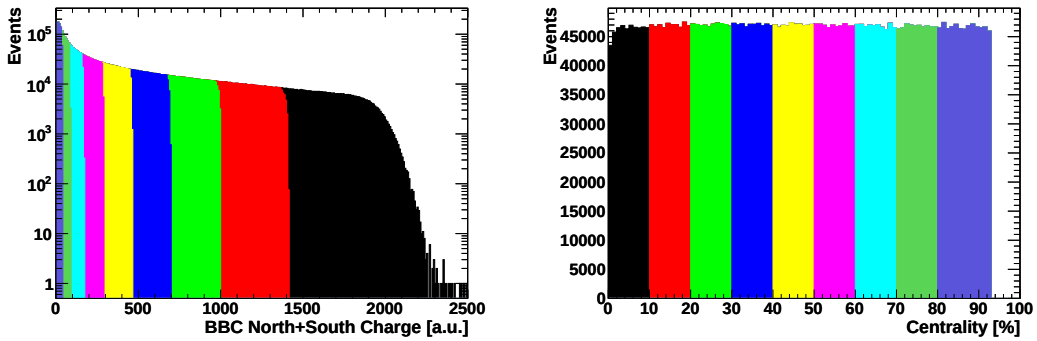

(a) (b)

Figure 4.1: (*a*) The BBC charge distribution of a 5 million event run using the min-bias trigger. Events were recorded within -30 cm $< z <$ 30 cm. Ten % centrality ranges are indicated by the different colored bands (most peripheral bin is 80-93%). Notice that despite the centrality calibration being applied, there is some charge overlap between centralities. This is not thought to be a significant source of systematic uncertainly. (*b*) The flat centrality distribution for the same run. Notice the empty bins for centrality $> 93\%$.

others within the histogram. Figure 4.1(*a*) shows the resulting BBC charge distribution from a 5 million event run segmented into 10% centrality ranges. Fig 4.1(*b*) shows the resulting flat centrality distribution for the same run.

Although not experimentally known on an event-by-event basis, it is possible to determine the mean quantities of b, N_{part}, and ε_{part} for a given centrality range using a Monte Carlo Glauber simulation [87]. In this type of simulation the nucleons of each colliding nuclei are distributed in 3-dimensional space based on a Fermi distribution, which has the same functional form as the Woods-Saxon potential [88]

$$\rho(r) = \frac{\rho(0)}{1 + \exp[(r - R)/a]}, \tag{4.1}$$

where $\rho(0)$ is the nucleon density at the center of the nucleus, r is the distance from the center of the nucleus, R is the nuclear radius parameterized as $r_0 A^{\frac{1}{3}}$, with $r_0 =$

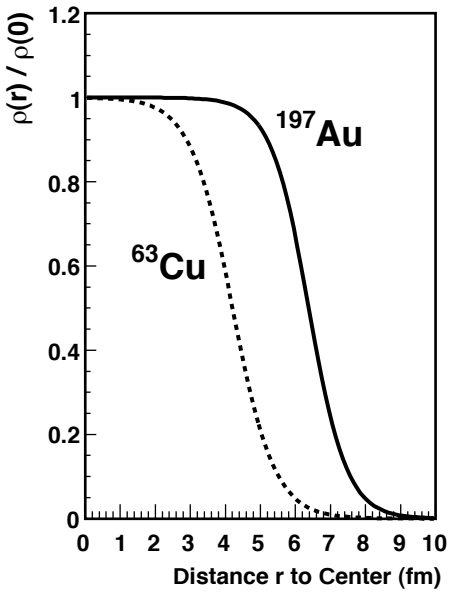

Figure 4.2: Fermi nuclear density distribution normalized to $\rho(0)$ for ^{197}Au and ^{63}Cu [89].

1.1 fm and A the number of nucleons in the nucleus, and a is related to the width of the edge region or "skin depth". For ^{197}Au, $R = 6.38$ fm and $a = 0.535$ fm. The Fermi distributions normalized to $\rho(0)$ for ^{197}Au and ^{63}Cu are shown in Fig 4.2.

In a Glauber simulation, nuclei pairs are created that each possess a distinct nucleon distribution based on the Fermi distribution. This uniqueness helps to simulate the fluctuations experienced in real collisions. Based on a realistic impact parameter distribution, these nuclei are then collided, with the participating nucleons undergoing binary collisions with other nucleons, simplistically simulating real collisions. From these collisions, experimental observables such as BBC hit multiplicity, and thus centrality, can be determined and thereby directly related to those event's b, N_{part}, and ε_{part}, as shown in Fig 4.3. Note the inverse nature of b and ε_{part} with respect to N_{part}. From these distributions the mean variable values can then be related to the experimentally determined centrality within a statistical and

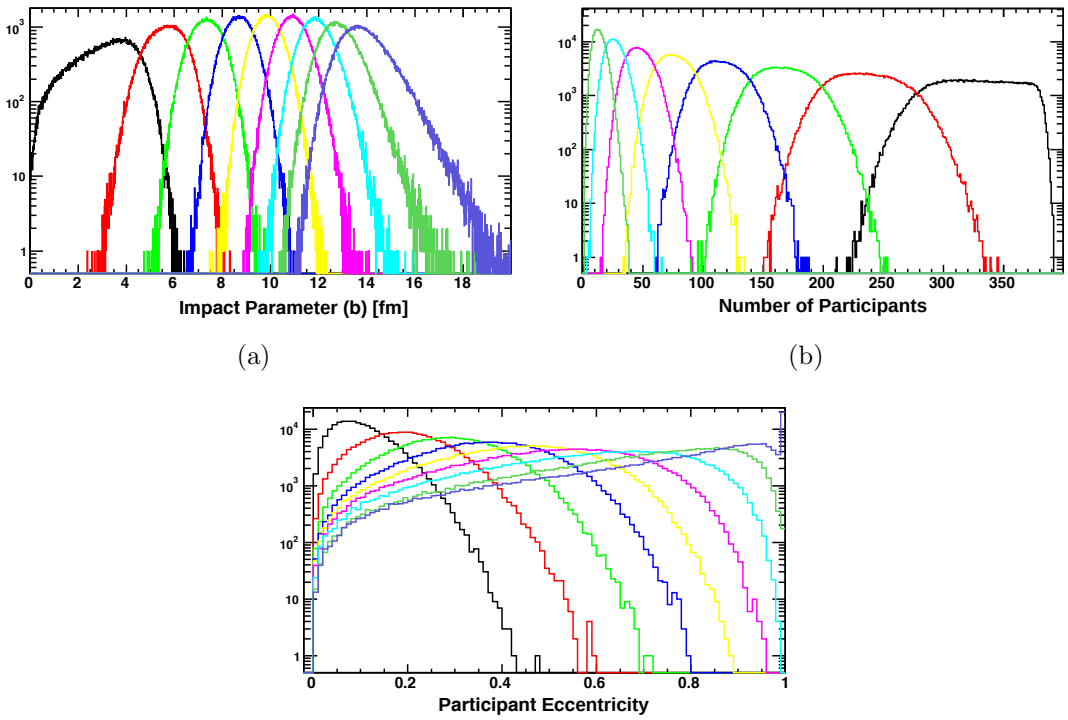

(a) (b)

(c)

Figure 4.3: Glauber model variable distributions in 10% centrality ranges, as indicated by the different colored lines (most peripheral bin is 80-93%). (a) The impact parameter, (b) the N_{part}, and (c) the ε_{part} distribution. Notice the centrality ranges overlaping in each histogram, illustrating the imperfection of the centrality method [89].

systematic uncertainty. Notice in the figure how the centrality ranges overlap each other in the variable distributions; thus, revealing the imperfections of the centrality method. Nonetheless, there is currently no better method to estimate the initial geometry. Using this Glauber model approach it was determined that the BBC had a min-bias trigger efficiency of ∼93%; thus, the centrality range in Fig 4.1(b) is between 0-93%.

4.2.3 Track Reconstruction in Muon Arms

The track reconstruction in the Muon Arms begins with the MuID since its hit occupancy is much smaller than the MuTr; thereby, helping to reduce background from false tracks. The first step in the reconstruction process is to construct two separate 2-dimensional (2D) tracks in the (x,z) and (y,z) planes using the vertical and horizontal two-packs, respectively. See Fig. 4.4 and Fig. 2.3 as visual guides for the following procedure. These tracks are "seeded" by clusters constructed from hits in either one two-pack or two neighboring two-packs in a shallow MuID gap. The cluster and collision vertex are then used to project a straight line track through the MuID. Additional hits in the two-packs of the other gaps are then searched for within a finite window around the projected track, starting with those gaps nearest to the original cluster. From these hits, 2D tracks are formed that must satisfy several requirements, including having at least two hits, along with having a hit to at least the depth of gap 2 (numbered $0 \rightarrow 4$). If these are satisfied the 2D tracks from the vertical and horizontal two-packs are combined to form a 3D *road*, so long as the number of hits in the 2D tracks do not differ by more than 2.

Since there is no magnetic field in the MuID, the trajectory of the road is a straight line that is extended to the MuTr station 3. Those roads that project to a similar position in station 3 are grouped together and only the road closest to the mean (x,y) position of the group is kept. Track "stubs" in station 3 are then constructed within a finite window of the road projection. The track stubs are formed by fitting a Mathieson function to the charge collected by adjacent cathode

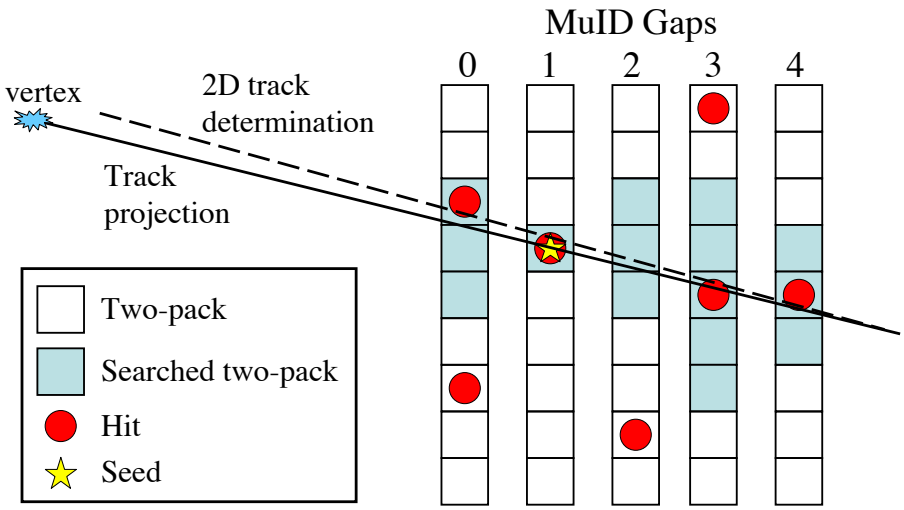

Figure 4.4: Example of a 2D track search in the MuID. Two-packs are represented by the boxes, searched two-packs by the colored boxes, and hits by the circles within the boxes. The search is seeded by the hit in gap 2, indicated by the star. A track projection is then made from the vertex to the seed, shown by the solid line. From the projection, additional hits are then searched for in the shallower and deeper gaps within the search window. Where the search is conducted in the next gap is dependent upon where the hit in the previous gap is found. In this example, no hit is found in the 3 two-pack wide search of gap 2 so the search is expanded to 5 two-packs in gap 3, where a hit is found. The search is then narrowed to a 3 two-pack wide search in gap 4. With the search complete, the 2D track determination is made, indicated by the dashed line. Adapted from [65].

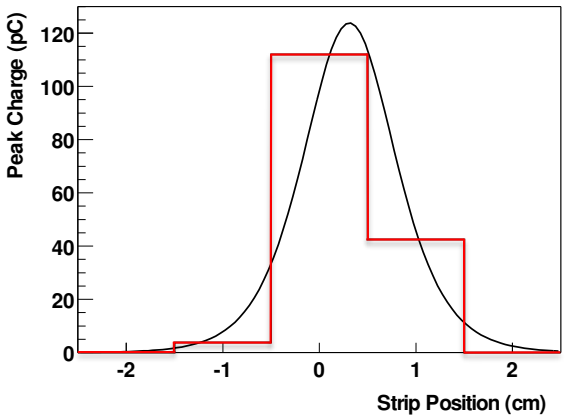

Figure 4.5: The histogram (red) displays the charge distribution collected from an ionizing particle by several cathode strips in the MuTr [62]. A Mathieson function (black) is fit to the distribution, with its centroid taken as the particle's position. See text for more details.

strips, as shown in Fig. 4.5. The fits centroid is then taken as the hit position, which has a resolution of $\sim$100 μm. Notice the figure's histogram bins are 1 cm wide despite the cathode strips being 0.5 cm wide. This is because only every other cathode strip is read out due to budget constraints during detector construction. This fitting procedure is done at each cathode layer in the station (see Fig. 2.12 as a reminder), after which hits are combined to form track stubs.

Next, despite the presence of the magnetic field in the MuTr, a straight line projection is made from station 3 to station 2. This is done because of the poor momentum resolution obtained from just using station 3. Within the projection window to station 2, track stubs are again created. Combinations of track stubs between stations 2 and 3 are then made and a bend-plane fit is applied to the track candidates, allowing for an initial determination of their momentum. This momentum estimate allows for a much more accurate projection to station 1, where again stubs are created within the projected window.

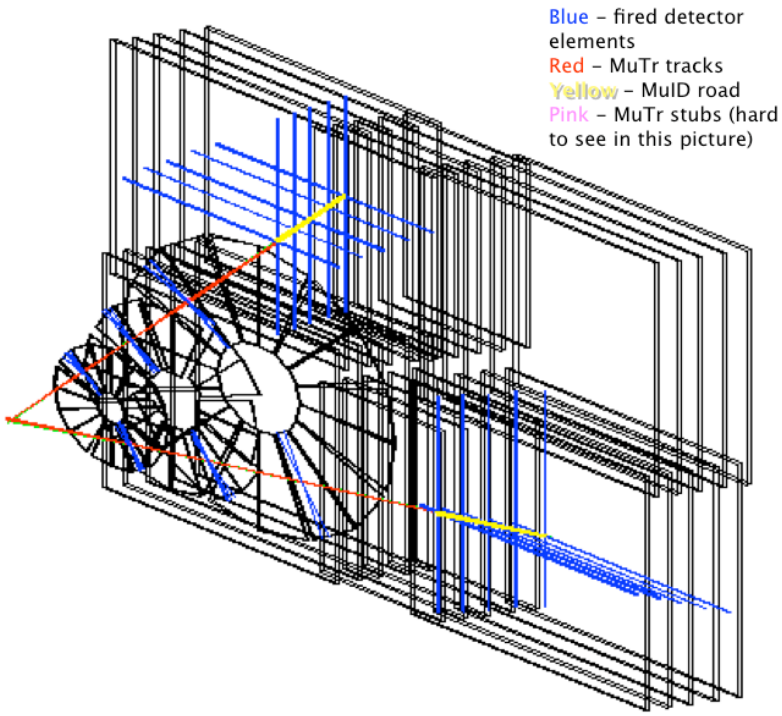

Figure 4.6: Muon Arm event display showing the reconstruction of two tracks through the MuTr and MuID [91]. See figure legend for more details.

From here, it is possible that track candidates share one or more hits. This sharing of hits is not allowed so each potential track is then refit using all three stations, with only the highest quality track kept (see Fig. 2.13 as a visual reference). Finally a Kalman fit [90] is performed using the hits at all 3 stations and the vertex position determined by the BBC. The fit extends from the BBC vertex to the first gap of the MuID and takes into account the expected multiple scattering energy loss from the initial absorber before the MuTr, as well as the energy loss from the Muon Magnet back plate. An example of two reconstructed tracks using this procedure is shown in an event display in Fig. 4.6. From the fit, useful variables such as p_T, η, and ϕ can be extracted and used for analysis.

For clarification, the term *road* is used when a particle's 3D trajectory is

limited to and based on the hits in the MuID. The term *track* is used when discussing a particle's 3D trajectory using MuTr hits or the more general case of combining MuTr tracks with MuID roads. Also, it is important to note that the reconstruction software requires the location of a track's stubs be within the same ϕ oriented octant at each station. Additionally, the software assumes that each reconstructed track is from a muon, which adds an uncertainty to the momentum of the hadrons used in this analysis, especially low momentum hadrons. For hadrons where $p \gg \mu_{mass}$ the uncertainty becomes small. This will be further discussed in Sec. 6.2. For further details on the Muon Arm reconstruction software see [42, 65].

Chapter 5

Analysis

5.1 Event Plane Method

This analysis uses the *standard EP method* to separately measure the v_2 of unidentified charged hadrons and decay muons in the Muon Arms, and is described in detail in [31]. This method measures v_2 by examining the magnitude of the emitted particle's 2^{nd} harmonic azimuthal anisotropy with respect to Ψ_{EP}, where $\Psi_{EP} = \Psi_2$ and $n = m = 2$. Ψ_{EP} is measured using the global detectors discussed in Sec. 2.2.1 and Chapter 3, while the particle distribution with respect to Ψ_{EP} is measured using the Muon Arm detectors discussed in Sec. 2.2.2. Various aspects of this method have already been described throughout this dissertation, but for clarity they will be briefly summarized here.

The emitted particle's asymmetric distribution with respect to Ψ_{RP} can be described by the Fourier expansion

$$\frac{d(wN)}{d(\phi - \Psi_{RP})} = \frac{\langle wN \rangle}{2\pi} \left(1 + \sum_n 2v_n \cos[km(\phi - \Psi_{RP})] \right), \tag{1.5}$$

where n is the harmonic of the particle distribution and v_n the anisotropy parameter representing the magnitude of the flow signal. From this same anisotropy, Ψ_{EP} is

measured using either the RXNP, BBC, SMD, or MPC by

$$\Psi_n = \frac{1}{n}\tan^{-1}\left(\frac{Y_n = \sum_i w_i \sin(n\phi_i)}{X_n = \sum_i w_i \cos(n\phi_i)}\right), \tag{1.6}$$

where X_n and Y_n are the event flow vectors.

By definition, the distribution of Ψ_{RP}, and thus its experimental measurement Ψ_{EP}, should be flat since it has an equal probability of occurring at any angle between $2\pi/n$. However, due to imperfect detector response, dead channels, beam offset, etc., the distribution is not flat and needs to be corrected (for a visual reference to the following step-by-step flattening calibration procedure see Fig. 3.13). The first step in flattening the distribution is to apply detector specific calibrations, such as gain corrections, which are typically applied during data reconstruction. The second step involves recentering the event flow vectors to zero with a width of unity by [31]

$$X_n^{corr} = \frac{X_n - \langle X_n \rangle}{\sigma_{X_n}}, \qquad Y_n^{corr} = \frac{Y_n - \langle Y_n \rangle}{\sigma_{Y_n}}, \tag{3.3}$$

where X_n^{corr} and Y_n^{corr} are the corrected flow vectors and σ_{X_n} and σ_{Y_n} are the uncorrected distribution widths. These corrected event flow vectors are then reinserted into Eq. 1.6, yielding a new EP distribution. The final step involves an event-by-event shifting of the angles using [73]

$$\Psi_n^{corr} = \Psi_n + \frac{1}{n}\sum_i \frac{2}{i}\left[-\langle \sin(in\Psi_n)\rangle \cos(in\Psi_n) + \langle \cos(in\Psi_n)\rangle \sin(in\Psi_n)\right], \tag{3.4}$$

where Ψ_n^{corr} is the corrected and final EP angle. For Run-7 this correction was applied out to the 5^{th} harmonic ($i = 5$).

Next the EP correction factor, referred to as the EP resolution, is calculated to correct for the dispersion in the measured particle distribution caused by the angular difference between Ψ_{RP} and Ψ_{EP} (see Fig. 3.1 for a futher explanation). By definition the resolution of a subevent is

$$\sigma_{_{EP}} = \langle \cos[km(\Psi_m - \Psi_{RP})] \rangle. \tag{3.1}$$

However, Ψ_{RP} is an unknowable quantity. Instead, two equal multiplicity subevents, (a) and (b), can be used to determine the resolution of each subevent by

$$\langle \cos[km(\Psi_m^a - \Psi_{RP})] \rangle = \sqrt{\langle \cos[km(\Psi_m^a - \Psi_m^b)] \rangle}. \tag{3.5}$$

The resolution of the combined subevent (a+b) can be determined by the 2-subevent method using

$$\langle \cos[km(\Psi_m^{(a+b)} - \Psi_{RP})] \rangle = \frac{\sqrt{\pi}}{2\sqrt{2}} \chi_m \exp(-\chi_m^2/4) \times [I_{(k-1)/2}(\chi_m^2/4) + I_{(k+1)/2}(\chi_m^2/4)], \tag{3.6}$$

where $\chi_m = v_m\sqrt{2N}$ with v_m being the measured flow signal of the m^{th} harmonic and $I_{(k-1)}$ and $I_{(k+1)}$ are modified Bessel functions. Figure 3.14 shows the EP resolution vs. centrality of the RXNP and BBC using this method. Alternatively, a subevent's EP resolution can also be determined by the 3-subevent method using 3 non-equal

multiplicity subevents, (a), (b), and (c), by

$$\langle \cos[km(\Psi_m^a - \Psi_{RP})]\rangle = \sqrt{\frac{\langle \cos[km(\Psi_m^a - \Psi_m^b)]\rangle \, \langle \cos[km(\Psi_m^a - \Psi_m^c)]\rangle}{\langle \cos[km(\Psi_m^b - \Psi_m^c)]\rangle}}. \tag{3.7}$$

Figure 3.15 shows the EP resolution vs. vertex of the RXNP using this method.

Once the EP resolution is determined, the measured flow signal is then calculated by

$$v_n^{meas} = \langle \cos\left[n\left(\phi - \Psi_{EP}\right)\right]\rangle, \tag{5.1}$$

where ϕ is measured from the tracks in the Muon Arms. Finally, the particle dispersion with respect to Ψ_{RP} inherent in v_n^{meas} is corrected using the EP resolution by

$$v_n^{corr} = \frac{v_n^{meas}}{\sigma_{EP}}, \tag{3.2}$$

where v_n^{corr} is the final flow signal value.

An important point to note in Eq. 5.1 is Ψ_{EP} and ϕ must be measured in different η ranges to avoid autocorrelation biases. This occurs when the same particle is used in the determination of both Ψ_{EP} and ϕ, resulting in a stronger correlation between the two and a larger v_n than reality. Unfortunately, the Muon Arms ($1.2 < |\eta| \lesssim 2.4$) and RXNP ($1.0 < |\eta| < 2.8$) overlap each other in η and are therefore susceptible to autocorrelations. Nevertheless, this analysis avoids autocorrelations by measuring Ψ_{EP} using the opposite RXNP Arm from the Muon Arm the track is traversing, instead of using the full detector (RXNP_NS). This avoids autocorrelations, but does result in a lower detector resolution and larger correc-

tion factor, meaning a less accurate measurement. However, as will be described in Sec. 5.7, this loss in resolution is ameliorated by combining the Ψ_{EP} of different global detectors to get a more accurate Ψ_{EP} and improved resolution.

5.2 Track Sources

The largest sources of tracks penetrating the Muon Arms are muons from hadron decays, referred to as *decay muons*, and hadrons that punch-through the absorber, referred to as *punch-through hadrons*. These sources are the tracks used in this analysis and, along with several other types of tracks, are shown in Fig. 5.1. Figure. 5.2 shows a schematic depiction of the relative quantity of track sources as they pass through the absorber material.

Decay muons originate from pions and kaons, which constitute the vast majority of emitted particles from heavy-ion collisions. Their decay branching ratios to muons are $\pi^{\pm} \rightarrow \mu^{\pm}\overset{(-)}{\nu_{\mu}}$ (99.99%), $\mathrm{K}^{\pm} \rightarrow \mu^{\pm}\overset{(-)}{\nu_{\mu}}$ (63.6%), and $\mathrm{K}^{\pm} \rightarrow \pi^{0}\mu^{\pm}\overset{(-)}{\nu_{\mu}}$ (3.4%) [4]. The mean proper lifetime ($c\tau$) for pions and kaons are 780 cm and 371 cm, respectively. When taking into account the relativistic effect of time dilation, the average distance traveled in the laboratory frame of reference before a decay is $\gamma c\tau$, where γ is the Lorentz factor described in Table 2.1. For a pion or kaon having a longitudinal momentum (p_z) of 1.5 GeV/c, which is approximately the minimum acceptable p_z for this analysis, the $\gamma c\tau$ is 8383 cm and 1127 cm, respectively. Comparatively, the last MuID gap is located ~870 cm from the nominal vertex. The probability of a pion or kaon decaying while traversing the Muon Arms is shown in

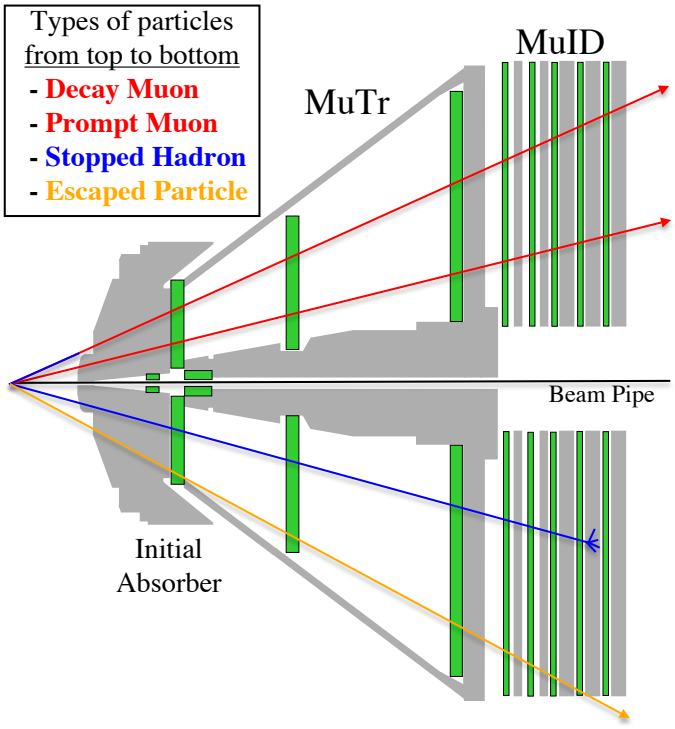

Figure 5.1: Illustration of several different types of tracks traversing the North Muon Arm. See legend for track description. The red lines indicate muons, blue hadrons, and orange escaped particles. Notice the decay muon is a hadron (blue) near the vertex.

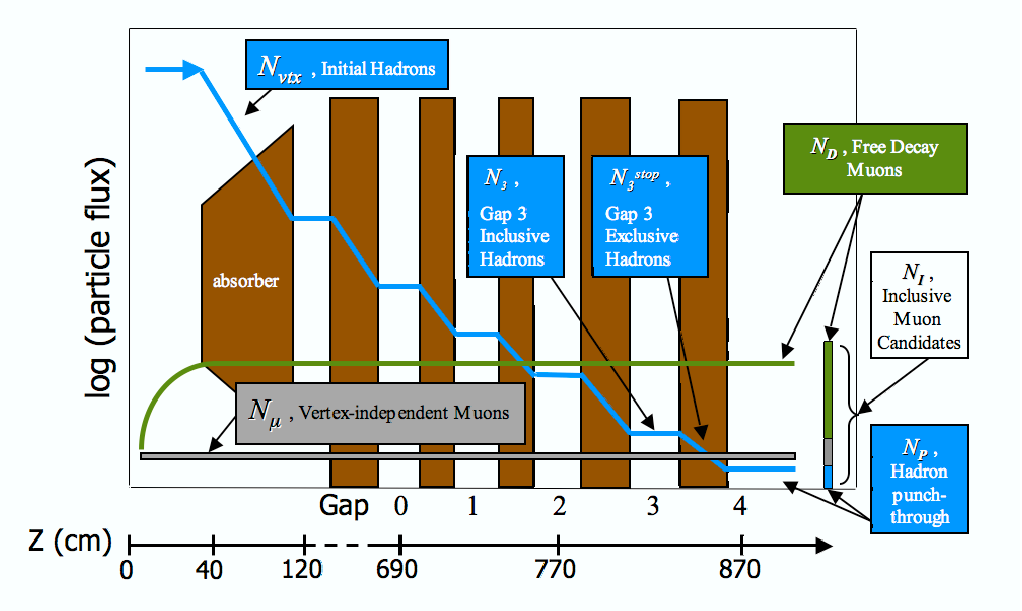

Figure 5.2: Schematic diagram showing relative fluxes of punch-through hadrons (blue), decay muons (green), and prompt muons (gray) vs. distance traveled through the Muon Arm absorber [92]. Notice the y-axis is a log scale. The number of punch-through hadrons that stop in a steel absorber layer is indicated by the difference in hadron flux before and after the layer.

Fig. 5.3 and mathematically described by [4]

$$P(\Delta z) = 1 - e^{-\frac{\Delta z}{\gamma c \tau}}, \tag{5.2}$$

where P is the decay probability and Δz the distance traveled by the particle.

From the figure, the decay probability is shown to increase approximately linearly. However, the largest fraction of decay muons results from pions and kaons decaying before reaching the first significant dE/dx material, the RXNP Pb converters, whose face is located at ± 36 cm from the nominal vertex. Talking into account the PHENIX vertex acceptance of ± 30 cm, the maximum (minimum) distance a particle could travel before hitting a converter is 66 cm (6 cm). Despite this

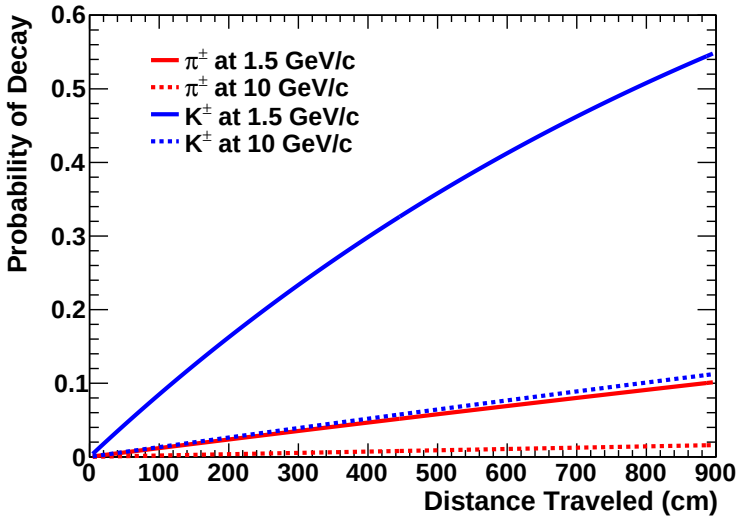

Figure 5.3: Decay probability of $\pi^{\pm}$ (red) and $K^{\pm}$ (blue) vs. distance traveled for $p_z = 1.5$ GeV/c (solid) and $p_z = 10$ GeV/c (dashed). The probabilities are based on Eq. 5.2.

relatively small distance compared to the distance to the last MuID gap, the much larger number of hadrons "inflight" before the converter results in a much larger number of decay muons originating before it, rather than after. As shown in gray in Fig. 5.2, a much less significant source of muons are prompt muons from heavy flavor decays, such as $\bar{D}^0 \to K^+\mu^-\bar{\nu}_\mu$. For the Run-7 Muon Arm detector configurations, both muon sources were indistinguishable and combined into one muon source for this analysis.

The other source of tracks are from punch-through hadrons that penetrate the Muon Arms despite the low probability of that ocurring. Unfortunately, hadrons that penetrate to the last gap of the MuID (gap 4) are indistinguishable from muons doing the same. To distinguish hadrons from muons, only tracks whose last recorded hit is in a shallow layer (gap 2 or 3) of the MuID are used. For these *stopped tracks*, muons are separated from hadrons by first plotting the stopped track's p_z

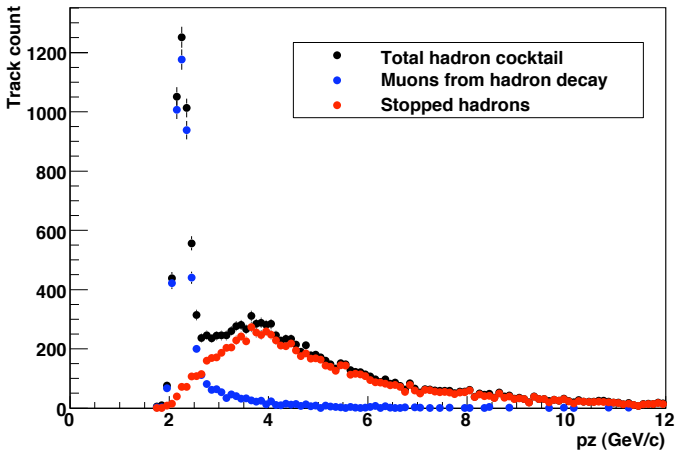

Figure 5.4: Simulated p_z distribution of stopped tracks in gap 3 of the MuID. Decay muons are shown in blue, stopped hadrons in red, and combined in black [91].

distribution, as shown in a simulation in Fig. 5.4. In this figure a sharp peak is seen at low p_z that is almost exclusively from decay muons (blue) ranging out from Bethe-Bloch ionization. This is followed by a long tail toward higher p_z that is almost exclusively from stopped hadrons (red) that experience a strong interaction in the proceeding steel layer and become absorbed; thus, unable to record a hit in the next gap. From this distribution a Gaussian fit can be applied to the low p_z peak and a cut made at 3σ, yielding a mostly pure sample of hadrons in the distribution tail due to high p_z muons rarely ranging out. These tracks can then be used for hadron analysis.

Despite eliminating most of the muon background in the hadron sample, there are two remaining sources of significant background tracks that are also present in the deep track muon sample. The first is *combinatoric* background, where random hits from shower or other background particles coincidentally line up in a fashion that the reconstruction software mistakes as a real particle. The second background

source is from the "knock-on" particles (Sec. 2.2.2.3), which carry with them much of the momentum from the original particle and can thus be mistaken for them. However, they do not carry all of the original momentum and are often not on the same ϕ or η trajectory, therefore distorting the information carried by the primary particle. These two additional sources of background tracks are dampened by applying requirements to track variables, referred to as *track cuts*, so only high quality tracks are used. See Sec. 5.4 for a detailed discussion of track cuts.

5.3 Quality Assurance

To ensure that only good data is analyzed, four types of *quality assurance* (QA) checks were performed on a run-by-run basis for the Run-7 data set: global, event plane, Muon Arm, and Shift Leader comments. During Run-7, 896 runs were collected totaling $\sim 4.4 \times 10^9$ min-bias events. After QA checks were applied, 731 runs totaling $\sim 3.6 \times 10^9$ min-bias events were found to be good and used in this analysis. The following sections describe the four QA checks.

5.3.1 Global QA

The global QA checks examine non-detector specific issues, such as DAQ or run problems. If a bad run is found for this check then it is bad for all detectors. The following is a list of the global QA checks performed on each run.

- Non-flatness in centrality distribution (see Fig. 4.1)
- Bad Global Level-1 trigger
- Low energy test run

- $> 2\%$ of events having incorrect run number
- ≥ 10 amps away from normal magnet current, which typically range between 1500 amps - 3000 amps, depending on the magnet. This could result from a magnet trip, zero-field run, fire alarm, etc. This does not include runs that ended from a frozen Run Control, *i.e.* DAQ control interface, which does not corrupt events.
- For a few days the magnet polarity was "++" instead of the Run-7 nominal "+−" or "−+"
- Runs not meeting minimal run criteria are automatically labeled as PREJECTED by the DAQ and not reconstructed. It was checked that these runs are not in the good run list.
- DAQ did not stop normally. These runs are not automatically bad so the Shift Leader comments were checked to see if anything specific is wrong with the run.
- < 5 min or < 500k events
- Did not have min-bias trigger enabled correctly
- Elog, an electronic log open to any collaborator to post comments to during a Run, was checked for entries such as "fire alarm", etc.

5.3.2 Event Plane QA

The event plane QA examines the flatness and stability of the Ψ_{EP} distribution for the different EP detectors: RXNP, BBC, SMD and MPC. The EP resolution is also checked for runs deviating from normal. These are detector specific checks so if a run is bad for one detector, it does not infer anything is wrong with another detector.

5.3.2.1 EP Flatness

As discussed in Sec. 3.5, the Ψ_{EP} distribution should be flat and several calibrations are applied to ensure this. For verification, the 2^{nd} harmonic Ψ_{EP} distribution

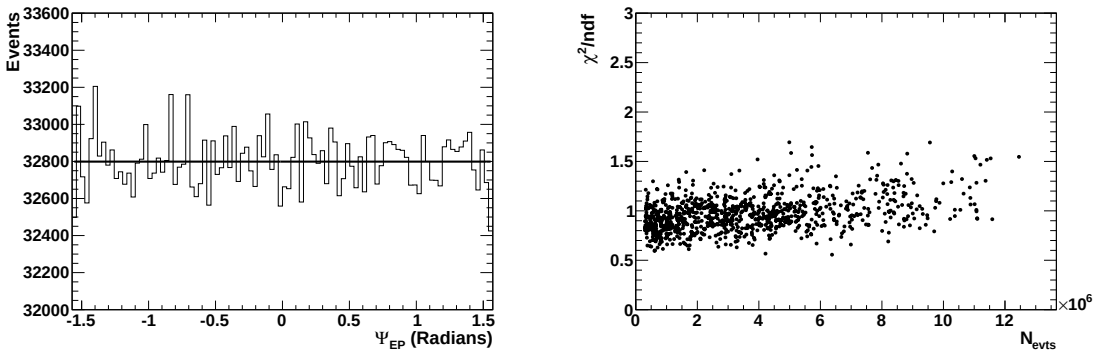

(a) (b)

Figure 5.5: (*a*) The RXNP_N 2nd harmonic Ψ_{EP} distribution for a typical run after a $< 70\%$ centrality requirement is applied. The distribution is fit with a straight horizontal line, which is used to extract the run's χ^2/ndf value. Notice the y-axis is zoomed in. (*b*) The χ^2/ndf values of the RXNP_N for all runs vs N_{evts}. No outliers or bad runs are found in this particular distribution.

was plotted for each run, fit with a straight horizontal line, as shown in Fig. 5.5(*a*), and a "goodness-of-fit" per number of degrees of freedom (χ^2/ndf) value extracted from the fit. However, as shown in Fig. 3.13 spikes can arise in the Ψ_{EP} distribution from the emitted particles of peripheral events only hitting one detector element, causing the element's ϕ angle to be overrepresented in the distribution. To avoid these spikes an event centrality requirement of typically $< 70\%$ was applied, which eliminated these spikes and allowed the underlying distribution to be examined. Despite this, it was still found that a run's χ^2/ndf value depended at least marginally on the number of events in the run (N_{evts}). Therefore, a single χ^2/ndf cut could not be applied to all runs. Instead the χ^2/ndf value for each run was plotted vs N_{evts}, as shown in Fig. 5.5(*b*), which was then examined for outliers. Those χ^2/ndf values deemed to be too far from the norm were eliminated from the analysis.

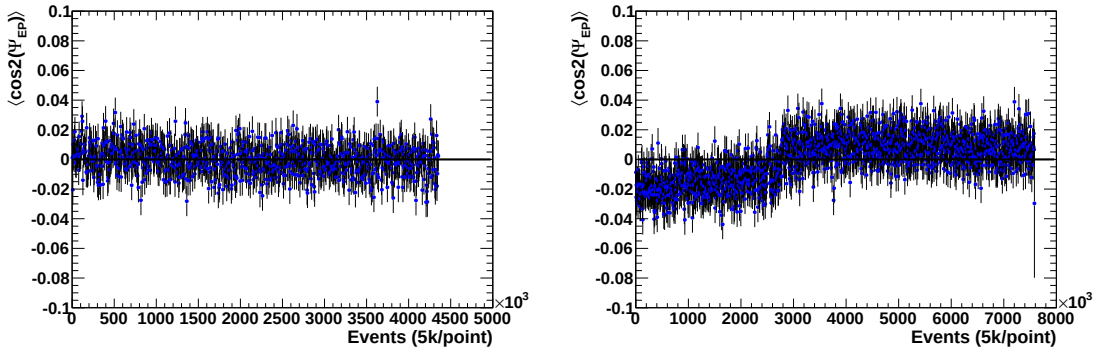

(a) (b)

Figure 5.6: (*a*) An example of the 2nd EP stability check of the RXNP_S for a good run, while (*b*) is a bad run. For this check $\langle\cos[n(\Psi_{EP})]\rangle$ and $\langle\sin[n(\Psi_{EP})]\rangle$ are plotted vs. events and a straight horizontal line is fit at zero, which is used to extract the run's χ^2/ndf value. A $\chi^2/ndf > 1.5$ is considered bad. For (*b*) $\chi^2/ndf = 2.31$.

5.3.2.2 EP Stability

During data collection, it is possible that the beam's (x, y) position changes due to drifting, RHIC adjustments, or beam problems. These changes can distort the Ψ_{EP} determination, since the calibrations depend on a stable beam throughout a run. To check the stability of beam conditions and success of the calibrations, $\langle\cos[n(\Psi_{EP})]\rangle$ and $\langle\sin[n(\Psi_{EP})]\rangle$ are plotted for each run every 5k events, such as in Fig. 5.6(*a*). A horizontal straight line is then fit at zero, the expected value, and the χ^2/ndf extracted from the fit. Any run having a $\chi^2/ndf > 1.5$, as shown in Fig. 5.6(*b*), is considered bad and removed from the analysis.

5.3.2.3 EP Resolution

After the EP flatness and stability checks were performed and bad runs eliminated, the EP resolution was plotted on a run-by-run basis for each detector using

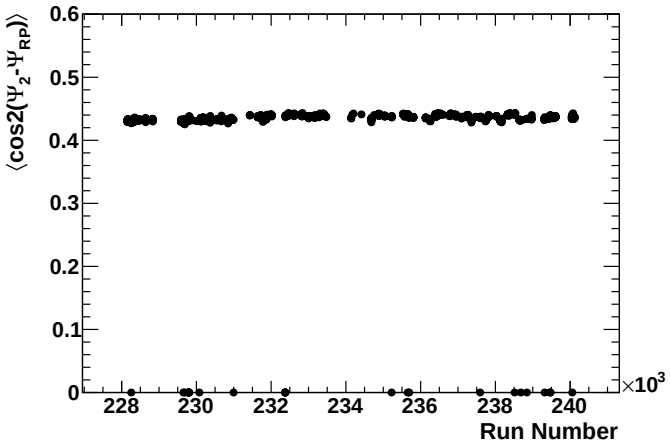

Figure 5.7: Average 2nd harmonic EP resolution vs. run number for RXNP_N. Those runs varying from the norm were marked bad and not used for the detector. In the figure no bad runs are found. See text for an explanation of runs having a resolution of zero.

the 3-subevent method (Sec. 3.6), as shown in Fig. 5.7. Those runs deviating too far from the norm were marked bad for that detector. Notice in the figure several runs have a resolution of zero. This is because of subevent (b) or (c) being bad for that run. To make sure all runs for each detector were checked with a good set of (b) and (c) subevents, the resolutions were calculated twice, each with a different subevent set, such as set 1 being (b) = MPC_S and (c) = MPC_N and set 2 being (b) = BBC_NS and (c) = SMD_NS. Exactly which (b) and (c) subevents were used varied depending upon which detector the resolution was being calculated for, *i.e.* subevent (a).

5.3.3 Muon Arm QA

The Muon Arm QA examines the Muon Arms for anomalies in (1) detector conditions, such as disabled high voltage channels, shown in Fig. 5.8(a), and (2)

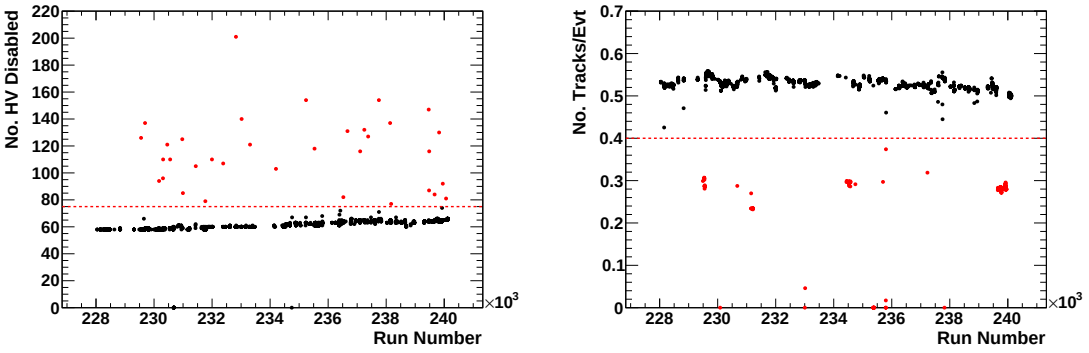

(a) (b)

Figure 5.8: (*a*) The number of disabled high voltage channels in the South MuTr vs. run number. (*b*) The number of tracks per event in the North MuTr vs run number. In both figures the variable requirement is shown by the red dashed line. Runs passing the requirement are in black and those failing are in red.

reconstructed data, such as number of tracks per event, displayed in Fig. 5.8(*b*).

The following is a list of the Muon Arm QA checks performed.

- Bad gain calibration in database during production
- $>$ 75 disabled high voltage channels
- Abnormal number of:
  - tracks per event
  - percent of events with fitted tracks
  - clusters per station per event
  - hot or dead packets
  - packet errors
  - hot or dead planes
  - hits per event
  - hits per event per packet
  - hits per event per station
  - hits per event per plane
  - hits per track
  - hits per track per station
  - roads per event
  - roads per event per panel
  - road hits per event
  - road hits per event per gap

- Abnormal:
  - cluster peak charge
  - cluster width

5.3.4 Shift Leader Comment QA

The Shift Leader comment QA check examines the Shift Leader comments database, where Shift Leaders are strongly encouraged to rate the runs they recently collected during their shift and describe any pertinent information about the run analyzers could use. A list of these comments for the Run-7 runs was made and filtered so only questionable runs remained. For those runs, online monitoring plots of the interested detector(s) were then examined for problems. From here, the list was filtered again by keeping only bad or suspicious runs. The Elog was then searched for information regarding those runs that remained questionable, before finalizing a list of bad runs for each detector.

5.4 Event and Track Requirements

To reduce the number of background tracks in the analysis, requirements are applied to the analysis variables. These "cuts" are primarily made in order to reduce the combinatoric background (Sec. 5.2). These types of tracks are formed from the coincidental alignment of hits from various background particles that emulate the trajectory of a real track and are thus reconstructed as such in the data. Thankfully, these background tracks are usually of poor quality and most can be eliminated through cuts. However, when making these cuts, a balance must be struck

between eliminating background and preserving signal. To optimize the cuts, a background reconstruction method was developed that will be discussed in Sec. 5.5. The following sections define the analysis variables and their requirements, along with demonstrating their effectiveness in eliminating background.

5.4.1 Variable Definitions

- **z-vertex:** The collision z-vertex as measured by the BBC
- **η:** Pseudorapidity (Sec 1.2.2)
- **p_{tot}:** Total momentum at MuTr station 1
- **p_T:** Transverse momentum at collision vertex
- **DG0:** Distance in cm's at MuID gap 0 between the (x,y) position of the MuTr track projection and the MuID road
- **DDG0:** Opening angle in degrees at MuID gap 0 between the MuTr track projection and the MuID road
- **Track χ^2/ndf:** χ^2/ndf value between the position of the MuTr track and the hits used to construct it
- **MuTr Hits:** Number of MuTr hits associated with the track. As described in Sec. 2.2.2.1, each MuTr arm provides a maximum of 16 track hits, one hit from each cathode plane. Two planes make up a gap and there are 3, 3, and 2 gaps in stations 1, 2, and 3, respectively.
- **Vertex Proximity:** Distance in cm's between the (x,y) position of the MuTr track projection to the collision vertex and the nominal vertex position of (x=0,y=0). The track projection is forced to go through the BBC z-vertex so there is no difference in z position.
- **$p\delta\theta$:** Opening angle ($\delta\theta$) between the MuTr station 1 momentum vector (p_{st1}) and position vector (v_{st1}), as illustrated in Fig. 5.9, multiplied by the average of the tracks momentum from the vertex (p_{vtx}) and p_{st1}. Here, the position vector is the vector between (0,0,BBC z-vertex) and the track's (x,y,z) position at MuTr station 1. Mathematically $p\delta\theta$ is

$$p\delta\theta = \frac{(p_{vtx} + p_{st1})}{2} \cos^{-1}\left(\frac{p_{st1} \cdot v_{st1}}{|p_{st1}||v_{st1}|}\right), \tag{5.3}$$

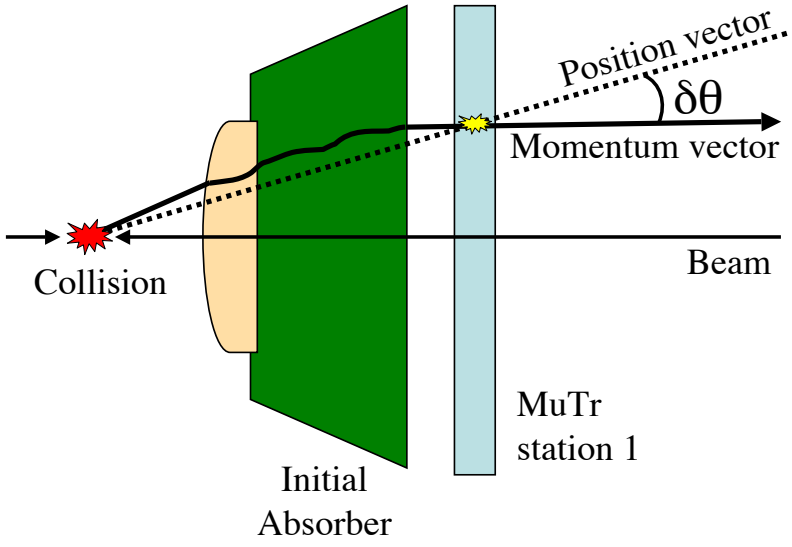

Figure 5.9: Illustration of $\delta\theta$ variable.

where the scalar product $p_{st1} \cdot v_{st1} = p^x_{st1} v^x_{st1} + p^y_{st1} v^y_{st1} + p^z_{st1} v^z_{st1}$. This cut helps reduce particles that underwent significant multiple scattering in the initial absorber, showered into a "knock-on" particle, or decayed before the MuTr. $\delta\theta$ is multiplied by the average momentum between the vertex and station 1 as a means of ensuring the variable distribution remains constant with changing momentum since angular deflection falls as $1/p$. That way a single cut value can be applied to all tracks.

- **Road Depth:** Depth of the road's deepest hit in the MuID. As described in Sec. 2.2.2.2 there are 5 MuID gaps numbered $0 \rightarrow 4$. Only shallow roads which have their deepest hit at gap 2 or 3 are considered hadron candidates. For deep track decay muons, a hit in the MuID gap 4 (deepest gap) is required. For both particle types the Road Depth cut is used in combination with the p_z cut.

- ***p_z*:** As discussed in Sec. 5.2, to separate muons from hadrons for the roads that stop in gap 2 or 3 of the MuID, a cut is applied to their MuTr station 1 p_z distribution. The p_z from MuTr station 1 is used instead of the vertex because the momentum at station 1 is calculated using actual hits, whereas the momentum at the vertex is from a projection using an assumed energy loss through the initial absorber. However, any difference between the two distributions, other than p_z magnitude, does not appear to be significant upon visual comparison. A separate distribution is made for the stopped roads of each gap in each arm, meaning four distributions requiring four distinct p_z cuts are needed. As seen in Fig. 5.10, these distributions have a sharp Gaussian shaped peak at low p_z from muons ranging out from ionization loss, followed by a long tail at higher p_z from hadrons that underwent a strong interaction in the steel and stopped. The tail is a mostly pure sample of hadrons, as

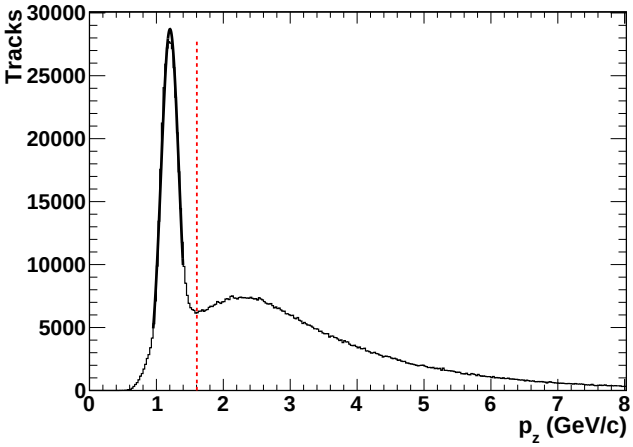

Figure 5.10: MuTr station 1 p_z distribution of stopped roads in North MuID gap 3. The muon peak at low p_z is fit with a Gaussian function and a cut, shown by the vertical red dashed line, is made at 3σ. The remaining long tail at high p_z is mostly hadrons that underwent a strong interaction in the proceeding layer of MuID steel. These higher p_z tracks are used to measure hadron flow.

demonstrated by the simulation shown in Fig. 5.4, which is separated from the muons by fitting the peak with a Gaussian function and applying a cut at 3σ. For deep track decay muons, a p_z requirement of $p_z > 1.05$ GeV/c and 1.17 GeV/c is used for the South and North Muon Arms. These numbers were calculated by others [93] as being the minimum energy a muon must have at MuTr station 1 to fully penetrate the Muon Arm steel layers to MuID gap 4.

- **Verify Shallow** Verifies that the road is shallow by projecting the road's (x,y) position to the next gap and checking that it is within the physical boundaries of the next gap's active region. This helps reduce *escaped particles*, illustrated by the orange track in Fig. 5.1. This requirement is only used for shallow hadrons and is not applicable to deep decay muons, which are required to have a hit in the last MuID gap (gap 4).

5.4.2 Variable Requirements

Table 5.1 lists the variable requirements for shallow hadrons and deep decay muons. All requirements are shared between the two particle types except the Road Depth, p_z, and Verify Shallow cuts. It should also be noted that the η requirement for both the South and North Muon Arms is $1.2 < |\eta| < 2.4$ despite the South Arm

Table 5.1: Track Variable Requirements

Shared Requirements	-30 cm $< z$-vertex < 30 cm $1.2 < \|\eta\| < 2.4$ $p_{tot} < 20$ GeV/c 0.6 GeV/c $< p_T < 5$ GeV/c DG0 < 20 cm South, 15 cm North DDG0 $< 15°$ Track $\chi^2/ndf < 5$ MuTr Hits $= 16$ Vtx Proximity < 10 cm $p\delta\theta < 0.20$ GeV·rad/c South, 0.15 GeV·rad/c North
Shallow Hadrons Only	Road Depth = gap 2 or 3 p_z (GeV/c) Gap 2 > 1.13353 South, 1.28859 North p_z (GeV/c) Gap 3 > 1.43302 South, 1.60444 North Verify Shallow = Yes
Deep Decay Muons Only	Road Depth = gap 4 p_z (GeV/c) Gap 4 > 1.05 South, 1.17 North Verify Shallow = No (Not Applicable)

only having a coverage at the nominal vertex of $-2.2 < \eta < -1.2$. The acceptable η coverage of the South Arm is expanded to -2.4 because when examining the data, it was found that the South Arm recorded a small amount of good data out to $\eta = -2.4$ (see Fig. 5.24). The reason for this is PHENIX's ± 30 cm acceptable vertex range, which results in the Muon Arms having a slightly different η coverage depending on the location of the vertex. The η range of the North Muon Arm was not expanded because after the track cuts were applied, essentially zero tracks were recorded outside $1.2 < \eta < 2.4$.

5.4.3 Effectiveness of Variable Requirements

As discussed in Sec. 5.2, the majority of muons in the Muon Arms originate from pions and kaons decaying before reaching the initial absorber. As shown in

Fig. 5.3, the longer the hadron's flight path the more likely they are to decay, resulting in more decay muons originating further away from the Muon Arm when normalized to the event vertex distribution. On the other hand, hadrons that don't decay should have a flat normalized distribution since they originate at the vertex. Therefore, the muon contamination in the hadron track sample can be estimated by the non-flatness of the normalized track distribution. In Fig. 5.11(a) and (b), the black lines show the normalized track distribution for the South and North Muon Arms, respectively, with all cuts applied except the p_z cut. Recall that the South Arm is located in the $-z$ direction, while the North is $+z$. The distributions in both arms show a strong vertex dependence, with a disproportionate number of tracks originating further away from the arm, indicating decay muon contamination. The distribution after the p_z cut is applied (red) is significantly flatter, although there is still a vertex dependence. This figure shows that the p_z cut does significantly reduce the decay muon contamination in the track sample, but it does not appear to eliminate all. The systematic error that this muon contamination causes to the measurement will be discussed later in Sec. 6.3.

Most of the other track requirements are used to reduce combinatoric background, which becomes a larger issue with increasing p_T due to the decreasing signal/background ratio. The effectiveness of the cuts in reducing this high p_T background is demonstrated in Fig. 5.12, where several p_T spectra are shown, each applying successively stricter cuts. The "Basic Cuts" are shown in black, which consists of all cuts fully implemented except for modifying MuTr Hits = no requirement, Track $\chi^2/ndf < 15$ and $p\delta\theta < 0.50$ GeV·rad/c. The green, blue, and red

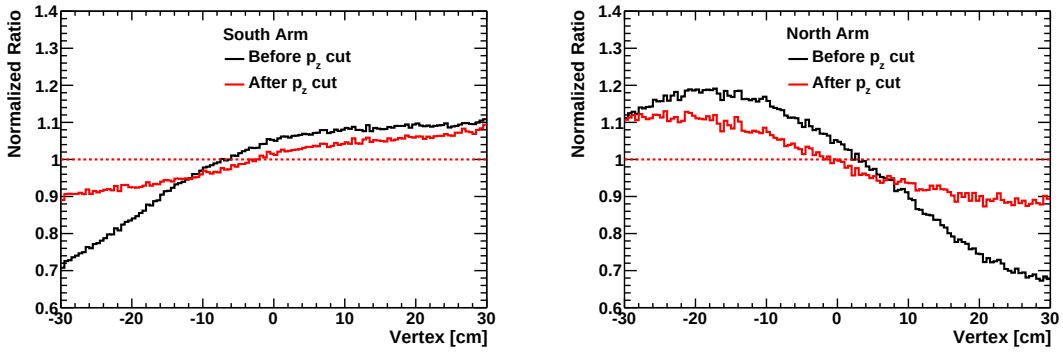

(a) (b)

Figure 5.11: Normalized track vertex distribution with respect to the event vertex distribution for the South Muon Arm (a) and North (b), and before (black) and after (red) applying the p_z cut.

spectra then show the results from the sequential implementation of MuTr Hits = 16, $\chi^2/ndf < 5$ and $p\delta\theta < 0.20$ GeV·rad/c South and 0.15 GeV·rad/c North. With each additional requirement the high p_T background clearly decreases, showing the effectiveness of the cuts in reducing the combinatoric background.

Further confidence in the cuts is provided by Fig. 5.13, which shows the p_T spectra of hadrons for different centrality ranges: 0-10%, 10-20%, 20-40%, 40-60%, and 60-93%. Since combinatoric background results from the coincidental alignment of hits forming falsely reconstructed tracks, the more hits in the detector the more likely the reconstruction of combinatoric tracks. Consequently, with more central events having a higher average particle multiplicity, the more detector hits these events will have, and thus the more combinatoric tracks. This behavior is clearly observed in Fig. 5.13(a) and (b), where the Basic Cuts are applied to the South and North Arms, respectively. However, when all the cuts are fully implemented, as seen in Fig. 5.13(c) and (d), the p_T spectra of the different centrality ranges are very

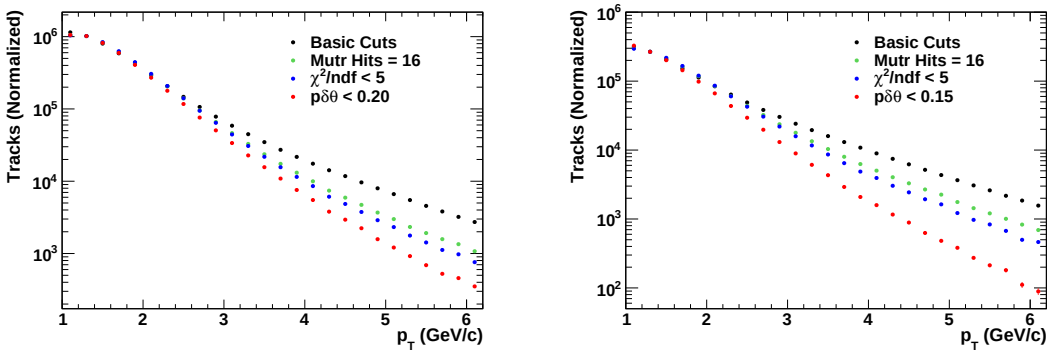

(a) (b)

Figure 5.12: Muon Arm hadron p_T spectra for South (a) and North (b) with increasingly tighter variable cuts. The spectra in each figure are normalized to be equal to the Basic Cuts at $p_T = 1.3$ GeV/c.

similar, indicating most of the combinatoric background has been removed from the track sample.

Overall, when the variable requirements are fully applied to the Run-7 data set 5.34×10^6 hadron tracks pass in the South Muon Arm and 1.43×10^6 in the North, for a total of 6.77×10^6 passed tracks. From the $\sim3.6\times10^9$ events collected, this averages to 1 passed track every $\sim$500 events. For deep track decay muons the number of passed tracks are 20.53×10^6 for the South Arm and 5.28×10^6 for the North, yielding a combined total of 25.81×10^6. The cause of the significant difference in number of passed tracks between the South and North Arms was not definitively found. Contributing factors could be the North Arm having tighter cuts to several variables, having 10 cm more steel than the South Arm, and/or an alignment issue with the North Arm that wasn't addressed until after the Run-7 production. The overall strictness of the cuts may also play a role since loosening them, specifically the MuTr Hit requirement, resulted in the number of passed tracks between the two

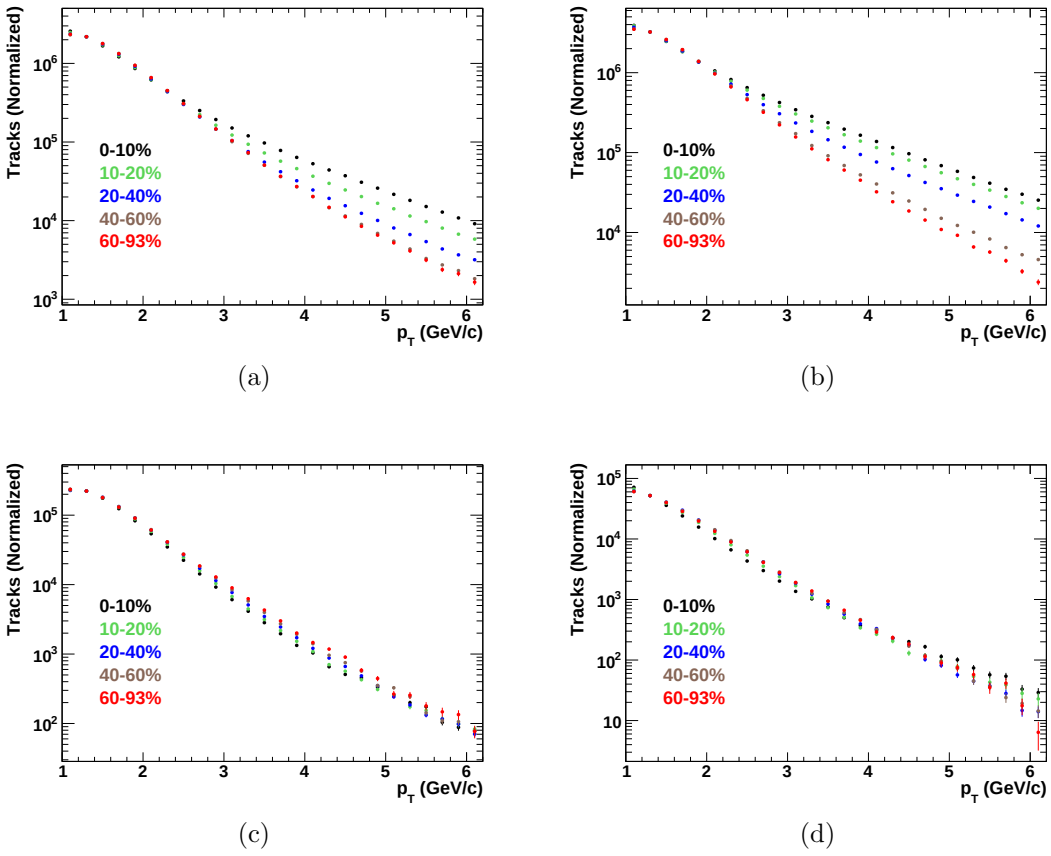

Figure 5.13: South (a) and North (b) Muon Arm hadron p_T spectra for different centrality ranges (indicated in the figures) using Basic Cuts. The same is shown in (c) South and (d) North, but with the variable cuts fully implemented. The spectra in each figure are normalized to be equal to the 0-10% centrality range at $p_T = 1.3$ GeV/c.

arms coming closer to parity.

5.5 Background Estimation

5.5.1 Swap Half-octant Method

As mentioned in Sec. 5.4, a background estimation method was developed to optimize variable cuts and estimate the background v_2 signal. This method, called the *swap half-octant* method [94], works by swapping the charge values collected by the MuTr station 2 cathode strips between half-octants of neighboring octants, as shown in Fig. 5.14, This results in the original position of the charges and the new position to be mirror images across the octant boundary. Regular reconstruction is then run with the swapped data and any track that is reconstructed is considered a background track from combinatorics. With this method it is impossible for real tracks to be reconstructed from their original hits because the station 2 hits that form station 2 track stubs for track reconstruction are moved to a different octant, thereby violating the requirement that all hits from a track occur within the same ϕ oriented octant. This prevents tracks having hits close to the station 2 octant boundary from being reconstructed despite their station 2 hits being moved only a few cm's. Along with moving the charges, the strip calibrations and dead maps were also moved appropriately.

Other methods were tested that also moved the charges, including rotating them by a half or full-octant and swapping them in various ways across the half-octant boundary within the same octant. Each of these competing methods proved

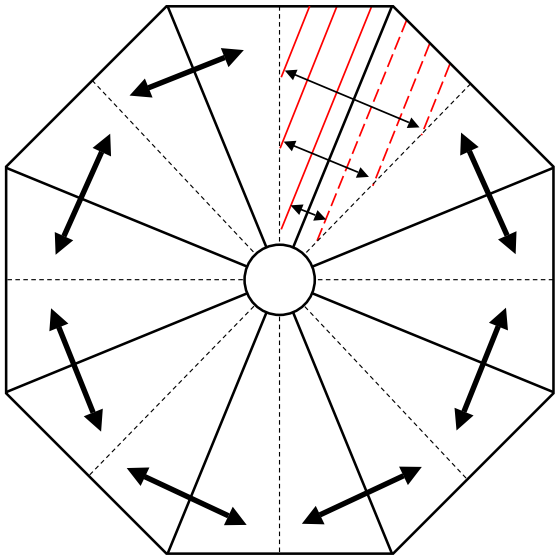

Figure 5.14: Illustration of the swap half-octant background estimation method. The figure represents a cathode strip layer in MuTr station 2 with octant boundaries indicated by solid lines and half-octants boundaries by short dashed lines. The large arrows show which half octants swap charges with which of its neighbors. At the "1 o'clock" position cathode strips are indicated in two neighboring half octants by the solid red and long dashed red lines. Mirror image strips of equal size and position that swap charges are indicated by the small arrows.

to have disadvantages, including rotating the hit multiplicity in one direction and potentially altering the background flow signal, moving charges between strips of different sizes, and reconstructing real tracks because the hits remain within the same octant. The swap half-octant method does not suffer from these drawbacks, but also does not conserve hit multiplicity within each octant, which is unavoidable if one wants to prevent reconstructing real tracks. However, the overall hit multiplicity within station 2 is conserved.

The background reconstruction using the swap half-octant method began by applying the needed software alterations to the original reconstruction code used for producing the real data. The original reconstruction was done using machines on the PHENIX CPU farm running Scientific Linux 4 (SL4); however, since that time PHENIX upgraded to SL5. To make sure there was no difference in the output between SL4 and SL5 machines, testing was done by reconstructing a small number of events on a SL5 machine using the original reconstruction code that was compiled on a SL4 machine. When comparing the two outputs they were found to be identical. Knowing this, the newly altered swapping code was then compiled on a legacy SL4 machine and used on the SL5 machines in the PHENIX computer farm in RCF.

With the software finalized, reconstruction was run over most of the runs determined to be good from Sec. 5.3; however, some runs, totaling a relatively small percentage of the overall events, were lost due to broken tapes at HPSS, causing their incomplete reconstruction. In total 677, runs were usable consisting of 3.26 $\times 10^9$ min-bias events, which provided ample statistics for background studies.

5.5.2 Variable Distributions

Shown here are the hadron tack variable distributions from the real and background data reconstructions that were used to optimize the cuts to minimize background while preserving signal. Since the 677 runs from the background reconstruction are a subset of the 731 good data runs determined from Sec. 5.3, only those 677 runs are used in the comparison, meaning no scaling or normalization is needed since both the real and background distributions are from the exact same data with the same number of events. All variable cuts are applied except the variable being shown. Each variable is presented in its own figure consisting of four subfigures $(a-d)$. Subfigures (a) and (c) show the real data (black) and swap-half octant background data (red) variable distributions for the South and North Muon Arms, respectively. Subfigures (b) and (d) display the ratio of the background/real variable distribution of the South and North Muon Arms, respectively. The exception to this layout is η, which shows both South and North Muon Arm distributions in (a) and their background/real ratio in (b).

An obvious trend in the figures is how much lower the background is in the South Muon Arm than the North. This could be related to the physical size difference between the two arms, as seen in Fig. 2.3, higher beam background in the North Arm, which has been a problem in the past [91], an alignment issue in the North Arm, which was addressed after the Run-7 production, or something else still. The reason for the significant difference was not rigorously investigated. The distributions of deep decay muons are similar to the hadron distributions shown,

but the background/real ratio is generally smaller.

The following is a list of the variable figures.

- p_T - Fig. 5.15
- p_{tot} - Fig. 5.16
- Track χ^2/ndf - Fig. 5.17
- MuTr Hits - Fig. 5.18
- DG0 - Fig. 5.19
- DDG0 - Fig. 5.20
- $p\delta\theta$ - Fig. 5.21
- Vertex Proximity - Fig. 5.22
- Centrality - Fig. 5.23
- η - Fig. 5.24

5.6 Correcting SMD Swapped Channels

The SMD is composed of seven vertical and eight horizontal scintillator slats positioned between the ZDC block modules one and two (Sec. 2.2.1.2). It was determined after the Run-7 production that all eight channel cables connected to the horizontal slats in the SMD North Arm were out of order, as shown in Fig. 5.25. These slats are used to measure the Y_n flow vector, which consequently reduced the SMD's EP resolution. This channel swapping was first noticed by others analyzing the 200 GeV p+p data from Runs-8 and 9. In p+p data, there is a high likelihood that only one neutron at a time will hit the ZDC−SMD causing, on average, a cone-shaped shower, with the largest energy deposited in the cone's center and decreasing to its edge. Therefore, one can use p+p data to determine the physical positioning of

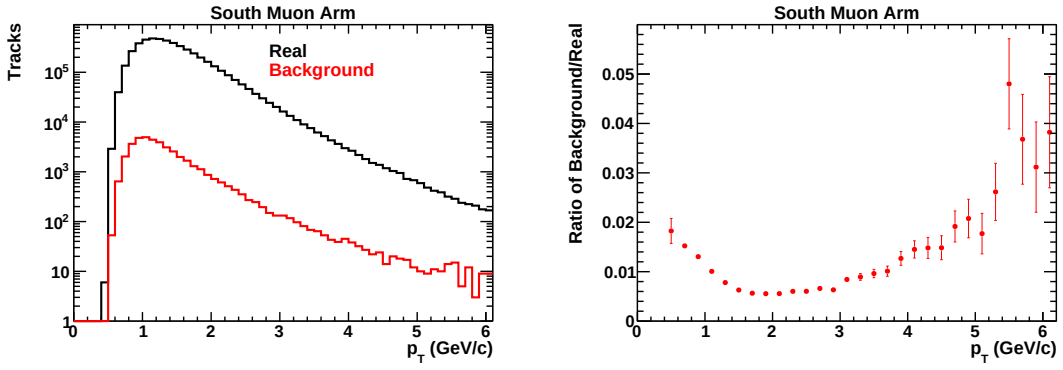

(a) (b)

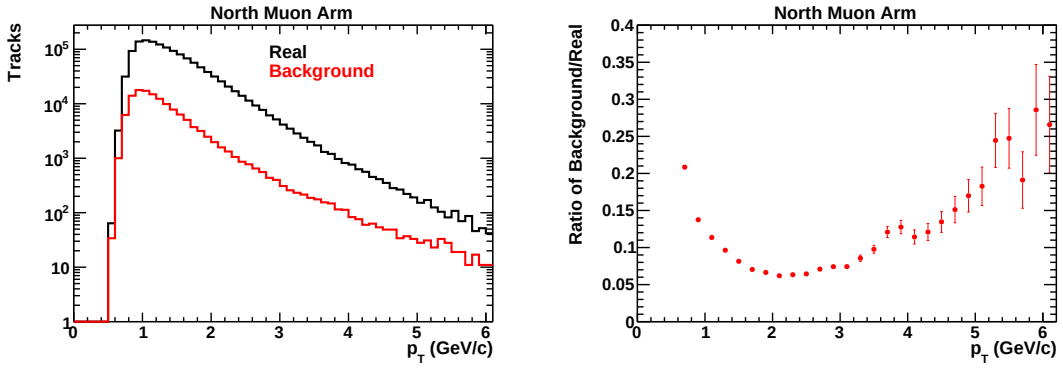

(c) (d)

Figure 5.15: The p_T variable distribution of hadron tracks from real data (black) and background data (red) in the South Muon Arm (a) and North Arm (c). The ratio of the background/real data from these variable distributions is shown for the South and North Muon Arms in (b) and (d), respectively.

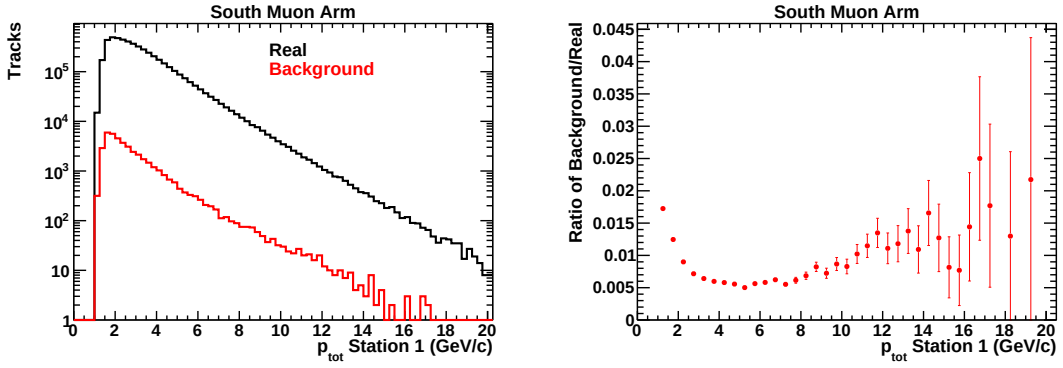

(a) (b)

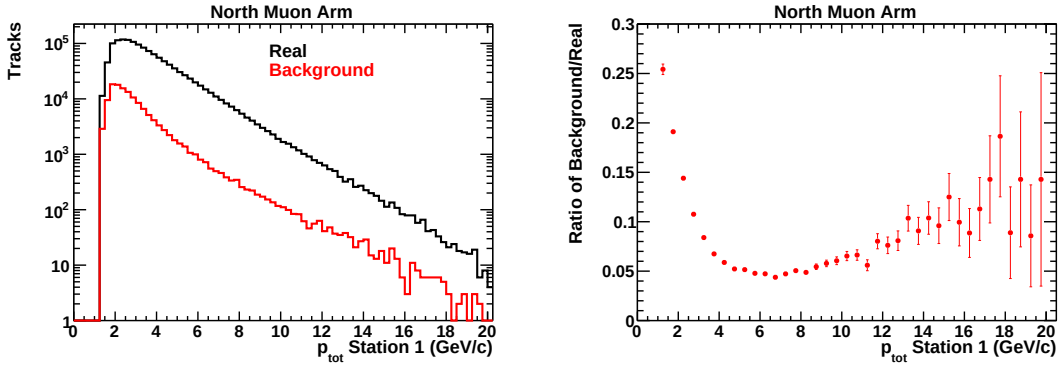

(c) (d)

Figure 5.16: The MuTr station 1 p_{tot} variable distribution of hadron tracks from real data (black) and background data (red) in the South Muon Arm (a) and North Arm (c). The ratio of the background/real data from these variable distributions is shown for the South and North Muon Arms in (b) and (d), respectively.

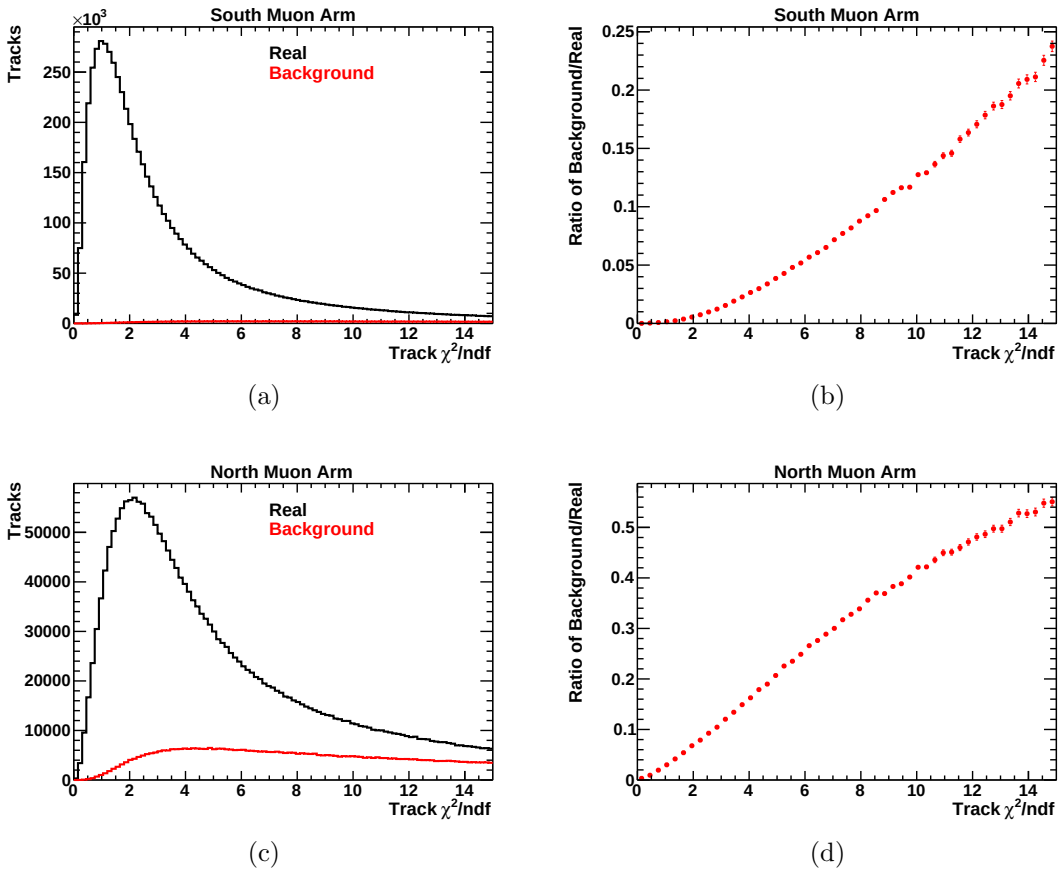

Figure 5.17: The Track χ^2/ndf variable distribution of hadron tracks from real data (black) and background data (red) in the South Muon Arm (a) and North Arm (c). The ratio of the background/real data from these variable distributions is shown for the South and North Muon Arms in (b) and (d), respectively.

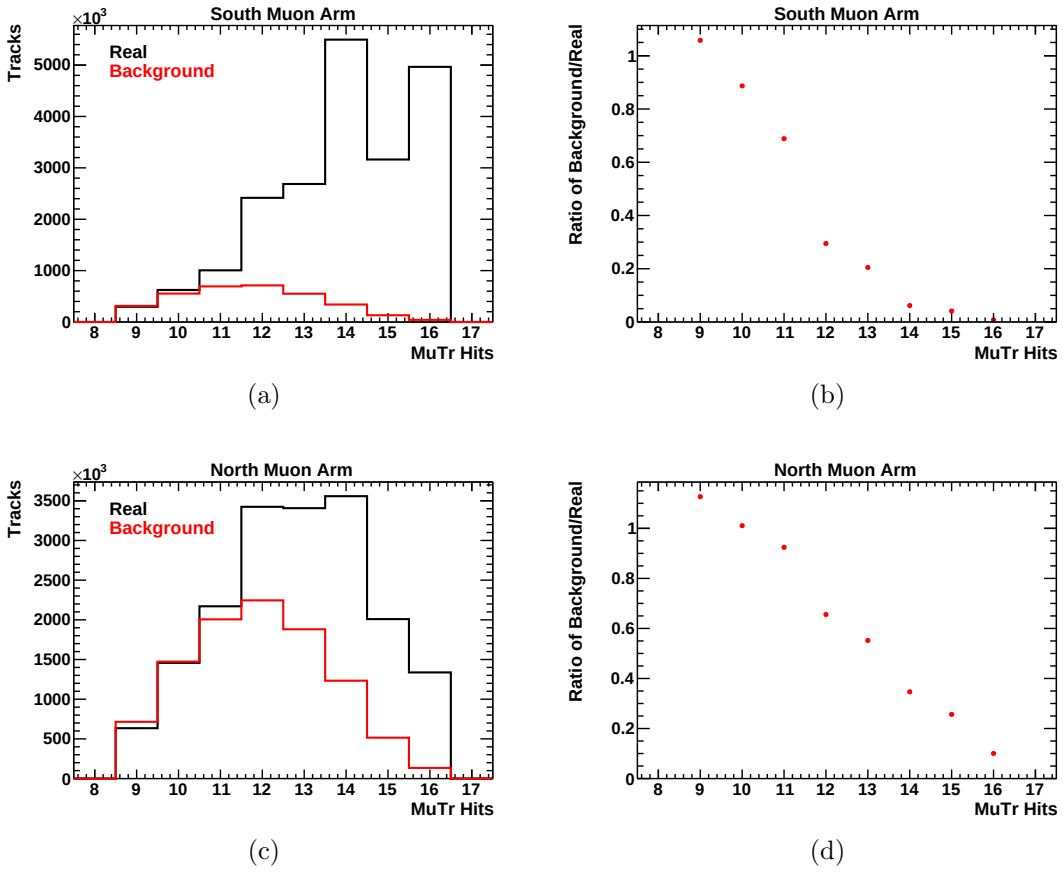

Figure 5.18: The MuTr hits variable distribution of hadron tracks from real data (black) and background data (red) in the South Muon Arm (a) and North Arm (c). The ratio of the background/real data from these variable distributions is shown for the South and North Muon Arms in (b) and (d), respectively.

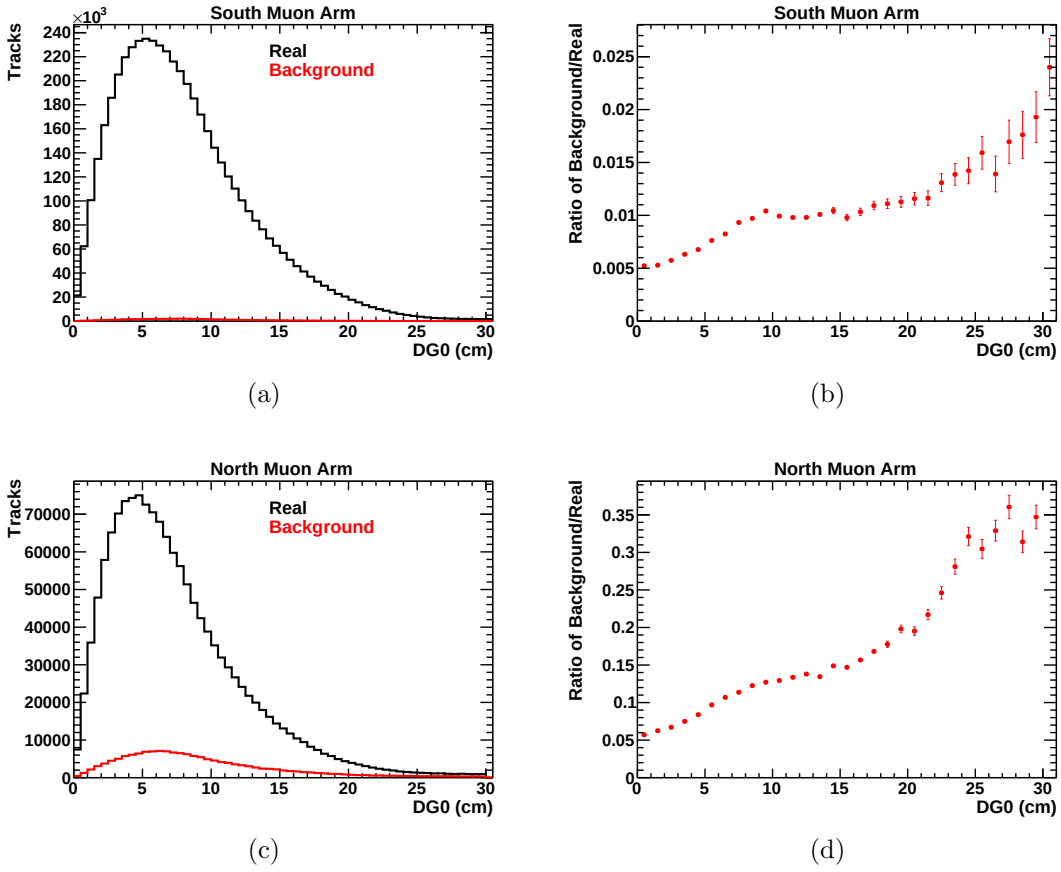

Figure 5.19: The DG0 variable distribution of hadron tracks from real data (black) and background data (red) in the South Muon Arm (a) and North Arm (c). The ratio of the background/real data from these variable distributions is shown for the South and North Muon Arms in (b) and (d), respectively.

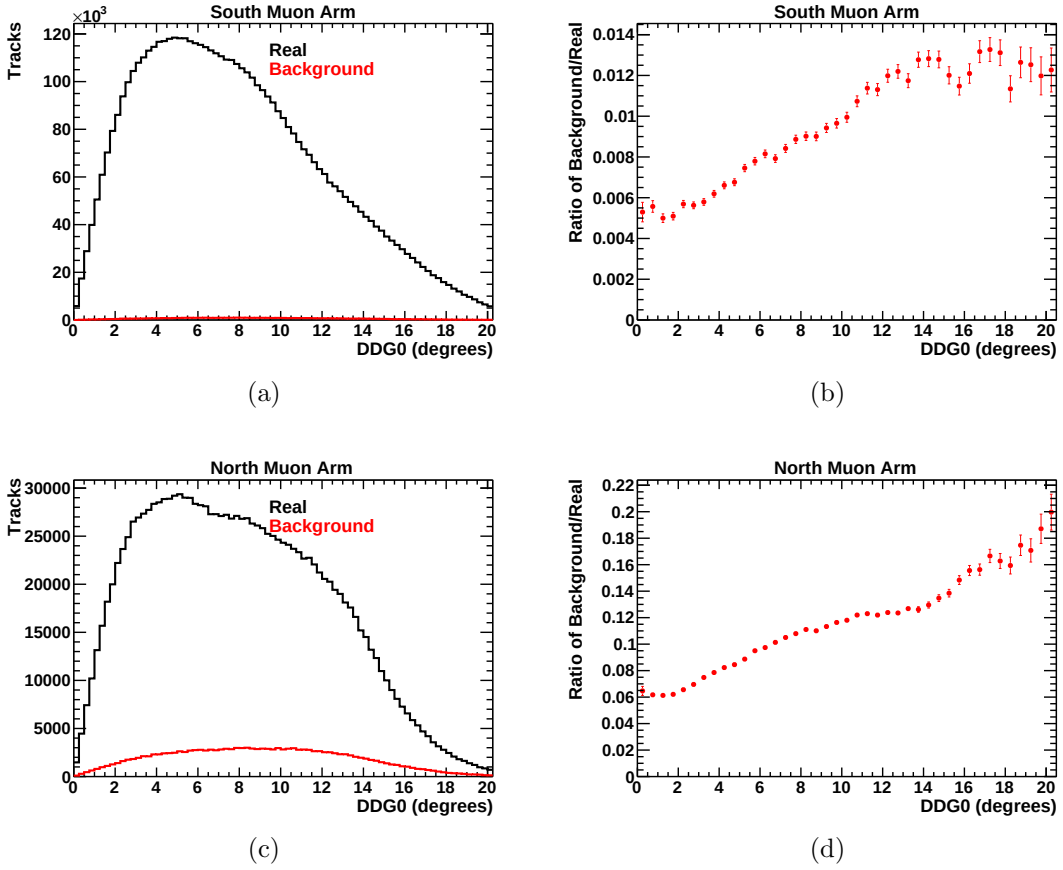

Figure 5.20: The DDG0 variable distribution of hadron tracks from real data (black) and background data (red) in the South Muon Arm (a) and North Arm (c). The ratio of the background/real data from these variable distributions is shown for the South and North Muon Arms in (b) and (d), respectively.

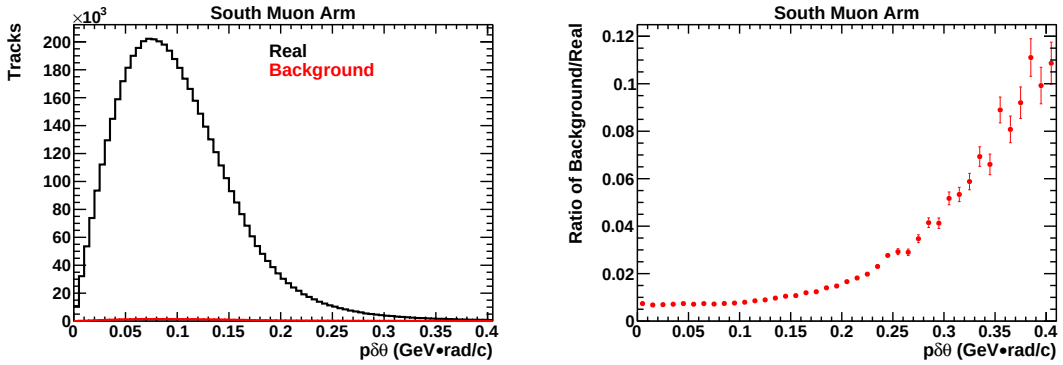

(a) (b)

(c) (d)

Figure 5.21: The $p\delta\theta$ variable distribution of hadron tracks from real data (black) and background data (red) in the South Muon Arm (a) and North Arm (c). The ratio of the background/real data from these variable distributions is shown for the South and North Muon Arms in (b) and (d), respectively.

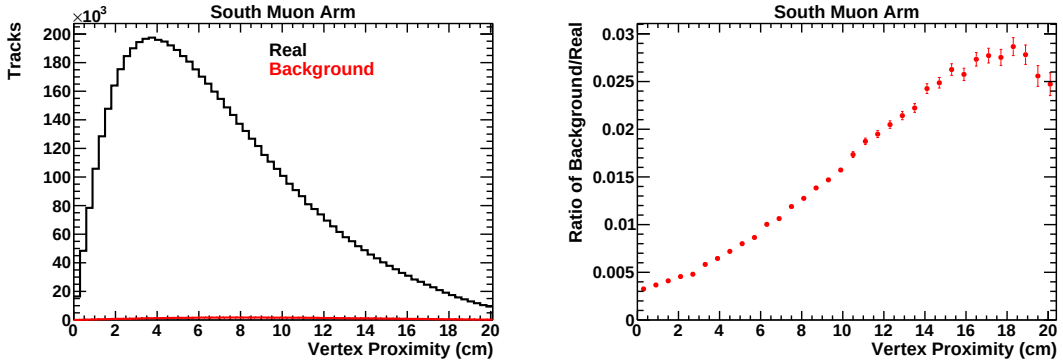

(a)

(b)

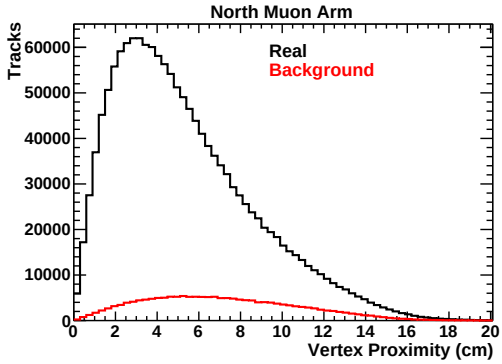

(c)

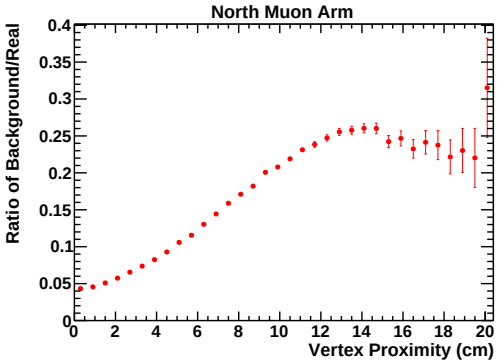

(d)

Figure 5.22: The Vertex Proximity variable distribution of hadron tracks from real data (black) and background data (red) in the South Muon Arm (a) and North Arm (c). The ratio of the background/real data from these variable distributions is shown for the South and North Muon Arms in (b) and (d), respectively.

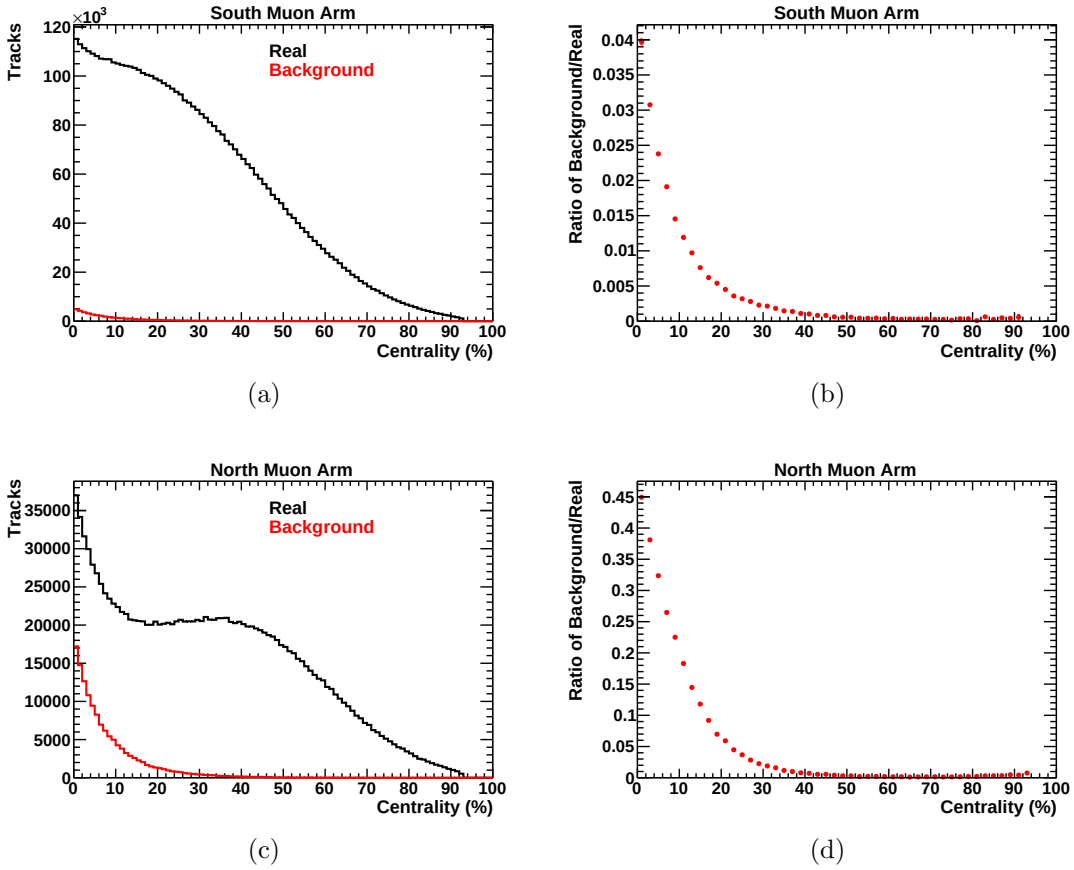

Figure 5.23: The centrality variable distribution of hadron tracks from real data (black) and background data (red) in the South Muon Arm (*a*) and North Arm (*c*). The ratio of the background/real data from these variable distributions is shown for the South and North Muon Arms in (*b*) and (*d*), respectively. Notice the significant rise in combinatoric background when approaching central events due to the increased detector occupancy, allowing for more combinations of false tracks. This was discussed in Sec. 5.4.3.

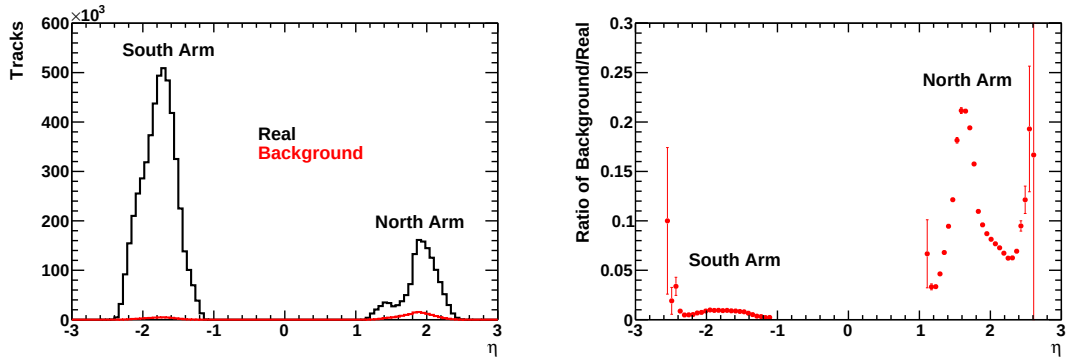

(a) (b)

Figure 5.24: (*a*) The η variable distribution of hadron tracks from real data (black) and background data (red) for the South Muon Arm (negative η) and North Arm (positive η). The ratio of the background/real data from the variable distribution is shown in (*b*). Notice the abnormal shape of the North Arm real data distribution in (*a*). The cause of this was not rigorously investigated, but did become more symmetric and of comparative size to the South Arm if the cuts were loosened.

the channels with respect to one another, and hence unswap the channels. This can be done by requiring one channel to have a high energy threshold (trigger channel) and all others to have a modest threshold (shower channels) and see how often each shower channel fires when the trigger channel does. The closer the shower channel is to the trigger channel the more often it should fire due to the above mentioned cone shape of the shower. Through this logic the swapped slat order in Fig. 5.25 was determined.

Unfortunately, this method could not be directly applied to the Run-7 data because in most Au+Au events many neutrons hit the ZDC−SMD. However, besides Run-8 and 9 200 GeV p+p collisions were also run in Run-6, where this method can be applied and where the channel swapping was also suspected. Therefore, if the order of the swapped channels was the same in Run-6 as in Run-8, one could safely assume the order was also the same in Run-7. Indeed, this was verified to be the

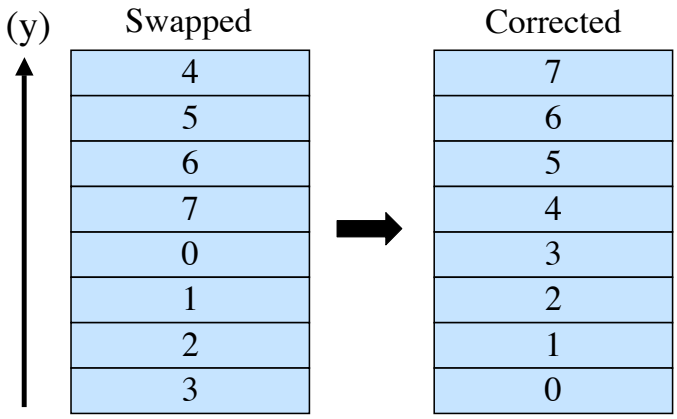

Figure 5.25: Illustration of the SMD swapped channel order (left) and corrected order (right) for the horizontal slats in the SMD North.

case using the trigger-shower technique.

With the incorrect channel order confirmed, the SMD's EP angle was then corrected by first reordering each slats calibrated charge to their correct position, followed by the usual Ψ_{EP} determination using Eq. 1.6 and the flattening calibrations using Eq. 3.3 and Eq. 3.4. Once the correct Ψ_{EP} was determined for an event it was written to a special SMD EP database, where it could be recalled by an analysis module.

5.7 Combining Event Planes (EPs)

5.7.1 Method

As mentioned in Sec. 5.1, when measuring flow in the Muon Arms using the standard EP method, only the opposite RXNP arm from the Muon Arm the particle is traversing can be used to determine Ψ_{EP}. This is done to avoid autocorrelations since the Muon Arms and RXNP overlap in η. However, by only using one arm

of the RXNP instead of both, the EP resolution decreases ∼20% for mid-central collisions, resulting in larger statistical errors. To counteract this loss, a method was developed to combine the EPs of the RXNP, MPC, and BBC for an improved Ψ_{EP} and resolution. Important to note is that the MPC and BBC do not occupy the same η as the Muon Arms, so both the North and South Arms of each detector can be used together to measure Ψ_{EP} without autocorrelations being a concern.

The EP combining method works by combining the X_n and Y_n event flow vectors of each detector before determining Ψ_{EP} from Eq. 1.6. However, to avoid overweighting the MPC and BBC, which occupy the same η, the method was divided into two steps: (1) the MPC and BBC flow vectors were added to form the MpcBbc flow vectors, and (2) the MpcBbc flow vectors were then added with the RXNP flow vectors. The flow vectors used in the additions were not the raw flow vectors, but instead already recentered using Eq. 3.3. This not only rendered any further recentering unnecessary, but also normalized the length of each detector's flow vectors, allowing for a simpler weighting scheme.

Different procedures were devised for combining the flow vectors, including simply summing them together or applying weights based on the detector's EP resolution or "raw resolution" from $\langle\cos[km(\Psi_m^a - \Psi_m^b)]\rangle$, where the weights would be different for different event centralities. However, after examining the resulting resolutions of the combined detectors from this testing, it was found that the weighting scheme that resulted in the best resolution was to weight the flow vectors using the value from the centrality bin with the best raw resolution (centrality = 23%) for all events, regardless of their centrality. Although there is no solid logic as to why this

weighting method resulted in the best EP resolution, it nonetheless did, and is thus the chosen method.

Therefore, in the first step the MPC and BBC X_n and Y_n flow vectors were combined by

$$W_n^{MPC} = \frac{raw_n^{MPC}}{raw_n^{BBC}}, \tag{5.4}$$

$$X_n^{MpcBbc} = X_n^{BBC} + X_n^{MPC} W_n^{MPC}, \tag{5.5}$$

$$Y_n^{MpcBbc} = Y_n^{BBC} + Y_n^{MPC} W_n^{MPC}, \tag{5.6}$$

where raw_n is the detector's raw resolution at centrality = 23%, and W_n is the weight. The distribution widths (σ_{X_n}, σ_{Y_n}) of the combined event flow vectors were also determined and used as normalizers in the second step, which combined the MpcBbc flow vectors with the RXNP's by

$$W_n^{RXNP} = \frac{raw_n^{RXNP}}{raw_n^{MpcBbc}}, \tag{5.7}$$

$$X_n^{RxnpMpcBbc} = \frac{X_n^{MpcBbc}}{\sigma_{X_n}^{MpcBbc}} + X_n^{RXNP} W_n^{RXNP}, \tag{5.8}$$

$$Y_n^{RxnpMpcBbc} = \frac{Y_n^{MpcBbc}}{\sigma_{Y_n}^{MpcBbc}} + Y_n^{RXNP} W_n^{RXNP}. \tag{5.9}$$

The MpcBbc and RxnpMpcBbc EP distributions from Eq. 1.6 were then flattened using Eq. 3.4 and checked on a run-by-run basis for flatness, stability, and EP resolution as described in Sec. 5.3.2. Comparisons of the EP resolution for the combined and non-combined detectors are shown in Fig. 5.26 and Fig. 5.27. All resolutions are calculated using the 3-subevent method (Eq. 3.7) with (b) = RXNP_Sout and (c) = SMD_NS. Notice that in Fig. 5.27 the EP resolution decreases for central-

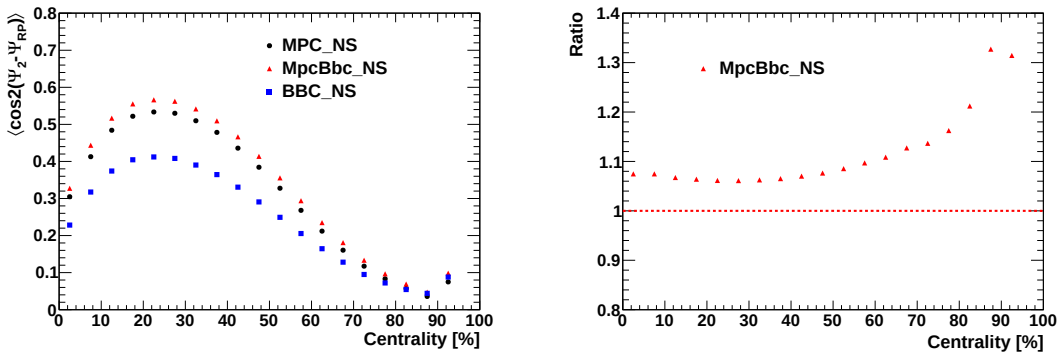

(a) (b)

Figure 5.26: (*a*) The 2nd harmonic EP resolution of MPC_NS (circle) and MpcBbc_NS (triangle). The BBC_NS (square) is shown for reference. (*b*) The ratio, *i.e.* resolution improvement, of the MpcBbc_NS compared to the MPC_NS.

ities $> 70\%$. This is because not all peripheral events that fire the min-bias trigger[1] have particles hitting the RXNP, resulting in the RXNP not being used in the Ψ_{EP} determination for those events, and thereby reducing the resolution.

The approximate resolution increase for the combined EPs between 0-50% centrality, where the vast majority of the tracks in this analysis originate (see Fig. 5.23), is shown in Table 5.2. Because it provides the highest resolution, RxnpN_MpcBbcNS and RxnpS_MpcBbcNS, collectively termed RxnpOpp_MpcBbcNS, will be the primary EPs for this analysis. For brevity, the term "Opp" may be used from here on to describe the use of the opposite EP from the Muon Arm, instead of individually stating "N" and "S".

A statistical error size comparison between using the RxnpOpp_MpcBbcNS and RXNP_Opp EPs when measuring $v_2(p_T)$ for 0-70% centrality is shown in Fig. 5.28(*a*). The statistical errors are calculated as $\sigma/\sqrt{N}$, where σ is the standard deviation of

[1]The min-bias trigger requires > 1 hit in each BBC arm.

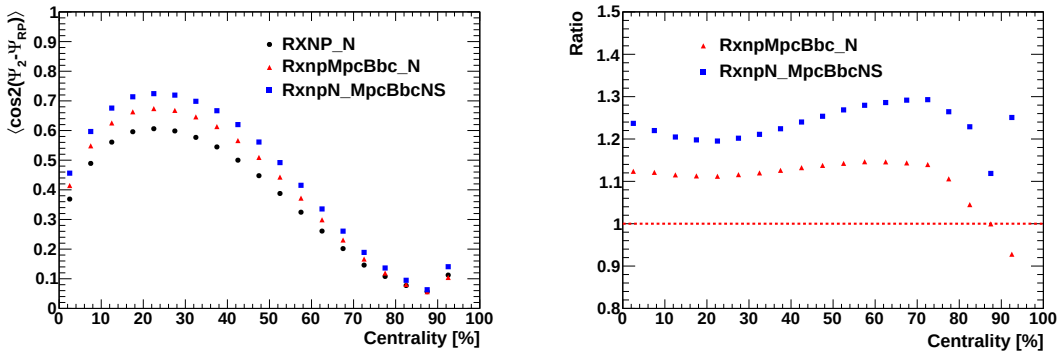

(a) (b)

Figure 5.27: (*a*) The 2nd harmonic EP resolution of RXNP_N (circle), RxnpMpcBbc_N (triangle) and RxnpN_MpcBbcNS (square). (*b*) The ratio, *i.e.* resolution improvement, of the combined detectors compared to the RXNP_N.

Table 5.2: Approximate EP Resolution Increase Within the 0-50% Centrality Range Using Combined EPs

Combined EP	Comparison EP	Approximate Resolution Increase (%)
MpcBbc_NS	MPC_NS	8
MpcBbc_N	MPC_N	6
MpcBbc_S	MPC_S	9
RxnpMpcBbc_NS	RXNP_NS	9
RxnpMpcBbc_N	RXNP_N	12
RxnpMpcBbc_S	RXNP_S	11
RxnpN_MpcBbcNS	RXNP_N	20-25
RxnpS_MpcBbcNS	RXNP_S	20-26

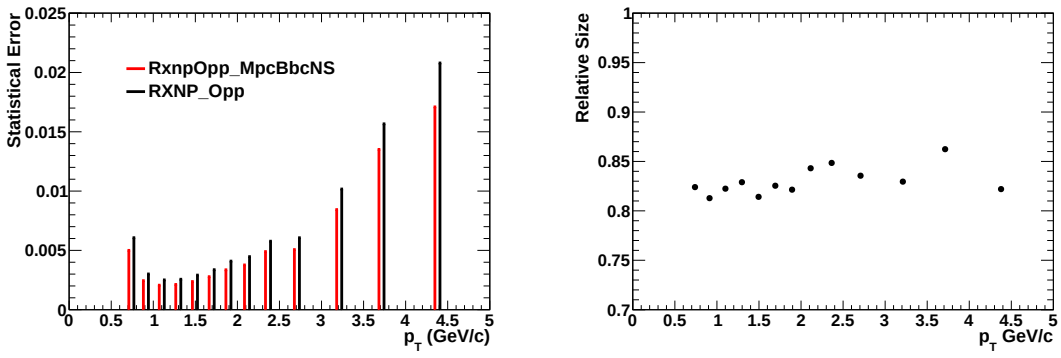

(a) (b)

Figure 5.28: (*a*) The size of statistical errors when measuring $v_2(p_T)$ using the RxnpOpp_MpcBbcNS (red) and RXNP_Opp (black) EPs. The centrality range is between 0-70%. (*b*) The relative size of the statistical errors from (*a*). The values are obtained by the ratio RxnpOpp_MpcBbcNS/RXNP_Opp.

Eq. 3.2 and N is the number of entries in the bin. Also in the figure, since there are statistical fluctuations in the v_2 values when using the different EPs and the error size is affected by the v_2 magnitude, the errors in each bin were normalized as if they had the same v_2 value, making any difference in error size the result of the different EP resolutions and not any difference in v_2. Figure 5.28(*b*) displays the relative size of the errors using RxnpOpp_MpcBbcNS compared to RXNP_Opp. The reduction in statistical error is generally between 15-20%.

5.7.2 Non-flow Effects on EP Resolution

Besides autocorrelations, non-flow effects, such as fluctuations in the participant geometry or jets, discussed earlier with Fig. 3.10, can bias a flow measurement. For flow measurements, non-flow effects can occur between the EP detectors and the tracking detector, or between subevent detectors used to measure the EP resolution. These effects generally become larger the closer the two detectors are in η.

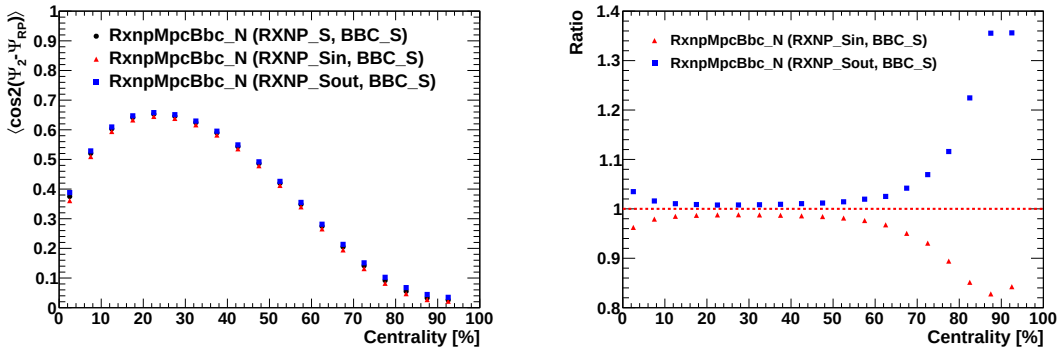

(a) (b)

Figure 5.29: Demonstrating how non-flow effects can influence 2$^{\text{nd}}$ harmonic EP resolution. (a) The EP resolution vs. centrality of RxnpMpcBbc_N using the 3-subevent method. All resolutions use BBC_S as subevent (c), but vary subevent (b) with RXNP_S (circle), RXNP_Sin (triangle), and RXNP_Sout (square). (b) The ratio vs. centrality of EP resolutions from figure (a) relative to that calculated using subevent (b) = RXNP_S.

Figure 5.29 shows how non-flow effects can influence the resolution of the RxnpMpcBbc_N. In Fig. 5.29(a), the resolution is calculated using the 3-subevent method with subevent (b) from RXNP_Sin or RXNP_Sout and (c) being the BBC_S. The lowest resolution is seen when (b) = RXNP_Sin due to its increased correlation with BBC_S from their relatively close proximity in η, causing a larger denominator in Eq. 3.7 and lowering the resolution. When (b) = RXNP_Sout there is less non-flow correlation resulting in a $\sim 2-8\%$ increase in resolution when centrality $< 70\%$, as displayed in Fig. 5.29(b). Notice in the figure the increased divergence in resolution for peripheral events, demonstrating here with data, their larger susceptibility to non-flow effects, which was discussed earlier with Fig. 3.10 using a simulation. The most central events ($< 10\%$) also show non-flow effects due to the decreased participant eccentricity, making them more susceptible to participant shape fluctuations.

To minimize non-flow effects the SMD_NS is used for subevent (c) because it provides the largest η gap between subevents, due to its very forward location ($|\eta| > 6.5$). Additionally it measures the EP using spectator neutrons instead of emitted particles, which the other detectors use. The SMD also has the added advantage of providing consistency to the resolution measurements of the different detectors since it can be used for all of the 3-subevent resolution calculations. The main disadvantage of using the SMD is its poor 2^{nd} harmonic EP resolution. However, this is largely overcome by the large event statistics in the Run-7 data set.

The reduction in non-flow effects when using the SMD is shown in Fig. 5.30, where the same (a) and (b) subevents from Fig. 5.29 are used in addition to including (b) = RxnpMpcBbc_S. With using the SMD_NS there is noticeably less dependence on the η range of subevent (b). Nonetheless, calculating different EP resolutions for the same detector, as done here, does expose the need to apply an EP resolution systematic error to the v_2 measurements in this analysis. This will be addressed later in Sec. 6.8.

5.8 Background Correction

The combinatoric background contribution to the v_2 signal is corrected by applying a background correction using

$$v_n^{(s+b)} = \frac{(v_n^s \times N^s) + (v_n^b \times N^b)}{(N^s + N^b)}, \tag{5.10}$$

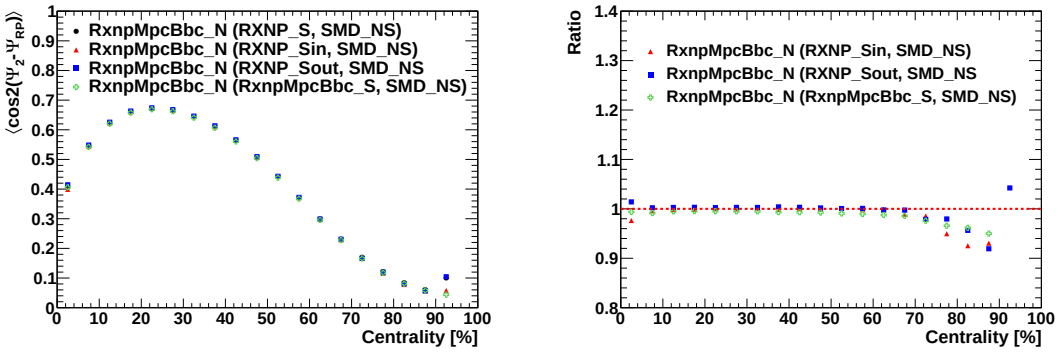

(a) (b)

Figure 5.30: (*a*) RxnpMpcBbc_N 2nd harmonic EP resolution using the 3-subevent method with SMD_NS as subevent (*c*). The different (*b*) subevents are RXNP_S (circle), RXNP_Sin (triangle), RXNP_Sout (square), and RxnpMpcBbc_S (cross). (*b*) The ratio vs. centrality of the resolutions from figure (*a*) relative to that calculated using subevent (*b*) = RXNP_S. A more consistent EP resolution with less non-flow effects is observed using subevent (*c*) = SMD_NS than when using (*c*) = BBC_S (Fig. 5.29).

where the "*s*" and "*b*" superscripts signify signal and background, respectively, N is the number of tracks, and $n = 2$. By utilizing the swap half-octant method from Sec. 5.5 to obtain the background variables in Eq. 5.10, all terms are known in the equation except v_n^s, *i.e.* the pure v_2 signal value. Combining N^s and N^b into $N^{(s+b)}$ and rearranging the terms, the equation becomes

$$v_n^s = \frac{v_n^{(s+b)} \times N^{(s+b)} - (v_n^b \times N^b)}{N^s}, \tag{5.11}$$

which must be calculated separately for each data point.

The process of calculating the terms in Eq.5.11 to solve for v_n^s started with using the standard EP method described in Sec. 5.1 to calculate $v_n^{(s+b)}$ from real data and v_n^b from background data. However, the track requirements from Table 5.1, by

Table 5.3: Loosened Track Requirements for Determining v_2^b

Track $\chi^2/ndf < 15$
MuTr Hits ≥ 14
$p\delta\theta < 0.25$ GeV·rad/c South, 0.20 GeV·rad/c North

design, eliminate most of the combinatoric background, leaving insufficient statistics to measure v_n^b from the background data. To compensate, several track requirements were loosened to increase background statistics. These changes are listed in Table. 5.3. All other track requirements remained the same. Even with these loosened cuts, the $v_n^b(p_T)$ signal can still experience significant statistical fluctuations, especially for peripheral or narrow centrality ranges. To moderate these fluctuations a 3$^{\text{rd}}$ order polynomial is fit to the background points and used to extract v_n^b at the desired p_T values.

The resulting hadron data and background flow signals for 0-20% centrality, are shown in Fig. 5.31. From here, $N^{(s+b)}$ and N^b are determined by first simply plotting the real and background data p_T dependence, respectively, similar to Fig. 5.15 but with the appropriate binning. N^s is then calculated by subtracting N^b from $N^{(s+b)}$, *i.e.* $N^s = N^{(s+b)} - N^b$. For clarity, the regular track cuts from Table 5.1 were used for determining $N^{(s+b)}$ and N^b, not the loose cuts in Table. 5.3.

The effectiveness in this background correction technique is shown in Fig. 5.32, where the uncorrected hadron $v_2(p_T)$ measurement for 0-20% centrality is shown for each Muon Arm in (a). Recall from Fig. 5.23 that central events contain the highest percentage of background tracks making this the ideal centrality range to test the effectiveness of the background correction method. Notice in (a) how the North

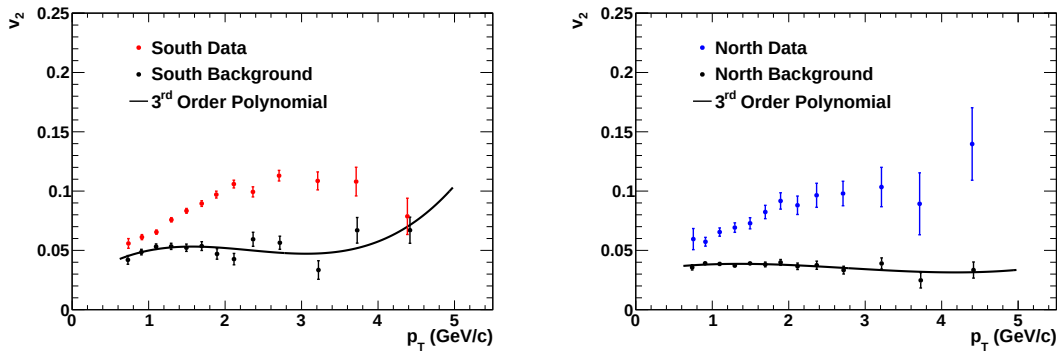

(a) (b)

Figure 5.31: Hadron $v_2(p_T)$ for 0-20% centrality from (a) South Muon Arm and (b) North. In (a), real data is shown in red and (b) blue. The background data is shown in black in both subfigures and is mostly flat, but does fluctuate, especially in the South Arm, due to low statistics. To moderate the fluctuations the background data is fit with a 3$^{\text{rd}}$ order polynomial, which is used to extract the v_2^b values.

Arm signal (blue) is noticeably lower than the South (red), due to its larger background contamination. The comparison is shown again in (b) with the background correction applied. Notice in (b) the substantially better agreement between the arms, demonstrating the effectiveness of the background correction.

5.9 Measurement Consistency

To demonstrate the analysis' consistency and stability in measuring flow, several figures are presented here which compare hadron v_2 signals between the South and North Muon Arms, different p_T ranges, MuID gaps, etc. All figures use the RxnpOpp_MpcBbcNS EP and have a centrality range of 0-70%. Only statistical errors defined as $\sigma/\sqrt{N}$ are shown in the figures.

Figure 5.33 shows hadron $v_2(\phi)$ in several p_T ranges for the South and North Muon Arms in solid and open data points, respectively. There are eight bins in ϕ,

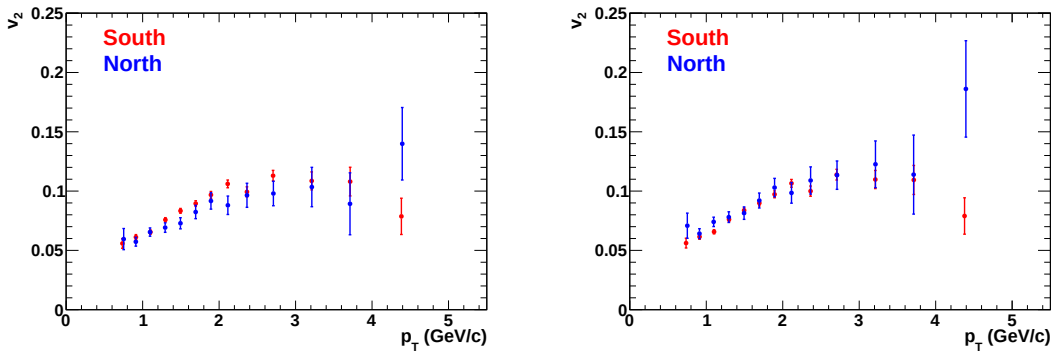

(a) (b)

Figure 5.32: Hadron $v_2(p_T)$ for 0-20% centrality before (a) and after (b) the combinatoric background correction is applied to the South (red) and North (blue) Muon Arms. Notice before the correction, the North Arm shows a systematically lower signal than the South, especially at mid-p_T, due to its larger background. After the correction is applied the signal agreement between the arms is significantly better.

each measuring v_2 using a different MuTr octant. Demonstrated here is the consistent v_2 signal within statistical errors between the different octants and between the North and South Arms.

Figure 5.34 displays hadron $v_2(z\text{-vertex})$ for the South (red) and North (blue) Muon Arms between -30 cm $< z <$ 30 cm. This figure shows that the v_2 signal is consistent throughout the vertex range for each arm and that the two arms mostly agree within statistical errors. Figure 5.35 combines the South and North Muon Arm measurements, but separates the hadron tracks into positive (blue) and negative (red) charges in (a), and stopping at MuID gap 2 (red) and 3 (blue) in (b). In both, (a) and (b) the data points mostly agree.

Finally, Fig. 5.36 compares the $v_2(p_T)$ for hadron tracks that stopped in either MuID gap 2 or 3 and deep tracks which recorded a hit in MuID gap 4. Good agreement is seen at low and high p_T, which one might expect since the deep tracks

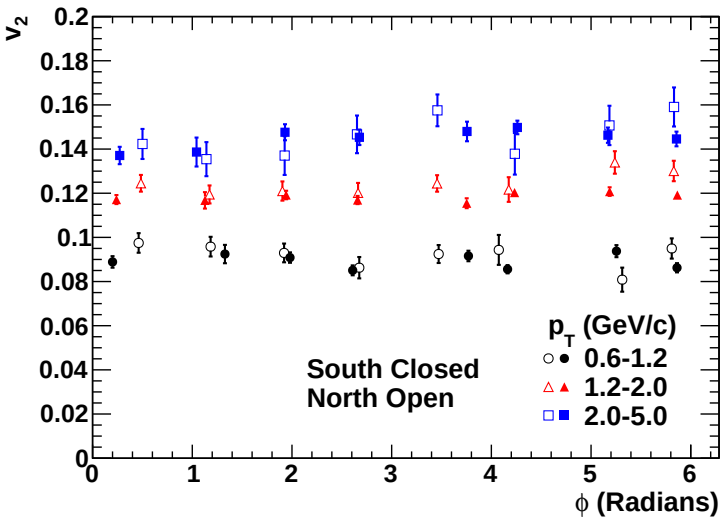

Figure 5.33: Hadron $v_2(\phi)$ between 0-70% centrality for South Muon Arm (closed) and North (open) using 3 different p_T ranges: $p_T = 0.6 - 1.2$ GeV/c (circles), $p_T = 1.2 - 2.0$ GeV/c (triangles), and $p_T = 2.0 - 5.0$ GeV/c (squares).

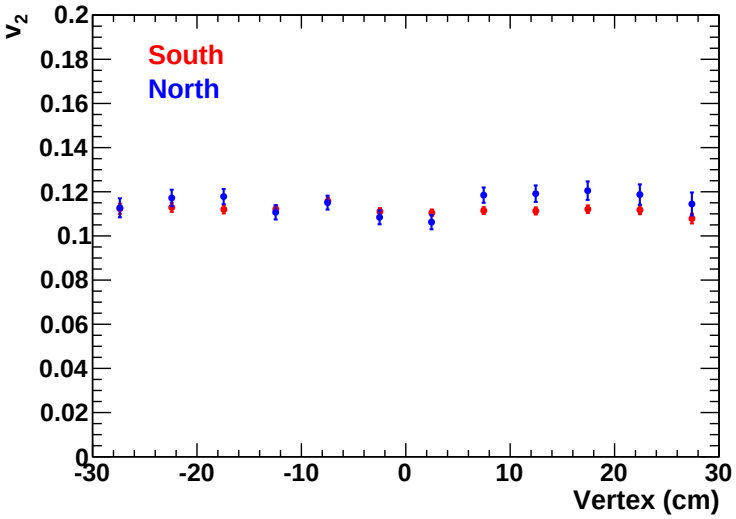

Figure 5.34: Hadron v_2(vertex) between 0-70% centrality for South Muon Arm (red) and North (blue).

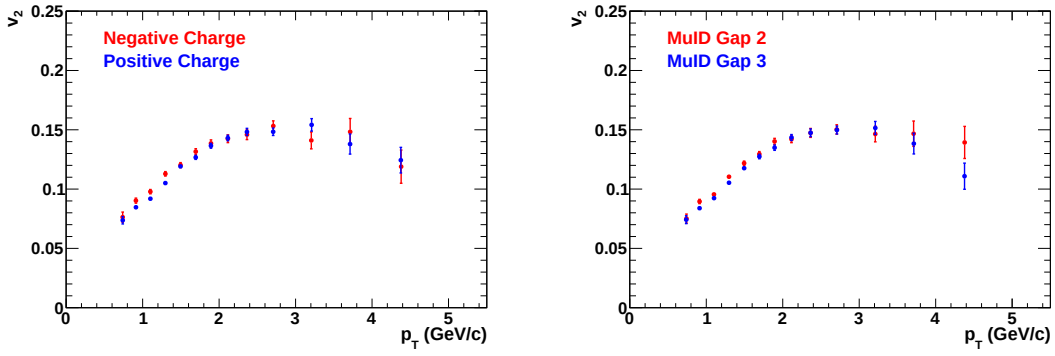

(a) (b)

Figure 5.35: Combined South and North Muon Arm $v_2(p_T)$ for negative (red) and positive (blue) charged hadron tracks in (a) and tracks stopping in MuID gap 2 (red) and 3 (blue) in (b). The centrality range for both figures is 0-70%. In each subfigure the data points mostly agree.

are mostly decay muons from pions and kaons (Sec. 5.2). However, significant deviation is seen at mid p_T, which can largely be explained by the reduced proton contribution to the deep track signal since protons have an extremely long half life and essentially don't decay, as presented in Table 1.4. This results in an insignificant proton contribution to the deep tracks except for a small contribution from those protons completely punching through the absorber material or generating knock-on particles which do the same. Furthermore, as seen in Fig. 1.15(a), protons at mid-rapidity have a larger v_2 than pions and kaons starting at $p_T \approx 2$ GeV/c, meaning protons increase the unidentified hadron v_2 above this p_T. If they are removed, as in the case of the deep tracks, then the v_2 signal would decrease, much like in Fig. 5.36. Additionally, BRAHMS measured the proton/pion p_T spectra ratio at forward η [95] and showed that protons become dominant at $p_T \approx 1.5$ GeV/c, peak at $\sim$2.5 GeV/c, and then appear to fall at higher p_T. This too helps explain the hadron and muon signal discrepancy in Fig. 5.36 in addition to indicating why the

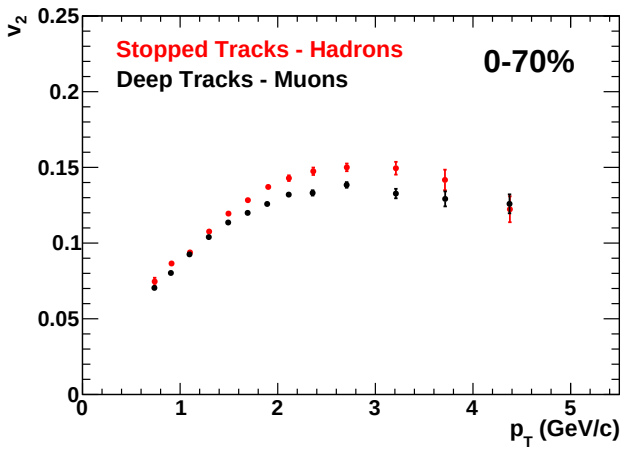

Figure 5.36: $v_2(p_T)$ for stopped hadron tracks (red) and deep muon tracks (black) between 0-70% centrality. The difference in signal at mid p_T can largely be attributed to the proton contribution in the hadron sample or lack thereof in the muon sample.

signals merge back into agreement at high p_T. Therefore, these observations help demonstrate that hadrons are the dominant source of stopped tracks and not decay muons, as well as the ability of protons to penetrate the absorber material and not just the lighter pions and kaons.

Chapter 6

Systematic Errors

While the statistical errors are rigidly determined as $\sigma/\sqrt{N}$, where N is the number of tracks, the systematic errors, whose estimate quantifies the analysis' robustness, are much more of an art form. For instance, as an analysis progresses subjective choices must be made along the way and it isn't always clear which choice is best, when in fact all may be equally correct. This can be likened to a pastry chef deciding if white or brown sugar should be used in a cake mix. Either one may produce a delicious cake, but only one can be chosen and each will result in a slightly different tasting cake. Analogous in this analysis are, for example, the choices for the track requirement values, or subevents used in the determination of the EP resolution. Changing either component, along with many others, can result in different yet equally correct results. Systematic errors are a means of displaying these differences.

Systematic errors can also be used to display how accurately a measurement can be made. This is often determined using a computer simulation which simulates a detector's response to particles passing through it. The simulation input can be compared to the simulation's reconstructed output, with the differences used to estimate a systematic error. Simulations can also be used to investigate other types of issues that can warrant a systematic error such as unwanted particle or

background contamination, detector acceptance and efficiency, and many other types of issues.

This chapter discusses the many checks used in estimating this analysis' systematic errors. Some are determined using data alone and others use a simulation. The different systematic errors are then aggregated to a final value.

6.1 Simulation Overview

The PHENIX integrated simulation application (PISA), which is based on GEANT3 libraries [71], is the standard PHENIX simulation software used in this analysis to estimate how accurately the Muon Arms can measure v_2. Fits to published BRAHMS data [96] (Fig. 5) of pion, kaon, and proton p_T spectra at y $\approx$ 1 were used for the simulation input "cocktail", whose particle composition and p_T distribution was based on the integral probabilities of the BRAHMS spectra. However, after a simulation test was run, an adjustment to increase the number of high p_T particles was made to the fits[1] to better match real data. Gaussian fits to BRAHMS' 0-5% centrality pion and kaon η spectra in [97] (Fig. 2) were used for the input η distributions. Since no proton η spectrum was published, the kaon spectrum was used for protons instead. The p_T and η ranges used for the input were 0.4 GeV/c $< p_T <$ 10 GeV/c and $1.1 < |\eta| < 4.0$.

The simulation production was run on the PHENIX computer farm at RCF and took over a month to complete. The first step in each simulation job was to use

[1] Functions used for the input spectra are: pion = P_0*$(1 + x/P_1^{-P_2})$, kaon = P_0*exp$(-\sqrt{(x^2 + 0.493677^2)}/P_1)$, and proton = P_0*exp$(-\sqrt{(x^2 + 0.938272^2)}/P_1)$. Floating fit parameters are indicated by P_x.

a "homemade" particle generator to create a single particle event cocktail input file based on the BRAHMS spectra. This file was then feed into the PISA simulation, which output a "hits file". The hits file was then filtered to only keep events having a hit to at least the depth of MuID gap 1. This filtered file was then used to create real hits based on the simulated response of the detector, which were then run through the usual PHENIX Muon Arm reconstruction chain with the Run-7 dead channel map, calibrations, and MuID efficiency applied. The output was a refined data file for analysis. In total, $\sim 270 \times 10^9$ single particle events were simulated with $\sim 4.9 \times 10^6$ shallow hadron and $\sim 9.80 \times 10^6$ deep muon tracks passing the track requirements.

Finally, to better match the real data spectrum, weights were applied to the-South and North Muon Arm Monte Carlo (MC) p_T distributions, where MC refers to the actual variable values of the input particle and not the reconstructed (Reco) values. These weights were determined by fitting a polynomial to the ratio of the MC and real data p_T spectrum for each Muon Arm. Lastly, an additional weight was applied to the North Arm to match the real data South/North track ratio. Figure 6.1 compares the resulting simulated Reco p_T spectrum to the real data spectrum.

6.2 Measurement Accuracy

The systematic error for the accuracy of the v_2 measurement was estimated using the PISA simulation described in Sec. 6.1. A number of factors, which will be discussed later in this section, contribute to the alteration of the measured flow

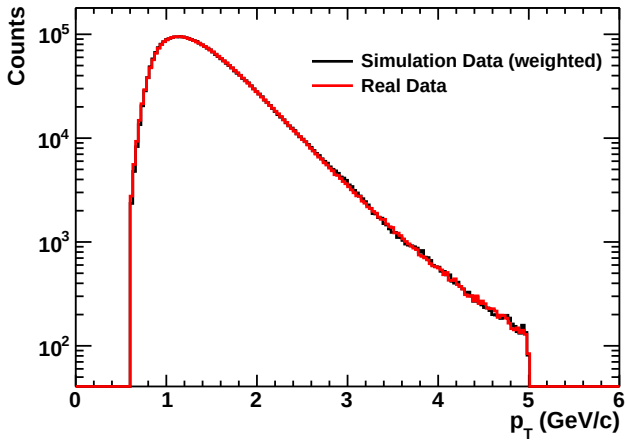

Figure 6.1: Combined (South+North) Muon Arm p_T distribution of simulated (black) and real (red) data hadron tracks. As described in the text, weights are applied to the simulated data to better match the real data. For a clearer overlay, the real data is also scaled to have the same integral as the simulated data.

signal from reality. This estimation method uses PHENIX's Central Arm identified particle v_2 for the simulation input signal and then compares it to what the simulation measures, *i.e.* the simulation output, with the difference used to estimate the systematic error.

The first step in the method is to fit the pion, kaon, and proton Central Arm $v_2(p_T)$ [98] with polynomial fits, as demonstrated in Fig. 6.2(a). These mid-rapidity v_2 values are used instead of forward values [99] because they extend to a higher p_T with much smaller statistical errors. However, the kaon v_2 in the Central Arm measurement is only measured to $p_T = 4.0$ GeV/c. To extend this range to 6 GeV/c to match the pion and proton, an estimation of the kaon v_2 signal is made by fitting the kaon/pion ratio with the exponential P_0+P_1*exp^{-x} having floating parameters P_x, from 1.5 GeV/c $< p_T <$ 4.0 GeV/c and extending the fit to 6 GeV/c, as shown in Fig. 6.2(b). The kaon's v_2 above a p_T of 3.0 GeV/c is then determined by multiplying

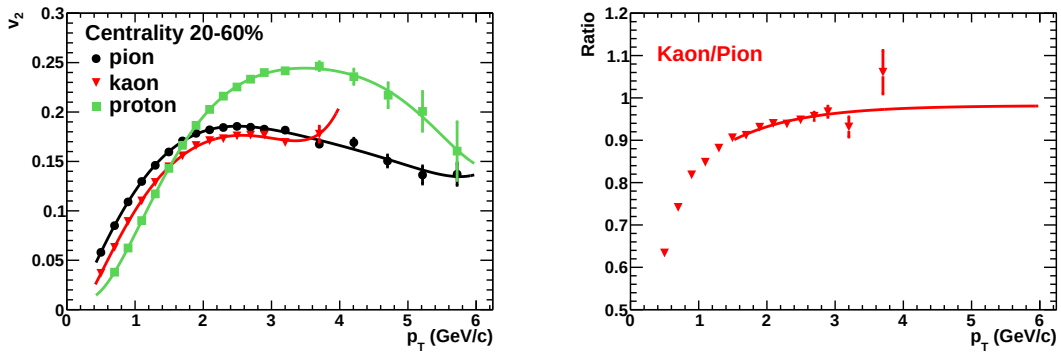

(a) (b)

Figure 6.2: (*a*) PHENIX Central Arm identified particle $v_2(p_T)$ for pions (circles), kaons (triangles), and protons (squares). Each particle type is fit with a polynomial. (*b*) The kaon/pion ratio from (*a*) fit with an exponential (P_0+P_1*exp^{-x}) from 1.5 GeV/c $< p_T <$ 4.0 GeV/c and extended to p_T = 6 GeV/c. This fit is used to estimate the kaons v_2 signal to p_T = 6 GeV/c by multiplying the pion fit in (*a*) by the ratio in (*b*) between the range of 3.0 GeV/c $< p_T <$ 6.0 GeV/c.

the v_2 extracted from the pion fit by the value extracted from this ratio fit. Any particle with a $p_T > 6$ GeV/c was not used in this error estimate.

These fits were then used by the cocktail particle generator to create an input v_2 signal by first selecting a particle type and p_T, as described in Sec. 6.1, and then extracting its v_2 value from the appropriate fit in Fig. 6.2. Then a pseudo φ angle $(\phi - \Psi_{EP})$ was randomly selected from the function 1+2*P_0*cos(2*x) (based on Eq.1.5), where the floating parameter P_0 is set to the v_2 value extracted from the fit. The simulation input v_2 value, which combines the pions, kaons, and protons, was then calculated over many events using $v_2 = \langle \cos 2(\varphi) \rangle$ (Eq. 5.1), with no EP resolution correction needed. This same procedure was used to calculate the simulation's MC and Reco output v_2 except for selecting the particle's identity and p_T, which was already determined. Additionally, before its v_2 was calculated, the Reco's φ angle was slightly shifted by the angular difference between the particle's

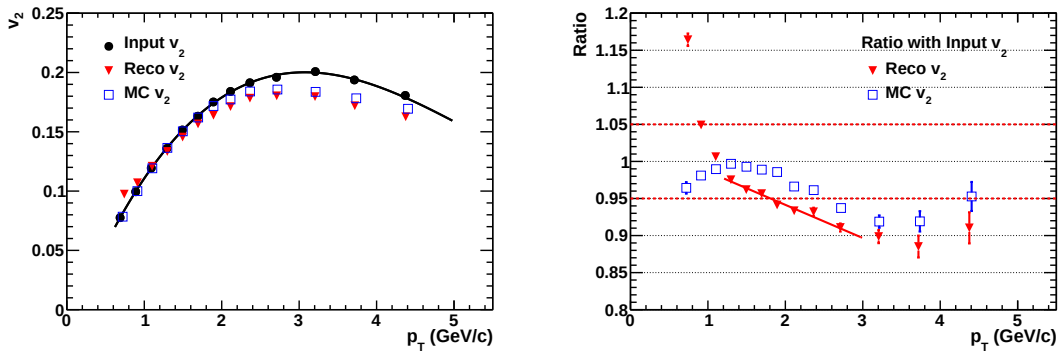

(a) (b)

Figure 6.3: (a) Hadron $v_2(p_T)$ comparison of simulation input (circles) to the output using Reco (triangles) and MC (squares) φ and p_T values. The input v_2 is fit with a polynomial, which is used to determine the Reco and MC ratio to the input in (b). As explained in the text, the Reco ratio and the straight line fit between 1.2 GeV/c $< p_T <$ 3.0 GeV/c are used to estimate the systematic error of the measurement accuracy.

MC and Reco ϕ angles. The difference in the MC and Reco ϕ angle is the result of the particles deflections in the steel absorber due to the multiple scattering and the imperfections of the track reconstruction.

The difference in simulation input and MC and Reco hadron $v_2(p_T)$ output is shown in Fig. 6.3(a). The MC output which uses the MC φ and p_T values is shown using open squares. The Reco output which uses the Reco φ and p_T is shown using triangles. Their ratio to the input v_2 (circles) fit (black line) is shown in Fig. 6.3(b). Only the Reco ratio values are used in the determination of the systematic errors, which are estimated to be -17%, -5%, and -1% for the lowest three p_T bins, respectively. At mid p_T a straight line fit is used for the error estimation between 1.2 GeV/c $< p_T <$ 3 GeV/c. Above $p_T = 3$ GeV/c, the errors are estimated to be +10%. These systematic errors, which are the largest source of error in the v_2 measurement, are used for all centrality ranges measuring hadron $v_2(p_T)$.

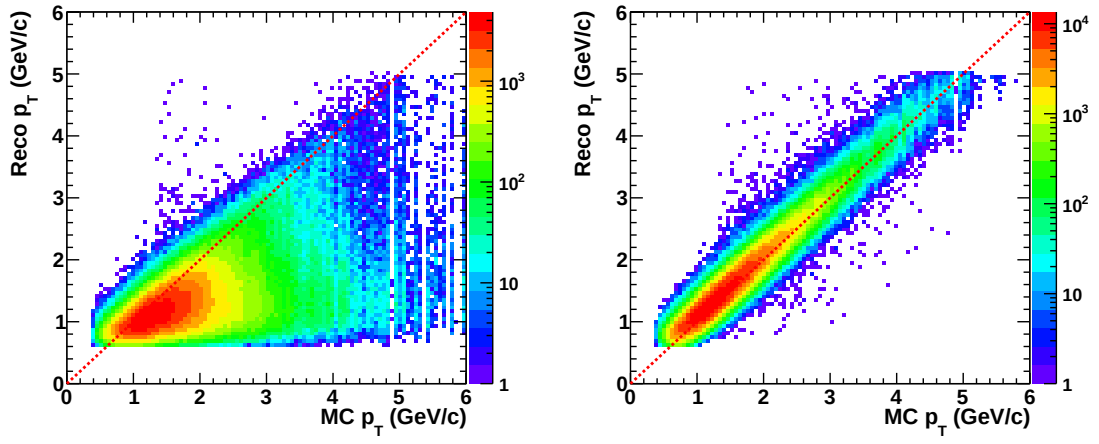

(a) (b)

Figure 6.4: Reco p_T vs. MC p_T for South Muon Arm. (a) The distribution for secondary particles that scattered or decayed before entering the MuTr. (b) The distribution for primary particles that passed through the MuTr.

A number of factors contribute to the input and output signal difference observed in Fig. 6.3. For $p_T < 1$ GeV/c the output Reco v_2 signal is larger than the input signal because of secondary scattered knock-on particles originating in the initial absorber. These particles often inherit only a small fraction of their parents momentum and are thus reconstructed to a lower P_T as seen in Fig. 6.4(a), but can still carry its parents v_2 signal, which is larger than that p_T bin's input v_2 when $p_T \lesssim 3$ GeV/c. This effect contaminates the low p_T bins with high p_T particles having larger v_2 signals, and thus driving the Reco v_2 higher than the input v_2. This effect is most noticeable for the low p_T bins because of their larger contamination of knock-on particles.

For $p_T > 1.2$ GeV/c several factors are at work resulting in a lower output Reco v_2 signal. One is the alteration in particle composition caused by the steel absorber due to some particles more easily traversing the steel than others. With

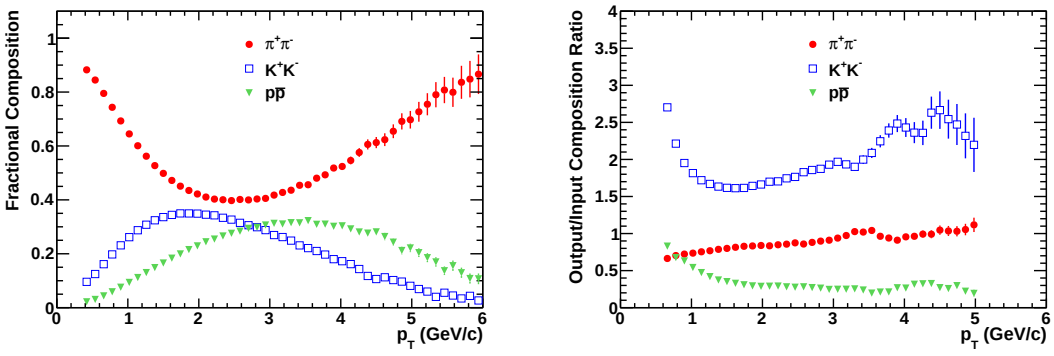

(a) (b)

Figure 6.5: (a) Fractional particle composition of the simulation input for pions (circles), kaons (squares), and protons (triangles). (b) The particle's fractional change in the simulation output compared to the input. The Reco p_T is used for the output data.

different particles having different v_2 signals, a change in the particle composition can alter the combined v_2 signal. Figure 6.5(a) shows the input fractional particle composition for pions, kaons, and protons, with Fig. 6.5(b) showing the % change in fractional particle composition between the simulation input and output. The decrease in output v_2 caused by a change in particle composition is mainly the result of a decrease in proton contribution, which has a significantly larger v_2 signal for $p_T > 2$ GeV/c than pions or kaons, as seen in Fig. 6.2, and undergoes the largest % decrease in contribution, as shown in Fig. 6.5(b). The effect on the v_2 signal resulting from the change in particle composition is closely represented by the MC v_2 in Fig. 6.3 since particle composition is the only alteration from the simulation input.

Another contributing factor to the decrease in output v_2 for $p_T > 1.2$ GeV/c are changes in the particles' ϕ angle caused by either deflections in the initial absorber from ionization energy loss or by knock-on particles having different ϕ angles than

their parents. Both effects cause a dispersion in the tracks ϕ distribution, resulting in a decrease in v_2.

An additional source of signal alteration is the error in p_T determination caused by the reconstruction software assuming that all the particles are muons. As displayed in Fig. 2.16, hadrons such as pions and protons undergo less ionization energy loss traversing the steel in the momentum range of this analysis (2 GeV/c $\lesssim p \lesssim$ 20 GeV/c) than muons. Therefore, the reconstruction software will overcorrect the energy loss hadrons suffer in the initial absorber, assigning them a larger p_T at the vertex than reality. The effect can be seen in Fig. 6.4(b) where the majority of the tracks are above the red dotted line. This can cause a reduction in v_2 signal for $p_T \lesssim 3$ GeV/c and increase the signal for $p_T \gtrsim 3$ GeV/c.

6.3 Muon Contamination

Although already incorporated into the measurement accuracy's systematic error check from Sec. 6.2, the muon contamination in the hadron sample is examined separately here. As discussed in Sec. 5.4.3, muon contamination in the hadron sample will cause non-flatness in the normalized track distribution with respect to the event vertex distribution, due to the increased muon decay probability for those hadrons originating further away from the initial absorber. This results in a ratio with an upward slope away from the arm, as seen in Fig. 5.11.

It was originally thought that this slope could be used to estimate the muon contamination by its non-flatness. However, it was found that the non-flatness

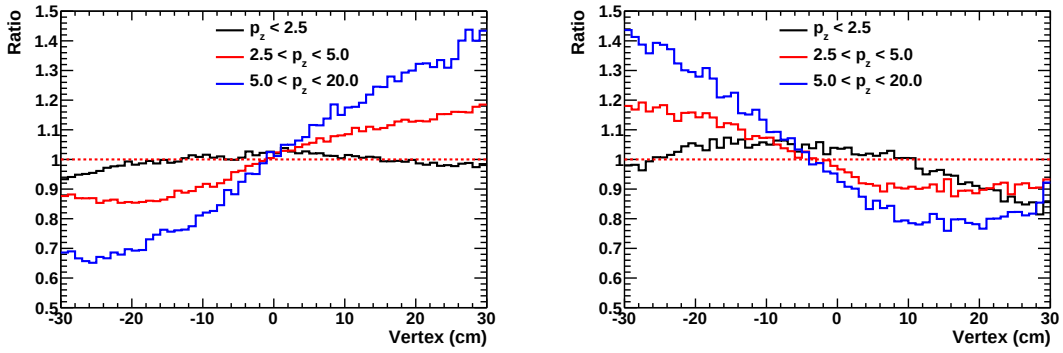

(a) (b)

Figure 6.6: Ratio of the normalized track distribution with respect to event vertex distribution for the South (a) and North (b) Muon Arms. The ratio is shown for different p_z ranges, where a larger slope is observed for higher p_z.

greatly depended on the p_z of the particles, as displayed in Fig. 6.6, which shows a larger slope for higher p_z particles, indicating higher muon contamination. However, this cannot be the case as higher p_z muons readily pass through the steel compared to low p_z muons, which are more susceptible to ranging out in the shallow MuID layers and being mistaken for a stopped hadron. This p_z dependence on the distribution is likely caused by an acceptance effect, leading to this method's unreliability in estimating muon contamination. Instead, the simulation is used.

Figure 6.7 shows the fractional composition of the output hadron tracks from the PISA simulation vs. Reco p_T in (a) and MC p_T in (b). In the figures the labels *primary hadrons*, *muons*, and *secondary* are used referring to the status of the particles after passing through the MuTr. The largest muon contamination is seen in the lowest p_T bins and always constitues $< 10\%$ of the tracks, including less than 2% for $p_T > 2$ GeV/c. This modest contamination combined with the similar v_2 signal for muons and hadrons at low p_T, as displayed in Fig. 5.36, shows that the

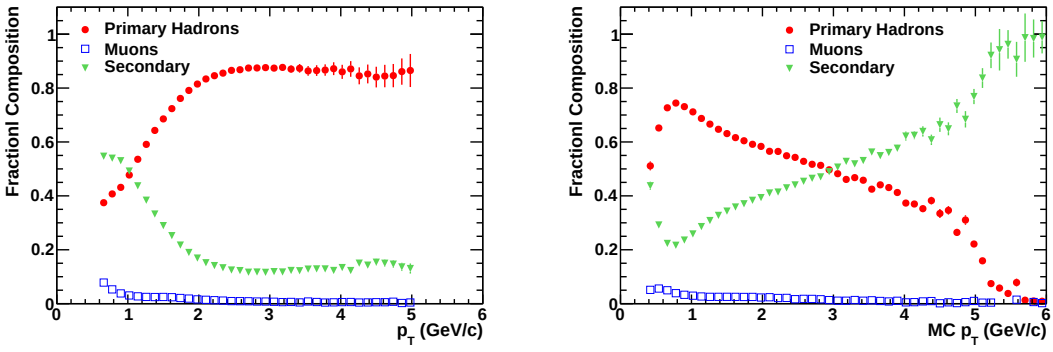

(a) (b)

Figure 6.7: Simulated fractional particle composition vs. Reco p_T (a) and MC p_T (b) after passing through the MuTr. The particle types are primary hadrons (circles), muons (squares), and secondary particles (triangles).

effect of the muon contamination on the measured hadron v_2 signal is small ($\sim$0%), requiring no additional systematic error. Additionally, since the actual Run-7 MuID tube efficiency was used in the simulation, this check also incorporates those muons which were mistakenly reconstructed as shallow due to imperfect MuID efficiency, even though they completely passed through the MuID.

6.4 Background Correction

The estimate of the background correction systematic error was determined by (1) loosening select track requirements to allow more background tracks into the measurement, (2) applying the usual background correction described in Sec. 5.8, and (3) comparing the resulting measurement to the measurement using the regular track requirements and quantifying the difference. The altered track requirements are (variable = regular $\rightarrow$ loosened): MuTr Hits = 16 $\rightarrow$ 14, χ^2/ndf = 5 $\rightarrow$ 15, and $p\delta\theta$ = 0.2 $\rightarrow$ 0.25 GeV·rad/c South and 0.15 $\rightarrow$ 0.20 GeV·rad/c North. Figure 6.8(a)

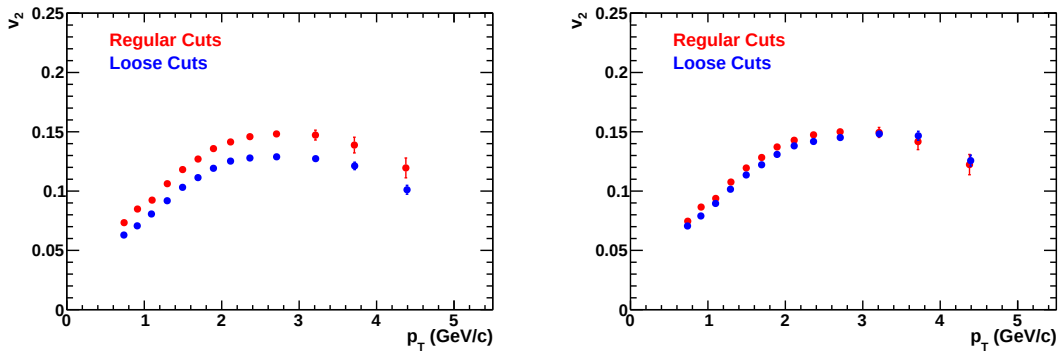

(a) (b)

Figure 6.8: (*a*) Hadron $v_2(p_T)$ between 0-70% centrality for regular (red) and loose (blue) cuts without the background correction. The loose cuts are described in the text. (*b*) The same data as (*a*) but with the background correction applied to both regular and loose cut measurements.

compares the non-background corrected $v_2(p_T)$ signal using the regular and loose cuts for 0-70% centrality. Figure 6.8(*b*) shows the same measurements, but with the background correction applied. Although there is still a noticeable difference in the two measurements, the agreement is much better than without the correction, providing additional confidence in the background correction method.

The systematic error was then calculated using

$$\frac{\text{Bkgrd Corr Sys Err}}{v_2\ \%\ \text{Difference}} = \frac{\%\ \text{Bkgrd Trks Tight Cuts}}{\%\ \text{Bkgrd Trks Loose Cuts}} \tag{6.1}$$

where the *% Bkgrd Trks Tight/Loose Cuts* was determined by dividing the number of reconstructed tracks from the swap half-octant background data, discussed in Sec. 5.5, by the number of passed tracks in the real data. This is shown for 0-70% centrality in Fig. 6.9(*a*). The v_2 *% Difference* was calculated from the % difference in background corrected v_2 from using the regular and loose cuts, such as the %

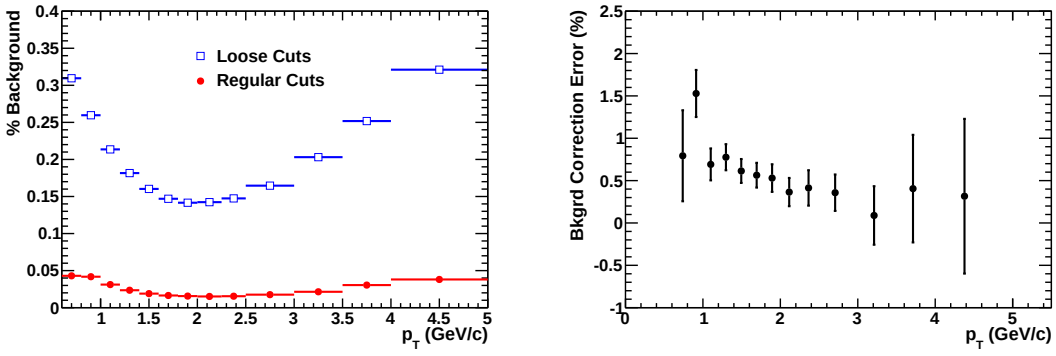

(a) (b)

Figure 6.9: (a) The percentage of background tracks in the 0-70% centrality v_2 measurement using regular (circles) and loose (squares) track cuts. (b) The systematic error of the background correction when using Eq. 6.1.

difference in v_2 in Fig. 6.8(b). The resulting *Bkgrd Corr Sys Err* from Eq. 6.1 is shown in Fig. 6.9(b), where the error is estimated to be 2% for the 0-20% centrality range and 1% for all other ranges.

6.5 v_2 Method

The standard EP method provides a number of ways to calculate the flow signal, with each yielding a slightly different result. The method used in this analysis calculates the measured v_2 by $v_2^{meas} = \langle \cos\left[2\left(\phi - \Psi_{EP}\right)\right]\rangle$ (Eq. 5.1), and then corrects for the EP resolution by $v_2^{corr} = v_2^{meas}/\sigma_{EP}$ (Eq. 3.2). This method will be referred to in this section as the *Regular* method. Another method, referred to as the *Alternative* method, applies the EP resolution correction to each track before averaging, *i.e.* $v_2^{corr} = \langle \cos\left[2\left(\phi - \Psi_{EP}\right)\right]/\sigma_{EP}\rangle$. Mathematically the Regular and Alternative methods are equivalent, but presumably due to the internal calculations and rounding done within ROOT's TProfile object, which is used for these calcu-

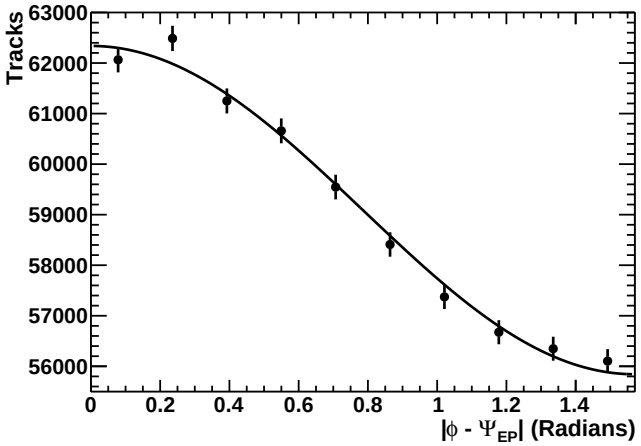

Figure 6.10: $|\phi - \Psi_{EP}|$ track distribution for 1.6 GeV/c $< p_T <$ 1.8 GeV/c. The distribution is fit with the function P_0*(1+2*P_1*cos(2*x)) which is based on the Fourier expansion from Eq. 1.5.

lations, differences in the measurement are observed. A third method, called the *Fitting* method, calculates the v_2 signal by plotting the $|\phi - \Psi_{EP}|$ distribution and fitting it with P_0*(1+2*P_1*cos(2*x)) (based on Eq.1.5), as shown in Fig. 6.10. The floating parameter P_1 is the v_2 signal.

The ratio in v_2 of the Alternative and Fitting methods compared to the Regular method is shown in Fig. 6.11(a) for 0-70% centrality collisions. The v_2 method systematic error is determined by averaging the absolute % difference in v_2 and fitting it with a straight line, as displayed in Fig. 6.11(b). The value of the fit is used as the v_2 method systematic error.

6.6 Track Requirements

The systematic error on the track requirements is estimated by examining how the v_2 signal changes when varying several cuts, one at a time. The altered track

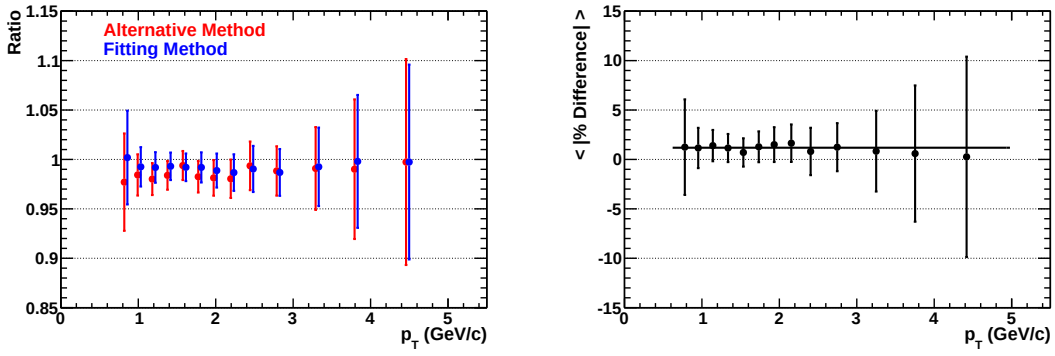

(a) (b)

Figure 6.11: (*a*) The ratio of the Alternative (red) and Fitting (blue) methods compared to the Regular method for 0-70% centrality collisions. (*b*) The averaged absolute % difference with a straight line fit, which is used as the v_2 method systematic error value.

requirements are (variable = regular → altered): Track $\chi^2/ndf = 5 \rightarrow 8$, DG0 = 20 cm → 15 cm South Arm and 15 cm → 10 cm North Arm, and DDG0 = 15° → 10°. The % change in the v_2 signal compared to the regular requirements is shown in Fig. 6.12(*a*) for 0-70% centrality collisions. The systematic error is calculated by adding the absolute % differences in quadrature and fitting the sum with a straight line, as shown in Fig. 6.12(*b*). The straight line fit avoids differences caused by statistical fluctuations and its value is used as the track requirements systematic error.

6.7 EP Detector

The EP detector combinations discussed in Sec. 5.7 to measure Ψ_{EP}, such as MpcBbc_NS, will from now on be referred to as a single detector. The RxnpOpp_MpcBbcNS detector is used in this analysis because it has the best EP resolution, which results in the most precise measurement and smallest statistical errors.

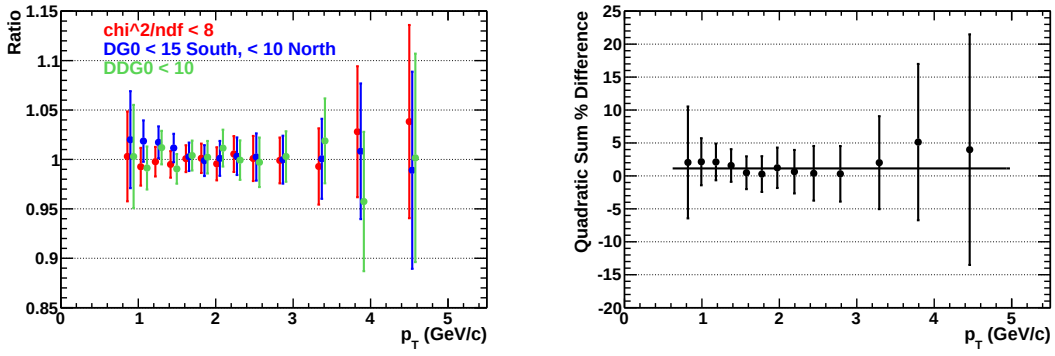

(a) (b)

Figure 6.12: (*a*) The v_2 ratio of the Regular cuts compared to using $\chi^2/ndf <$ 8 (red), DG0 $<$ 15 cm South Arm and 10 cm North Arm (blue), and DDG0 $<$ 10° (green). (*b*) The quadratic sum of the absolute % difference from (*a*) with a straight line fit applied. The fit is used as the systematic error value for the track requirements.

However, alternative EP detectors could have been used to measure Ψ_{EP} instead, with each yielding a slightly different v_2 result. This systematic error check examines these differences.

The alternative detectors used for this check are the RxnpMpcBbc_Opp, RXNP_Opp, MpcBbc_NS, and MpcBbc_Opp. All of their EP resolutions were determined using the 3-subevent method, where subevent (*b*) = RXNP_OppOut and (*c*) = SMD_NS, just like the resolution determination for RxnpOpp_MpcBbcNS. This subevent consistency avoided introducing measurement differences caused by using different (*b*) and (*c*) subevents, which is another type of systematic error that will be examined in Sec. 6.8.

The v_2 ratios using the alternative EP detectors compared to using the RxnpOpp_MpcBbcNS are shown in Fig. 6.13(*a*) for 0-70% centrality collisions. The systematic error is determined by averaging the absolute % differences and fitting

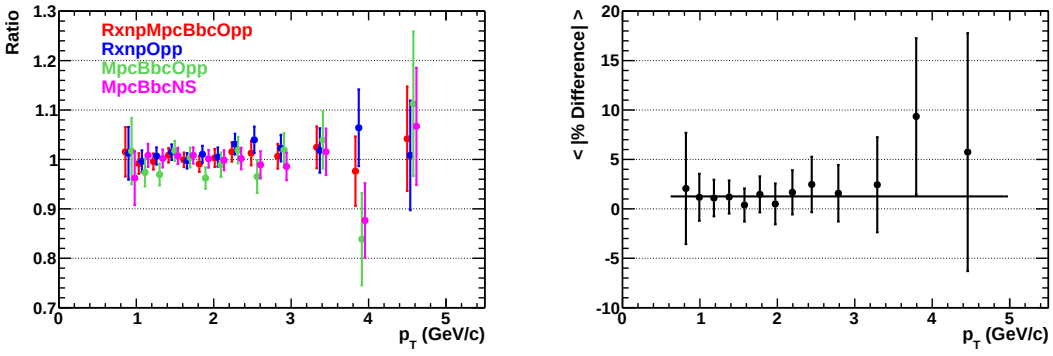

(a) (b)

Figure 6.13: (*a*) The v_2 ratio of RxnpOpp_MpcBbcNS compared to using RxnpMpcBbc_Opp (red), RXNP_Opp (blue), MpcBbc_NS (green) and MpcBbc_Opp (magenta). (*b*) The averaged absolute % difference with a straight line fit, whose value is used as the EP detector systematic error value.

them with a straight line, as shown in Fig. 6.13(*b*). The EP detector systematic error is taken as the value of the straight line fit.

6.8 EP Resolution

The systematic error of the RxnpOpp_MpcBbcNS's EP resolution is determined by varying components in the resolution's calculation and comparing how the altered resolutions change the v_2 signal. However, the RxnpOpp_MpcBbcNS utilizes nearly all of PHENIX's EP detectors, limiting the options for varying its resolution calculation. Instead, the RxnpMpcBbc_Opp detector was used as a substitute, since it has more calculation options.

The four different calculations used to determine the resolution of the RxnpMpcBbc_S are listed in Table 6.1, with calculation one considered the standard calculation since it uses the same (*b*) and (*c*) subevents as those used in determining

Table 6.1: Methods and Subevent Combinations for Determining the EP Resolution Systematic Error

Calc.	Method	Subevents, (a) = RxnpMpcBbc_S
1	3-subevent (Eq. 3.7)	(b) = RXNP_Nout, (c) = SMD_NS
2	3-subevent (Eq. 3.7)	(b) = RXNP_Nin, (c) = SMD_NS
3	3-subevent (Eq. 3.7)	(b) = MpcBbc_N, (c) = SMD_NS
4	$\sqrt{\langle\cos[2(\Psi^a - \Psi^b)]\rangle}$ (Eq. 3.5)	(b) = RxnpMpcBbc_N

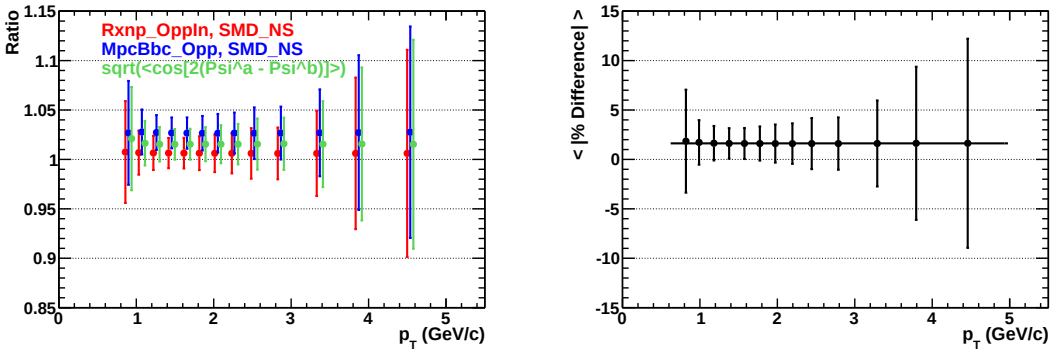

(a) (b)

Figure 6.14: (a) The v_2 ratio using different EP resolution calculations for RxnpMpcBbc_Opp (see Table 6.1). The ratios are shown relative to the standard calculation, *i.e.* calculation 1 in Table 6.1. (b) The averaged absolute % difference with a straight line fit, which is used as the EP resolution systematic error value.

the RxnpS_MpcBbcNS's resolution. For RxnpMpcBbc_N the same methods and subevent combinations were used except for switching S $\longleftrightarrow$ N. The ratios of the v_2 signal when using the non-standard calculations compared to calculation one are presented in Fig. 6.14(a) for 0-70% centrality collisions. The systematic error is determined by averaging the absolute % differences and fitting them with a straight line, as shown in Fig. 6.14(b). The value of the fit is used as the EP resolution systematic error.

6.9 Non-flow Effects

Incorporated into the EP Detector (Sec. 6.7) and EP Resolution (Sec. 6.8) systematic errors are biases caused by non-flow effects (introduced in Sec. 3.3 and Sec. 5.7.2). In both cases the size of the effects depends on the proximity of the different detectors to one another. In the former case it is the proximity of the EP detector to the Muon Arms, and for the latter it is the relative positions of the subevents to one another. With differing η coverage for the different detectors, varying degrees of non-flow effects influence each measurement, allowing for an examination of their biases on the measurement.

For the EP Detector systematic error, if a detector experienced significantly more non-flow effects than another, its v_2 measurement would be noticeably and consistently higher, especially toward higher p_T due to the emergence of jets. However, Fig. 6.13(a) shows that there is not a significant difference in v_2 when using the different EP detectors, indicating that the non-flow effects from using the RxnpOpp_MpcBbcNS are small. At higher p_T the differences with the RxnpOpp_MpcBbcNS become larger, but this can largely be attributed to statistical fluctuations since the data points are mixed above and below 1.

Regarding the EP resolution, non-flow effects can lead to either an increase or decrease in the v_2 signal. For instance, when using the 3-subevent method, if a strong non-flow correlation is present between subevents (a) and (b) then the numerator in Eq. 3.7 will be larger than in the absence of non-flow effects, causing a decrease in v_2. Conversely, if there is a strong non-flow correlation between subevents (b) and

(c) then the denominator will be artificially large, causing a decrease in v_2.

With the changing η coverage of subevent (b) in Fig. 6.14(a), and hence changing proximity of the subevents, biases caused by non-flow effects can be examined. For calculations 1, 2, and 3 in Table 6.1, the η gap grows between subevents (a) and (b) and decreases between (b) and (c). This results in a decrease of any non-flow bias in the numerator and an increase of any in the denominator, resulting in an increased v_2 signal due to an overcorrection, which is exhibited in the figure's ratio trend. However, by using the SMD_NS for subevent (c) the non-flow effects should be minimized in the denominator since it uses spectator neutrons to measure the EP and not emitted particles, like the other detectors. What Fig. 6.14 shows is that the non-flow bias on the EP resolution is not larger than a few percent and well covered by the EP Resolution systematic error.

6.10 Aggregating Errors

The final step before applying the systematic errors to the v_2 measurement was to aggregate the individual errors into a final error. This was done by first quadratically summing the Background Correction, v_2 Method, Track Requirements, EP Detector, and EP Resolution systematic errors. These errors were summed in quadrature instead of a simple additive sum to avoid an overestimation of the systematic errors. To this quadratic sum the Measurement Accuracy and Acceptance[2] systematic errors were added asymmetrically, meaning added to only the upper or lower bound of the error. These errors are not included in the quadratic sum because

[2]The Acceptance systematic error has not yet been discussed, but will be described in Sec. 7.4.

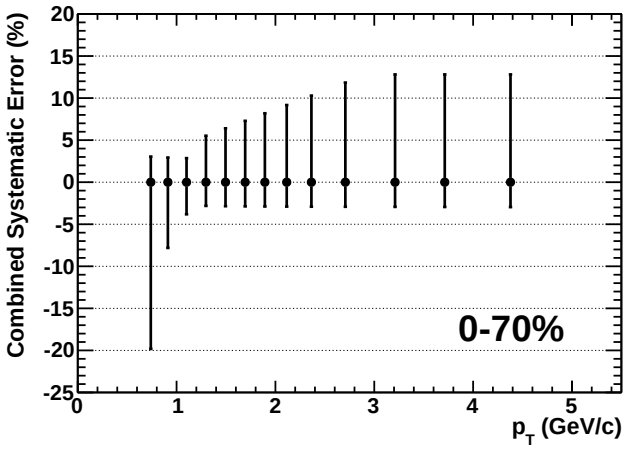

Figure 6.15: Combined systematic error of $v_2(p_T)$ for 0-70% centrality.

there is an underlying understanding of their trends and why they indicate a higher or lower v_2 signal. For instance, it was discussed in Sec. 6.2 that knock-on particles are the reason in the PISA simulation for the artificial increase in v_2 at low p_T, shown in Fig. 6.3. Therefore, only applying a lower systematic error is appropriate since knock-on particles will not artificially lower the v_2 for low p_T particles. An example of the final systematic error as a percentage of v_2 signal is displayed in Fig. 6.15 for 0-70% centrality collisions.

The systematic error procedure described in this chapter is used for the $v_2(p_T)$, $v_2(centrality)$, and $v_2(N_{part})$ measurements. $v_2(\eta)$ has also been measured, but due to acceptance effects it requires a modified analysis and systematic error procedure, which is discussed in Chapter 7.

Chapter 7

$v_2(\eta)$

7.1 Muon Arm Acceptance

Originally it was thought that $v_2(\eta)$ could be measured with the technique described in Chapters 5 and 6. The results of such a measurement are shown in Fig. 7.1 for 0-70% centrality collisions. In the figure the $\langle p_T \rangle$ is also shown, with it having a definite correlation with the decrease in v_2. From this figure it appeared that the decrease in v_2 toward forward η seen by STAR and PHOBOS in Fig. 1 and Fig. 3.16 was mainly caused by a decrease in $\langle p_T \rangle$ and not a change in v_2.

However, this notion was negated when it was discovered that the Muon Arms had a p_T acceptance bias caused by the p_z requirement that cut off the lower p_T particles toward mid-rapidity, resulting in a nonuniform $\langle p_T \rangle(\eta)$. This bias is demonstrated in Fig. 7.2(a). Figure 7.2(b) shows this bias is from the p_z requirement by the different smooth edges seen for tracks penetrating to different layers of the MuID. From this finding, a new method had to be devised to properly measure $v_2(\eta)$ that would negate any change in $\langle p_T \rangle$ as a function of η in the Muon Arms.

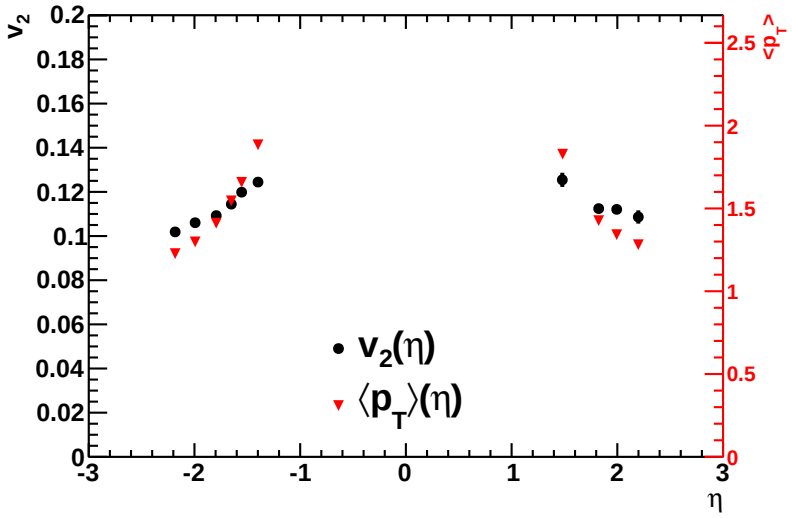

Figure 7.1: $v_2(\eta)$ (circles) using the analysis technique described in Chapter 5. $\langle p_T \rangle(\eta)$ (triangles) is also displayed. Both use 0-70% centrality collisions. Only statistical errors are shown.

7.2 Measurement Procedure

A method was developed to measure $v_2(\eta)$ that minimized the bias effect of a changing $\langle p_T \rangle(\eta)$ in the Muon Arms. The method was applied separately to both shallow hadrons and deep decay muons. The steps of this procedure are:

1. Plot a triple differential $v_2(p_T(\eta, centrality))$. Because of the decreased statistics in each plot the number of p_T bins is reduced from 13 $\rightarrow$ 5.
2. Plot a double differential $v_2(p_T(centrality))$ using normal p_T binning and the full Muon Arm η range.
3. Fit plots obtained in step (2) with a 3rd order polynomial. This gets the average $v_2(p_T)$ signal shape for the entire η range.
4. Fit each centrality range set of $v_2(p_T(\eta, centrality))$ plots from step (1) (only η range varies within a set) with the fit obtained from the same centrality range in step (3). When the fit is applied to the triple differential only its height varies, *i.e.* v_2 signal strength.
5. Extract the v_2 value from each applied fit at a specified p_T.
6. Plot these v_2 values as a function of η using the $\langle \eta \rangle$ value in each η range.

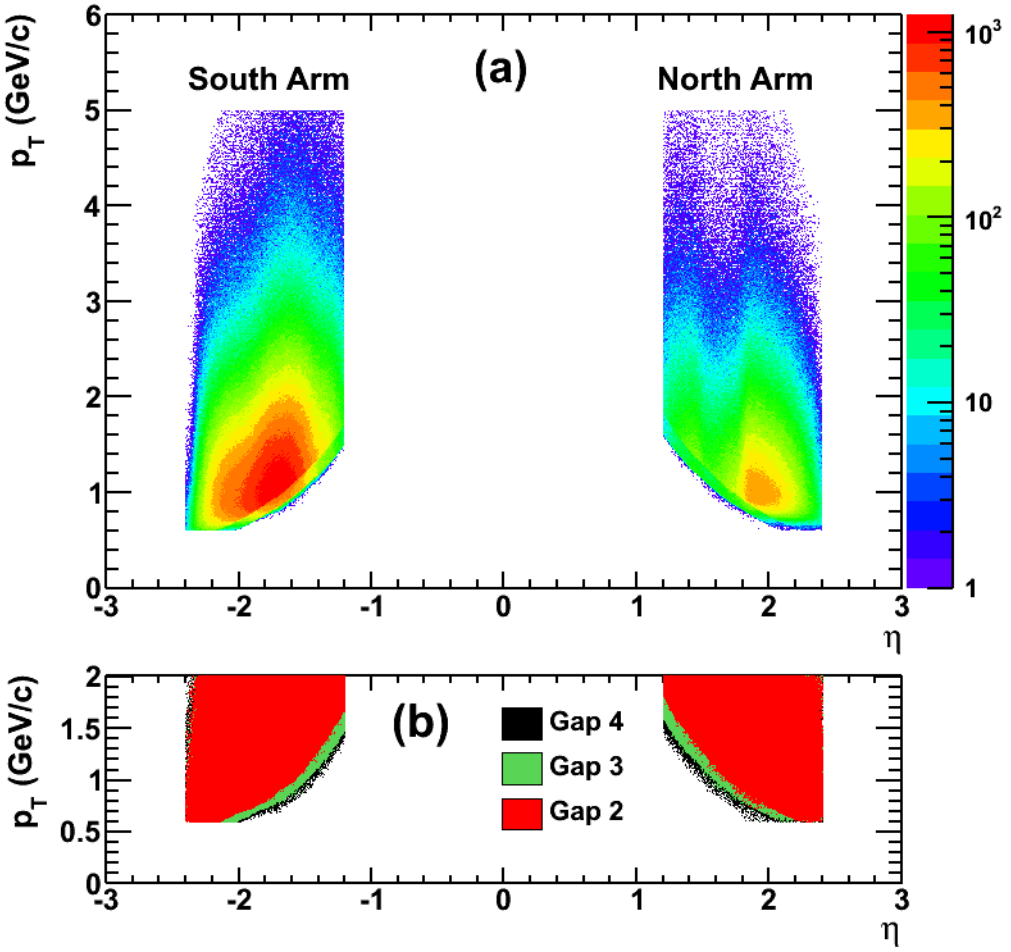

Figure 7.2: (*a*) $p_T(\eta)$ scatter plot of shallow hadron tracks showing the p_T acceptance bias of the Muon Arms at low p_T. (*b*) $p_T(\eta)$ scatter plot for tracks having $p_T < 2$ GeV/c and whose deepest hit in the MuID is at gap 2 (red), gap 3 (green), or gap 4 (black). An essentially smooth edge facing mid-rapidity is seen for each gap, caused by their different p_z requirements. Both subfigures use 0-70% centrality collisions and have the South (North) Muon Arm located at negative (positive) η.

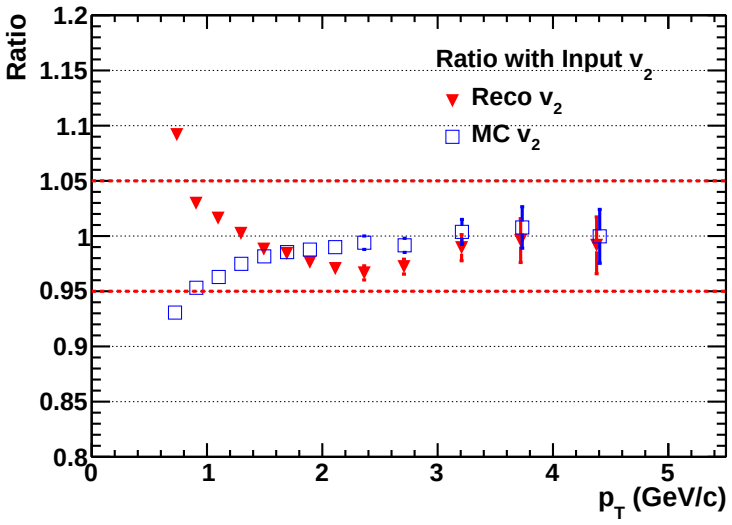

Figure 7.3: Simulated input and output $v_2(p_T)$ ratio for deep tracks, which are mostly muons from pion and kaon decays. For measuring the v_2, the Reco data (triangles) use the Reco φ and p_T, while the MC data (squares) use the MC φ and p_T.

Similar to hadrons in Sec. 6.2, it was checked that the decay muon v_2 could also be accurately measured in the Muon Arms by determining the ratio of the simulation input and output v_2, as displayed in Fig. 7.3. Since nearly all of the deep tracks are from pions and kaons, as shown by the PISA simulation particle composition ratio in Fig. 7.4(a), only pions and kaons were used for the input v_2.

Notice in Fig. 7.3 that, like hadrons in Fig. 6.3, deep tracks also exhibit a rise in v_2 below $p_T \approx 1$ GeV/c. However, unlike hadrons, the effect is not caused by knock-on particles, but by some muons experiencing significant energy loss in the initial absorber due to substantial multiple scattering, thereby reducing their p_T. Also causing a reduction in p_T is the bifurcation of the primary hadron's momentum to the muon and neutrino decay products. In some of these decays a substantial portion of the available momentum is acquired by the neutrino, leaving the muon with

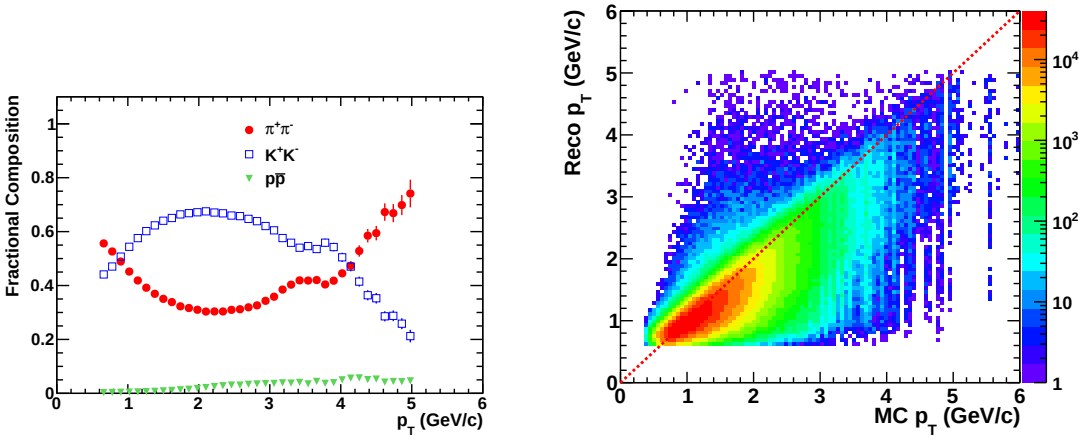

(a) (b)

Figure 7.4: (*a*) The sources for the deep tracks in the PISA simulation vs. Reco p_T. The vast majority are shown to originate from pions (circles) and kaons (squares) with protons (triangles) constituting $\lesssim 5\%$. (*b*) The MC and Reco p_T of deep track decay muons. The figure shows that the rise in v_2 at low p_T seen in Fig. 7.3 is caused by the reconstruction of higher p_T particles to a lower p_T.

a reduced momentum compared to the primary particle, as indicated in Fig. 7.4(*b*). Despite a reduction in p_T, these lower energy muons can still carry much of their parent's v_2 signal, which is generally larger than the v_2 of primary particles at lower p_T, thereby noticeably increasing the measured v_2 at low p_T due to this contamination. For $p_T \gtrsim 1$ GeV/c this effect is reduced due to higher track statistics and consequently the output v_2 is within 4% of the input v_2. As a result of this increased v_2 at low p_T for both hadrons and muons, the $v_2(p_T)$ fit for more forward η ranges could artificially increase since those η ranges include lower p_T particles (Fig. 7.2). Therefore, it was decided to restrict the p_T range for this $v_2(\eta)$ method to $p_T > 1$ GeV/c.

The first step in the method was to plot a triple differential of the v_2 signal, *i.e.* $v_2(p_T(\eta, centrality))$. Table 7.1 shows the binning of these variables used for these

Table 7.1: $v_2(p_T(\eta, centrality))$ Bin Ranges for Hadrons and Decay Muons

	Hadrons	Decay Muons
Centrality (%)	0−20−40−70	0−15−30−45−70
p_T (GeV/c)	1.0−1.2−1.5−2.0−2.5−5.0	
$\|\eta\|$	1.2−1.5−1.8−2.1−2.4	

plots. In the table, the centrality ranges vary between the hadrons and decay muons due to the higher statistics of the decay muons allowing for more bins. These plots were made using the same procedure described in Chapter 5, except for excluding $p_T < 1$ GeV/c, as mentioned earlier.

From here, the average double differential $v_2(p_T(centrality))$ signal shapes for the different centrality ranges were determined using the full η range ($1.2 < |\eta| < 2.4$), regular p_T binning above $p_T = 1.0$ GeV/c, and fitting the data with a 3$^{\text{rd}}$ order polynomial, as demonstrated in Fig 7.5. These fits were then used to fit the triple differential data for the different η ranges within a centrality range, where only the height of the fit varied, *i.e.* v_2 signal strength. Fits to the 0-15% and 30-45% centrality ranges are shown in Fig. 7.6. The $\langle p_T \rangle$ value within 1.0 GeV/c $< p_T <$ 5.0 GeV/c was then somewhat arbitrarily chosen for where the v_2 signal values would be extracted from the fits. These $\langle p_T \rangle$ values were 1.59 GeV/c and 1.45 GeV/c for hadrons and decay muons, respectively. Since the functional shape is the same for all fits within a centrality range, the specific p_T chosen for the v_2 extraction is to some extent immaterial since the difference in v_2 would be the same at any p_T value.

The next step was to determine the $\langle |\eta| \rangle$ within each η bin for each centrality range by plotting $v_2(|\eta|)$, from here on referred to as $v_2(\eta)$, using the method in

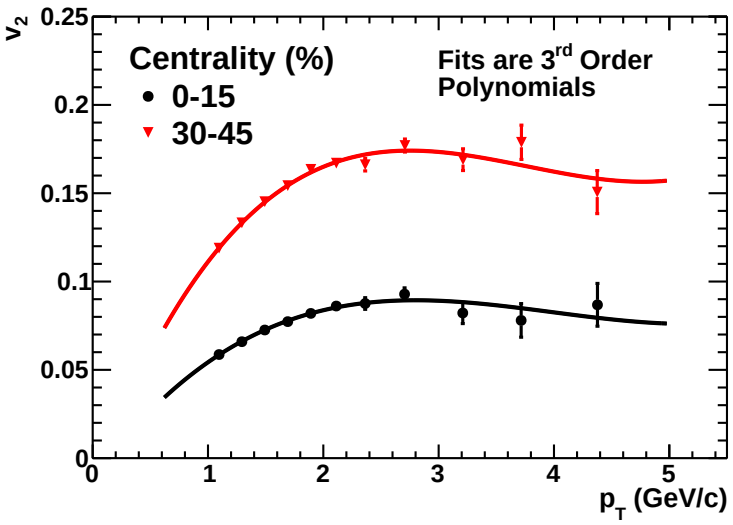

Figure 7.5: $v_2(p_T(centrality))$ of deep tracks for the centrality ranges of 0-15% (circles) and 30-45% (triangles). Each is fit with a 3$^{\text{rd}}$ order polynomial. The full η range of the Muon Arms is used ($1.2 < |\eta| < 2.4$).

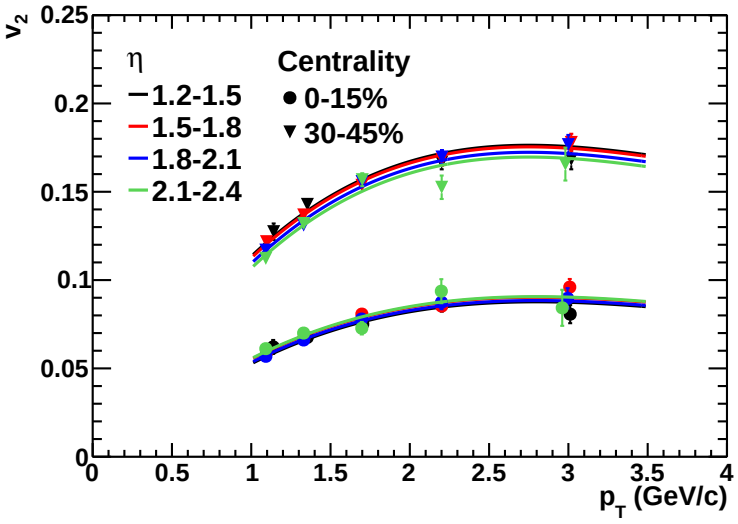

Figure 7.6: $v_2(p_T(\eta, centrality))$ of deep tracks for the centrality ranges of 0-15% (circles) and 30-45% (triangles).

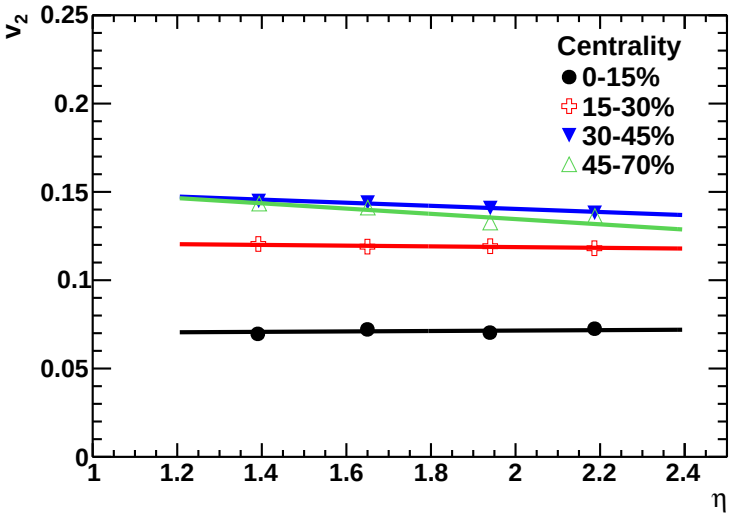

Figure 7.7: $v_2(\eta)$ of deep tracks from the method described in the text. See figure legend for the different centrality ranges. Each name is fit with a straight line to better observe any signal trend. Statistical errors taken from the fit are shown, but are smaller than the data points.

Chapter 5 except with the $p_T > 1$ GeV/c requirement. These p_T acceptance biased v_2 values were then reset to the v_2 values extracted at the previously specified p_T from the triple differential fits demonstrated in Fig. 7.6. The resulting $v_2(\eta)$ measurement for decay muons in different centrality ranges is shown in Fig. 7.7, with a straight line fit applied to each centrality range.

7.3 Systematic Error

From the method described in Sec. 7.2 to measure $v_2(\eta)$, the resulting magnitude of the v_2 is not as well-founded as the trend of the slope. This is because the v_2 magnitude depends on the somewhat arbitrarily chosen p_T value used to extract the v_2 value, and can therefore vary greatly. On the other hand, the slope of the $v_2(\eta)$ fit would remain constant for any chosen p_T value due to the fixed shape of

Table 7.2: Method Alterations for Determining Systematic Error of $v_2(\eta)$ Slope Fit

Method	Alterations to Regular Method
1	Fit triple differential using exponential function P_0+P_1*exp^{-x} to each η range in the centrality range. Average P_1 and fix it to the average value. Then refit so only parameter P_0 varies, *i.e.* v_2 magnitude.
2	Same as method 2, but force exponential fit through origin.
3	p_T bins = 1.0−1.4−2.0−5.0 GeV/c.

the fit. Therefore, the scientific value of this $v_2(\eta)$ measurement is in the slope of Fig. 7.7's fits, which provide insights into the trend of how v_2 changes with η. For this reason the $v_2(\eta)$ systematic error focuses on the slope of the fit instead of the v_2 strength of the individual data points.

The systematic error of the slope was determined by independently varying several components in the $v_2(\eta)$ measurement and comparing their slope fit to that of the regular method. Table 7.2 lists these alterations. The resulting fit from each method was then normalized to be equal to the regular method fit at $\eta = 1.8$, as shown in Fig. 7.8. The absolute % difference of each alternative fit to the regular fit was determined at $\eta = 1.2$ and added in quadrature to get the final systematic error of the slope, which is shown in Fig. 7.9. The % error is applied to the ends of the slope fit at $\eta = 1.2$ and 2.4.

7.4 $v_2(p_T)$ Acceptance Systematic Error

As a result of the Muon Arm's non-uniform p_T acceptance, shown in Fig. 7.2, an additional systematic error was applied to the hadron $v_2(p_T)$, $v_2(centrality)$, and $v_2(N_{part})$ measurements. However, since the procedures are similar for each, only

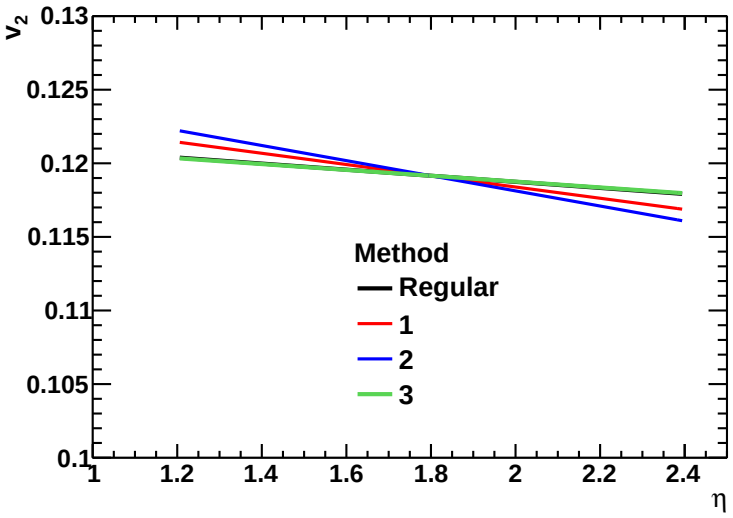

Figure 7.8: Fits from the methods described in Table 7.2 for determining the $v_2(\eta)$ slope systematic error. The fits are for deep tracks of 15-30% centrality.

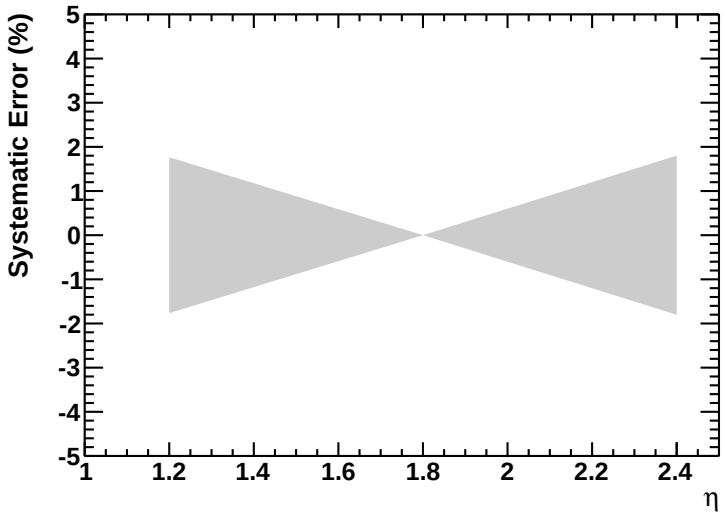

Figure 7.9: Percent systematic error for the $v_2(\eta)$ slope fit for deep tracks of 15-30% centrality.

the $v_2(p_T)$ error is discussed here. The $\langle\eta\rangle$ for all centrality ranges examined in this analysis was ~1.8, however, individual data points can deviate from this average. This acceptance systematic error uses the $v_2(\eta)$ slope fit method from Sec. 7.2 to estimate the expected change in v_2 signal caused by the difference in the data point's $\langle\eta\rangle$ from that of the measurement's overall $\langle\eta\rangle$ of 1.8.

The first step in this error estimation was to determine the $\langle\eta\rangle$ of each data point by plotting $\langle\eta\rangle(p_T)$, presented in Fig. 7.10 for 40-60% centrality collisions. Next, the $v_2(\eta)$ slope fit of each centrality range was determined using the method described in Sec. 7.2. The slope fits from the deep decay muons, like those obtained in Fig. 7.7, were used for the shallow hadrons because the decay muons have a larger slope, resulting in a larger systematic error, and therefore an upper estimate of the error. Then a polynomial fit was made to the decay muon $v_2(p_T)$ measurement of each centrality range using the full η range ($1.2 < |\eta| < 2.4$) and regular p_T binning above $p_T = 1.0$ GeV/c, like that done in Fig. 7.5. For each data point, a v_2 value was then extracted from the polynomial fit at the p_T value of the data point. The height of that centralities slope fit was then adjusted to have this same v_2 value at $\eta = 1.8$. The acceptance systematic error for each data point was then determined from the height adjusted slope fit as the % difference in v_2 at $\eta = 1.8$ and the $\langle\eta\rangle$ value of the data point like that obtained from Fig. 7.10. The resulting % error for 40-60% centrality is shown in Fig. 7.11.

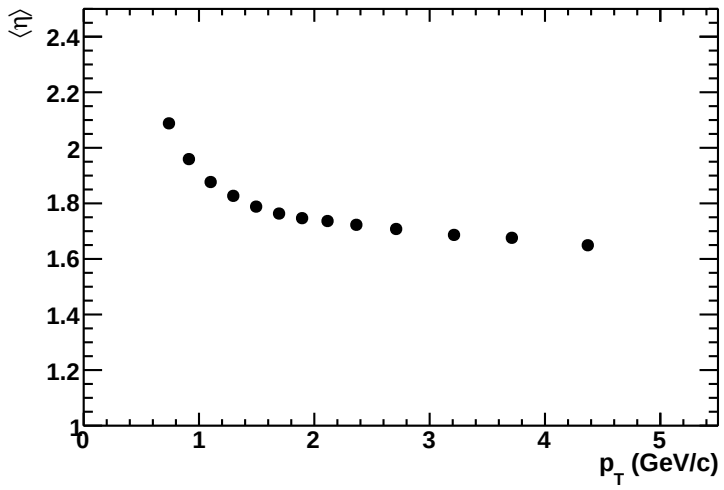

Figure 7.10: Hadron $\langle\eta\rangle(p_T)$ for 40-60% centrality. Statistical errors are smaller than the points.

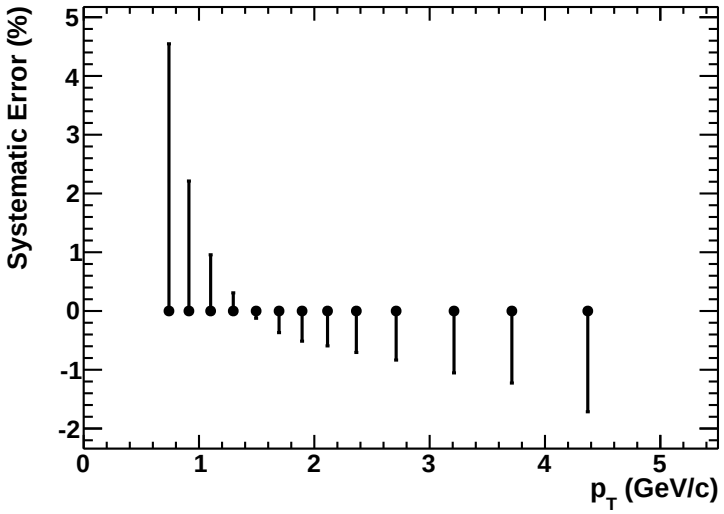

Figure 7.11: Hadron $v_2(p_T)$ acceptance systematic error for 40-60% centrality collisions.

Chapter 8

Results

8.1 $v_2(p_T)$

The final results for forward rapidity unidentified charged hadron and decay muon $v_2(p_T)$ are shown in Figs. 8.1−8.9 for centrality ranges 0-70%, 0-20%, 20-40%, 40-60%, 20-60%, 0-25%, 25-50%, 0-60%, and 10-40%, respectively. All results use 0.6 GeV/c $< p_T <$ 5.0 GeV/c and $1.2 < |\eta| < 2.4$ with $\langle\eta\rangle \approx 1.8$. Systematic errors were calculated for hadrons only. The data point values along with statistical and systematic errors are provided in Tables D.1−D.18.

8.2 $v_2(centrality)$ and $v_2(N_{part})$

The final results for forward rapidity unidentified charged hadron and decay muon $v_2(centrality)$ and $v_2(N_{part})$ using 0.6 GeV/c $< p_T <$ 5.0 GeV/c and $1.2 < |\eta| < 2.4$ are shown in Figs. 8.10 and 8.11, respectively. The only difference between the two results is the conversion of the 5% centrality bins in $v_2(centrality)$ to their respective $\langle N_{part}\rangle$ value for $v_2(N_{part})$. These values were determined using a Glauber model described in [89]. Systematic errors were calculated for hadrons only. The data point values along with statistical and systematic errors for both figures are provided in Tables D.19 and D.20.

8.3 $v_2(\eta)$

The final results for forward rapidity $v_2(\eta)$ are shown in Figs. 8.12 and 8.13 for unidentified charged hadrons and decay muons, respectively, using 0.6 GeV/c $< p_T <$ 5.0 GeV/c and $1.2 < |\eta| < 2.4$. The results were obtained from the unconventional method described in Chapter 7, where the v_2 values were extracted from fits to the triple differential $v_2(p_T(\eta, centrality))$ data at the $\langle p_T \rangle$ values of 1.59 GeV/c and 1.45 GeV/c for hadrons and decay muons, respectively. The centrality ranges used are 0-20%, 20-40%, and 40-70% for hadrons and 0-15%, 15-30%, 30-45%, and 45-70% for decay muons. Only statistical errors are calculated for the data points. Straight line fits are applied to the data points of each centrality range with their systematic errors shown by the bands. The data point values and their statistical errors along with the parameters and systematic errors for the straight line fits are provided for each centrality range in Tables D.21−D.23.

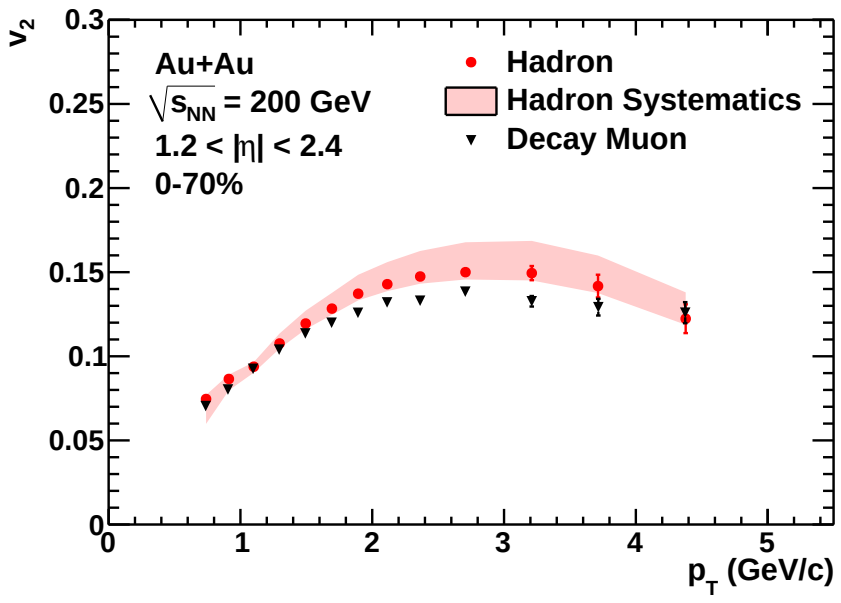

Figure 8.1: Forward rapidity hadron (circles) and decay muon (triangles) $v_2(p_T)$ for 0-70% centrality Au+Au collisions at $\sqrt{s_{NN}} = 200$ GeV. Statistical errors are shown by the bars and the hadron systematic errors by the band. Data values are provided in Tables D.1 and D.2.

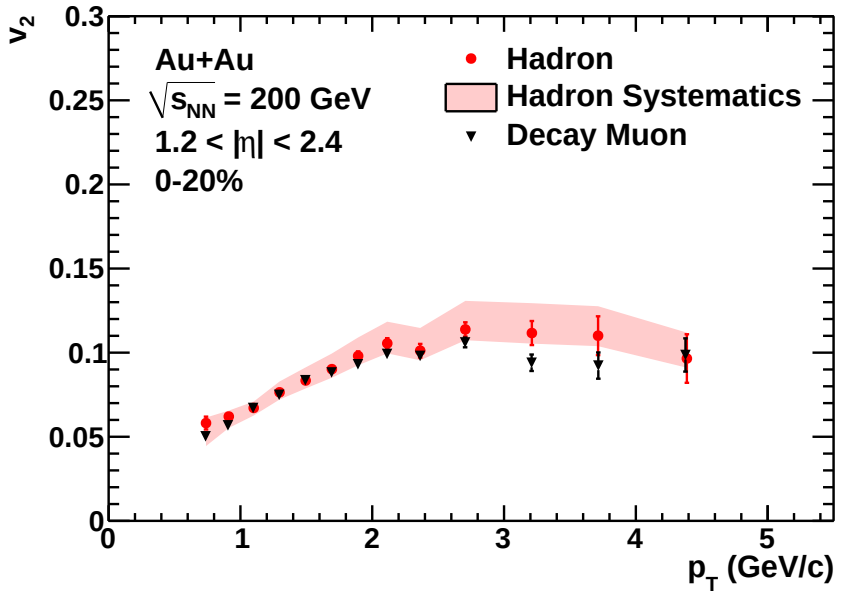

Figure 8.2: Forward rapidity hadron (circles) and decay muon (triangles) $v_2(p_T)$ for 0-20% centrality Au+Au collisions at $\sqrt{s_{NN}} = 200$ GeV. Statistical errors are shown by the bars and the hadron systematic errors by the band. Data values are provided in Tables D.3 and D.4.

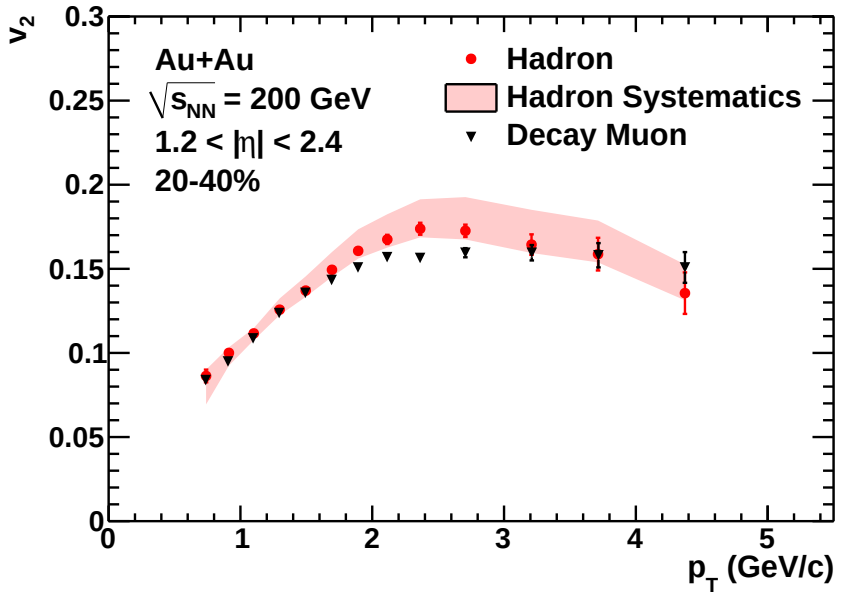

Figure 8.3: Forward rapidity hadron (circles) and decay muon (triangles) $v_2(p_T)$ for 20-40% centrality Au+Au collisions at $\sqrt{s_{NN}} = 200$ GeV. Statistical errors are shown by the bars and the hadron systematic errors by the band. Data values are provided in Tables D.5 and D.6.

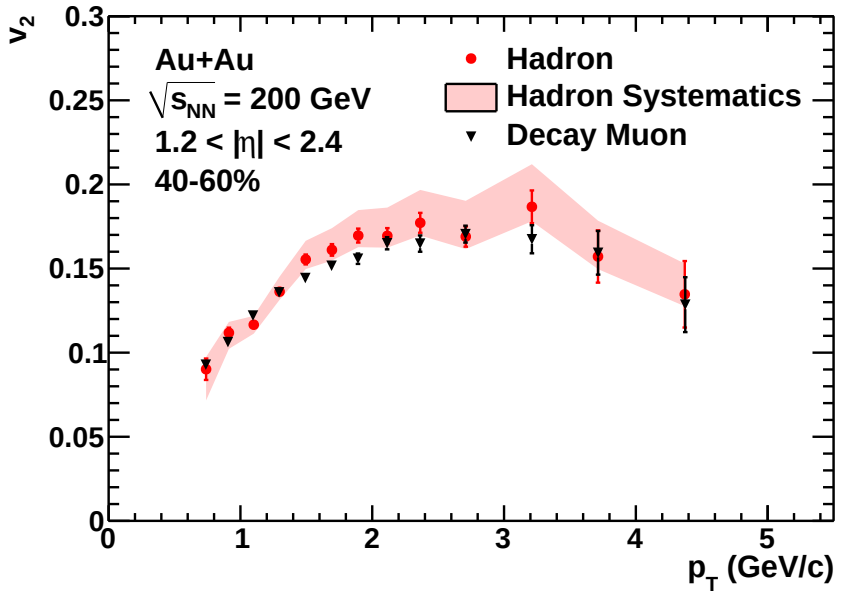

Figure 8.4: Forward rapidity hadron (circles) and decay muon (triangles) $v_2(p_T)$ for 40-60% centrality Au+Au collisions at $\sqrt{s_{NN}} = 200$ GeV. Statistical errors are shown by the bars and the hadron systematic errors by the band. Data values are provided in Tables D.7 and D.8.

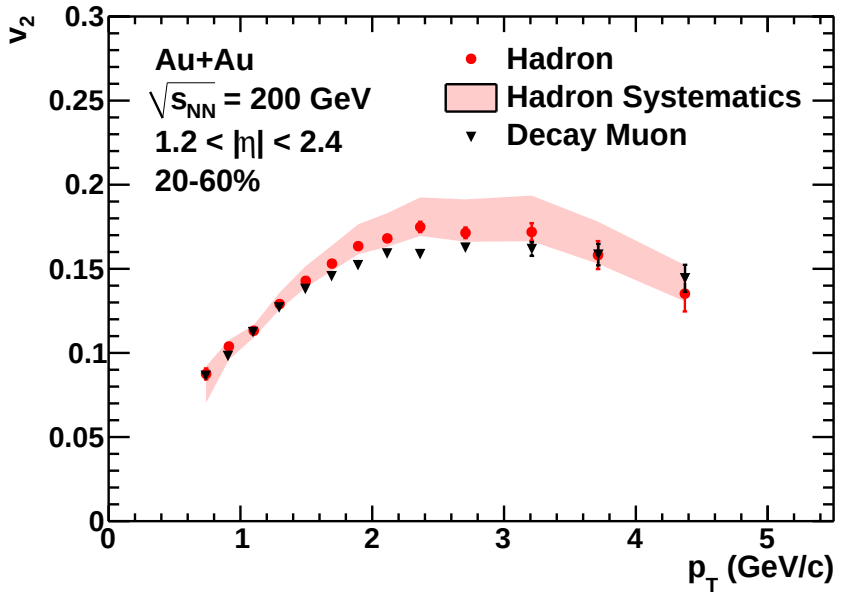

Figure 8.5: Forward rapidity hadron (circles) and decay muon (triangles) $v_2(p_T)$ for 20-60% centrality Au+Au collisions at $\sqrt{s_{NN}} = 200$ GeV. Statistical errors are shown by the bars and the hadron systematic errors by the band. Data values are provided in Tables D.9 and D.10.

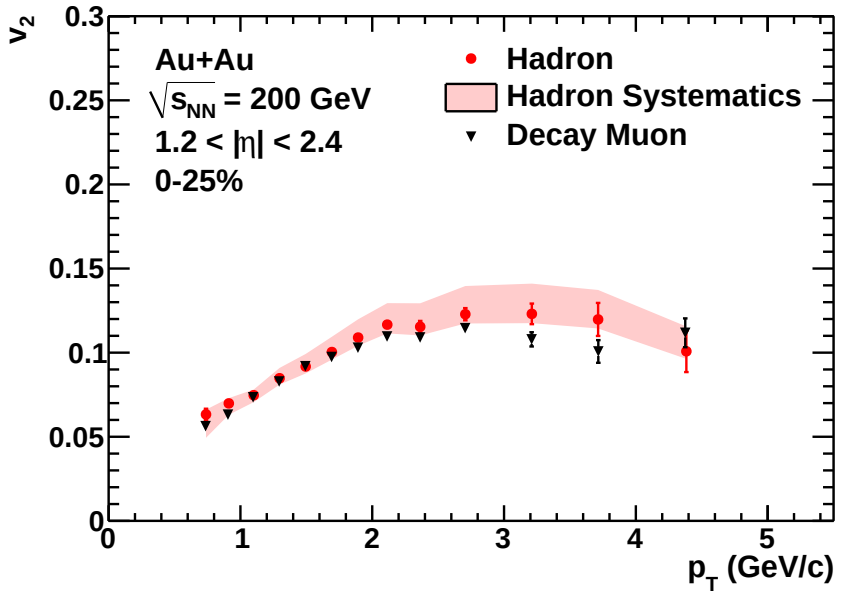

Figure 8.6: Forward rapidity hadron (circles) and decay muon (triangles) $v_2(p_T)$ for 0-25% centrality Au+Au collisions at $\sqrt{s_{NN}} = 200$ GeV. Statistical errors are shown by the bars and the hadron systematic errors by the band. Data values are provided in Table D.11 and D.12.

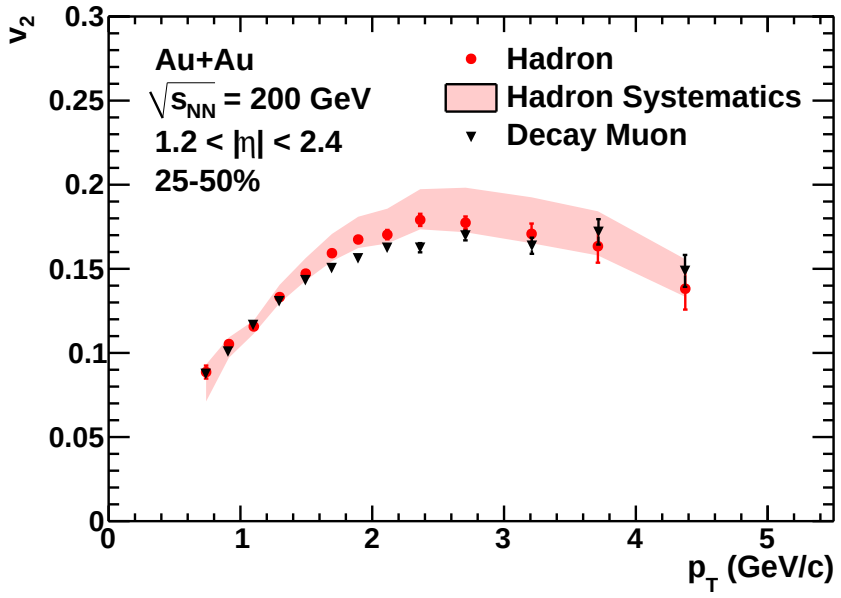

Figure 8.7: Forward rapidity hadron (circles) and decay muon (triangles) $v_2(p_T)$ for 25-50% centrality Au+Au collisions at $\sqrt{s_{NN}} = 200$ GeV. Statistical errors are shown by the bars and the hadron systematic errors by the band. Data values are provided in Tables D.13 and D.14.

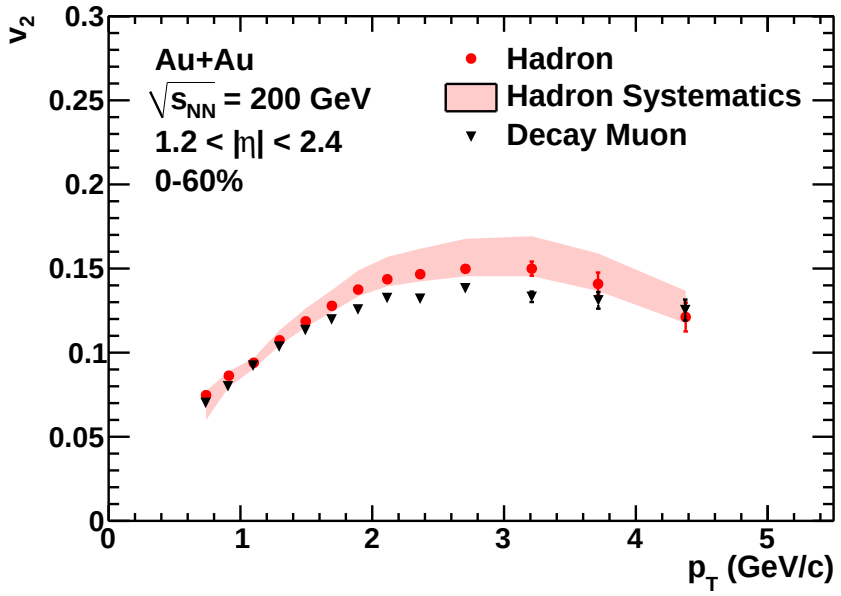

Figure 8.8: Forward rapidity hadron (circles) and decay muon (triangles) $v_2(p_T)$ for 0-60% centrality Au+Au collisions at $\sqrt{s_{NN}} = 200$ GeV. Statistical errors are shown by the bars and the hadron systematic errors by the band. Data values are provided in Tables D.15 and D.16.

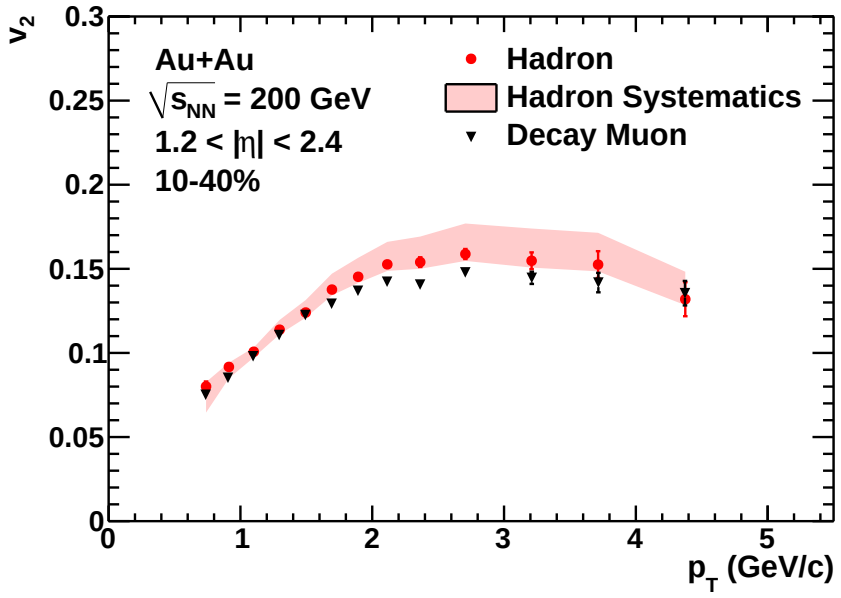

Figure 8.9: Forward rapidity hadron (circles) and decay muon (triangles) $v_2(p_T)$ for 10-40% centrality Au+Au collisions at $\sqrt{s_{NN}} = 200$ GeV. Statistical errors are shown by the bars and the hadron systematic errors by the band. Data values are provided in Tables D.17 and D.18.

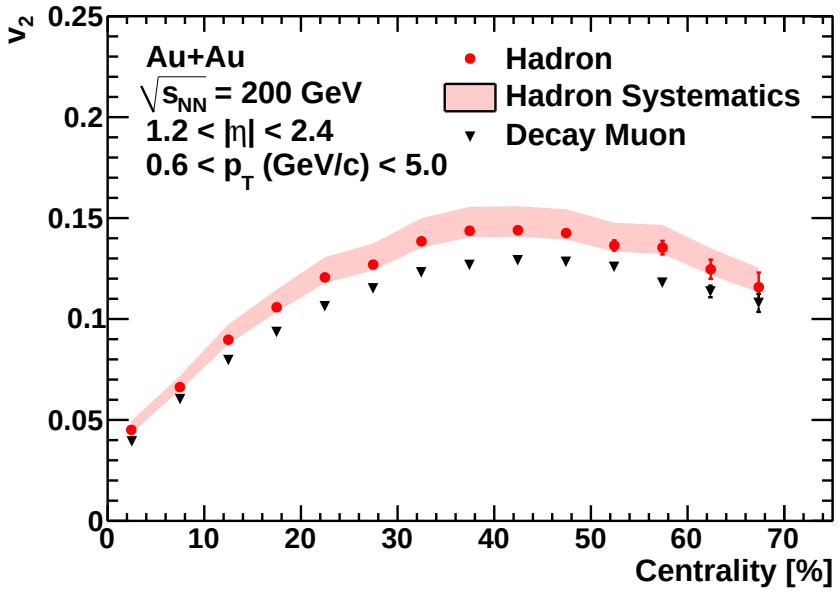

Figure 8.10: Forward rapidity hadron (circles) and decay muon (triangles) $v_2(centrality)$ from 0.6 GeV/c $< p_T <$ 5.0 GeV/c for Au+Au collisions at $\sqrt{s_{NN}} =$ 200 GeV. Statistical errors are shown by the bars and the hadron systematic errors by the band. Data values are provided in Tables D.19 and D.20.

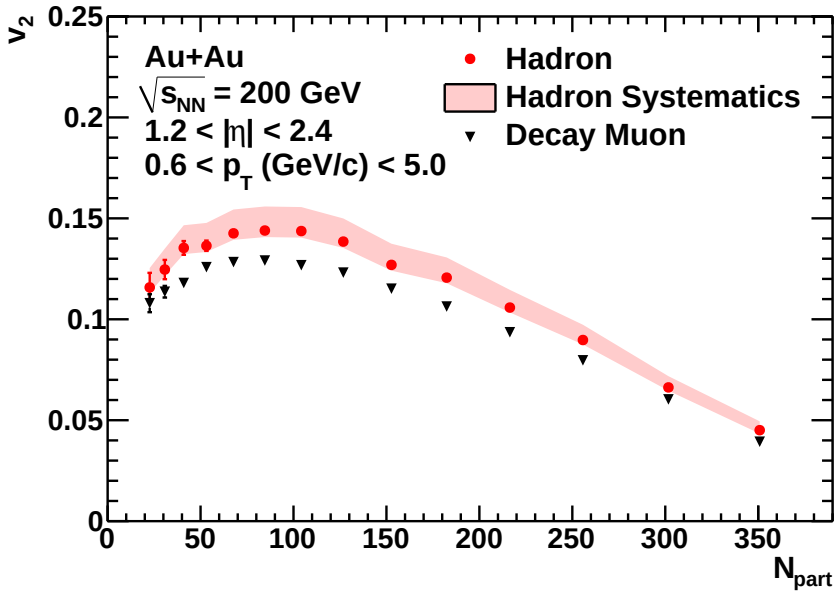

Figure 8.11: Forward rapidity hadron (circles) and decay muon (triangles) $v_2(N_{part})$ from 0.6 GeV/c $< p_T <$ 5.0 GeV/c for Au+Au collisions at $\sqrt{s_{NN}} =$ 200 GeV. Statistical errors are shown by the bars and the hadron systematic errors by the band. Data values are provided in Tables D.19 and D.20.

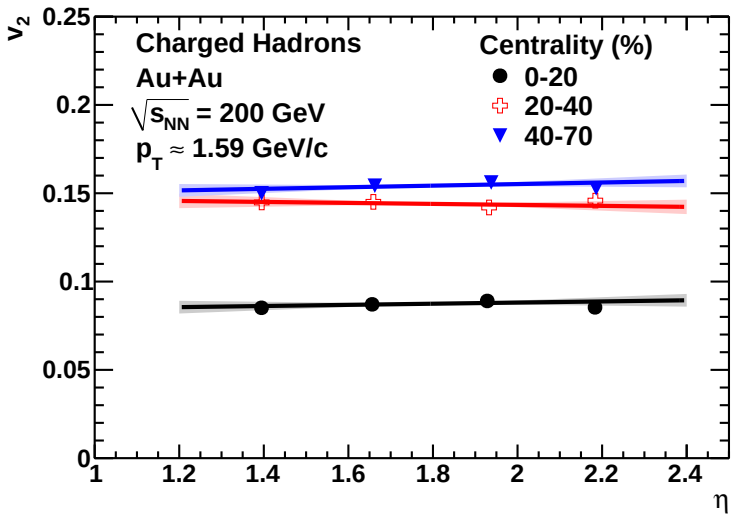

Figure 8.12: Forward rapidity hadron $v_2(\eta)$ from 0.6 GeV/c $< p_T <$ 5.0 GeV/c for Au+Au collisions at $\sqrt{s_{NN}} = 200$ GeV. The centrality ranges are 0-20% (circles), 20-40% (crosses), and 40-70% (triangles). The data points are shown with statistical errors only. Each centrality range is fit with a straight line, with the fits systematic error shown by the band. Data and fit values are provided in Tables D.21 and D.23.

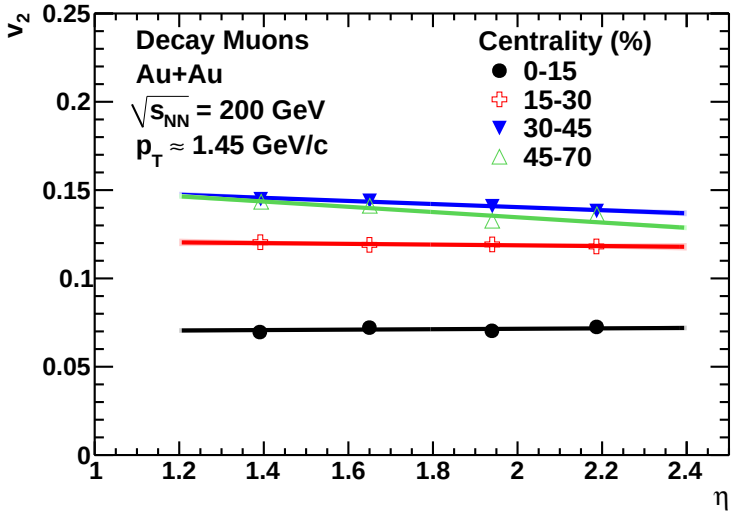

Figure 8.13: Forward rapidity decay muon $v_2(\eta)$ from 0.6 GeV/c $< p_T <$ 5.0 GeV/c for Au+Au collisions at $\sqrt{s_{NN}} = 200$ GeV. The centrality ranges are 0-15% (circles), 15-30% (crosses), 30-45% (closed triangles), and 45-70% (open triangles). The data points are shown with statistical errors only. Each centrality range is fit with a straight line, with the fits systematic error shown by the band, although some are not much wider than the fit line. Data and fit values are provided in Tables D.22 and D.23.

Chapter 9

Discussion

As shown in Fig. 1 and redisplayed here, PHOBOS and STAR have measured a significant decrease in v_2 at forward η for 0-40% and 10-40% centrality collisions, respectively. Figure 9.1 compares these results to a 0-40% centrality Muon Arm measurement. Recall from Sec. 7.1 that this measurement has a $\langle p_T \rangle(\eta)$ acceptance bias that significantly contributes to the signal decrease toward forward η. Notice in the figure that the Muon Arm results are also significantly higher than either STAR's or PHOBOS's. This is because of differences in the p_T ranges used. STAR uses 0.15 GeV/c $< p_T <$ 2.0 GeV/c and PHOBOS used a hit based method that didn't select events by p_T. The Muon Arms used 0.6 GeV/c $< p_T <$ 2.0 GeV/c. PHOBOS has additionally measured a decreasing $v_2(\eta)$ trend for 3-15%, 15-25%, and 25-50% centrality collisions, as shown in Fig. 3.16. *Ansäntze* have emerged speculating on the source of the STAR and PHOBOS signal behavior, including incomplete thermalization [100], late stage viscous effects [101], changing dynamics [102], a decrease in energy density [103], or a "softening" of the p_T spectrum, resulting in a reduced $\langle p_T \rangle$ [104].

The origin of the $v_2(\eta)$ results measured in this dissertation challenge the interpretation of the PHOBOS and STAR results by displaying a weaker η dependence on v_2 within $1.2 < |\eta| < 2.4$. For hadrons (Fig. 8.12), no significant η depen-

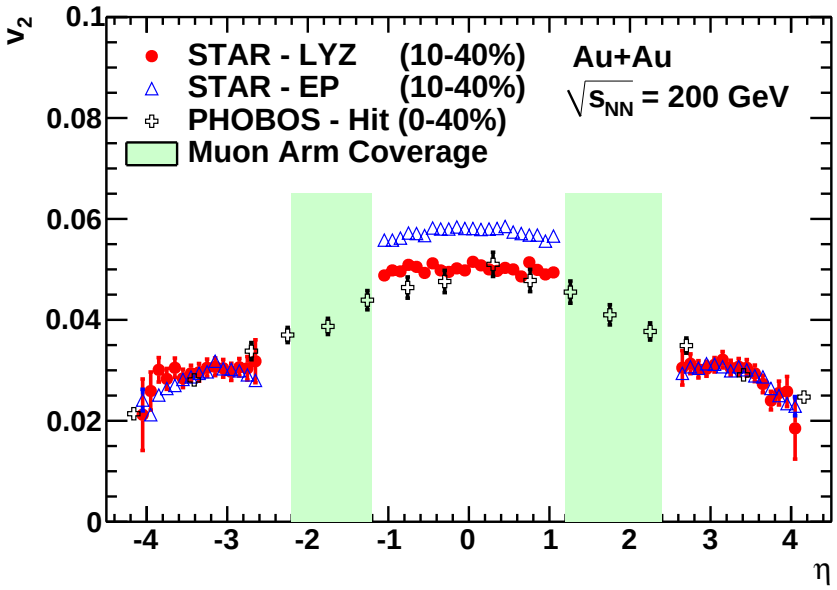

Figure 1: STAR and PHOBOS charged hadron $v_2(\eta)$ from $\sqrt{s_{NN}} = 200$ GeV Au+Au collisions [2, 3]. STAR results from 10-40% centrality collisions and 0.15 GeV/c $< p_T <$ 2.0 GeV/c are shown using the Lee-Yang Zero (LYZ) method (circles) and Event Plane (EP) method (triangles). PHOBOS results from 0-40% centrality collisions using an EP Hit-based (Hit) method requiring no p_T information are displayed using crosses. Only statistical errors are shown. The coverage of the Muon Arms at the nominal vertex is indicated by the green bands.

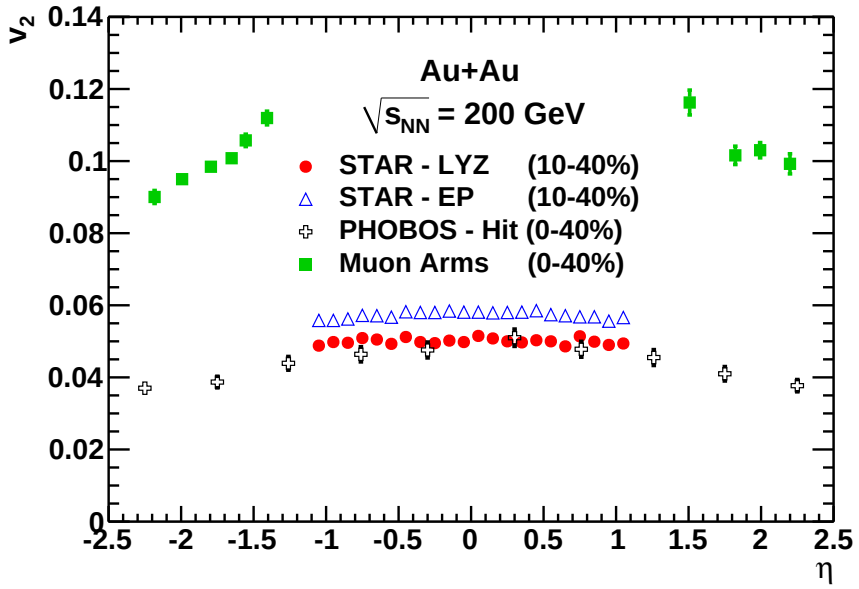

Figure 9.1: Charged hadron $v_2(\eta)$ from $\sqrt{s_{NN}} = 200$ GeV Au+Au collisions. STAR results [2] from 10-40% centrality collisions and 0.15 GeV/c $< p_T <$ 2.0 GeV/c are shown using the Lee-Yang Zero (LYZ) method (circles) and Event Plane (EP) method (triangles). PHOBOS measurements [3] from 0-40% centrality collisions using an EP Hit-based (Hit) method requiring no p_T information are displayed using crosses. Muon Arm results (squares) are displayed for 0-40% centrality collisions and 0.6 GeV/c $< p_T <$ 2.0 GeV/c using the standard EP method. Only statistical errors are shown.

dence is seen in the 0-20%, 20-40%, and 40-70% centrality ranges. For decay muons (Fig. 8.13), no η dependence is observed for the central 0-15% and 15-30% centralities, but a modest decrease is observed toward forward η for the more peripheral 30-45% and 45-70% collisions.

The difference in signal trends between hadrons and decay muons for peripheral events has not been determined, but may be explained by residual acceptance effects in combination with the knock-on particle effect of increasing the measured v_2 of lower p_T hadrons, as described in Sec 6.2. Despite having a p_T cutoff of 1.0 GeV/c in the $v_2(\eta)$ measurement, the more forward η bins still contain more low p_T particles than those closer to mid-rapidity (see Fig. 7.2). This could make them more susceptible to this knock-on effect than points closer to mid-rapidity. However, if this is the cause of the discrepancy it is not understood why the effect appears to be absent for central collisions, where the hadrons and decay muons agree on a flat $v_2(\eta)$ signal.

Regardless of this discrepancy, the reduced η dependence on v_2 for both hadrons and decay muons compared to the PHOBOS and STAR measurements is likely due to this analysis method's reduced susceptibility to the affects of a changing $\langle p_T \rangle$ (see Sec. 7.2 for method details), which the PHOBOS and STAR measurements do not account for. The extent of this influence would be most apparent in central collisions, where the Muon Arm measurements suggest there is little or no change in v_2 from mid-rapidity to at least $\eta = 2.4$. However, the PHOBOS 3-15% centrality data from Fig. 3.16 displays a roughly 8% reduction in v_2 within $|\eta| < 2$, which could arguably be attributed to a softening of the spectrum. If the v_2 is similar for

central collisions throughout $\eta < 2.4$, as indicated by the Muon Arm measurement, it would indicate a longitudinally extended thermalized medium with similar eccentricity and pressure gradients. Such behavior would counter the argument for late stage viscous effects or changing dynamics at forward η, at least out to the Muon Arm η region.

For peripheral collisions, the negative slopes of the decay muons toward forward η may be signaling the breakdown of complete thermalization, leading to a reduced v_2. The cause of this underdeveloped thermalization could be due to the decreased energy density of the smaller system. As shown in Fig. 9.2, the $dN/d\eta$ particle distribution, which essentially represents energy density, begins to decrease in the Muon Arm's η region. This could cause the formation of a medium that is too short lived to thermalize completely, or even too dilute to have the short mean free path lengths necessary for rapid binary interactions and complete thermalization before expansion. Conversely, the greater particle density of central collisions may be sufficiently high in the Muon Arm's η region to overcome any moderate decrease in particle density from mid-rapidity, allowing for complete thermalization to develop and no measurable decrease in v_2.

For peripheral collisions in Fig. 3.16, an indication of the magnitude of non-$\langle p_T \rangle$ related effects on the v_2 can be approximated from a signal comparison to the central collisions of the same figure. With Figs. 8.12 and 8.13 showing no loss in signal for central events toward forward η, and assuming similar changes in $\langle p_T \rangle$ for peripheral and central events, any additional decrease in v_2 for peripheral collisions in Fig. 3.16 beyond the 8% previously seen for the central collisions would be due

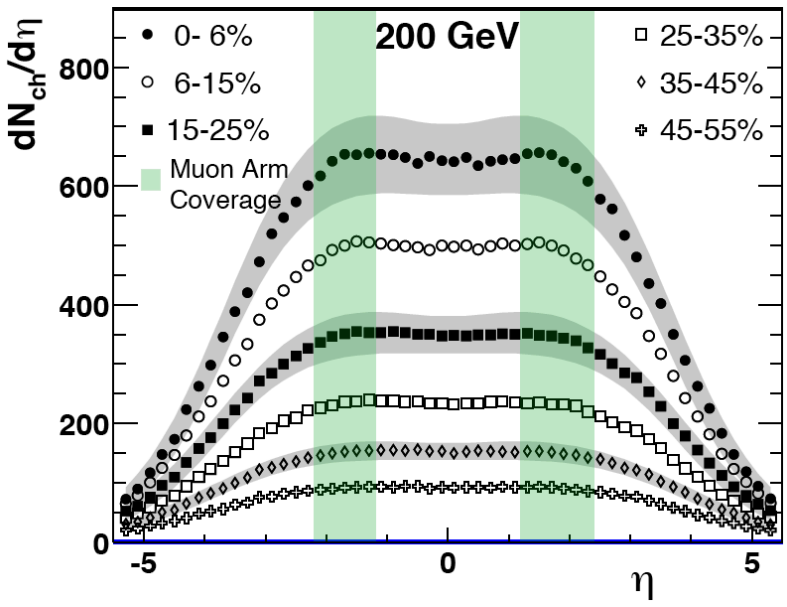

Figure 9.2: $dN/d\eta$ charged particle multiplicity distributions of 200 GeV Au+Au collisions as measured by PHOBOS for a number of centrality ranges. Statistical errors are negligible. Systematic errors for select centrality ranges are shown using gray bands [105]. The η coverage of the Muon Arms from the nominal vertex is shown by the green vertical bands.

to physics related effects such as incomplete thermalization. From Fig. 3.16, the v_2 of 25-50% collisions decreases roughly 15% from $\eta = 0 \rightarrow 2$. Subtracting from this value the previously assumed 8% due to a decreasing $\langle p_T \rangle$ leaves 7%, or $\sim$1/2, of the signal decrease due to medium changes and $\sim$1/2 due to a changing $\langle p_T \rangle$. This simplistic calculation is comparable to BRAHMS's conclusion in [104] that 2/3$^{\text{rds}}$ of the decreasing v_2 is due to a softening of the p_T spectrum, further indicating the non-trivial role the changing $\langle p_T \rangle$ plays in the $v_2(\eta)$ signal measured by PHOBOS and STAR.

An additional argument can be made for this by examining ATLAS [106] results from the Large Hadron Collider (LHC) [21], which has thus far collided lead (Pb) nuclei at 2.76 TeV. ATLAS has measured $v_2(\eta)$ within $|\eta| < 2.4$ for relatively

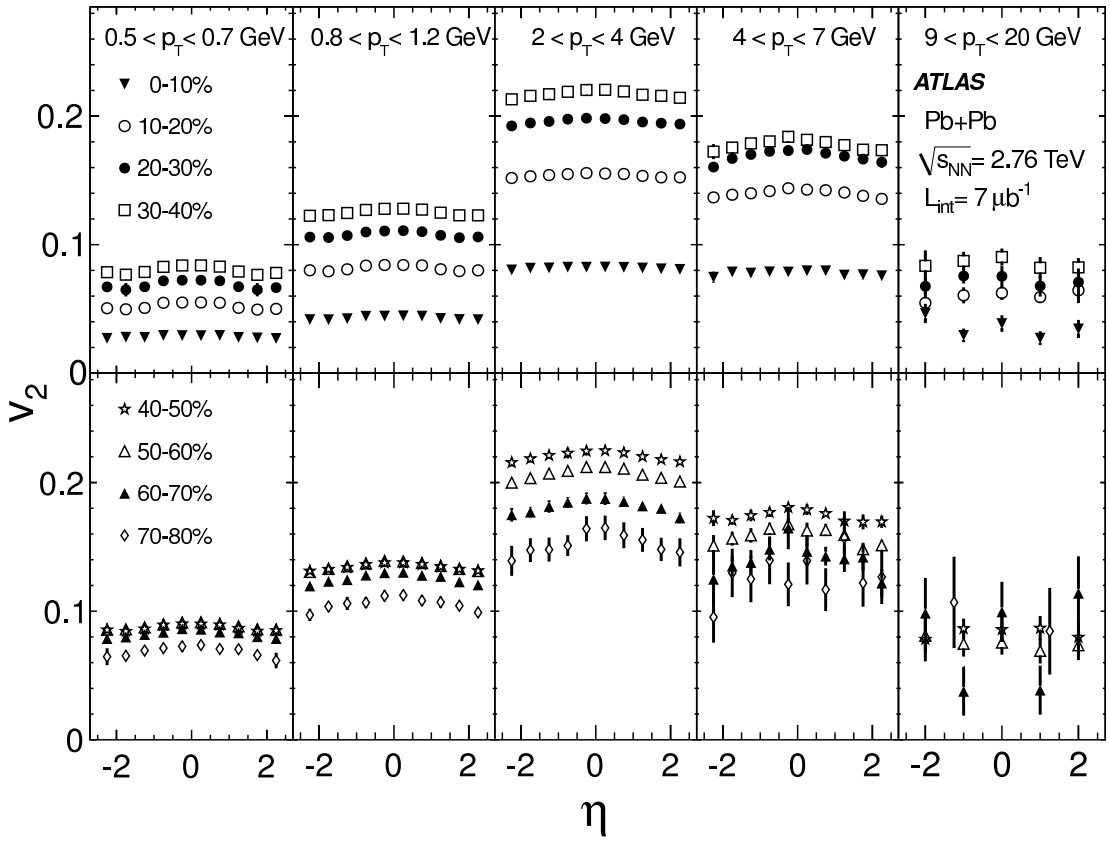

Figure 9.3: ATLAS $v_2(\eta, p_T)$ for 2.76 TeV Pb+Pb collisions. The measurement covers $|\eta| < 2.4$ and 0.5 GeV/c $< p_T <$ 20 GeV/c. The data is segmented in 10% centrality bins and five p_T bins to minimize the affects of a changing $\langle p_T \rangle$ on the signal. Errors show statistical and systematic errors added in quadrature [107].

narrow p_T ranges, reducing the affects of a changing $\langle p_T \rangle$. The results, shown in Fig. 9.3, display an essentially flat η dependence on v_2 for central collisions in the different p_T ranges. This is similar to the Muon Arm results, reinforcing the argument that the decrease in v_2 with increasing η for central events measured by PHOBOS is significantly dependent on a change in $\langle p_T \rangle$.

For increasingly peripheral events, a slightly more noticeable decrease in v_2 toward forward η is seen in the ATLAS data, similar to the Muon Arm measurement for decay muons. This behavior further indicates a growing change to the medium

of smaller systems toward forward η. In addition, the similar trends for both central and peripheral events between the ATLAS and Muon Arm data indicates that, despite the significant difference in beam energies, the two mediums have similar properties. This has been argued by others examining $v_2(p_T)$ in [107–109].

Further examination of the η dependence of v_2 can be done by comparing Muon Arm and mid-rapidity $v_2(p_T)$ measurements, and in particular PHENIX Central Arm mid-rapidity measurements from [39, 110], where $|\eta| < 0.35$ and EP = RXNP_NS. The advantage of this comparison is that both measurements use the same Run-7 data set, meaning they share the same beam conditions, EP detectors, and certain calibrations. The two measurements also used the standard EP method to measure v_2, further reducing differences caused by non-physics related issues.

Figure 9.4 shows the ratio of the $v_2(p_T)$ of the Muon Arms compared to the Central Arms for centrality ranges of 0-20%, 20-40%, and 40-60%. For 0-20%, a ratio near unity is observed for $p_T \gtrsim 1.5$ GeV/c, indicating similar degrees of eccentricity and thermalization at the two η's. This agrees with the lack of a $v_2(\eta)$ slope seen for central collisions in Figs. 8.12 and 8.13. The ratio increase below $p_T \approx 1.5$ GeV/c is likely due to knock-on particles artificially increasing the signal due to a decrease in their measured p_T as a result of an energy loss from a strong interaction in the initial absorber. These higher p_T particles can carry with them a stronger v_2 signal and thereby increase the measured v_2 at low p_T (see Sec 6.2). For the 20-40% and 40-60% collisions, a ratio < 1 is seen, with a $\sim$10-30% decrease from unity observed for the most peripheral bin. This trend agrees with the increasingly steeper slope for more peripheral collisions observed for decay muons in Fig. 8.13, further indicating

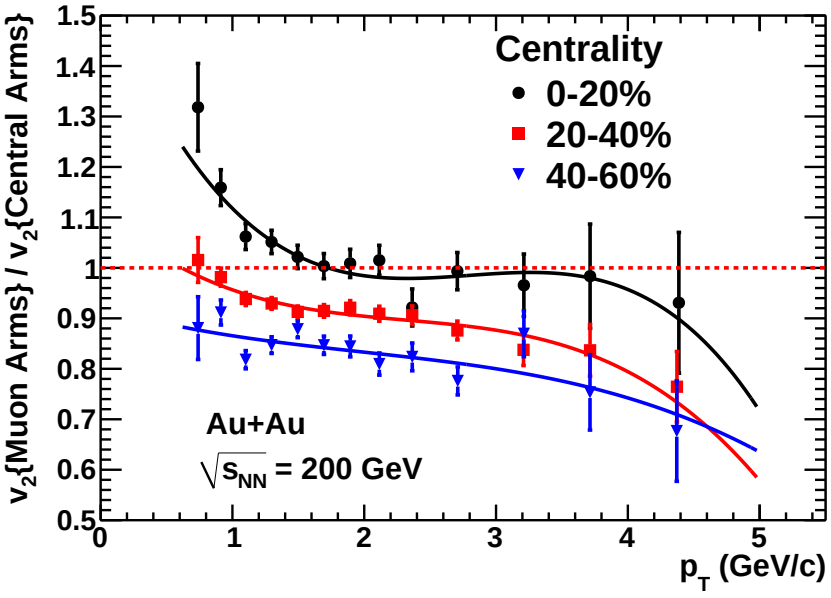

Figure 9.4: Charged hadron $v_2(p_T)$ ratio of Muon Arms compared to Central Arms [39, 110] for centralities of 0-20% (circles), 20-40% (squares), and 40-60% (triangles). Third order polynomial fits are shown to guide the eye. For clarity only statistical errors are shown.

that from mid-rapidity to the Muon Arm η region there is a growing change in the medium's properties for increasingly non-central collisions.

BRAHMS has also measured $v_2(p_T)$ at forward angles of $\eta \approx 1$ and 3 for 0-25% and 25-50% centralities using a spectrometer with a solid angle coverage of 0.8 millisteradian [111]. The 0-25% centrality results are shown in Fig. 9.5 along with similar PHENIX Central Arm and Muon Arm measurements. The systematic errors on the BRAHMS results (shown by the boxes) are a conservative 25% [112]. This consists of a 15% correlated error from the EP resolution (correlated meaning all points would move up and down the same ammount in unison) and a 10% error from run dependent EP flattening, which may be different for the two η ranges. The systematic error for the PHENIX Central Arm data is estimated to be $\sim$5%.

The BRAHMS data at $\eta \approx 1$ is consistent with the Central Arm and Muon Arm results of 10-15% and 0-25% centralities, respectively. This further reinforces the notion of a consistent v_2 signal toward forward η for central events. However, BRAHMS's $\eta \approx 3$ measurement shows a suppressed v_2 signal at low p_T, which then rises and eclipses the other measurements at $p_T \approx 2$ GeV/c. The suppressed signal at low p_T may signal a change in the medium's behavior despite its eventual rise above the other measurements. This is because the move upwards may be explained by the increased proton contribution to the particle composition from mid-rapidity [113] to forward angles [95], combined with the proton's larger v_2 signal than pions and kaons for $p_T \gtrsim 1.5$ GeV/c. This larger proton signal has been indicated by BRAHMS at forward rapidity in [99, 114] and displayed at mid-rapidity in Fig. 6.2(a).

For 25-50% centrality, shown in Fig. 9.6, BRAHMS's $\eta \approx 1$ measurement agrees with the Central Arm 35-40% data for $p_T \lesssim 1.5$ GeV/c and then rises above it for higher p_T. For $\eta \approx 3$, the BRAHMS data is again lower than the other measurements for $p_T \lesssim 1.5$ GeV/c, including the Muon Arm data of the same centrality, which itself is lower than the BRAHMS $\eta \approx 1$ and Central Arm data. This continues the previously seen trend of a decreasing v_2 signal toward forward η for non-central collisions.

The results discussed so far demonstrate the importance of taking centrality into account when trying to understand how v_2 evolves from mid to forward rapidity. To more explicitly demonstrate their difference, Fig. 9.7 directly compares $v_2(N_{part})$ from the Muon Arms to the PHENIX Central Arms and PHOBOS ($0 < \eta < 1.0$) mid-rapidity measurements. However, due to using a different p_T range than the

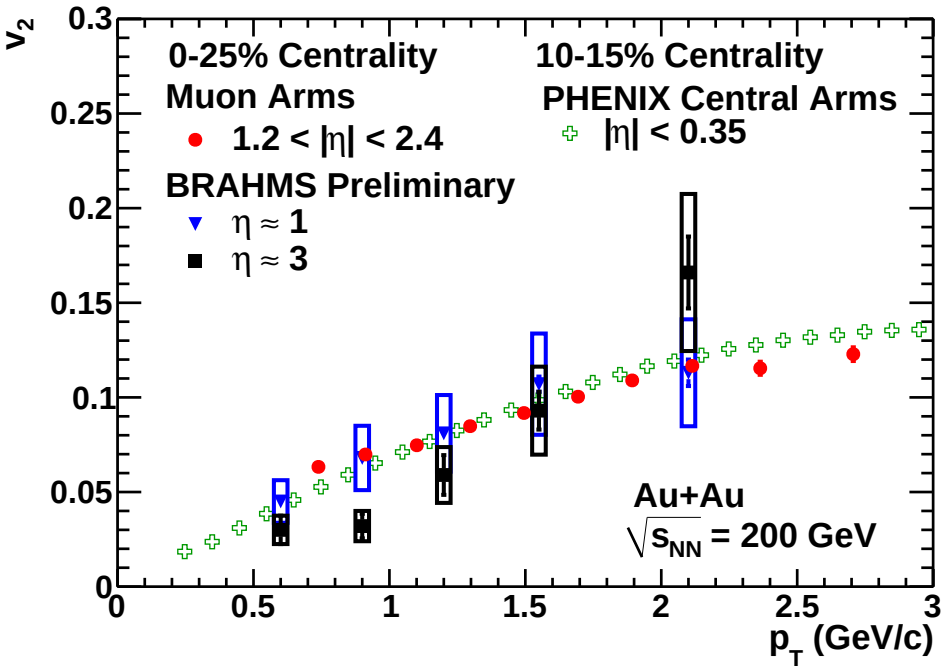

Figure 9.5: $v_2(p_T)$ for Muon Arms ($1.2 < |\eta| < 2.4$, circles), PHENIX Central Arms ($|\eta| < 0.35$, crosses) [39], and BRAHMS $\eta \approx 1$ (triangles) and $\eta \approx 3$ (squares) [99, 114]. The centrality range is 0-25% for the Muon Arm and BRAHMS measurements, while the Central Arm is 10-15%. Statistical errors are shown by the bars and for clarity systematic errors are shown only for BRAHMS by the boxes, which are conservatively estimated to be 25% [112]. The PHENIX Central Arm systematic errors are estimated to be ∼5%.

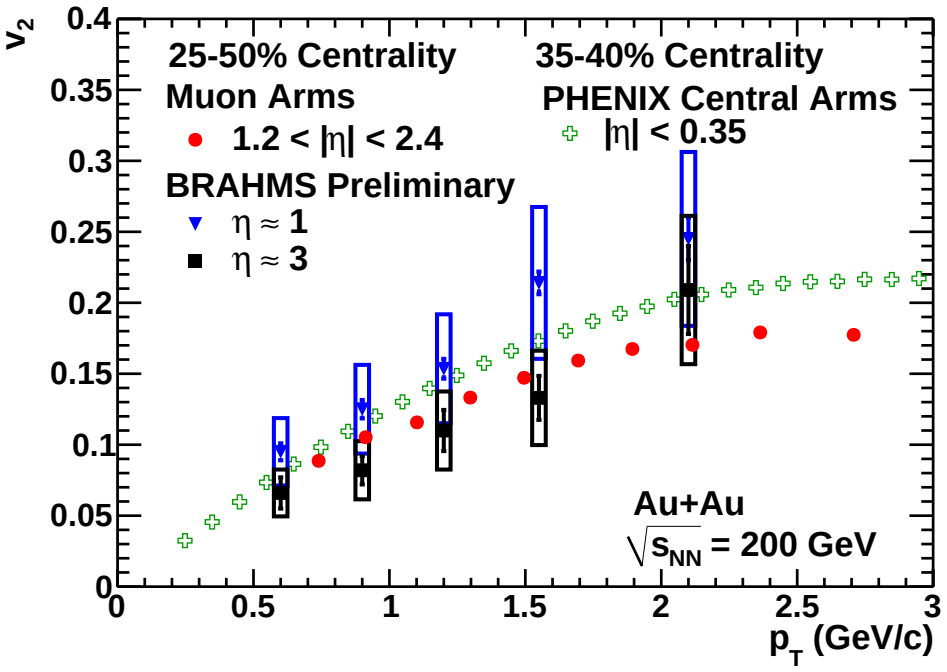

Figure 9.6: $v_2(p_T)$ of Muon Arms ($1.2 < |\eta| < 2.4$, circles), PHENIX Central Arms ($|\eta| < 0.35$, crosses) [39], and BRAHMS $\eta \approx 1$ (triangles) and $\eta \approx 3$ (squares) [99, 114]. The centrality range is 0-25% for the Muon Arm and BRAHMS measurements, while the Central Arm is 35-40%. Statistical errors are shown by the bars and for clarity systematic errors are shown only for BRAHMS by the boxes, which are conservatively estimated to be 25% [112]. The PHENIX Central Arm systematic errors are estimated to be $\sim$5%

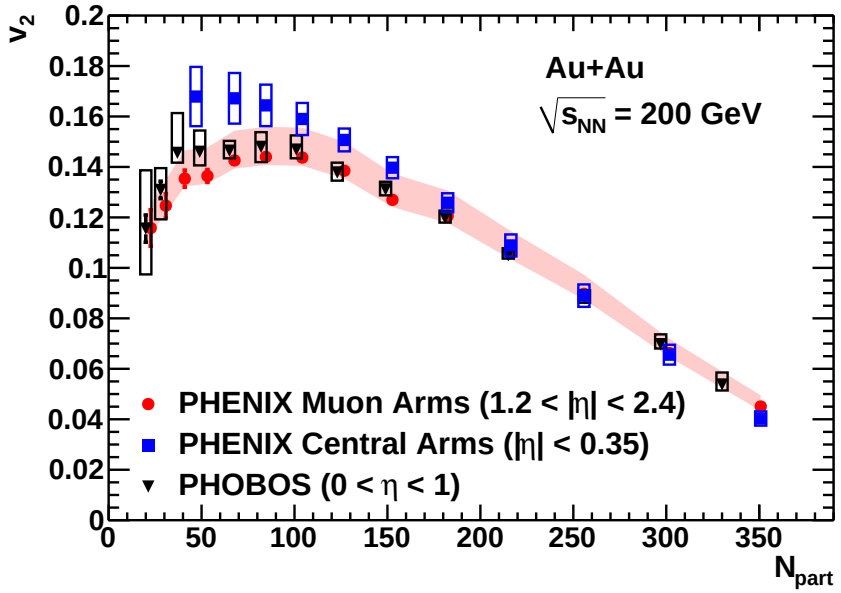

Figure 9.7: $v_2(N_{part})$ comparison between the Muon Arms (circles), PHENIX Central Arms (squares) [39], and PHOBOS (triangles) [15] for 200 GeV Au+Au collisions. The η and p_T ranges for the Muon Arms are $1.2 < |\eta| < 2.4$ and 0.6 GeV/c $< p_T <$ 5.0 GeV/c; Central Arms are $|\eta| < 0.35$ and 1.2 GeV/c $< p_T <$ 1.6 GeV/c; and PHOBOS are $0 < \eta < 1.0$ and $p_T <$ 4 GeV/c. The PHOBOS data is scaled by a factor of 2.16 to closely match the Muon Arm central collision values. The Central Arm data was not scaled. Statistical errors are shown by the bars. The systematic errors for the Muon Arms are shown by the band, with boxes used for the Central Arms and PHOBOS data.

Muon Arms (0.6 GeV/c $< p_T <$ 5.0 GeV/c), a scaling factor of 2.16 is applied to the PHOBOS data ($p_T <$ 4.0 GeV/c) to closely match its central collision v_2 values to those of the Muon Arms. A different p_T range is also used for the Central Arm data (1.2 GeV/c $< p_T <$ 1.6 GeV/c) but a scaling factor is not needed.

The comparison shows a good agreement in the signal shape for central collisions. However, a divergence from the Muon Arm data emerges at $N_{part} \approx 150$ for the Central Arms, approximately equivalent to a centrality of 25%. The shape of the PHOBOS data agrees with the Muon Arm measurement within errors throughout the N_{part} range. Although not a flawless juxtaposition due to the different p_T

ranges, the comparison does, nevertheless, show a consistent $v_2(N_{part})$ shape for central collisions between the different η measurements, followed by a divergence for most peripheral collisions between the Muon Arm and Central Arm measurements. This further indicates the emergence of a changing medium towards forward η for these smaller systems.

Chapter 10

Conclusion

Unidentified charged hadron and decay muon v_2 has been measured for 200 GeV Au+Au collisions within $1.2 < |\eta| < 2.4$ using the PHENIX Muon Arms. For $v_2(\eta)$, a consistent signal is observed for central collisions, indicating the creation of a longitudinally extended thermalized medium with similar eccentricity throughout. For peripheral collisions, no η dependence is observed for hadrons. However, for decay muons a modest decrease in v_2 toward forward η is measured and becomes more pronounced the more peripheral the centrality. This indicates a change in the medium's properties, possibly due to incomplete thermalization. These central and peripheral collision Muon Arm results challenge the interpretation of previous PHOBOS and STAR measurements that show a significant η dependence on v_2, thought from this analysis to be caused to a large extent by a changing $\langle p_T \rangle$.

The $v_2(p_T)$ was also measured within the Muon Arm η range and the hadron results show good agreement with PHENIX Central Arm results for central collisions and a decreasing Muon Arm/Central Arm v_2 signal ratio for increasingly peripheral collisions, agreeing with the $v_2(\eta)$ trends of decay muons. For hadron $v_2(p_T, \eta)$, good agreement is observed in 0-25% centrality collisions for the Central Arms, BRAHMS $\eta \approx 1$, and Muon Arm measurements. However, a difference is seen for BRAHMS's $\eta \approx 3$ measurement at low p_T, indicating that only at very forward angles does the

medium properties of central collisions change. For the corresponding 25-50% centrality measurements, a decreasing hadron $v_2(p_T)$ is observed toward forward η for the different measurements, providing further evidence of the changing properties of smaller systems approaching forward η. In addition, to underscore the repeatedly seen behavioral dichotomy of the consistent central and changing peripheral v_2 signals as a function of η, hadron $v_2(N_{part})$ was measured and compared to mid-rapidity Central Arm and PHOBOS results. This comparison shows a similar signal shape between the different measurements for central collisions, but a deviation for peripheral collisions.

Looking forward, it has been shown here that the measured $v_2(\eta)$ signal trend of 200 GeV Au+Au collisions largely depends on the system size and $\langle p_T \rangle$. However, it is unclear what role a changing particle composition toward forward η plays in the signal of unidentified charged hadrons, since different particles have different signal strengths and BRAHMS has shown in [95] that particle ratios change with η. Moreover, the change in v_2 signal for the different particle types toward forward η may not be the same. To shed light on this unknown, identified particle $v_2(p_T)$ measurements at forward η are needed. BRAHMS has already undertaken this measurement in [99, 114], which indicates $v_2(p_T)$ does decrease for the individual particle types at $\eta \approx 3$ compared to mid-rapidity, but the statistical errors are large. A higher statistics measurement over a broader η range and to higher p_T is needed for a more robust assessment. However, with the decommissioning of BRAHMS in 2006 it is unclear whether such a measurement will be done in the near future at RHIC, given that its two remaining experiments, PHENIX and STAR, have limited

detector coverage and particle identification capabilities at forward η.

With regard to improving any future analysis based on the method used in this dissertation, several advancements can be exploited. These include the increased statistics provided by newer data sets, such as Run-10, which contains roughly twice the Au+Au statistics of Run-7. From these larger data sets finner centrality, η, and p_T binning can be applied, along with an extension to higher p_T. Additionally, the recent installation for Run-12 of the Forward Silicon Vertex Detector (FVTX) [115], located in front of the initial absorber, should significantly improve particle tracking and reduce backgrounds. However, these improvements could be offset by the decommissioning of the RXNP, which was removed between Run-10 and 11 to make room for the FVTX. The FVTX is expected to have a similar EP resolution as the RXNP, but this needs to be confirmed with data. Also, the recent installation of additional absorber material in front of the MuTr [116] could offset any increase in statistics provided by later Runs, due to increased hadron absorption. The new absorber would also increase the measurement's lower p_T limit.

Going beyond 200 GeV Au+Au collisions, interesting insights into the created medium could be gained by examining lower energy collisions. For instance, PHENIX has recently collected Au+Au data at 62.4 and 39 GeV, where mid-rapidity v_2 measurements have yielded comparable results to 200 GeV measurements, as shown in Figs. 1.20 and 1.21. Is this consistency extended to forward angles, or does the v_2 of central collisions start to decrease in the Muon Arm η region before it does at mid-rapidity? If so, at what energy does this occur?

Additionally, this dissertation showed that system size is an important factor in

understanding v_2's evolution toward forward η. The larger the system size the more time available for the onset of thermalization and therefore a more comparable v_2 signal with mid-rapidity. But what role does eccentricity play? Interesting insights into how the interplay of system size and eccentricity affect the medium was first examined by PHOBOS in [15, 17, 117, 118] with Run-5 Cu+Cu collisions. Their results show that these two factors do indeed play a significant role in v_2 at mid-rapidity by demonstrating that dissimilar Au+Au and Cu+Cu v_2 results agree very well if scaled by their participant eccentricity while matching the N_{part} of the two systems. It would be interesting to see if this scaling behavior holds at forward rapidity or does it break down? Furthermore, it is anticipated that the ongoing Run-12 at RHIC will deliver novel collision systems of Cu+Au and U+U, providing opportunities for a deeper understanding of the dependence of system size on v_2 and other variables. By studying v_2 at forward η for these different collision systems and energies, additional experimental and theoretical insights will be gained that will provide a deeper understanding of the created medium's properties.

Appendix A

Rapidity and Pseudorapidity

Rapidity (y) is a dimensionless variable that describes the rate at which a particle moves with respect to a reference point along the line of motion. For collider experiments, the chosen reference point is the nominal collision vertex and the line of motion is the direction of the z-axis. Rapidity is mathematically defined as

$$\mathrm{y} = \frac{1}{2} \ln \frac{1 + \beta \cos\theta}{1 - \beta \cos\theta} = \frac{1}{2} \ln \frac{1 + \beta_z}{1 - \beta_z}, \tag{1.3}$$

where $\beta = v/c$, velocity divided by the speed of light, and θ is the particle's polar angle with respect to the z-axis. Figure A.1 shows graphically how rapidity is related to β. Note that a particle can have a positive or negative rapidity depending on its direction in velocity compared to the reference point. Although a particle's potential rapidity range is unlimited, in practice its logarithmic dependence leads to small numeric values. For instance, the rapidity of RHIC's 100 GeV Au ion beam is only 5.36 despite traveling at 99.996% the speed of light.

The advantage of using rapidity to describe a particle's rate of motion is that, unlike velocity, rapidity is additive even for velocities approaching the speed of light. In other words

$$\mathrm{y} = \mathrm{y}' + \mathrm{y}_0, \tag{A.1}$$

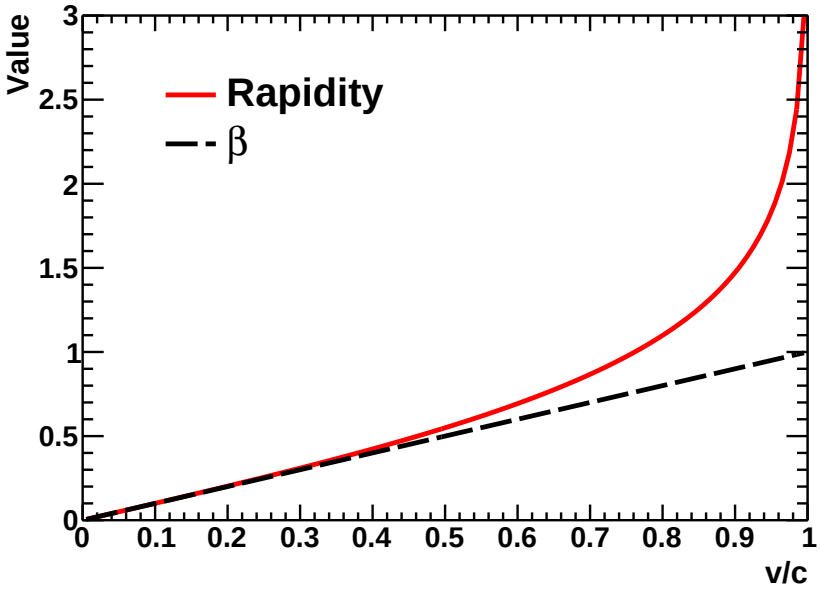

Figure A.1: Relation between rapidity (solid) and β (dashed) as a function of v/c.

where y_0 is the nominal vertex's rapidity, y' the rapidity of the traversing particle, and y their sum. This leads to the consequence that differences in rapidity are invariant. That is to say, the difference in the rapidities of two particles in one frame of reference is the same in all other frames of reference. For instance, using equation A.1, the rapidities of two particles A and B are

$$y_A = y'_A + y_0 \tag{A.2a}$$

$$y_B = y'_B + y_0 \tag{A.2b}$$

Subtracting A.2b from A.2a yields

$$y_A - y_B = y'_A - y'_B \tag{A.3}$$

demonstrating the invariant property of rapidity by the cancelation of y_0, the rapidity of the "observation" reference frame. Hence rapidity differences are invariant.

Despite its usefulness, rapidity has the disadvantage of being difficult to measure experimentally due to the need for particle identification to determine its mass. This is overcome for ultrarelativistic particles ($\beta \approx 1$), making a particle's rapidity only dependent on θ (see middle term of Eq. 1.3). This allows for the introduction of a substitute variable for rapidity called pseudorapidity (η), which is similarly defined as

$$\eta = \frac{1}{2} \ln \frac{1 + \cos\theta}{1 - \cos\theta} \tag{1.4}$$

and is only dependent on the θ angle of the emitted particle. For ultrarelativistic particles, rapidity and η are nearly indistinguishable quantities except at angles near $0°$ and $180°$. For slower particles, differences emerge between the two variables. Figure A.2 compares rapidity and η as a function of θ with various β values used in calculating the rapidity functions. For more details on rapidity and η see [119], where much of the information presented here is borrowed.

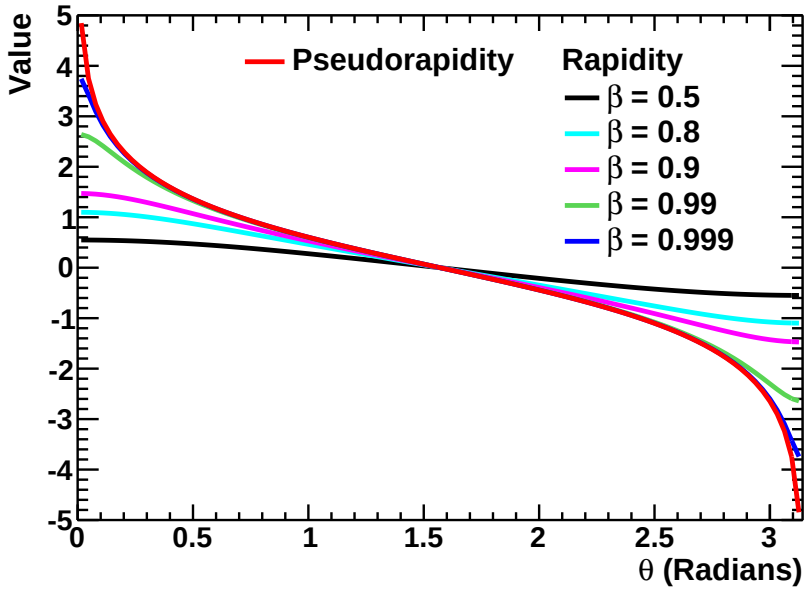

Figure A.2: Relation between rapidity and pseudorapidity as a function of θ. For rapidity, different values of β are used. See legend for details.

Appendix B

Lorentz Contraction

Einstein's special and general theories of relativity explain that our observation or measurement of things traveling at very high speeds (> 0.1c) is very much dependent on our frame of reference. For instance, at RHIC and other heavy-ion accelerators where nuclei travel at nearly the speed of light, an effect called length contraction or *Lorentz contraction* occurs to the moving nuclei's length when measured in the laboratory's reference frame. This contraction is described by the Lorentz factor $\gamma = 1/\sqrt{1-\beta^2}$, where $\beta = v/c$, velocity divided by the speed of light. The relationship between β, called the speed parameter, and γ is shown in Fig. B.1.

At RHIC, γ can be calculated for accelerated Au nuclei using $E = \gamma\langle m\rangle c^2$, where the beam energy per nucleon (E) is 100 GeV and the average nucleon mass ($\langle m\rangle$) is 0.9390 GeV/c^2. This results in $\gamma = 106.5$. For these relativistic Au nuclei, the measured length L in the laboratory's reference frame is calculated by $L = L_0/\gamma$, where L_0 is the length of the nuclei when at rest. For Au, L_0 is 14 fm, resulting in a length L at RHIC of 0.1315 fm.

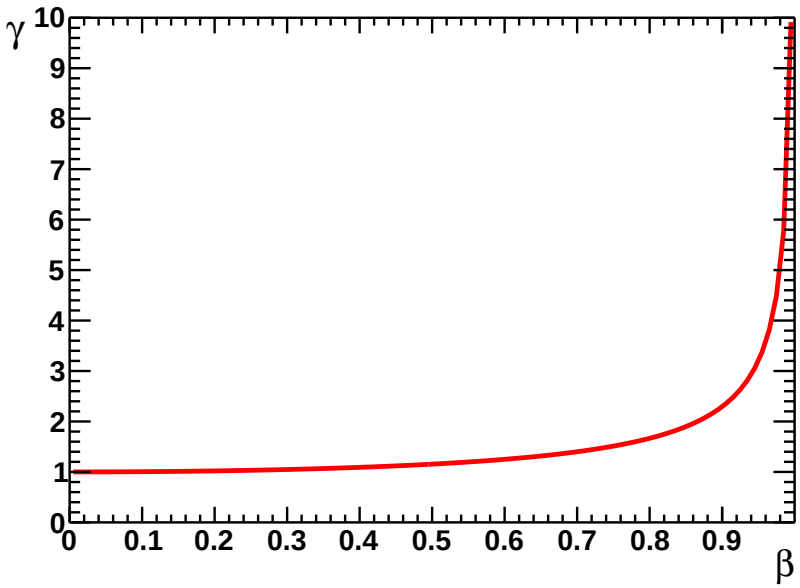

Figure B.1: Relation between Lorentz factor (γ) and the speed parameter (β).

Appendix C

Luminosity

Beam luminosity or *instantaneous luminosity* ($\mathscr{L}$) is a parameter used to characterize the effectiveness of colliding beams. Mathematically it is defined as [4]

$$\mathscr{L} = fn\frac{N_1 N_2}{4\pi\sigma_x\sigma_y} = f'\frac{N_1 N_2}{4\pi\sigma_x\sigma_y}, \tag{C.1}$$

where N_1 and N_2 are the number of particles in each beam bunch, σ_x and σ_y are the x and y transverse bunch profiles, respectively, n is the number of bunches in either beam, and f is the beam's revolution frequency. The product of f and n can be combined into f', *i.e.* $f' = fn$, which is simply the bunch crossing frequency. This luminosity definition assumes each beam has the same number of bunches, those bunches have the same transverse profile, the profiles are independent of position along the bunch, and the particle distributions are not altered durring bunch crossings. Luminosity is generally expressed in units of $\mathrm{cm}^{-2}\ \mathrm{s}^{-1}$ or $\mathrm{b}^{-1}\ \mathrm{s}^{-1}$, where a barn (b) = $10^{-24}\ \mathrm{cm}^2$. After an accelerator's buckets are fully populated with bunches, the luminosity can still be increased by either increasing the number of particles in each bunch or decreasing the bunch's transverse profile.

Of particular importance to a collider Run is the *integrated luminosity* ($\mathscr{L}_i$) or *delivered luminosity* defined as the integral of the instantaneous luminosity over time, *i.e.* $\mathscr{L}_i = \int \mathscr{L}\ dt$. It is generally expressed in units of cm^{-2} or b^{-1}. In

addition to the previously mentioned beam improvements, the integrated luminosity can be improved by increasing the beam's lifetime via decreasing beam loss or beam degradation, as well as decreasing the turn around time between stores.

In practice, it is impossible for an experiment to archive to disk all of the delivered luminosity. The amount that is archived is called the *collected* or *recorded luminosity* ($\mathscr{L}_r$), and is defined for min-bias collisions as

$$\mathscr{L}_r = \frac{N_{MB}}{\sigma_{NN}}, \tag{C.2}$$

where N_{MB} is the number of min-bias events recorded and σ_{NN} is the inelastic nucleon-nucleon cross section, which depends on colliding species and collision energy. Taking into account the min-bias trigger efficiency (ϵ_{MB}) yields

$$\mathscr{L}'_r = \frac{N_{MB}}{\epsilon_{MB}\sigma_{NN}}, \tag{C.3}$$

which can be an essential calculation for certain analyses such as those determining a particle's invariant yield. For $\sqrt{s_{NN}} = 200$ GeV Au+Au collisions $\sigma_{NN} = 6.85$ b and the PHENIX min-bias trigger efficiency is $\epsilon_{MB} \approx 93\%$. For more information about min-bias events and the PHENIX min-bias trigger efficiency see Sec. 2.2.1.1 and 4.2.2, respectively. Aside from the previously mentioned improvements, increasing an experiments recorded luminosity can be done by decreasing the bunch's longitudinal profile so more collisions occur in the experiments acceptable vertex region. It can also be accomplished by improving the trigger efficiency through

experimental upgrades, or decreasing DAQ dead time, *i.e.* the time the DAQ isn't recording events because of a bottleneck in the system.

Another luminosity term called *sampled luminosity* is used when the trigger rate is larger than the DAQ's maximum recording rate. In these instances the DAQ triggers are pre-scaled to only record a subset or sample of the events that pass the trigger requirements.

Appendix D

Data Tables

All data is for unidentified charged hadrons or decay muons from $\sqrt{s_{NN}} = 200$ GeV Au+Au collisions within $1.2 < |\eta| < 2.4$ and between 0.6 GeV/c $< p_T <$ 5.0 GeV/c. See each table description for additional details.

Table D.1: Hadron $v_2(p_T)$ for 0-70% Centrality from Fig. 8.1

p_T	v_2	Stat. Err	Sys. Err. High	Sys. Err. Low
0.739273	0.0746007	0.00250043	0.00239495	0.01478064
0.912194	0.0865203	0.00122354	0.00258111	0.00675983
1.100947	0.0938118	0.00103224	0.00268876	0.00357704
1.297174	0.1076161	0.00106335	0.00594363	0.00303208
1.495170	0.1194817	0.00118680	0.00765041	0.00340772
1.694125	0.1283380	0.00139136	0.00935968	0.00368503
1.893385	0.1372071	0.00168199	0.01124137	0.00395339
2.114319	0.1428685	0.00188555	0.01310532	0.00412718
2.364075	0.1474336	0.00244956	0.01517533	0.00427085
2.707464	0.1500122	0.00253380	0.01776594	0.00435753
3.210346	0.1494430	0.00422012	0.01914812	0.00435797
3.713051	0.1417266	0.00675734	0.01815943	0.00415148
4.378063	0.1223322	0.00854979	0.01567442	0.00360715

Table D.2: Decay Muon $v_2(p_T)$ for 0-70% Centrality from Fig. 8.1

p_T	v_2	Stat. Err
0.736351	0.0704113	0.00250043
0.905296	0.0802570	0.00122354
1.095939	0.0925509	0.00103224
1.293647	0.1039638	0.00106335
1.492329	0.1135947	0.00118680
1.691695	0.1199471	0.00139136
1.891673	0.1258410	0.00168199
2.112607	0.1320210	0.00188555
2.363142	0.1330310	0.00244956
2.705896	0.1384152	0.00253380
3.210144	0.1327053	0.00422012
3.715215	0.1291919	0.00675734
4.374490	0.1259232	0.00854979

Table D.3: Hadron $v_2(p_T)$ for 0-20% Centrality from Fig. 8.2

p_T	v_2	Stat. Err	Sys. Err. High	Sys. Err. Low
0.738890	0.0581383	0.00382587	0.00327993	0.01366445
0.911724	0.0620485	0.00190094	0.00350053	0.00681682
1.100658	0.0671247	0.00161683	0.00378691	0.00450883
1.296879	0.0764314	0.00168082	0.00642514	0.00431196
1.494866	0.0834267	0.00188909	0.00780925	0.00470660
1.693741	0.0902002	0.00223590	0.00928327	0.00508874
1.893079	0.0980414	0.00271830	0.01099249	0.00553111
2.114088	0.1055223	0.00307423	0.01288171	0.00595315
2.363893	0.1011691	0.00402549	0.01350007	0.00570756
2.706387	0.1138101	0.00422486	0.01696798	0.00642072
3.211130	0.1116609	0.00714239	0.01775242	0.00629947
3.713489	0.1100699	0.01154139	0.01752919	0.00620971
4.387072	0.0965045	0.01443072	0.01540122	0.00544441

Table D.4: Decay Muon $v_2(p_T)$ for 0-20% Centrality from Fig. 8.2

p_T	v_2	Stat. Err
0.735616	0.0502654	0.00382587
0.905275	0.0567825	0.00190094
1.096236	0.0671049	0.00161683
1.293761	0.0749173	0.00168082
1.492347	0.0836148	0.00188909
1.691686	0.0882295	0.00223590
1.891513	0.0930807	0.00271830
2.112333	0.0992387	0.00307423
2.363145	0.0980764	0.00402549
2.704592	0.1060589	0.00422486
3.209154	0.0939923	0.00714239
3.715271	0.0923106	0.01154139
4.376468	0.0986187	0.01443072

Table D.5: Hadron $v_2(p_T)$ for 20-40% Centrality from Fig. 8.3

p_T	v_2	Stat. Err	Sys. Err. High	Sys. Err. Low
0.739510	0.0863103	0.00377060	0.00379263	0.01690102
0.912553	0.1000333	0.00182814	0.00333126	0.00758422
1.101371	0.1116111	0.00153694	0.00314841	0.00399757
1.297477	0.1257152	0.00157366	0.00665246	0.00325228
1.495379	0.1370644	0.00175115	0.00845919	0.00374663
1.694492	0.1494271	0.00203844	0.01055208	0.00420381
1.893387	0.1606862	0.00245746	0.01279334	0.00458969
2.114405	0.1674650	0.00274532	0.01497421	0.00484779
2.364046	0.1738240	0.00355308	0.01748964	0.00509625
2.706750	0.1725933	0.00365959	0.02004101	0.00513214
3.208561	0.1643925	0.00609918	0.02068336	0.00497593
3.713188	0.1587260	0.00971188	0.01997041	0.00490606
4.372512	0.1355421	0.01234199	0.01705349	0.00426716

Table D.6: Decay Muon $v_2(p_T)$ for 20-40% Centrality from Fig. 8.3

p_T	v_2	Stat. Err
0.736537	0.0838549	0.00377060
0.905451	0.0949117	0.00182814
1.095978	0.1086495	0.00153694
1.293710	0.1237100	0.00157366
1.492420	0.1357158	0.00175115
1.691767	0.1433697	0.00203844
1.891818	0.1508093	0.00245746
2.112790	0.1569447	0.00274532
2.363074	0.1564568	0.00355308
2.706508	0.1595734	0.00365959
3.210461	0.1595540	0.00609918
3.716306	0.1580641	0.00971188
4.372439	0.1508137	0.01234199

Table D.7: Hadron $v_2(p_T)$ for 40-60% Centrality from Fig. 8.4

p_T	v_2	Stat. Err	Sys. Err. High	Sys. Err. Low
0.739584	0.0901401	0.00636457	0.00730040	0.01852508
0.912575	0.1118200	0.00303676	0.00644467	0.00956221
1.100989	0.1165905	0.00256695	0.00525602	0.00530653
1.297269	0.1362528	0.00264738	0.00895224	0.00483892
1.495449	0.1553884	0.00294096	0.01109696	0.00571026
1.694236	0.1610757	0.00344129	0.01293668	0.00631304
1.893933	0.1695945	0.00414356	0.01514722	0.00689398
2.114541	0.1694402	0.00459491	0.01679395	0.00702348
2.364342	0.1771863	0.00591447	0.01954618	0.00754273
2.709504	0.1689920	0.00602102	0.02126161	0.00741253
3.211269	0.1867076	0.00972512	0.02530155	0.00859739
3.712828	0.1571578	0.01554753	0.02129713	0.00750816
4.371148	0.1346841	0.01976474	0.01825163	0.00709323

Table D.8: Decay Muon $v_2(p_T)$ for 40-60% Centrality from Fig. 8.4

p_T	v_2	Stat. Err
0.737588	0.0928433	0.00636457
0.905156	0.1062820	0.00303676
1.095305	0.1220420	0.00256695
1.293327	0.1358436	0.00264738
1.492215	0.1443608	0.00294096
1.691562	0.1516490	0.00344129
1.891839	0.1558408	0.00414356
2.112838	0.1650212	0.00459491
2.363309	0.1648189	0.00591447
2.707514	0.1704443	0.00602102
3.211520	0.1674020	0.00972512
3.713537	0.1593473	0.01554753
4.374788	0.1285249	0.01976474

Table D.9: Hadron $v_2(p_T)$ for 20-60% Centrality from Fig. 8.5

p_T	v_2	Stat. Err	Sys. Err. High	Sys. Err. Low
0.739538	0.0875321	0.00327133	0.00454168	0.01712927
0.912561	0.1038494	0.00157919	0.00386051	0.00786050
1.101226	0.1132011	0.00132910	0.00337837	0.00404030
1.297399	0.1290503	0.00136353	0.00688334	0.00331547
1.495405	0.1428556	0.00151610	0.00879867	0.00391163
1.694396	0.1530956	0.00176794	0.01079192	0.00438088
1.893592	0.1634876	0.00213053	0.01299585	0.00479085
2.114456	0.1680873	0.00237632	0.01500874	0.00501187
2.364159	0.1748931	0.00307038	0.01757524	0.00531343
2.707820	0.1713990	0.00315443	0.01988080	0.00531539
3.209640	0.1719027	0.00520478	0.02160668	0.00548751
3.713043	0.1581664	0.00831215	0.01988015	0.00519341
4.371966	0.1352152	0.01055537	0.01699538	0.00462574

Table D.10: Decay Muon $v_2(p_T)$ for 20-60% Centrality from Fig. 8.5

p_T	v_2	Stat. Err
0.736889	0.0863703	0.00327133
0.905351	0.0981662	0.00157919
1.095754	0.1123860	0.00132910
1.293585	0.1270277	0.00136353
1.492353	0.1380473	0.00151610
1.691701	0.1455921	0.00176794
1.891825	0.1521553	0.00213053
2.112805	0.1591181	0.00237632
2.363151	0.1587297	0.00307038
2.706841	0.1625753	0.00315443
3.210817	0.1617547	0.00520478
3.715357	0.1584255	0.00831215
4.373248	0.1443578	0.01055537

Table D.11: Hadron $v_2(p_T)$ for 0-25% Centrality from Fig. 8.6

p_T	v_2	Stat. Err	Sys. Err. High	Sys. Err. Low
0.738925	0.0632881	0.00336734	0.00283553	0.01389793
0.911838	0.0698391	0.00167022	0.00312904	0.00675359
1.100749	0.0747018	0.00141471	0.00334691	0.00412636
1.296969	0.0847939	0.00146372	0.00611953	0.00379907
1.494968	0.0917547	0.00164112	0.00746603	0.00411094
1.693864	0.1003664	0.00193677	0.00908166	0.00449677
1.893013	0.1089748	0.00234790	0.01085353	0.00488245
2.114043	0.1166592	0.00264931	0.01277227	0.00522674
2.363998	0.1154025	0.00345918	0.01393717	0.00517044
2.706268	0.1228478	0.00362003	0.01675087	0.00550402
3.210854	0.1230490	0.00612049	0.01798566	0.00551303
3.713639	0.1197436	0.00981672	0.01751789	0.00536494
4.383277	0.1007996	0.01234543	0.01476147	0.00451618

Table D.12: Decay Muon $v_2(p_T)$ for 0-25% Centrality from Fig. 8.6

p_T	v_2	Stat. Err
0.735716	0.0563063	0.00336734
0.905318	0.0631503	0.00167022
1.096208	0.0734647	0.00141471
1.293750	0.0828604	0.00146372
1.492359	0.0919398	0.00164112
1.691721	0.0974191	0.00193677
1.891507	0.1029504	0.00234790
2.112419	0.1096077	0.00264931
2.363184	0.1090270	0.00345918
2.704800	0.1145600	0.00362003
3.209306	0.1079073	0.00612049
3.715167	0.1007074	0.00981672
4.374820	0.1117986	0.01234543

Table D.13: Hadron $v_2(p_T)$ for 25-50% Centrality from Fig. 8.7

p_T	v_2	Stat. Err	Sys. Err. High	Sys. Err. Low
0.739624	0.0886168	0.00387410	0.00449151	0.01745844
0.912662	0.1052734	0.00186528	0.00394234	0.00810716
1.101318	0.1157267	0.00156868	0.00356438	0.00428310
1.297405	0.1332018	0.00160807	0.00727375	0.00359785
1.495425	0.1471604	0.00178596	0.00925794	0.00420402
1.694346	0.1592975	0.00207898	0.01143924	0.00473638
1.893674	0.1674310	0.00250923	0.01353018	0.00507897
2.114625	0.1703162	0.00279463	0.01543244	0.00525130
2.364033	0.1790932	0.00360859	0.01823357	0.00561426
2.707833	0.1774109	0.00369948	0.02081216	0.00566768
3.208902	0.1708134	0.00609446	0.02169510	0.00560022
3.712152	0.1634433	0.00980350	0.02075901	0.00549427
4.375023	0.1381577	0.01238540	0.01754747	0.00480470

Table D.14: Decay Muon $v_2(p_T)$ for 25-50% Centrality from Fig. 8.7

p_T	v_2	Stat. Err
0.736851	0.0875478	0.00387410
0.905358	0.1007959	0.00186528
1.095818	0.1166143	0.00156868
1.293624	0.1307268	0.00160807
1.492435	0.1432495	0.00178596
1.691730	0.1504334	0.00207898
1.891950	0.1562249	0.00250923
2.112816	0.1625042	0.00279463
2.363094	0.1625414	0.00360859
2.706902	0.1697805	0.00369948
3.211115	0.1637169	0.00609446
3.716502	0.1719761	0.00980350
4.373101	0.1487689	0.01238540

Table D.15: Hadron $v_2(p_T)$ for 0-60% Centrality from Fig. 8.8

p_T	v_2	Stat. Err	Sys. Err. High	Sys. Err. Low
0.739232	0.0747248	0.00250216	0.00242650	0.01484206
0.912179	0.0862950	0.00122418	0.00261128	0.00678476
1.100972	0.0939804	0.00103279	0.00273652	0.00362979
1.297170	0.1073366	0.00106369	0.00598110	0.00307936
1.495172	0.1186071	0.00118692	0.00765287	0.00344249
1.694118	0.1278343	0.00139148	0.00938596	0.00373392
1.893377	0.1374925	0.00168203	0.01133253	0.00402938
2.114305	0.1436307	0.00188526	0.01324604	0.00421954
2.364051	0.1466314	0.00244891	0.01516504	0.00431897
2.707253	0.1498127	0.00253422	0.01781616	0.00442441
3.210217	0.1499229	0.00422001	0.01928352	0.00444402
3.713216	0.1408695	0.00677066	0.01811904	0.00419338
4.377986	0.1211659	0.00856003	0.01558471	0.00362944

Table D.16: Decay Muon $v_2(p_T)$ for 0-60% Centrality from Fig. 8.8

p_T	v_2	Stat. Err
0.736284	0.0701332	0.00250216
0.905316	0.0800169	0.00122418
1.095979	0.0922751	0.00103279
1.293668	0.1035907	0.00106369
1.492350	0.1134355	0.00118692
1.691694	0.1197336	0.00139148
1.891678	0.1256547	0.00168203
2.112585	0.1324761	0.00188526
2.363148	0.1320488	0.00244891
2.705823	0.1382606	0.00253422
3.210075	0.1331989	0.00422001
3.715319	0.1310771	0.00677066
4.374695	0.1253019	0.00856003

Table D.17: Hadron $v_2(p_T)$ for 10-40% Centrality from Fig. 8.9

p_T	v_2	Stat. Err	Sys. Err. High	Sys. Err. Low
0.739294	0.0800614	0.00297890	0.00260549	0.01552167
0.912428	0.0916853	0.00145598	0.00251410	0.00677298
1.101255	0.1007086	0.00122561	0.00250810	0.00341121
1.297406	0.1138117	0.00125847	0.00580122	0.00273710
1.495323	0.1240270	0.00140325	0.00741335	0.00307097
1.694290	0.1376628	0.00164059	0.00945359	0.00346273
1.893384	0.1452708	0.00198151	0.01128349	0.00368274
2.114324	0.1526578	0.00221927	0.01335330	0.00389852
2.364125	0.1539837	0.00288237	0.01519390	0.00395758
2.706693	0.1588079	0.00297919	0.01813143	0.00411096
3.209111	0.1547816	0.00498823	0.01917312	0.00404493
3.713605	0.1525210	0.00796190	0.01889309	0.00402820
4.375061	0.1319270	0.01010275	0.01634207	0.00352964

Table D.18: Decay Muon $v_2(p_T)$ for 10-40% Centrality from Fig. 8.9

p_T	v_2	Stat. Err
0.736276	0.0751395	0.00297890
0.905473	0.0852374	0.00145598
1.096126	0.0980074	0.00122561
1.293739	0.1106401	0.00125847
1.492422	0.1225278	0.00140325
1.691766	0.1292447	0.00164059
1.891687	0.1369431	0.00198151
2.112607	0.1423274	0.00221927
2.363081	0.1406311	0.00288237
2.705840	0.1478733	0.00297919
3.210367	0.1446401	0.00498823
3.715571	0.1418198	0.00796190
4.372691	0.1355204	0.01010275

Table D.19: Hadron $v_2(centrality)$ and $v_2(N_{part})$ for 0.6 GeV/c $< p_T <$ 5.0 GeV/c from Figs. 8.10 and 8.11

Centrality (%)	N_{part}	v_2	Stat. Err	Sys. Err. High	Sys. Err. Low
2.44760	350.8	0.0450688	0.00185043	0.00439468	0.00169731
7.47576	301.7	0.0662464	0.00144085	0.00557723	0.00161356
12.4861	255.7	0.0897322	0.00128601	0.00756106	0.00219059
17.4854	216.4	0.1058065	0.00123186	0.00876739	0.00243124
22.4805	182.4	0.1206364	0.00123414	0.01000053	0.00277106
27.4728	152.7	0.1269564	0.00127526	0.01048089	0.00286595
32.4670	126.8	0.1384967	0.00136100	0.01144763	0.00313262
37.4540	104.2	0.1437103	0.00149461	0.01188344	0.00324603
42.4462	84.59	0.1439721	0.00171005	0.01190846	0.00324683
47.4314	67.73	0.1425812	0.00203845	0.01180283	0.00321639
52.4180	53.16	0.1364304	0.00255766	0.01130760	0.00308373
57.4075	40.96	0.1353517	0.00339642	0.01123383	0.00306926
62.3914	30.77	0.1246388	0.00477123	0.01036894	0.00284420
67.3619	22.64	0.1157966	0.00720615	0.00961577	0.00262042

Table D.20: Decay Muon $v_2(centrality)$ and $v_2(N_{part})$ for 0.6 GeV/c $< p_T <$ 5.0 GeV/c from Figs. 8.10 and 8.11

Centrality (%)	N_{part}	v_2	Stat. Err
2.50306	350.8	0.0393490	0.00185043
7.49582	301.7	0.0603213	0.00144085
12.4871	255.7	0.0796668	0.00128601
17.4764	216.4	0.0935783	0.00123186
22.4652	182.4	0.1063157	0.00123414
27.4563	152.7	0.1151613	0.00127526
32.4443	126.8	0.1231239	0.00136100
37.4328	104.2	0.1267932	0.00149461
42.4235	84.59	0.1291021	0.00171005
47.4083	67.73	0.1283329	0.00203845
52.3945	53.16	0.1258287	0.00255766
57.3820	40.96	0.1179910	0.00339642
62.3639	30.77	0.1136541	0.00477123
67.3498	22.64	0.1079635	0.00720615

Table D.21: Hadron $v_2(\eta)$ for 0.6 GeV/c $< p_T <$ 5.0 GeV/c from Fig. 8.12

Centrality (%)	η	v_2	Stat. Err.
0-20	1.39452	0.0851447	0.00203806
	1.65621	0.0871051	0.00115542
	1.92839	0.0890192	0.00142434
	2.18323	0.0853951	0.00283364
20-40	1.39502	0.144810	0.00199015
	1.65902	0.145116	0.00110675
	1.93269	0.141946	0.00124595
	2.18400	0.145817	0.00237641
40-70	1.39476	0.149971	0.00353350
	1.66254	0.154259	0.00191317
	1.93770	0.156077	0.00194061
	2.18597	0.152748	0.00351011

Table D.22: Decay Muon $v_2(\eta)$ for 0.6 GeV/c $< p_T <$ 5.0 GeV/c from Fig. 8.13

Centrality (%)	η	v_2	Stat. Err.
0-15	1.39049	0.0696274	0.001197710
	1.64962	0.0721472	0.000782929
	1.93931	0.0703411	0.000896067
	2.18690	0.0725410	0.001568870
15-30	1.39170	0.120506	0.001030080
	1.64973	0.119005	0.000667500
	1.94006	0.119252	0.000745846
	2.18647	0.118111	0.001295490
30-45	1.39265	0.144854	0.001359570
	1.65022	0.143945	0.000873628
	1.94028	0.140872	0.000952514
	2.18709	0.138168	0.00165574
45-70	1.39377	0.143376	0.00242732
	1.65063	0.141102	0.00155178
	1.94015	0.132636	0.00165255
	2.18765	0.136373	0.00288948

Table D.23: $v_2(\eta)$ Straight Line Fits from Figs. 8.12 and 8.13

P_0 and P_1 are provided for the fit. The single systematic error is applicable to $\eta = 1.2$ and 2.4. Systematic error for $\eta = 1.8$ is 0.0.

Particle Type	Centrality (%)	P_0	P_1	Sys. Err.
Hadrons	0-20	0.0816245	0.00323979	0.00359843
	20-40	0.1489910	-0.00279157	0.00408537
	40-70	0.1462520	0.004469210	0.00361562
Decay Muons	0-15	0.0690809	0.00120019	0.00132106
	15-30	0.1228700	-0.00206458	0.00212504
	30-45	0.1578790	-0.00875553	0.00168881
	45-70	0.1643170	-0.01485510	0.00140740

Bibliography

[1] U. Heinz. The strongly coupled quark-gluon plasma created at RHIC. *J. Phys. A*, 42:214003, 2009.

[2] B. Abelev et al. Centrality dependence of charged hadron and strange hadron elliptic flow from $\sqrt{s_{NN}}$ = 200 GeV Au+Au collisions. *Phys. Rev. C*, 77:054901, 2008.

[3] B.B. Back et al. Energy dependence of elliptic flow over a large pseudorapidity range in Au+Au collisions at the BNL Relativistic Heavy Ion Collider. *Phys. Rev. Lett.*, 94:122303, 2005.

[4] K. Nakamura and Particle Data Group. Review of particle physics. *J. Phys. G*, 37:075021, 2010.

[5] R.A. Dunlap. *An introduction to the physics of nuclei and particles*. Brooks/Cole – Thomson Learning Inc., 2003.

[6] The Particle Adventure: The Fundamentals of Matter and Force, http://www.particleadventure.org.

[7] F. Piquemal. Double beta decay review. *J. Phys.: Conf. Ser.*, 120:052004, 2008.

[8] R.P. Feynman. Very high-energy collisions of hadrons. *Phys. Rev. Lett.*, 23:1415, 1969.

[9] R.P. Feynman. Structure of the proton. *Science*, 183:601, 1974.

[10] R.G. Roberts. *The structure of the proton*. Cambridge University Press, 1990.

[11] T.A. Armstrong et al. Total hadronic cross section of γ rays in hydrogen in the energy range 0.265-4.215 GeV. *Phys. Rev. D*, 5:1640, 1972.

[12] L.W. Alvarez and F. Bloch. A quantitative determination of the neutron moment in absolute nuclear magnetons. *Phys. Rev.*, 57:111, 1940.

[13] G.L. Greene et al. Measurement of the neutron magnetic moment. *Phys. Rev. D*, 20:2139, 1979.

[14] R. Kikuchi et al. Production of neutral pions from electron-proton collisions. *Il Nuovo Cimento*, 4:1178, 1966.

[15] R. Bindel. *Elliptic flow measured with the PHOBOS spectrometer at RHIC*. PhD thesis, University of Maryland, College Park, MD, 2008.

[16] B. Jacak. The future of quark matter at RHIC. Quark Matter 2006, Shanghai, China, 2006, http://www.sinap.ac.cn/qm2006/.

[17] R. Bindel. Fluid-like properties of hot and dense nuclear matter. Analytical, Nuclear and Environmental Chemistry PhD Exit Seminar, University of Maryland, College Park, MD, 2007.

[18] A. Bickley. Quarkonium production in PHENIX. Hard Probes 2006, Pacific Grove, CA, 2006, http://hp2006.lbl.gov/.

[19] M. Harrison, T. Ludlam, and S. Ozaki. RHIC project overview. *Nucl. Inst. and Meth. A*, 499:235, 2003.

[20] H. Hahn et al. The RHIC design overview. *Nucl. Inst. and Meth. A*, 499:245, 2003.

[21] L. Evans and P. Bryant. LHC machine. *J. Inst.*, 3:S08001, 2008.

[22] C. Sturm and H. Stöcker. The Facility for Antiproton and Ion Research FAIR. *Phys. Part. Nucl. Lett.*, 8:865, 2011.

[23] F. Karsch. Lattice QCD at high temperature and density. *Lect. Notes Phys.*, 583:209, 2002.

[24] K. Adcox et al. Formation of dense partonic matter in relativistic nucleus-nucleus collisions at RHIC: Experimental evaluation by the PHENIX collaboration. *Nucl. Phys. A*, 757:184, 2005.

[25] H. Satz. Colour screening in SU(N) gauge theory at finite temperature. *Nucl. Phys. A*, 418:447, 1984.

[26] A. Adare et al. Enhanced production of direct photons in Au+Au collisions at $\sqrt{s_{NN}} = 200$ GeV and implications for the initial temperature. *Phys. Rev. Lett.*, 104:132301, 2010.

[27] A. Adare et al. Detailed measurement of the e^+e^- pair continuum in $p+p$ and Au+Au collisions at $\sqrt{s_{NN}} = 200$ GeV and implications for direct photon production. *Phys. Rev. C*, 81:034911, 2010.

[28] D.R. Williams. Sun fact sheet (NASA). 2004, http://nssdc.gsfc.nasa.gov/planetary/factsheet/sunfact.html.

[29] A. Bickley. *Charged antiparticle to particle ratios near midrapidity in d+Au and p+p collisions at* $\sqrt{s_{NN}}$ *= 200 GeV*. PhD thesis, University of Maryland, College Park, MD, 2004.

[30] C. Vale. *Elliptic flow in Au+Au collisions at 200 GeV per nucleon pair*. PhD thesis, Massachusetts Institute of Technology, Cambridge, MA, 2004.

[31] A.M. Poskanzer and S.A. Voloshin. Methods for analyzing anisotropic flow in relativistic nuclear collisions. *Phys. Rev. C*, 58:1671, 1998.

[32] B. Jacak and P. Steinberg. Creating the perfect liquid in heavy-ion collisions. *Physics Today*, 63:39, 2010.

[33] B.B. Back et al. Centrality and pseudorapidity dependence of elliptic flow for charged hadrons in Au+Au collisions at $\sqrt{s_{NN}}$ = 200 GeV. *Phys. Rev. C*, 72:051901, 2005.

[34] A. Adare et al. Scaling properties of azimuthal anisotropy in Au+Au and Cu+Cu collisions at $\sqrt{s_{NN}}$ = 200 GeV. *Phys. Rev. Lett.*, 98:162301, 2007.

[35] A. Adare et al. Azimuthal anisotropy of π^0 production in Au+Au collisions at $\sqrt{s_{NN}}$ = 200 GeV: Path-length dependence of jet quenching and the role of initial geometry. *Phys. Rev. Lett.*, 105:142301, 2010.

[36] B. Alver et al. Triangular flow in hydrodynamics and transport theory. *Phys. Rev. C*, 82:034913, 2010.

[37] S. Esumi. Collective flow measurement from the PHENIX experiment. *J. Phys. G*, 38:124010, 2011.

[38] A. Adare et al. Measurements of higher order flow harmonics in Au+Au collisions at $\sqrt{s_{NN}}$ = 200 GeV. *Phys. Rev. Lett.*, 107:252301, 2011.

[39] A. Adare et al. Elliptic and hexadecapole flow of charged hadrons in Au+Au collisions at $\sqrt{s_{NN}}$ = 200 GeV. *Phys. Rev. Lett.*, 105:062301, 2010.

[40] S. Esumi. Collective flow measurement from the PHENIX experiment. Quark Matter 2011, Annecy, France, 2011, http://qm2011.in2p3.fr/node/12.

[41] S. Huang. Measurements of charged hadron v_2 and v_4 in Au+Au collisions at different beam energy from PHENIX. 27$^{\text{th}}$ Winter Workshop on Nuclear Dynamics, Winter Park, CO, 2011, http://star.physics.yale.edu/ww2011/.

[42] M. Wysocki. *J/ψ production and suppression in Au+Au collisions at $\sqrt{s_{NN}}$=200 GeV*. PhD thesis, University of Colorado, Boulder, CO, 2011.

[43] B.B. Back et al. The PHOBOS detector at RHIC. *Nucl. Inst. and Meth. A*, 499:603, 2003.

[44] I. Arsene et al. Quark gluon plasma and color glass condensate at RHIC? The perspective from the BRAHMS experiment. *Nucl. Phys. A*, 757:1, 2005.

[45] K.H. Ackermann et al. STAR detector overview. *Nucl. Inst. and Meth. A*, 499:624, 2003.

[46] K. Adcox et al. PHENIX detector overview. *Nucl. Inst. and Meth. A*, 499:469, 2003.

[47] RHIC tunnel photograph. http://www.flickr.com/photos/brookhavenlab/sets/72157613690851651/.

[48] A. Pikin et al. RHIC EBIS: basics of design and status of commissioning. *J. Inst.*, 5:C09003, 2010.

[49] RHIC Design Manual. http://www.agsrhichome.bnl.gov/NT-share/rhicdm/00_toc1i.htm.

[50] PHENIX Drawings https://www.phenix.bnl.gov/WWW/run/drawing/index.html.

[51] T.K. Hemmick et al. PHENIX Central Arm tracking detectors. *Nucl. Inst. and Meth. A*, 499:489, 2003.

[52] A.D. Frawley et al. PHENIX Central Arm paricle ID detectors. *Nucl. Inst. and Meth. A*, 499:508, 2003.

[53] G. David et al. PHENIX calorimeter. *Nucl. Inst. and Meth. A*, 499:521, 2003.

[54] A. Franz et al. PHENIX magnet system. *Nucl. Inst. and Meth. A*, 499:480, 2003.

[55] K.F. Read et al. PHENIX Muon Arms. *Nucl. Inst. and Meth. A*, 499:537, 2003.

[56] Y. Tsuchimoto. Introduction to PHENIX Beam Beam Counter (BBC), PHENIX Focus Seminar, 2004, https://www.phenix.bnl.gov/WWW/run/04/focus/index_run4.

[57] M. Allen et al. PHENIX inner detectors. *Nucl. Inst. and Meth. A*, 499:549, 2003.

[58] K. Ikematsu et al. A start-timing detector for the collider experiment PHENIX at RHIC-BNL. *Nucl. Inst. and Meth. A*, 411:238, 1998.

[59] S. White et al. The RHIC Zero Degree Calorimeters. *Nucl. Inst. and Meth. A*, 470:488, 2001.

[60] M. Chiu. RHIC Zero Degree Calorimeter. PHENIX Focus Seminar, 2003, https://www.phenix.bnl.gov/WWW/run/04/focus/index_run4.

[61] J. Koster. *Measurement of transverse spin asymmetries in polarized proton-proton collisions, and the realization of new electromagnetic calorimeters for forward physics*. PhD thesis, University of Illinois, Urbana-Champaign, IL, 2010.

[62] A. Glenn. *Single muon production and implications for charm in* $\sqrt{s_{NN}} = 200$ *GeV Au+Au collisions*. PhD thesis, University of Tennessee, Knoxville, TN, 2004.

[63] K. Shoji. Illustration of Muon Identifier coordinates. Private Correspondence, 2011.

[64] E. Iarocci. Plastic streamer tubes and their applications in high energy physics. *Nucl. Inst. and Meth. A*, 15:30, 1983.

[65] R. Newby. *J/ψ production in Au-Au collisions at $\sqrt{s_{NN}}$ = 200 GeV*. PhD thesis, University of Tennessee, Knoxville, TN, 2003.

[66] C. Wong. *Introduction to high-energy heavy-ion collisions*. World Scientific Publishing Co. Pte. Ltd., 1994.

[67] R.M. Sternheimer, M.J. Berger, and S.M. Seltzer. Density effect for the ionization loss of charged particles in various substances. *Atomic Data and Nuclear Data Tables*, 30:261, 1984.

[68] E. Richardson et al. A Reaction Plane Detector for PHENIX at RHIC. *Nucl. Inst. and Meth. A*, 636:99, 2011.

[69] R. Bindel. Illustration of particle dispersion. Private Correspondence, 2007.

[70] W. Anderson et al. Design, construction, operation and performance of a Hadron Blind Detector for the PHENIX experiment. Submitted to *Nucl. Inst. and Meth. A*, 2011, http://arxiv.org/abs/1103.4277.

[71] GEANT — Detector Description and Simulation Tool, CERN Program Library Long Write-up W5013, CERN Geneva.

[72] E. Garcia et al. Array of scintillator counters for PHOBOS at RHIC. *Nucl. Inst. and Meth. A*, 474:38, 2001.

[73] J. Barrette et al. Proton and pion production relative to the reaction plane in Au + Au collisions at 11A GeV/c. *Phys. Rev. C*, 56:3254, 1997.

[74] B.B. Back et al. Energy dependence of directed flow over a wide range of pseudorapidity in Au + Au collisions at the BNL Relativistic Heavy Ion Collider. *Phys. Rev. Lett.*, 97:012301, 2006.

[75] A. Adare et al. Observation of direct-photon collective flow in $\sqrt{s_{NN}}$ = 200 GeV Au+Au collisions. Submitted to *Phys. Rev. Lett.*, 2011, http://arxiv.org/abs/1105.4126v2.

[76] A. Adare et al. Suppression of away-side jet fragments with respect to the reaction plane in Au + Au collisions at $\sqrt{s_{NN}}$ = 200 GeV. *Phys. Rev. C*, 84:024904, 2011.

[77] A. Adare et al. Transition in yield and azimuthal shape modification in dihadron correlations in relativistic heavy ion collisions. *Phys. Rev. Lett.*, 104:252301, 2010.

[78] A. Adare et al. Azimuthal correlations of electrons from heavy-flavor decay with hadrons in p+p and Au+Au collisions at $\sqrt{s_{NN}}$=200 GeV. *Phys. Rev. C*, 83:044912, 2011.

[79] A. Adare et al. Deviation from quark number scaling of the anisotropy parameter v_2 of pions, kaons, and protons in Au+Au collisions at $\sqrt{s_{NN}} = 200$ GeV. http://arxiv.org/abs/1203.2644.

[80] J. Haggerty et al. Letter of intent for PHENIX Reaction Plane Detector. Internal PHENIX Document, 2006, https://www.phenix.bnl.gov/WWW/p/detectors/rxn/RP_hp.html.

[81] J.C. Hill et al. PHENIX on-line systems. *Nucl. Inst. and Meth. A*, 499:560, 2003.

[82] B.G. Gibbard and T.G. Throwe. The RHIC Computing Facility. *Nucl. Inst. and Meth. A*, 499:814, 2003.

[83] T.G. Throwe et al. The Linux farms of the RHIC Computing Facility. *Nucl. Inst. and Meth. A*, 499:819, 2003.

[84] R. Brun and F. Rademakers. ROOT – an object oriented data analysis framework. *Nucl. Inst. and Meth. A*, 389:81, 1997. http://root.cern.ch.

[85] CERN Homepage, http://www.cern.ch.

[86] D.P. Morrison, W.A. Zajc, et al. PHENIX on-line and off-line computing. *Nucl. Inst. and Meth. A*, 499:593, 2003.

[87] M.L. Miller, K. Reygers, S.J. Sanders, and P. Steinberg. Glauber modeling in high energy nuclear collisions. *Ann. Rev. Nucl. Part. Sci.*, 57:205, 2007.

[88] R.D. Woods and D.S. Saxon. Diffuse surface optical model for nucleon-nuclei scattering. *Phys. Rev.*, 95:577, 1954.

[89] R. Wei et al. Glauber calculations of centrality dependent variables in Au+Au collisions at $\sqrt{s_{NN}} = 200$ GeV (Run 7). Internal PHENIX Document, 2009, https://www.phenix.bnl.gov/phenix/WWW/p/info/an/768/participant_ecc_main_v3-02.pdf.

[90] R. Frühwirth. Application of Kalman filtering to track and vertex fitting. *Nucl. Inst. and Meth. A*, 262:444, 1987.

[91] D. Hornback. *A measurement of open charm using single muons at forward angles for p+p collisions at center of mass energy 200 GeV.* PhD thesis, University of Tennessee, Knoxville, TN, 2008.

[92] S. Adler et al. Measurement of single muons at forward rapidity in p + p collisions at $\sqrt{s} = 200$ GeV and imlications for charm production. *Phys. Rev. D*, 76:092002, 2007.

[93] C. Silvestre et al. PHENIX suppression and elliptic flow measurements for $J/\psi \to \mu^+\mu^-$ in Run-7 au+au at $\sqrt{s_{NN}} = 200$ gev. Internal PHENIX Document, 2008, https://www.phenix.bnl.gov/phenix/WWW/p/info/an/669/run7_jpsi_muon_note.pdf.

[94] E. Richardson and A.C. Mignerey. Examining combinatoric background in the Muon Arms via a swap method for Run-7 $\sqrt{s_{NN}} = 200$ GeV Au+Au collisions. Internal PHENIX Document, 2010, https://www.phenix.bnl.gov/phenix/WWW/p/info/an/925/muon_arm_bkgrd_study.pdf.

[95] I.G. Arsene et al. Rapidity dependence of the proton-to-pion ratio in Au + Au and p + p collisions at $\sqrt{s_{NN}} = 62.4$ and 200 GeV. *Phys. Lett. B*, 684:22, 2010.

[96] I. Arsene et al. Centrality dependent particle production at y = 0 and y $\sim$ 1 in Au+Au collisions at $\sqrt{s_{NN}} = 200$ GeV. *Phys. Rev. C*, 72:014908, 2005.

[97] I.G. Bearden et al. Charged meson rapidity distributions in central Au + Au collisions at $\sqrt{s_{NN}} = 200$ GeV. *Phys. Rev. Lett.*, 94:162301, 2005.

[98] S. Huang. Identified particle v_2 measurements in Run7 200GeV Au+Au collisions. Internal PHENIX Document, 2011, https://www.phenix.bnl.gov/phenix/WWW/p/info/an/683/Identified_particle_v2_run7_6-1-03.pdf.

[99] S.J. Sanders. Forward-rapidity azimuthal and radial flow of identified particles for $\sqrt{s_{NN}} = 200$ GeV Au+Au and Cu+Cu collisions. Quark Matter 2009, Knoxville, TN, 2009, http://www.phy.ornl.gov/QM09.

[100] U. Heinz and P.F. Kolb. Rapidity dependent momentum anisotropy at RHIC. *J. Phys. G*, 30:S1229, 2004.

[101] D. Teaney, J. Lauret, and E.V. Shuryak. Flow at the SPS and RHIC as a quark-gluon plasma signature. *Phys. Rev. Lett.*, 86:4783, 2001.

[102] L. Chen, V. Greco, C.M. Ko, and P.F. Kolb. Pseudorapidity dependence of anisotropic flows in relativistic heavy-ion collisions. *Phys. Lett. B*, 605:95, 2005.

[103] C. Adler et al. Elliptic flow from two- and four-particle correlations in Au+Au collisions at $\sqrt{s_{NN}}$=130 GeV. *Phys. Rev. C*, 66:034904, 2002.

[104] S.J. Sanders. Rapidity and p_T dependence of identified-particle elliptic flow at RHIC. *J. Phys. G*, 34:S1083, 2007.

[105] B.B. Back et al. Significance of the fragmentation region in ultrarelativistic heavy-ion collisions. *Phys. Rev. Lett.*, 91:052303, 2003.

[106] G. Aad et al. The ATLAS experiment at the CERN Large Hadron Collider. *J. Inst.*, 3:S08003, 2008.

[107] G. Aad et al. Measurement of the pseudorapidity and transverse momentum dependence of the elliptic flow of charged particles in lead+lead collisions at $\sqrt{s_{NN}}$ = 2.76 TeV with the ATLAS detector. *Phys. Lett. B*, 707:330, 2012.

[108] CMS Collaboration. Azimuthal correlations of charged hadrons in PbPb collisions at $\sqrt{s_{NN}}$ = 2.76 TeV. 2011, http://cdsweb.cern.ch/record/1347788?ln=en.

[109] K. Aamodt et al. Elliptic flow of charged particles in Pb-Pb collisions at $\sqrt{s_{NN}}$ = 2.76 TeV. *Phys. Rev. Lett.*, 105:252302, 2010.

[110] A. Taranenko, R. Lacey, and S. Salnikov. Elliptic flow of charged hadrons in Au+Au collisions at $\sqrt{s_{NN}}$ = 200 GeV: Detailed comparison of PHENIX and STAR results. Internal PHENIX Document, 2009, https://www.phenix.bnl.gov/phenix/WWW/p/info/an/869/AN869-01.pdf.

[111] M. Adamczyk et al. The BRAHMS experiment at RHIC. *Nucl. Inst. and Meth. A*, 499:437, 2003.

[112] S.J. Sanders. Private Correspondence, 2009.

[113] S. Adler et al. Identified charged particle spectra and yields in Au+Au collisions at $\sqrt{s_{NN}}$ = 200 GeV. *Phys. Rev. C*, 69:034909, 2004.

[114] S.J. Sanders. Forward-rapidity azimuthal and radial flow of identified particles for $\sqrt{s_{NN}}$ = 200 GeV Au+Au collisions. *Nucl. Phys. A*, 830:179c, 2009.

[115] R. K. Choudhury et al. Technical design report of the Forward Silicon Vertex Tracker (FVTX). 2007, http://www.phenix.bnl.gov/WWW/fvtx/home/Documents/fvtx-proposal_11-1-07.pdf.

[116] T. Kempel. Evaluation of absorber effects on J/ψ mesons in the PHENIX Muon Arms. Internal PHENIX Document, 2010, https://www.phenix.bnl.gov/phenix/WWW/p/info/an/907/Absorber_Note-01.pdf.

[117] B. Alver et al. System size, energy, pseudorapidity, and centrality dependence of elliptic flow. *Phys. Rev. Lett.*, 98:242302, 2007.

[118] B. Alver et al. The importance of correlations and fluctuations on the initial source eccentricity in high-energy nucleus-nucleus collisions. *Phys. Rev. C*, 77:014906, 2008.

[119] T. Abbott, L. Kowalski, and L.P. Remsberg. Rapidity and invariant cross sections. http://www.phenix.bnl.gov/WWW/publish/erichard/tutorials/abbotkinematics.pdf.